NASA Conference Publication 2205

Sixth Annual Flight Mechanics/Estimation Theory Symposium October 1981

Eugene Lefferts, Editor
Goddard Space Flight Center

Proceedings of a Symposium
held at Goddard Space Flight Center
Greenbelt, Maryland
October 27-28, 1981

NASA

SIXTH ANNUAL

FLIGHT MECHANICS/ESTIMATION

THEORY SYMPOSIUM

OCTOBER 1981

EUGENE LEFFERTS, EDITOR

GODDARD SPACE FLIGHT CENTER

PROCEEDING OF A SYMPOSIUM
HELD AT GODDARD SPACE FLIGHT CENTER
GREENBELT, MARYLAND
OCTOBER 27-28, 1981

FOREWARD

The papers presented here have been derived primarily from speakers' summaries of talks presented at the Six Annual Flight Mechanics/Estimation Theory Symposium held October 27 and 28, 1981, at Goddard Space Flight Center. For the sake of completeness, abstracts are included of those talks for which summaries were unavailable at press time. Papers included in this document are presented as received from the authors with little or no editing.

CONTENTS

Papers No.

Foreward

SESSION I

"A Comparative Study of the Harris-Priester and Jacchia-Roberts and MSIS Atmospheric Density Models in the Context of Satellite Orbit Determination"

J. Cappellari, R. Kuseski, T. Lee, M. Mallick, and R. Shanklin (CSC) 1

"A General Method for Computing the Total Solar Radiation Force on Complex Spacecraft Structures"

F. Chan (Scientific Analysts and Consultants, Inc.) 2

"Solar Radiation Force Modeling for TDRS Orbit Determination"

T. Lee, M. Lucas, and R. Shanklin (CSC) 3

"Precision Orbit Computations for an Operational Environment"

D. Eggbert, R. Smith (CSC), and C. Doll (GSFC) 4

"Techniques for Increasing the Efficiency of Earth Gravity Calculations for Precision Orbit Determination"

A. Lyubomirsky and R. Smith (CSC) 5

"An Analysis of Simultaneous Satellite Visibility Time Span for Two Earth Observation Stations"

F. Chan (Phoenix Corporation) 6

SESSION II

"Distortion-Free Mapping of VISSR Imagery Data from Geosynchronous Satellites"

F. Chan (Scientific Analysts and Consultants, Inc.) 7

"Computational Aspects of Geometric Correction Data Generation on the Landsat-D Imagery Processing"

I. Levine (General Electric) 8

CONTENTS

(cont'd)

Papers No.

"Gipar System Capabilities and Initial Results"

N. Cyprych (CSC) and H. Heuberger (GSFC) 9

"The MMS Control Point Location Error Filter for Landsat-D"

I. Levine (General Electric) 10

"Onboard Utilization of Ground Control Points for Image Correction"

J. Lowrie (Martin Marietta Corporation) 11

SESSION III

"Effective Covariance Deweighting for Precision Estimation"

C. Velez and V. Tate (CTA) 12

"Spin-Axis Attitude Estimation and Sensor Bias Determination for AMPTE"

G. Neal and R. Thompson (CSC) and M. Shuster (BTS) 13

"A Mathematical Model of Landsat-D Attitude Dynamics with Internal Motion"

S. Oh (CSC) 14

"Spacecraft Attitude Pointing Performance During Orbit Adjust as a Function of Compensator Order"

S. Basuthankun, R. Duelfer, A. Peckjirn, and T. Stick (General Electric) 15

"Efficient Algorithms for Single Axis Attitude Estimation"

M. Shuster (BTS) 16

SESSION I

C. Newman, Chairman

A COMPARATIVE STUDY OF THE HARRIS-PRIESTER, JACCHIA-ROBERTS, AND MSIS ATMOSPHERIC DENSITY MODELS IN THE CONTEXT OF SATELLITE ORBIT DETERMINATION*

R. E. Shanklin, Jr., T. Lee, M. K. Mallick, R. A. Kuseski, and J. O. Cappellari, Jr.

Computer Sciences Corporation

ABSTRACT

Extensive comparisons of the Harris-Priester, Jacchia-Roberts, and MSIS (Mass Spectrometer/Incoherent Scatter) atmospheric density models as used in satellite orbit determination are summarized. The quantities compared include Bayesian weighted least squares differential correction statistics and orbit solution consistency and accuracy.

*This work was supported by the Operations Analysis Section, Operational Orbit Support Branch, Goddard Space Flight Center, National Aeronautics and Space Administration, under Contract NAS 5-24300.

SECTION 1 - INTRODUCTION

Atmospheric drag is a significant perturbation of Earth satellite orbits with perigee heights of less than 1000 kilometers. The acceleration of a spherical satellite due to atmospheric drag is given by the equation

$$\vec{A}_{drag} = -\frac{1}{2}\frac{C_D}{m} A \rho |\vec{V}| \vec{V}$$

where ρ = atmospheric density at the position of the satellite

$\vec{V}$ = satellite velocity relative to the atmosphere

A = satellite reference cross-sectional area

C_D = satellite drag coefficient

m = satellite mass

Therefore, calculation of the drag acceleration requires knowledge of the atmospheric density as a function of position and time.

This paper presents the results of a comparative study of three different global atmospheric density models in the context of orbit determination. The three models compared are the Harris-Priester (H-P) model, the Jacchia-Roberts (J-R) model, and the Mass Spectrometer/Incoherent Scatter (MSIS) model.

The Harris-Priester model is based on theoretical temperature profile solutions of the heat conduction equation under hydrostatic equilibrium conditions. The model assumes two heat sources: solar extreme ultraviolet (EUV) heating and an artificial heat source that produces the diurnal variation deduced from satellite drag calculations. In the modified Harris-Priester model used for this study, the EUV

heating level is selected by choosing among 10 different altitude-density profile tables representing 10 different levels of solar flux, and the diurnal variation is modeled by a correction calculated using a power of a cosine (References 1 and 2).

The Jacchia-Roberts model is based on empirical temperature profiles scaled by an upper boundary exospheric temperature (T_∞). Analytic density calculation is accomplished through integration of thermodynamic equations. The modeling includes corrections for EUV heating, solar particle flux (so-called geomagnetic) heating, semiannual variations, seasonal variations, and the diurnal variation (References 2 and 3).

The MSIS model is based on fitting spherical surface harmonic expansions to match the angular dependence exhibited by mass spectrometer and incoherent scatter measurements. The MSIS formulation includes sections that model EUV heating, solar particle flux heating, annual variations, semiannual variations, diurnal variations, semidiurnal variations, terdiurnal variations, and departures from diffusive equilibrium. MSIS modeling has been implemented in a special GTDS load module. Dr. Hedin and his associates at the Goddard Space Flight Center, who developed the model (Reference 4), contributed advice and some of their program subroutines during the GTDS implementation.

Table 1 shows sample density profiles for the three atmospheric models with two different solar EUV levels and one geomagnetic activity level. Figure 1 shows the Jacchia-Roberts and MSIS densities, relative to the Harris-Priester density, as a function of altitude. The figure shows maximum ratios as high as 2.0 but, as is apparent from the table, the three profiles are quite similar in overall shape.

TABLE 1. ATMOSPHERIC DENSITIES COMPUTED USING HARRIS-PRIESTER, JACCHIA-ROBERTS, AND MSIS MODELS

ALTITUDE (km)	DENSITY (kg/km^3)					
	HARRIS-PRIESTER		JACCHIA-ROBERTS		MSIS	
	$F_{10.7} = 125.0$	$F_{10.7} = 150.0$	$F_{10.7} = 116.2$ $\bar{F}_{10.7} = 135.1$	$F_{10.7} = 140.0$ $\bar{F}_{10.7} = 165.3$	$F_{10.7} = 116.2$ $\bar{F}_{10.7} = 135.1$	$F_{10.7} = 140.0$ $\bar{F}_{10.7} = 165.3$
150	.205 E + 1	.206 E + 1	.193 E + 1	.210 E + 1	.203 E + 1	.204 E + 1
200	.224 E 0	.255 E 0	.228 E 0	.270 E 0	.274 E 0	.313 E 0
250	.459 E – 1	.583 E – 1	.559 E – 1	.721 E – 1	.636 E – 1	.802 E – 1
300	.129 E – 1	.178 E – 1	.177 E – 1	.249 E – 1	.187 E – 1	.255 E – 1
350	.425 E – 2	.631 E – 2	.637 E – 2	.977 E – 2	.633 E – 2	.926 E – 2
400	.155 E –2	.247 E – 2	.246 E – 2	.413 E – 2	.236 E – 2	.368 E – 2
450	.521 E – 3	.879 E – 3	.835 E – 3	.157 E – 2	.780 E – 3	.131 E – 2
500	.218 E – 3	.392 E – 3	.353 E – 3	.724 E – 3	.324 E – 3	.582 E – 3
550	.963 E – 4	.182 E – 3	.155 E – 3	.344 E – 3	.139 E – 3	.266 E – 3
600	.451 E – 4	.851 E – 4	.706 E – 4	.169 E – 3	.619 E – 4	.125 E – 3
650	.227 E – 4	.451 E – 4	.339 E – 4	.851 E – 4	.285 E – 4	.600 E – 4
700	.112 E – 4	.217 E – 4	.154 E – 4	.394 E – 4	.120 E – 4	.259 E – 4
750	.691 E – 5	.127 E – 4	.878 E – 5	.219 E – 4	.623 E – 5	.134 E – 4
800	.464 E – 5	.804 E – 5	.548 E – 5	.128 E – 4	.352 E – 5	.728 E – 5
850	.316 E – 5	.462 E – 5	.348 E – 5	.737 E – 5	.200 E – 5	.378 E – 5
900	.245 E – 5	.301 E – 5	.258 E – 5	.500 E – 5	.137 E – 5	.236 E – 5
950	.198 E – 5	.201 E – 5	.201 E – 5	.361 E – 5	.102 E – 5	.158 E – 5
1000	.163 E – 5	.141 E – 5	.155 E – 5	.262 E – 5	.761 E – 6	.107 E – 5

8226/81

NOTES: 1. Kp = 3.3 FOR JACCHIA-ROBERTS DENSITY AND Ap = 33 FOR MSIS DENSITY ARE USED.

2. THESE PROFILES ARE FOR AUGUST 30, 1978, AT A LATITUDE OF 46^{o} N, AN EAST LONGITUDE OF 205^{o}, AND A LOCAL SOLAR TIME OF 1:40 P.M.

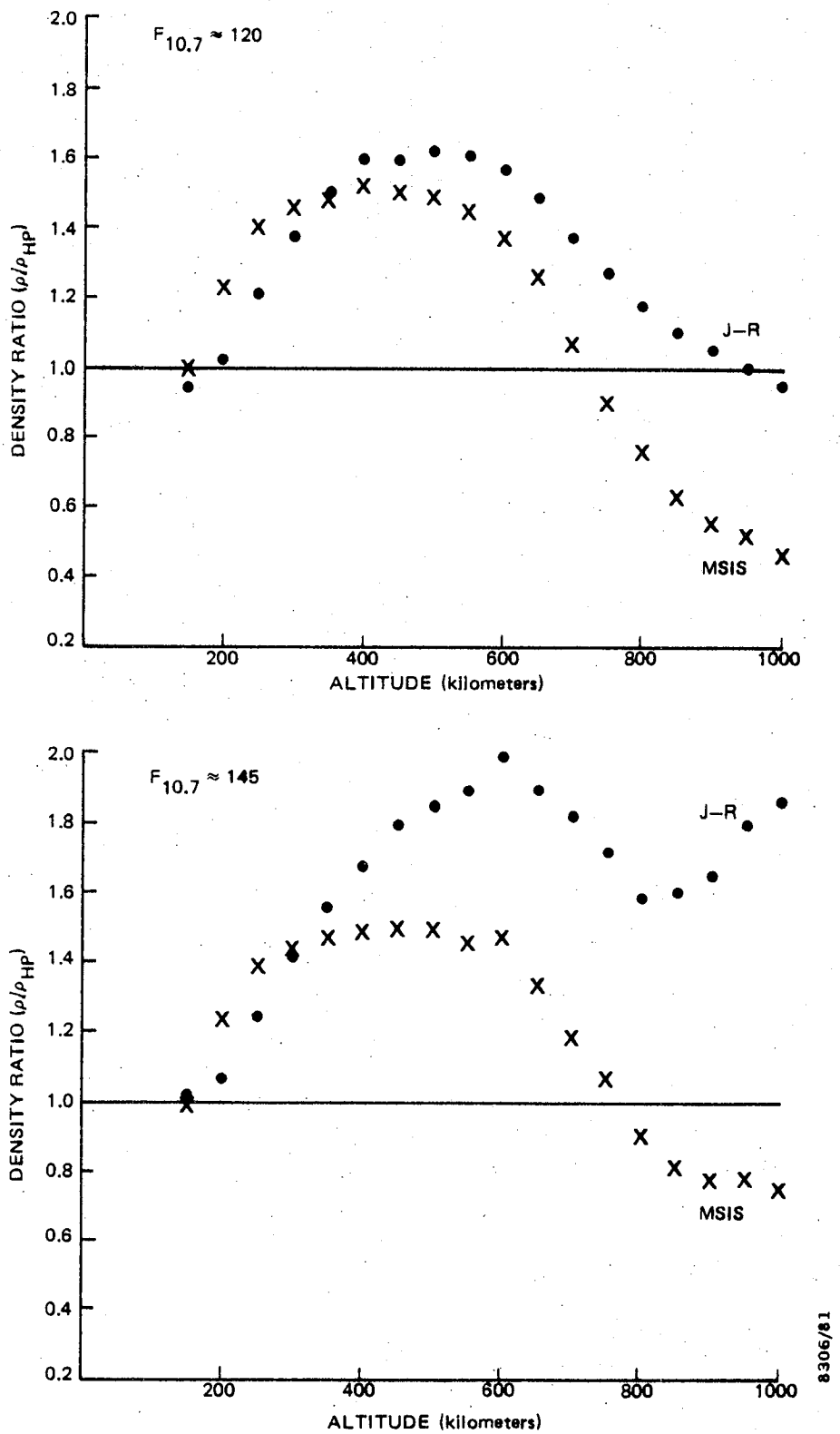

FIGURE 1. ATMOSPHERIC MODEL DENSITY RATIOS

SECTION 2 - COMPARATIVE STUDY STRUCTURE

All the results presented in Section 3 of this paper are based on Goddard Trajectory Determination System (GTDS) Bayesian weighted least squares differential correction solutions. Nine different series of six GTDS Differential Correction (DC) Program runs were made for each of the three atmospheric models. Three different satellites, with perigee heights between 310 and 560 kilometers, were studied; other orbital parameters for these satellites are given in Table 2. The nine series of orbit determination arcs are listed in Table 3.

Each series contains six 30-hour-arc solutions. The solutions are used to generate 30-hour ephemerides that overlap adjacent ephemerides by 6 hours. The ephemerides are then compared in order to determine the maximum position differences (in the orbital reference frame) during the overlap periods. The 162 DC Program solutions produce 135 maximum overlap position differences. These differences are used to evaluate the consistency and accuracy obtained when each of the three atmospheric models is used.

Each differential correction solution is made up of seven numbers: three position coordinates, three velocity coordinates, and the drag variation parameter (ρ_1), which is a scaling factor in the drag acceleration equation, i.e.,

$$\vec{A}_{drag} = -\frac{1}{2}\frac{C_D}{m} A \rho(1 + \rho_1) |\vec{V}| \vec{V}$$

This scaling factor is applied during generation of the ephemeris that uses the differential correction solution.

TABLE 2. SATELLITE ORBITAL ELEMENTS

SATELLITE	DATE	PERIGEE HEIGHT (kilometers)	APOGEE HEIGHT (kilometers)	INCLINATION (degrees)
AE-3	AUGUST 1, 1978	331	341	68
MAGSAT	OCTOBER 31, 1979	352	561	97
	MARCH 1, 1980	323	471	97
SAGE	FEBRUARY 19, 1979	560	655	55

8347/81

TABLE 3. COMPARATIVE STUDY SERIES

SERIES NUMBER	SATELLITE	TIMESPAN
1	AE-3	AUGUST 1—6, 1978
2		AUGUST 14—19, 1978
3		SEPTEMBER 2—8, 1978
4	MAGSAT	OCTOBER 31—NOVEMBER 5, 1979
5		DECEMBER 1—6, 1979
6		JANUARY 1—6, 1980
7		FEBRUARY 1—6, 1980
8		MARCH 1—6, 1980
9	SAGE	FEBRUARY 19—25, 1979

8347/81

Spacecraft attitude is not considered, since a spherical model is employed. Furthermore, no aerodynamic forces (e.g., lift) other than drag are modeled. The spherical approximation is crude for all three satellites, and it is possible that other aerodynamic forces are nonnegligible. However, it is reasonable to expect that both assumptions have a negligible effect on the results of this study, because the results are obtained by applying each of the three atmospheric models to the same arcs with the same observation sets. Simply stated, unmodeled aerodynamic forces should perturb the solutions for all three atmospheric models in a similar manner.

SECTION 3 - COMPARATIVE STUDY RESULTS

This section summarizes the results of this comparative study of atmospheric density models in the context of short-arc (30-hour) orbit determination. A detailed, run-by-run presentation of these results is available in Reference 5. Two cautionary remarks are appropriate.

First, these results should not be interpreted as a comparison of atmospheric models; conclusions about the relative merits of the models must be limited to this highly specialized context--short-arc orbit determination in which an average drag scaling factor is solved for.

Second, any series of orbit determination and ephemeris comparison runs may contain a few sporadic large overlap differences and a few differential corrections with large RMS residuals. Some of the runs included in this study show such large differences and/or high RMSs.

The average weighted RMSs and the average maximum position differences for the three AE-3 series are given in Table 4. The averages over all three series are also given, along with the ranges of the EUV heating index ($F_{10.7}$) and the solar particle flux index (K_p). The averages show that the Jacchia-Roberts overlap differences are about 11.5 percent (24 meters) smaller than the Harris-Priester averages and that the MSIS averages are about 19 percent (38 meters) larger than the Harris-Priester averages. The 62-meter difference between the Jacchia-Roberts and MSIS averages cannot be considered either large or significant.

The same information is given for Magsat in Table 5. This study includes five series of arcs. The Magsat results show that both the Jacchia-Roberts and MSIS average differences are about 9 percent larger than the Harris-Priester average

TABLE 4. COMPARATIVE ATMOSPHERIC DENSITY MODEL STUDY RESULTS FOR AE-3 (AUGUST AND SEPTEMBER 1978)

SERIES	RANGE OF $F_{10.7}$ $\left(10^{-22}\ \text{watt}/(\text{m}^2\text{-Hz})\right)$	RANGE OF K_p	HARRIS-PRIESTER MODEL		JACCHIA-ROBERTS MODEL		MSIS MODEL	
			AVERAGE WEIGHTED RMS	MAXIMUM POSITION DIFFERENCE (meters)	AVERAGE WEIGHTED RMS	MAXIMUM POSITION DIFFERENCE (meters)	AVERAGE WEIGHTED RMS	MAXIMUM POSITION DIFFERENCE (meters)
AUGUST 1-6	106.0-117.6	0-6	4.9	191	5.2	175	8.4	265
AUGUST 14-19	115.6-134.9	0-6	7.3	225	7.8	217	8.5	324
SEPTEMBER 2-8	159.8-181.1	0-6	7.3	209	8.4	163	7.2	164
AVERAGES	–	–	6.5	208	7.2	184	8.0	251

8226/81

TABLE 5. COMPARATIVE ATMOSPHERIC DENSITY MODEL STUDY RESULTS FOR MAGSAT (NOVEMBER AND DECEMBER 1979; JANUARY, FEBRUARY, AND MARCH 1980)

PERIOD	RANGE OF $F_{10.7}$ VARIATION (10^{-22} watts m^{-2} Hz^{-1})	RANGE OF K_p VARIATION	HARRIS-PRIESTER RESULTS		JACCHIA-ROBERTS RESULTS		MSIS RESULTS	
			WEIGHTED RMS	MAXIMUM POSITION DIFFERENCE (meters)	WEIGHTED RMS	MAXIMUM POSITION DIFFERENCE (meters)	WEIGHTED RMS	MAXIMUM POSITION DIFFERENCE (meters)
OCT. 31 NOV. 5, 1979	207.5–214.9	0–4	8.3	204	7.8	176	8.0	190
DEC. 1–6, 1979	152.2–223.4	0–4	12.4	204	11.5	175	12.8	255
JAN. 1–6, 1980	188.9–212.4	1–5	9.4	213	9.5	166	11.3	288
FEB. 1–6, 1980	212.6–231.7	0–4	12.7	326	12.5	298	13.8	313
MAR. 1–6, 1980	170.2–176.7	0–3	9.8	161	13.4	396	10.0	169
AVERAGES	--		10.6	222	10.9	242	11.2	243

8226/81

differences. As in the case of AE-3, the Magsat results demonstrate that the three atmospheric density models are comparable in the context of this study.

The average RMSs and overlap position differences for the series of SAGE arcs are given in Table 6. Both the RMSs and the overlap differences agree to within 3 percent; all three atmospheric models produce essentially equivalent errors.

TABLE 6. COMPARATIVE ATMOSPHERIC DENSITY MODEL STUDY RESULTS FOR SAGE (FEBRUARY 19–25, 1979)

ATMOSPHERIC DENSITY MODEL USED	AVERAGE WEIGHTED RMS	AVERAGE MAXIMUM POSITION DIFFERENCE (meters)
HARRIS–PRIESTER	10.9	108
JACCHIA–ROBERTS	11.2	114
MSIS	11.0	112

8226/81

NOTE: DURING THIS PERIOD, $F_{10.7}$ VARIED FROM 196.0 TO 237.7 X 10^{-22} WATTS METER^{-2} HERTZ^{-1}, AND K_p VARIED FROM 1 TO 7.

SECTION 4 - CONCLUSION

The results presented in this paper support the conclusion that, for satellites above 300 kilometers, the Harris-Priester, Jacchia-Roberts, and MSIS atmospheric density models all produce roughly similar density profiles and essentially comparable orbit determination results when the drag variation parameter is solved for and orbit quality is measured by adjacent arc overlap comparisons. It is impossible to predict which of the three models will produce the best fit or best predictions for any given orbit determination arc. However, for some problem arcs, switching atmospheric models may result in marked solution improvements.

REFERENCES

1. I. Harris and W. Priester, "Atmospheric Structure and Its Variations in the Region From 120 to 800 Km," COSPAR International Reference Atmosphere (CIRA) 1965, Space Research IV, North Holland Publishing Co., Amsterdam

2. Goddard Space Flight Center, X-582-76-77, Mathematical Theory of the Goddard Trajectory Determination System, J. O. Cappellari, Jr., C. E. Velez, and A. J. Fuchs (editors), April 1976

3. L. G. Jacchia, Revised Static Models of the Thermosphere and Exosphere With Empirical Temperature Profiles, Smithsonian Astrophysical Observatory Special Report No. 332, Cambridge, Massachusetts, May 1971

4. A. E. Hedin et al., "A Global Tropospheric Model Based on Mass Spectrometer and Incoherent Scatter Data: MSIS 1. N_2 Density and Temperature," Journal of Geophysical Research, 1977, vol. 82, pp. 2139-2147

5. Computer Sciences Corporation, CSC/TM-81/6166, Comparative Study of Atmospheric Density Models in the Context of Spacecraft Orbit Determination, R. Kuseski, T. Lee, M. Mallick, and R. Shanklin, Jr., September 1981

A GENERAL METHOD FOR COMPUTING THE TOTAL SOLAR RADIATION FORCE ON COMPLEX SPACECRAFT STRUCTURES

F. K. Chan

Scientific Analysts and Consultants, Inc.

4114 Heathfield Road, Rockville, Md. 20853

ABSTRACT

A general approach has been developed for computing the force due to solar radiation on an object of arbitrary shape. This method circumvents many of the existing difficulties in computational logic presently encountered in the direct analytical or numerical evaluation of the appropriate surface integral. It may be applied to complex spacecraft structures for computing the total force arising from either specular or diffuse reflection or even from non-Lambertian reflection and re-radiation.

SECTION 1 - INTRODUCTION

The problem of computing the total force or total torque on a spacecraft due to solar radiation is, in general, very difficult. Mathematically, it requires the evaluation of a surface integral over only the illuminated region of the surface. Even if the illuminated region is known by some other means, the evaluation of the surface integral can still be very difficult analytically in the case of complex spacecraft structures. Moreover, if the illuminated region is not known a priori, the difficulties are compounded by having to determine self-shadowing. For non-convex objects, it is not trivially governed by a condition such as $\cos\theta \gtrless 0$ where θ is the angle between the sun vector and the outward vector normal to the surface. In fact, the logic in the present methods becomes extremely complicated and is also not fool-proof. Additional difficulties are introduced by choosing a set of points (vertices) on the surface to form a network in approximating it; this inadvertently leads to book-keeping problems associated with selecting appropriate sets of points for computing surface elements.

This paper presents a general method for performing the computations without encountering the difficulties described above. It does not attempt to evaluate the surface integral directly as it presents itself as done in the usual methods, but considers the same problem from a slightly different point of view which leads to the same results.

SECTION 2 - ANALYSIS

Consider an arbitrarily shaped object as illustrated in Figure 1.1.

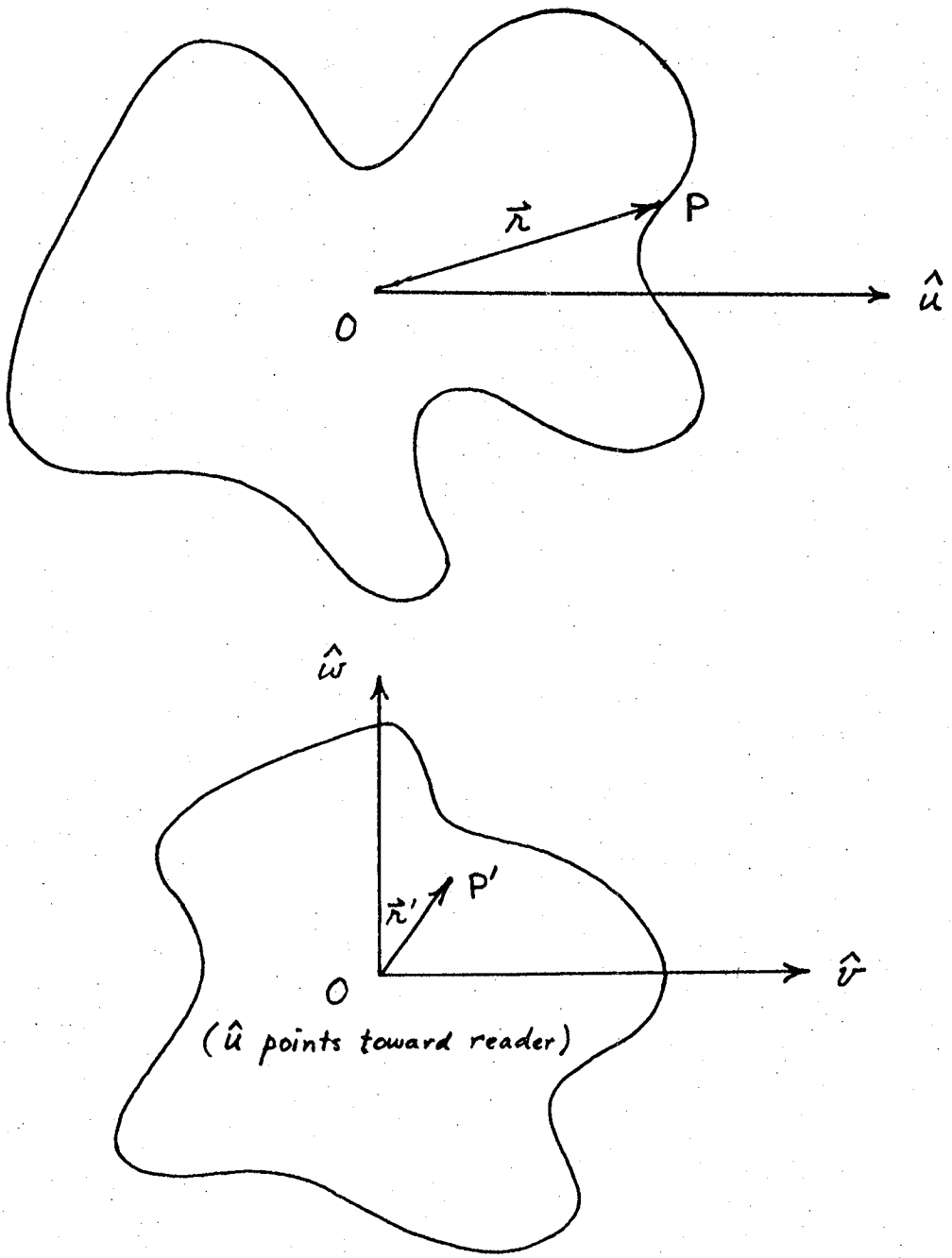

Figure 1.1 - Illustration of an Arbitrarily Shaped Object

For convenience, let us use the following notation:

$\hat{u}$ = unit vector along a specified direction

$\hat{v}$ = any unit vector orthogonal to $\hat{u}$, i.e., $\hat{u} \cdot \hat{v} = 0$

$\hat{w}$ = third unit vector forming orthogonal triad, i.e., $\hat{w} = \hat{u} \times \hat{v}$

O = origin of coordinate system

P = any point on object's surface

$\vec{r}$ = vector from O to P

P' = projection of P onto (v,w)-plane

$\vec{r}'$ = projection of $\vec{r}$ onto (v,w)-plane

(x,y,z) = reference orthogonal system for describing object's surface.

In the present analysis, it is advantageous to choose $\hat{u}$ to be opposite in direction to the incident solar radiation. (Alternatively, it can also be chosen to be in the same direction.)

The vectors $\hat{u}$ and $\vec{r}$ are known in the (x,y,z) system. In general, if $\vec{V}$ is any vector, then it may be more explicitly written in the (x,y,z)-space as $\vec{V}_{(x,y,z)}$ and has components V_x, V_y, V_z. That is, we implicitly mean

$$\vec{V}_{(x,y,z)} = V_x \hat{x} + V_y \hat{y} + V_z \hat{z} \tag{1.1}$$

In view of the definition of the vector $\hat{v}$, we may choose $v_z = 0$. Then, it may be shown that the other two components are given by

$$v_x = \pm \frac{u_y}{\sqrt{(u_x^2 + u_y^2)}} \tag{1.2}$$

$$v_y = - \frac{u_x v_x}{u_y} \tag{1.3}$$

From the definition of $\hat{w}$, we obtain

$$\hat{w} = -u_z v_x \hat{x} + u_z v_x \hat{y} + (u_x v_y - u_y v_x) \hat{z} \tag{1.4}$$

Therefore, any vector $\vec{V}_{(x,y,z)}$ can be transformed to $\vec{V}_{(u,v,w)}$ by the equation

$$\vec{V}_{(u,v,w)} = T \vec{V}_{(x,y,z)} \tag{1.5}$$

where the transformation matrix T is given by

$$T = \begin{bmatrix} u_x & u_y & u_z \\ v_x & v_y & 0 \\ w_x & w_y & w_z \end{bmatrix} \tag{1.6}$$

Then, using equation (1.6), the vector $\vec{r}_{(x,y,z)}$ is transformed and we obtain

$$r_u = r_x u_x + r_y u_y + r_z u_z \tag{1.7}$$

$$r_v = r_x v_x + r_y v_y \tag{1.8}$$

$$r_w = r_x w_x + r_y w_y + r_z w_z \tag{1.9}$$

Consequently, the projection vector $\vec{r}'$ is simply given by

$$\vec{r}' = r_v \hat{v} + r_w \hat{w} \tag{1.10}$$

The component r_u of the vector $\vec{r}$ is particularly important because, for a complex spacecraft structure, it can be used to yield the surface element which is directly exposed to solar radiation. This can be seen

as follows: For any given point on the (v,w)-plane (i.e., for any given vector $\vec{r}'$), the point on the spacecraft which is not shadowed is the one which has the maximum value of r_u, independent of where the origin of the (u,v,w) coordinate system is chosen. (It would be the minimum value of r_u if the vector $\hat{u}$ had been chosen to be in the same direction as the incident solar radiation.) To find the illuminated surface of the spacecraft, we proceed by dividing the (v,w)-plane into cells of area $\Delta v \Delta w$ with cell centers (v_i, w_j). At these cell centers, the illuminated surface element is the one which has the maximum value of r_u. In this way, the logic of determining self-shadowing is extremely simple as compared to other methods which encounter considerable difficulty conceptually and computationally. Thus, given a vector $\vec{r}' = (0, v_i, w_j)$, the vector $\vec{r} = ([r_u]_{max}, v_i, w_j)$ corresponding to the illuminated point is determined. It is then transformed to the (x,y,z)-space by the equation

$$\vec{r}_{(x,y,z)} = T^T \vec{r}_{(u,v,w)} \tag{1.11}$$

At this point $\vec{r}_{(x,y,z)}$, the unit vector $\hat{n}_{(x,y,z)}$ normal to the surface is then obtained by

$$\hat{n}_{(x,y,z)} = \frac{\nabla \Phi}{|\nabla \Phi|} \tag{1.12}$$

where $\Phi(x,y,z) = 0$ denotes the equation of the surface in a region containing $\vec{r}$. For convenience, the direction of $\hat{n}$ is chosen such that

$$\hat{n} \cdot \hat{u} \geq 0 \tag{1.13}$$

This choice of direction automatically makes $\hat{n}$ the outward unit normal

if the surface element belongs to a closed surface. Moreover, it establishes a direction for $\hat{n}$ in the case of a surface for which an outward unit normal is meaningless (such as a finite planar surface). The vector $\hat{n}_{(x,y,z)}$ is then transformed to the (u,v,w)-space using the equation

$$\hat{n}_{(u,v,w)} = T\,\hat{n}_{(x,y,z)} \tag{1.14}$$

The cell (v_i, w_j) whose area is $\Delta v \Delta w$ corresponds to a surface element whose area is denoted by ΔA. It is evident that we have

$$\Delta A = \frac{\Delta v \Delta w}{(\hat{n} \cdot \hat{u})} = \frac{\Delta v \Delta w}{n_u} \tag{1.15}$$

Therefore, the force $\Delta\vec{F}$ exerted on this surface element is given by

$$\Delta \vec{F} = \vec{p}\,\Delta A \tag{1.16}$$

where $\vec{p}$ is the solar radiation pressure vector acting on the surface element. Under very general conditions of surface reflection and re-radiation, it can be shown that this pressure vector has the form

$$\vec{p} = -\frac{S\cos\theta}{c}\left[C_1\,\hat{u} + (C_2\cos\theta + C_3)\,\hat{n}\right] \tag{1.17}$$

where S is the solar radiation flux per unit area normal to the flux, c is the velocity of light, and θ is the angle between the sun vector and the normal to the surface element, i.e.,

$$\cos\theta = \hat{n} \cdot \hat{u} \tag{1.18}$$

The coefficients C_1, C_2 and C_3 may change with time due to aging of

of the surface material by some complex process.

For the case of specular reflection and diffuse (Lambertian) reflection, the C_k's are given by [1]

$$C_1 = (1 - k_1) \tag{1.19}$$

$$C_2 = 2k_1 \tag{1.20}$$

$$C_3 = \frac{2}{3} k_2 \tag{1.21}$$

where k_1 = the fraction of incident radiation reflected specularly

k_2 = the fraction of incident radiation reflected diffusely by a Lambertian surface.

It is to be noted that in equations (1.19) - (1.21), it is <u>not</u> implicitly assumed that the surface is radiating the entire energy incident on it, i.e., it is <u>not</u> necessary that we require the condition $k_1 + k_2 = 1$ in order to obtain these equations.

For the case of specular reflection and non-Lambertian reflection and re-radiation [2], a little consideration will reveal that the C_k's are given by

$$C_1 = (1 - \beta\gamma) \tag{1.22}$$

$$C_2 = 2\beta\gamma \tag{1.23}$$

$$C_3 = B_f \left[\gamma(1-\beta) + \frac{(B_f e_f - B_b e_b)}{B_f (e_f + e_b)} (1-\gamma) \right] \tag{1.24}$$

where γ = the fraction of incident radiation reflected (specularly and otherwise)

β = the fraction of reflected radiation that is specular

B_f, B_b = non-Lambertian coefficients for front and back surfaces respectively

e_f, e_b = emission values for front and back surfaces respectively.

In passing, it may be noted that we have the relations

$$k_1 = \beta\gamma \tag{1.25}$$

$$k_2 = \gamma(1-\beta) \tag{1.26}$$

Moreover, it may be remarked that the form of equation (1.17) is valid for the more general non-Lambertian reflection and re-radiation which have a period of π in the azimuthal variable. In other words, Lambertian reflection means that the intensity I of the reflection is given by

$$I = I_0 \cos\theta \tag{1.27}$$

Then, the case of non-Lambertian reflection and re-radiation expressed by equation (1.24) would correspond to an intensity which is independent of the azimuthal variable ϕ and is of the form

$$I = I_0 f(\theta) \tag{1.28}$$

where implicitly we exclude the case of Lambert's law, i.e.,

$$f(\theta) \neq \cos\theta \tag{1.29}$$

The even more general case means that we can have reflection and re-radiation for which the intensity is of the form

$$I = I_0 f(\theta, \phi) \tag{1.30}$$

where $$f(\theta, \phi) = f(\theta, \phi + \pi) \tag{1.31}$$

Finally, to compute the total force $\vec{F}$ due to solar radiation, we obtain from equations (1.15) - (1.19) the following expressions

$$F_u = -\Delta v \, \Delta w \, \frac{S}{c} \sum_{\{v_i, w_j\}} \left[C_1 + (C_2 n_u + C_3) n_u \right] \tag{1.32}$$

$$F_v = -\Delta v \, \Delta w \, \frac{S}{c} \sum_{\{v_i, w_j\}} \left[(C_2 n_u + C_3) n_v \right] \tag{1.33}$$

$$F_w = -\Delta v \, \Delta w \, \frac{S}{c} \sum_{\{v_i, w_j\}} \left[(C_2 n_u + C_3) n_w \right] \tag{1.34}$$

It is also trivial to compute the total torque $\vec{M}$ on the spacecraft by using the equations

$$\Delta \vec{M} = \vec{r} \times \Delta \vec{F} \tag{1.35}$$

$$\vec{M} = \sum_{\{v_i, w_j\}} (\vec{r} \times \Delta \vec{F}) \tag{1.36}$$

but this will not be done here.

SECTION 3 - DISCUSSION

It is obvious that the method just discussed does not encounter logic problems in determining self-shadowing. Moreover, because the points $\{v_i, w_j\}$ are first chosen on the projection plane, it circumvents the difficulties in book-keeping experienced in the other method of choosing vertices on the surface of the object. Furthermore, it does not require excessive core for storing the vertex data such as coordinates, area of surface element, normal vector, solar incidence angle, etc. This advantage becomes evident by evaluating the expressions in equations (1.32) - (1.34) using three accumulators (one for each force component), not having to store the set of points $\{v_i, w_j\}$. Finally, if greater accuracy is desired, it suffices only to choose smaller values $\Delta v^* \Delta w^*$, multiply the previous result by the factor $\left(\frac{\Delta v^* \Delta w^*}{\Delta v \, \Delta w}\right)$, and then perform computations only for the additional points newly introduced into the set $\{v_i, w_j\}$. This advantage cannot be realized in the other method of choosing vertices on the surface of the object. In that case, in going to a refined model with additional vertices, it is necessary to perform the entire computations starting from the beginning each time.

SECTION 4 - CONCLUSION

From the foregoing discussion, it may be concluded that the present method has the following advantages:

1. It does not experience logic problems in determining self-shadowing.
2. It does not encounter the book-keeping problems arising in the case of choosing vertices on the surface of the object.
3. It does not require excessive core for storing vertex data.
4. It can utilize previously obtained results in going to progressively more refined models.

REFERENCES

(1) Eliasberg, P. E., "Introduction to the Theory of Flight of Artificial Earth Satellites," Moscow (1965). Translation, Jerusalem (1967).

(2) Wright, J., "Solar Sail Force Model," Jet Propulsion Laboratory Interoffice Memorandum 312/77.3-201 (28 March 1977).

SOLAR RADIATION FORCE MODELING FOR TDRS ORBIT DETERMINATION*

Taesul Lee, Michael J. Lucas, and Robert E. Shanklin, Jr.

Computer Sciences Corporation

ABSTRACT

The relative orbit determination accuracies resulting from several TDRS models used for solar radiation force calculations are evaluated. These models include spherical, single-plate, and restricted two-plate models. The plate models can be adjusted in both area and reflectivity through differential correction. The restricted two-plate model has an Earth-pointing plate and a solar plate; the orientation of the solar plate is restricted to rotation about an axis perpendicular to the satellite's orbital plane.

Simulated TDRS observations are generated from an ephemeris obtained using a 69-component TDRS model. These observations are processed by least squares differential correction in order to find optimized parameters for the spherical, single-plate, and multi-plate models. The solutions for the parameters and the state vector are then used to generate ephemerides that are compared with the 69-component ephemeris to estimate the expected orbit determination accuracies achievable with the various TDRS models.

*This work was supported by the Operations Analysis Section, Operational Orbit Support Branch, Goddard Space Flight Center, National Aeronautics and Space Administration, under Contract NAS 5-24300.

SECTION 1 - INTRODUCTION

A study of the solar radiation pressure (SRP) effect on orbit determination for a Tracking and Data Relay Satellite (TDRS) has been carried out using simulated data. The TDRS System consists of three geosynchronous satellites--TDRS East, TDRS West, and TDRS Spare--and one common ground tracking facility. These satellites will be placed in circular, nearly equatorial orbits at a height of 36,000 kilometers above the surface of the Earth. The study is designed to determine whether a complex SRP model for a TDRS can be satisfactorily replaced by a simpler SRP model, such as a constant-effective-area model or a two-plate model. In addition, different tracking station configurations are used to investigate the possible dependence of the results on the tracking station geometry.

A similar study carried out by Chan et al. (Reference 1) used a 69-component TDRS SRP model and a two-plate model with four adjustable parameters. The adjustable parameters were determined by using a least squares procedure to minimize the position differences between two ephemerides, one obtained using the 69-component model and one obtained using the two-plate model.

Another investigation related to the present study was carried out by Shanklin et al. (Reference 2) in which a constant-effective-area SRP model and a two-plate model were compared using real ATS-6 S-Band tracking data. This study, however, was somewhat incomplete due to the limited availability of ATS-6 tracking data. The current study is an extension of that work and follows the same approach as that used in Reference 1 in constructing the TDRS SRP models. The current study, however, uses simulated bilateration and S-Band tracking data in the differential correction process

instead of position differences between the two ephemerides as used by Chan.

The study plan is as follows. First, a 69-component SRP model of a TDRS, which is available in the Research and Development version of the Goddard Trajectory Determination System (RDGTDS), is used to compute a truth ephemeris, which is subsequently used to generate various types of simulated observations using the Mission Data Generation System (MDGS). The MDGS produces raw data in a 75-byte format, and the Generalized Data Handler (GDH) converts these raw data into the 60-byte format for the Goddard Trajectory Determination System (GTDS). Second, these simulated data are used in regular GTDS Differential Correction (DC) Program runs to find optimized SRP parameters for the constant-effective-area model and for the two-plate model. The constant-effective-area model contains one adjustable parameter, and the two-plate model contains four adjustable parameters. Any combination of the four parameters of the two-plate model can be solved for in a given DC Program run. Third, ephemerides are generated using the final elements and SRP parameters obtained from the DC Program runs, and these ephemerides are then compared with the original truth ephemeris.

Brief descriptions of the TDRS solar radiation pressure models are given in Section 2 and generation of the simulated data is discussed in Section 3. The results of various DC Program runs and ephemeris comparisons are presented in Section 4, and the conclusions are summarized in Section 5.

SECTION 2 - DESCRIPTION OF MODELS

The 69-component model is composed of 69 distinctive parts. The components with relatively large areas are the two solar panels, whose normals make minimum angles with the satellite-Sun line; the antennas; the antenna feeds; and the top, bottom, and six sides of the main body (see Reference 1 for details).

The simplest SRP model used to approximate the 69-component model is the constant-effective-area model. In this model, the area for the SRP calculation is assumed to be constant and always normal to the satellite-Sun line. The force due to the solar radiation pressure (Reference 3) is given by

$$\vec{f}_{SRP} = -\nu\, a\, P\, (1 + \eta)\, \vec{u}_{Sun} \qquad (2\text{-}1)$$

where ν = eclipse factor

a = constant area

P = solar radiation pressure on a perfectly absorbing surface at the position of the satellite

η = surface reflectivity

$\vec{u}_{Sun}$ = unit vector along the satellite-Sun line

The solar radiation pressure is inversely proportional to the square of the distance from the Sun, and the eclipse factor, ν, equals zero if the satellite is in the Earth's shadow and equals one if it is not. The right-hand side of Equation (2-1) represents the sum of two parts: the part due to the absorption of the solar radiation, which is proportional to $(1 - \eta)$, and the part due to the reflected radiation, which is proportional to 2η. This model is currently available in GTDS.

The second model used to approximate the 69-component model is a two-plate model, which has an Earth-pointing plate and

a solar plate. The solar plate is hinged along an axis normal to the satellite's orbital plane and is always rotated about that axis so as to maximize the amount of sunlight falling on the plate. The force due to the solar radiation pressure for the two-plate model is given by the sum of four terms:

$$\begin{aligned}\vec{f}_{SRP} = -aP[&2\alpha_E\eta_E|\vec{u}_{Sun}\cdot\vec{R}|(\vec{u}_{Sun}\cdot\vec{R})\,\vec{R}\\&+\alpha_E(1-\eta_E)|\vec{u}_{Sun}\cdot\vec{R}|\,\vec{u}_{Sun}\\&+2\alpha_s\eta_s\left(\vec{u}_{Sun}\cdot\vec{N}_s\right)^2\vec{N}_s\\&+\alpha_s(1-\eta_s)(\vec{u}_{Sun}\cdot\vec{N}_s)\,\vec{u}_{Sun}]\end{aligned} \qquad (2\text{-}2)$$

where a = reference area

P = solar radiation pressure on a perfectly absorbing surface at the position of the satellite

α_E = scale factor for the area of the Earth-pointing plate

α_S = scale factor for the area of the solar plate

η_E = reflectivity of the Earth-pointing plate

η_S = reflectivity of the solar plate

$\vec{u}_{Sun}$ = unit vector along the satellite-Sun line

$\vec{R}$ = unit position vector of the satellite

$\vec{N}_S$ = unit vector normal to the sunny side of the solar plate

In Equation (2-2), the first term is due to the reflection by the Earth-pointing plate, the second term is due to the absorption by the Earth-pointing plate, the third term is due to the reflection by the solar plate, and the fourth term is due to the absorption by the solar plate. The two area scale factors, α_E and α_S, and the two reflectivities, η_E and η_S, are adjustable parameters. In a given DC Program

run, any combination or all of these four parameters can be solved for. Instead of α_E, η_E, α_s, and η_s, an alternative set of four parameters, ξ_1, ξ_2, ξ_3, and ξ_4, may also be defined (and solved for):

$$\xi_1 = \alpha_E \eta_E$$

$$\xi_2 = \alpha_E (1 - \eta_E)$$

$$\xi_3 = \alpha_s \eta_s$$

$$\xi_4 = \alpha_s (1 - \eta_s)$$

SECTION 3 - GENERATION OF SIMULATED DATA

Tracking data for this study were generated using a satellite ephemeris tape obtained from a special RDGTDS Program load module that contains a 69-component TDRS model for SRP evaluation. This ephemeris tape was used by the MDGS Program to generate a second tape of raw range and Doppler simulated data. This simulated data tape was used by the GDH Program to generate tracking data in a format appropriate for use in the GTDS two-plate load module. Two types of tracking data were generated in this manner: Applications Technology Satellite Ranging (ATSR) bilateration data and Unified S-Band (USB) two-way data.

3.1 ATSR BILATERATION DATA

ATSR bilateration data were generated using the ground station at White Sands, New Mexico, as the ATSR tracker and the ground stations at Mojave, California; Rosman, North Carolina; Madrid, Spain; Quito, Ecuador; and Santiago, Chile, as the ATSR ground transponders. Figure 1 shows the positions of these six sites in relation to the expected subsatellite point for the relay satellite.

Using these five tracker/ground transponder pairs, tracking data with the following characteristics were produced:

- Frequency: 5600 MHz (C-Band)
- Primary frequency offset: 5.8875 MHz
- Transponder delay: 0.0 km
- Tracking mode: satellite-to-ground phase-locked transponder
- Major range tone/minor range tone: 100 kHz/8 Hz

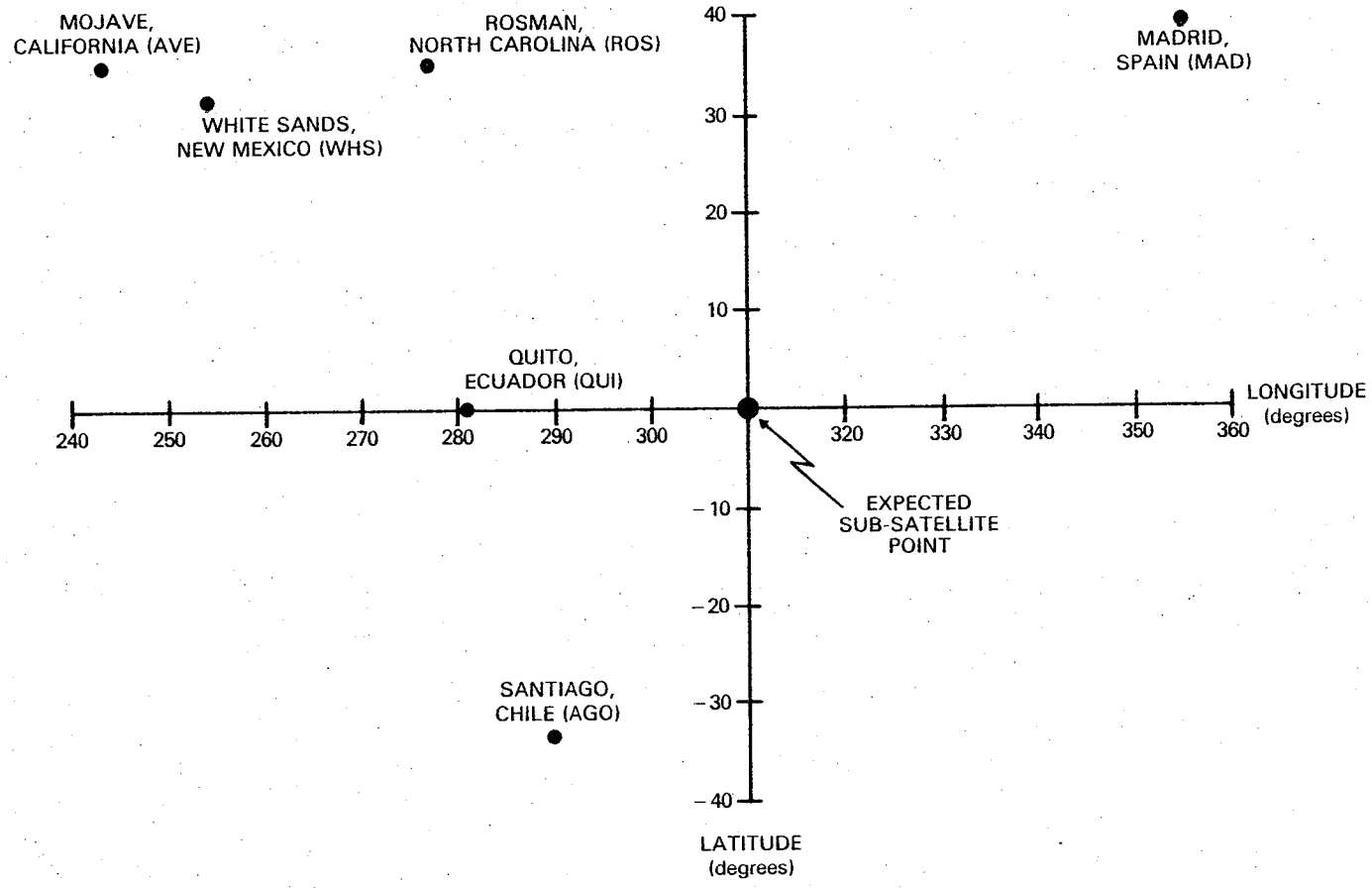

FIGURE 1. SITE LOCATIONS AND EXPECTED SUB-SATELLITE POINT

- Uplink pilot frequency/downlink pilot frequency: 6150 MHz/4150 MHz
- Doppler count mode: nondestruct

Data were produced at a rate of six observations per minute for the first 25 minutes of each hour, starting at 0.0 hours on October 2, 1980, and ending at 0.0 hours on October 3, 1980. Each tracker/ground transponder pair was enabled for tracking over the discrete time interval shown in Table 1. No observation corrections were applied and no observation noise was applied.

3.2 USB TWO-WAY DATA

USB two-way data (for which the receiving and transmitting sites are the same) were generated using the ground stations at Mojave, Rosman, Madrid, Quito, and Santiago. Tracking data with the following characteristics were produced:

- Transmit frequency: 2106 MHz
- Transponder delay: 0.0 km
- Ranging equipment: Spaceflight Tracking and Data Network (STDN) Ranging Equipment (SRE)
- Major range tone: 20 kHz

Data were produced for the first 25 minutes of each hour, over the same time period, at the same rate, and with the same corrections that were used for the ATSR bilateration data. Each ground station was enabled for tracking over the discrete time interval shown in Table 2.

TABLE 1. TRACKING INTERVALS FOR ATSR TRACKER/ GROUND TRANSPONDER PAIRS

TRACKER/GROUND TRANSPONDER PAIR	MINUTES OF THE HOUR DURING WHICH THE PAIR IS ENABLED
WHITE SANDS/ROSMAN	00 TO 05
WHITE SANDS/MOJAVE	05 TO 10
WHITE SANDS/QUITO	10 TO 15
WHITE SANDS/MADRID	15 TO 20
WHITE SANDS/SANTIAGO	20 TO 25

8347/81

TABLE 2. TRACKING INTERVALS FOR USB GROUND STATIONS

GROUND STATION	MINUTES OF THE HOUR DURING WHICH GROUND STATION IS ENABLED
ROSMAN	00 TO 05
MOJAVE	05 TO 10
QUITO	10 TO 15
MADRID	15 TO 20
SANTIAGO	20 TO 25

SECTION 4 - DIFFERENTIAL CORRECTION SOLUTIONS AND EPHEMERIS COMPARISON RESULTS

Differential correction solutions were obtained using different SRP models, different types of simulated observations, and different tracking station configurations.

4.1 RESULTS OBTAINED USING BILATERATION DATA AND TWO GROUND TRANSPONDERS

The results of DC Program solutions obtained using bilateration range and Doppler data and five different combinations of solve-for parameters in the two-plate model are presented in Tables 3 and 4. The simulated bilateration data used were obtained using the TDRSS ground station at White Sands and two ground transponders at Rosman, North Carolina, and Mojave, California. The five different SRP options used were

- Constant-effective-area model with C_R solved for
- Two-plate model with α_E and α_s solved for
- Two-plate model with ξ_1 and ξ_2 solved for
- Two-plate model with ξ_3 and ξ_4 solved for
- Two-plate model with ξ_1, ξ_2, and ξ_3 solved for

The third option, in which ξ_1 and ξ_2 are solved for, is equivalent to solving for α_E and η_E, the scale factor and reflectivity of the Earth-pointing plate, respectively. Similarly, the fourth option is equivalent to solving for α_s and η_s. In this particular set of DC Program runs, the values of the SRP parameters in the two-plate model that were not solved for were set equal to zero. Thus, the third and fourth options discussed above actually represent single-plate models rather than two-plate models.

An identical set of a priori elements, obtained from the truth ephemeris of the 69-component SRP model, was used for all of the options. It is seen from Tables 3 and 4 that the option of using the Earth-pointing plate alone gives the

TABLE 3. DIFFERENCES BETWEEN THE FINAL AND A PRIORI ELEMENTS (FINAL MINUS A PRIORI)

CHANGES IN ELEMENTS	RUN CONFIGURATION				
	CONSTANT EFFECTIVE AREA SOLVED FOR	TWO-PLATE MODEL α_E AND α_S SOLVED FOR	TWO-PLATE MODEL ξ_1 AND ξ_2 SOLVED FOR	TWO-PLATE MODEL ξ_3 AND ξ_4 SOLVED FOR	TWO-PLATE MODEL ξ_1, ξ_2, AND ξ_3 SOLVED FOR
ΔX (meters)	−5.81	−3.42	−24.16	−1.62	−2.63
ΔY (meters)	−12.62	−9.57	−18.43	−8.59	−7.61
ΔZ (meters)	−24.80	16.07	−109.73	−38.56	11.17
$\Delta \dot{X}$ (cm/sec)	0.052	0.036	0.250	0.008	0.029
$\Delta \dot{Y}$ (cm/sec)	−0.041	−0.024	−0.221	−0.005	−0.025
$\Delta \dot{Z}$ (cm/sec)	−0.118	−0.138	0.243	−0.141	−0.084

8316/81

NOTES: 1. THE SAME SET OF A PRIORI ELEMENTS WAS USED FOR ALL DC PROGRAM RUNS.

2. THE QUANTITIES α_E AND α_S DENOTE SCALE FACTORS FOR THE AREAS OF THE EARTH-POINTING PLATE AND THE SOLAR PLATE, RESPECTIVELY. THE PARAMETERS ξ_1, ξ_2, ξ_3, AND ξ_4 ARE DEFINED AS FOLLOWS: $\xi_1 = \alpha_E \eta_E$, $\xi_2 = \alpha_E (1 - \eta_E)$, $\xi_3 = \alpha_S \eta_S$, $\xi_4 = \alpha_S (1 - \eta_S)$, WHERE η_E AND η_S DENOTE THE REFLECTIVITY OF THE EARTH-POINTING PLATE AND THE SOLAR PLATE, RESPECTIVELY.

TABLE 4. DC PROGRAM STATISTICS AND SRP PARAMETERS SOLVED FOR

PARAMETERS	RUN CONFIGURATION				
	CONSTANT EFFECTIVE AREA SOLVED FOR	TWO-PLATE MODEL α_E AND α_S SOLVED FOR	TWO-PLATE MODEL ξ_1 AND ξ_2 SOLVED FOR	TWO-PLATE MODEL ξ_3 AND ξ_4 SOLVED FOR	TWO-PLATE MODEL ξ_1, ξ_2, AND ξ_3 SOLVED FOR
WEIGHTED RMS	0.0558	0.0346	0.3238	0.0546	0.0329
STANDARD DEVIATION					
RANGE (meters)	0.514	0.584	2.206	0.481	0.593
DOPPLER (millihertz)	0.914	0.473	5.416	0.898	0.431
SRP PARAMETERS SOLVED FOR	C_R = 1.38	α_E = 0.281 α_S = 1.219	ξ_1 = 1.971 ξ_2 = 0.551	ξ_3 = 19.482 ξ_4 = −37.588	ξ_1 = 0.175 ξ_2 = 0.146 ξ_3 = 0.602

8316/81

poorest results, whereas the other options all give comparable results. Similar conclusions are supported by Figures 2 and 3, which represent 24-hour ephemeris comparison results between the original 69-component ephemeris and the ephemerides obtained using the DC Program solutions for different SRP options. The results obtained using the second option, in which α_E and α_s were solved for, are not shown because they are very similar to the results obtained using the fourth option. Only the along-track and cross-track position differences are shown in Figures 2 and 3, because the radial position differences were much smaller than the along-track or cross-track position differences.

The single-plate option using the Earth-pointing plate alone gives the worst position errors. The single-plate option using the solar plate alone gives significantly better results. In fact, the option using the solar plate alone gives the smallest along-track position differences of all the different options used.

There are two features worth mentioning. First, there is no significant difference between the constant-effective-area model and the more complex two-plate model options. Second, in all cases studied, there are quite sizable cross-track position differences, equal to or larger than the along-track differences.

In order to examine the influence of the tracking geometry on the orbit determination results, a different pair of ground transponders (Rosman and Santiago) was used for the same series of DC Program solutions discussed above. Ephemeris comparison results obtained using these differential correction solutions were then compared with the corresponding results obtained using the pair of ground transponders at Rosman and Mojave; the only significant difference between

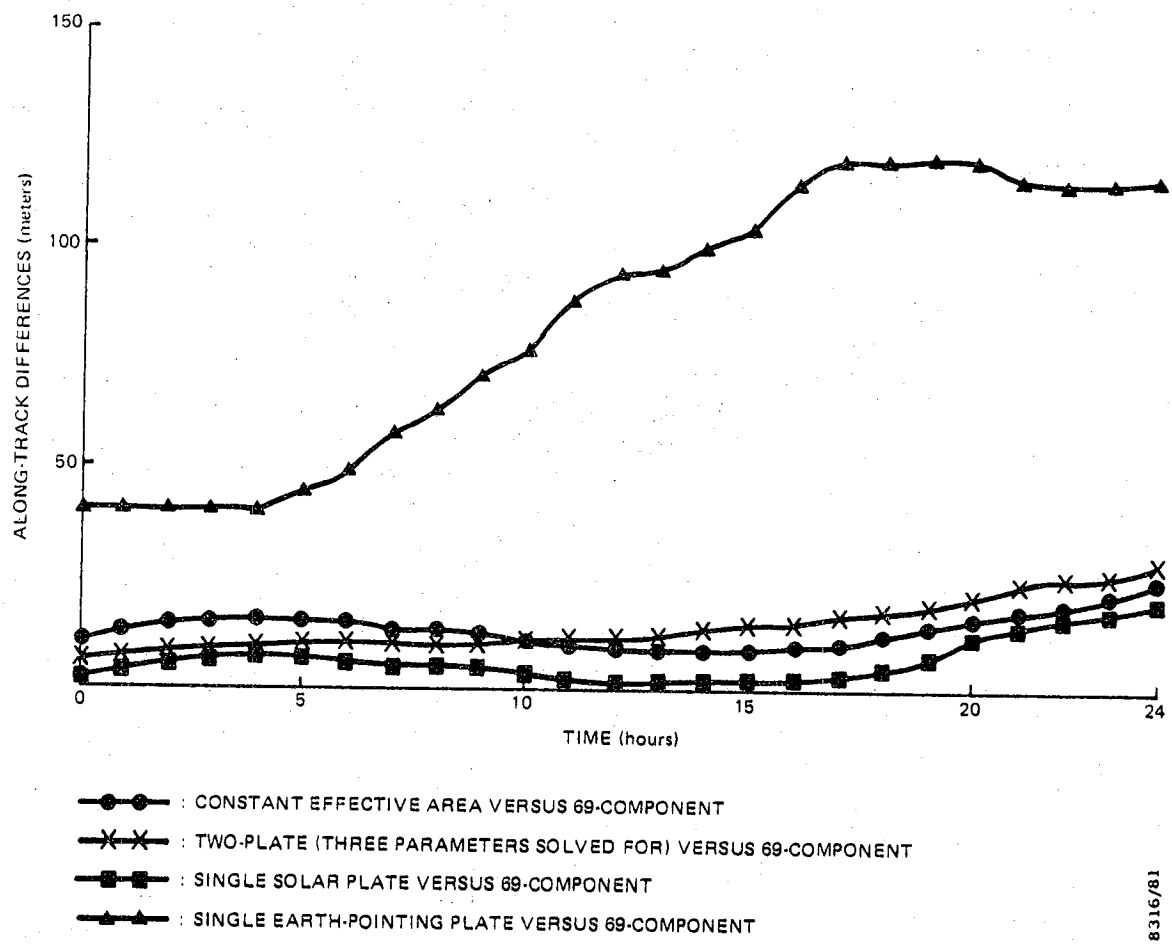

FIGURE 2. ALONG-TRACK POSITION DIFFERENCES FROM 24-HOUR EPHEMERIS COMPARISON RESULTS

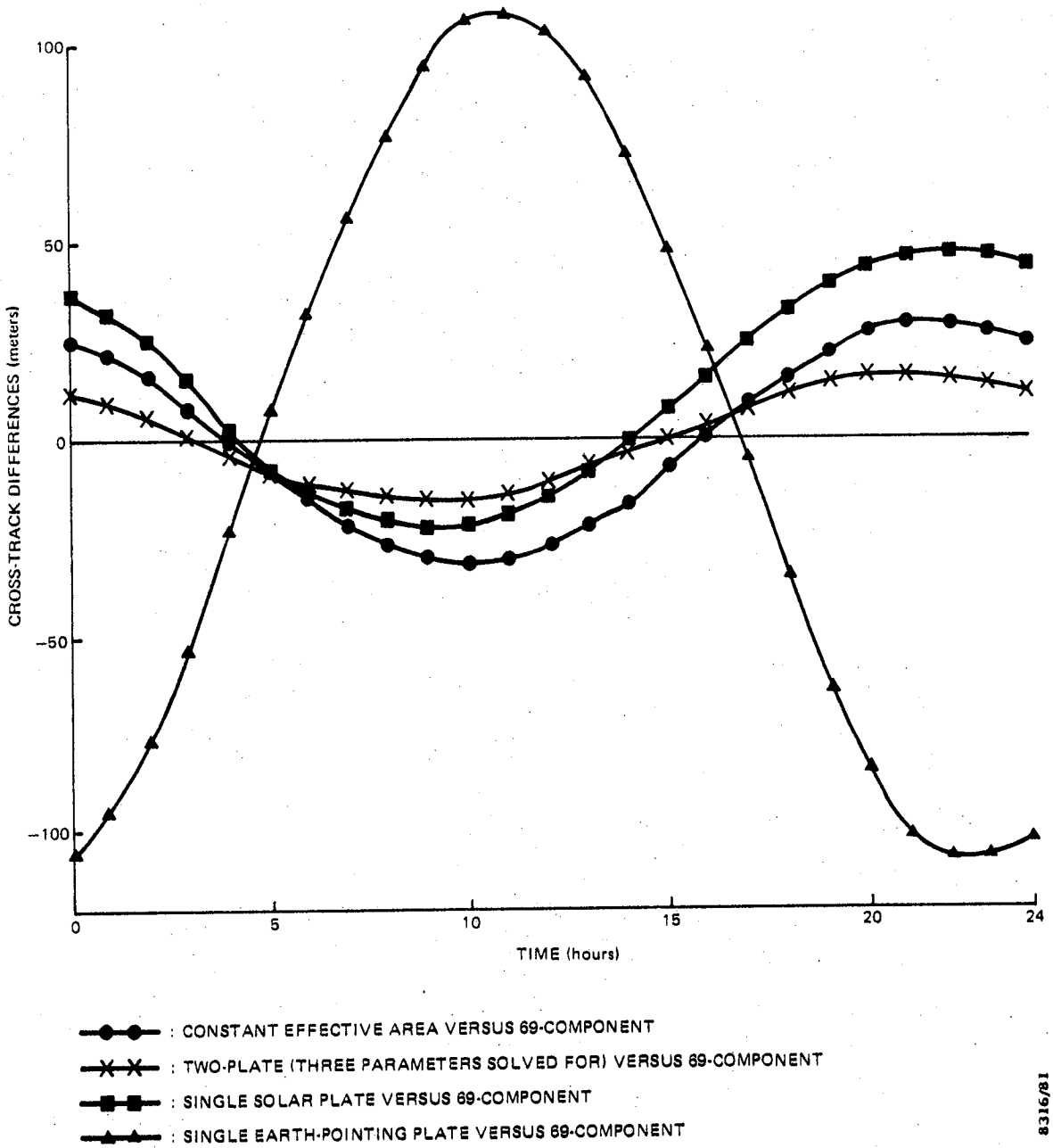

FIGURE 3. CROSS-TRACK POSITION DIFFERENCES FROM 24-HOUR EPHEMERIS COMPARISON RESULTS

the two sets of results was in the cross-track position differences. The maximum cross-track position differences obtained using the Rosman and Santiago ground transponders were found to be less than 10 meters, whereas the corresponding differences obtained using the Rosman and Mojave ground transponders were larger than 20 meters.

4.2 RESULTS OBTAINED USING S-BAND RANGE DATA AND TWO GROUND TRACKING STATIONS

Differential correction solutions for a 24-hour TDRS arc were obtained using S-Band range data and two different tracking station configurations. In the first set of solutions, the two ground stations at Rosman and Mojave were used, and in the second set of solutions, the two stations at Rosman and Santiago were used. The results of 24-hour ephemeris comparisons are summarized in Figures 4 and 5. It is seen from Figures 4 and 5 that the results obtained using S-Band range data are generally worse than the corresponding results obtained using bilateration data. The along-track position differences shown in Figure 4 indicate that the Rosman/Mojave configuration gives somewhat better results than does the Rosman/Santiago configuration. In the case of the cross-track position differences shown in Figure 5, the situation is reversed; the Rosman/Santiago configuration gives somewhat better results than does the Rosman/Mojave configuration.

4.3 RESULTS OBTAINED USING MORE THAN TWO GROUND TRACKING STATIONS

The same 24-hour TDRS arc studied in Sections 4.1 and 4.2 was used in a set of DC Program runs using more than two ground tracking facilities. In the case of bilateration data, three ground transponders, located at Mojave, Santiago, and Madrid, and five ground transponders, located at Mojave, Santiago, Madrid, Rosman, and Quito, were used. Ephemeris

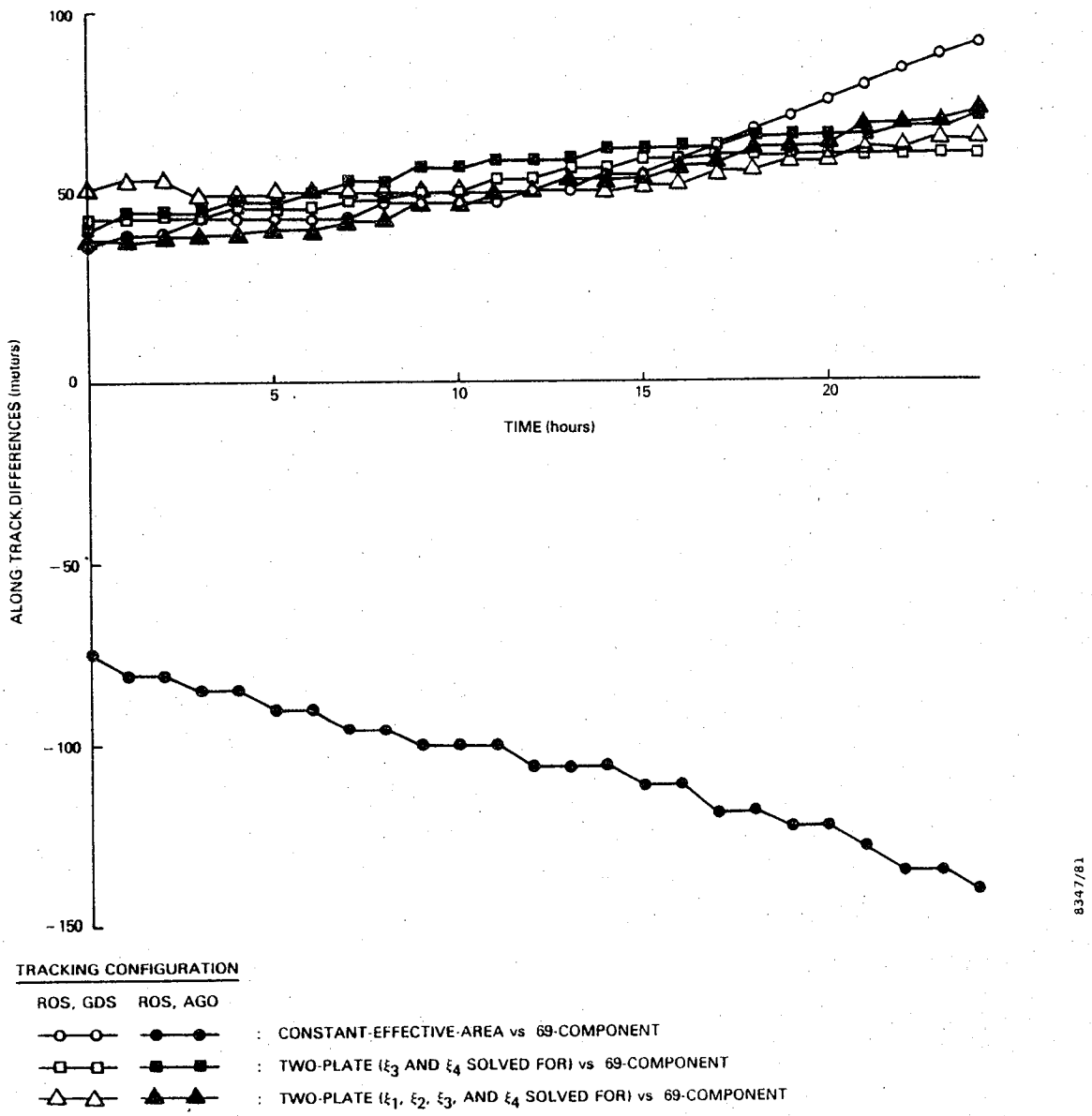

FIGURE 4. ALONG-TRACK POSITION DIFFERENCES FROM 24-HOUR EPHEMERIS COMPARISON RESULTS

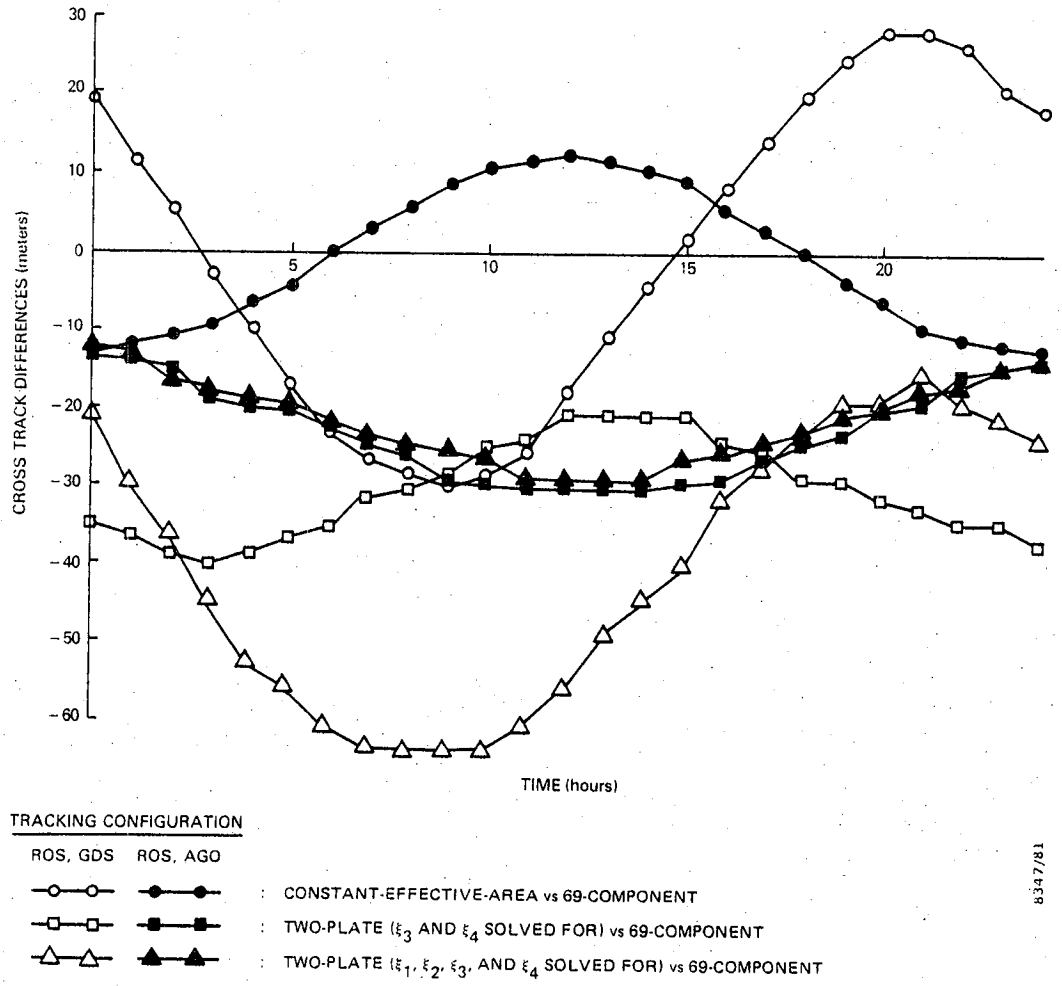

FIGURE 5. CROSS-TRACK POSITION DIFFERENCES FROM 24-HOUR EPHEMERIS COMPARISON RESULTS

comparison results obtained using the three ground transponders were similar to the results obtained using the five ground transponders. Typical along-track, cross-track, and radial position differences were 6.0, 1.0, and 1.0 meters, respectively. No significant difference was found among the different models used for the solar radiation pressure computation as long as the initial state vector and the solar radiation pressure parameters were solved for.

Similar analyses were carried out using more than two S-Band tracking stations. Two sets of differential correction solutions were obtained using three tracking stations at Mojave, Madrid, and Santiago and four tracking stations at Mojave, Rosman, Madrid, and Santiago. Ephemeris comparison results obtained using these differential correction solutions are summarized in Tables 5 and 6. There is no essential difference between the results obtained using three tracking stations and the results obtained using four tracking stations. These results show a significant improvement over the corresponding results obtained using only two S-Band tracking stations. Cross-track position differences were reduced by almost a factor of 10 and along-track differences were also substantially reduced. However, none of the results obtained using S-Band tracking data were as good as the corresponding results obtained using bilateration data.

TABLE 5. CROSS-TRACK AND ALONG-TRACK POSITION DIFFERENCES OBTAINED USING THREE USB GROUND STATIONS (MAD, AVE, AGO)

EPHEMERIDES COMPARED	MAXIMUM CROSS-TRACK DIFFERENCE (meters)	MAXIMUM ALONG-TRACK DIFFERENCE (meters)
CONSTANT-EFFECTIVE-AREA vs 69-COMPONENT	3.1	24.6
TWO-PLATE (α_E AND α_S SOLVED FOR) vs 69-COMPONENT	2.8	23.5
SINGLE SOLAR PLATE (ξ_3 AND ξ_4 SOLVED FOR) vs 69-COMPONENT	7.1	22.2
TWO-PLATE (ξ_1, ξ_2, ξ_3, AND ξ_4 SOLVED FOR) vs 69-COMPONENT	6.5	20.2

8347/81

TABLE 6. CROSS-TRACK AND ALONG-TRACK POSITION DIFFERENCES OBTAINED USING FOUR USB GROUND STATIONS (MAD, AVE, AGO, ROS)

EPHEMERIDES COMPARED	MAXIMUM CROSS-TRACK DIFFERENCE (meters)	MAXIMUM ALONG-TRACK DIFFERENCE (meters)
CONSTANT-EFFECTIVE-AREA vs 69-COMPONENT	3.3	26.2
TWO-PLATE (α_E AND α_S SOLVED FOR) vs 69-COMPONENT	3.2	25.9
SINGLE SOLAR PLATE (ξ_3 AND ξ_4 SOLVED FOR) vs 69-COMPONENT	4.4	26.7
TWO-PLATE (ξ_1, ξ_2, ξ_3, AND ξ_4 SOLVED FOR) vs 69-COMPONENT	4.2	25.0

8347/81

SECTION 5 - CONCLUSIONS

A study of solar radiation pressure (SRP) as it affects TDRS orbits was performed using simulated bilateration data, simulated direct two-way data, and various ground station configurations. Orbit determination results obtained using constant-effective-area and two-plate SRP modeling were compared with each other and with an ephemeris obtained using a 69-component TDRS SRP model. The conclusion of this study can be summarized as follows:

- The constant-effective-area solar radiation pressure model and the two-plate model give essentially the same quality results when both the state and the SRP parameters are solved for. The maximum position differences between the 69-component model truth ephemeris and an ephemeris determined using solved-for elements and SRP parameters can be reduced to less than 10 meters if proper bilateration tracking configurations are used in solving for the elements and the SRP parameters.
- When using only two ground tracking facilities, the Rosman/Santiago combination gives smaller cross-track position errors than does the Rosman/Mojave combination.
- Results obtained using three ground tracking facilities (located in a triangular configuration) are significantly better than the corresponding results obtained using two ground tracking facilities.
- Results obtained using more than three ground tracking facilities are of essentially the same

quality as the results obtained using three ground tracking facilities.

- Bilateration data appear to give better orbit determination results than S-Band tracking data.

REFERENCES

1. Systems and Applied Sciences Corporation, Feasibility Study of Using a Two-Plate Model to Approximate the Tracking and Data Relay Satellite, F. K. Chan, M. H. Toporek, and J. R. Bohse, August 1979

2. Computer Sciences Corporation, CSC/TM-80/6030, Task 758 Final Report, R. E. Shanklin et al., October 1980

3. Goddard Space Flight Center, X-582-76-77, Mathematical Theory of the Goddard Trajectory Determination System (GTDS), J. O. Cappelleri, Jr., C. E. Velez, and A. J. Fuchs (editors), April 1976

PRECISION ORBIT COMPUTATIONS FOR AN OPERATIONAL ENVIRONMENT

C. E. Doll, Goddard Space Flight Center
David F. Eggert, Computer Science Corporation
Richard L. Smith, Computer Science Corporation

ABSTRACT

Analyses have been performed at the Goddard Space Flight Center (GSFC) to establish the operational procedures that would be required to provide precision orbit computations to meet current and future operational requirements set forth by different NASA projects. Taking advantage of the improvements to the earth's gravitation field and tracking station coordinates, an orbital computational consistency of the order of 5 meters were achieved for total position differences between orbital solutions for the Seasat and GEOS-3. The main source of error in these solutions has been in the mathematical models that are required to generate these results, i.e., gravitation, atmospheric drag, etc. Different earth's gravitation fields and tracking coordinates have been analyzed and evaluated in obtaining these computational results.

Comparisons and evaluations of the Seasat results have been obtained in terms of different solution types such as the Doppler only, Laser only, Doppler and Laser, etc. Other investigation using the Seasat data have been made in order to determine their effect on the computational results at this particular level of consistency.

INTRODUCTION

It is expected that in the next few years that NASA missions will require additional computational precision in determining spacecraft position in order to support both project and scientific requirements. In order for the Goddard Space Flight Center to support these NASA mission in a precision orbit computations environment both methods and techniques for computations and operational procedures must be established.

The definitive orbit computations requirements for the Seasat mission were the most accurate in terms of consistency between orbital solutions that had been performed at the GSFC for any given mission prior to its launch in June 1978 by the Operations Support Computing Division (OSCD). The computations requirements set forth by the Seasat Project was to maintain a maximum deviation of 65 meters between orbital solutions for the mission lifetime. With these project requirements, the OSCD established the computational techniques, the operational procedures and the tracking data distribution in order to fulfill these commitments.

Due to the amount and distribution of USB/SRE and Laser tracking data required to support definitive orbit computations and precision orbit computations for the Seasat mission, the OSCD has taken the initiative to determine what level of consistency between orbital solutions can be reached for an operational environment. The results of these investigations for the Seasat and GEOS-III missions are based on the mathematical models and station geodetics that have

been established at GSFC by the Geodynamics Branch. The computational procedures and observational tracking data distributions have been established through the analyses which have been performed for each of the satellites.

The information in this particular report is presented in three different areas, the method for precision orbit computations, Seasat precision computations and GEOS-III precision orbit computations.

METHODS FOR PRECISION COMPUTATIONS

Orbit Determination Procedure

The computations of the precision orbits for both Seasat and GEOS-III were performed at the GSFC on the 360 computer complex using the Goddard Trajectory Determination System (GTDS). GTDS has the capability to perform orbit determinations and generate spacecraft ephemeris data in the form of position and velocity to different levels of consistency based on force model representations, station geodetics and tracking data distributions. The orbital solutions obtained for Seasat and GEOS-III from GTDS used Cowell's method of integration for the equations of motion and the variational equations and a least squares adjustment technique for the improvement of orbital parameters. The earth's gravity field, the solar gravitational perturbations, the lunar gravitational perturbations and the solid earth tidal perturbations are modeled for these orbital computations. In addition, The nonconservative forces of solar radiation pressure and atmospheric drag have been modeled. It should be stated that the JPL planetary ephemeris DE-96 was adopted for these computations along with the BIH polar motion and the UT1 and A.1 corrections.

The Seasat and GEOS-III spacecraft were modeled in the GTDS as specularly reflecting spheres. In the precision orbit computations for Seasat a drag coefficient for each data arc was solved for.

In addition, an analysis was performed to determine the best integration step size for the equations of motion and the variational equations and in obtaining orbital solutions which are consistent in terms of numerical processes. The integraton step size which was established for Seasat and GEOS-III was 45 seconds.

Physical Parameters, Environmental Parameters and Tracking Station Geodetics For Precision Orbit Determination

In obtaining the orbital solutions for the Seasat and GEOS-III in the precision orbit computations environment different sets of physical and environmental parameters and station geodetics were used and evaluated. One of the fundamental capabilities that exist in GTDS is its capability to make use of different size gravitational models along with other parameters, which is essential in an operational environment. In this investigation the three earth's gravitational fields which were used and evaluated were the GEM 9, GEM 10B, and the PGS 1040. These three gravitational fields were determined at the GSFC using observational tracking data from both NASA and non-NASA stations and global gravimetric data while making use of the research and development orbit computations system GEODYN. When a specific gravitational field is used for orbit computations then the earth's gravitational constant (GM), the mean equatorial radius of the earth (a_e) and the earth's inverse flattening factor (1/f) must be properly specified. These particular parameters for each of the three gravitational fields are listed in Table 1. The orbital and physical parameters that were used in this investigation are listed in Table 2. It should be understood that in the computations for the nonconservative forces of drag and solar radiation that both spacecrafts were assumed to have a spherical shape, although this is usually an extreme idealization.

Through the analysis and evaluations which have been performed in this investigation for precision orbit computations, it has become apparent that good

(Physical Parameters, etc., continued)

or precise station geodetics are very essential in obtaining specific levels of consistency between orbital solutions. The evaluations which have performed indicates that the quality of station geodetics are not as important at the 20 to 40 meter level of consistency between orbital solutions as they are at the 5 to 15 meter level of consistency between solutions. Therefore, the station geodetics which have been used for the precision orbit computations for both Seasat and GEOS-III are the coordinates which have been derived by J. Marsh of the GSFC which are given in Table 3. It should be pointed out that selected code letters are assigned to specific stations in order to represent that station on the tracking data distribution figures that are presented in Figures 1 through 3.

TRACKING DATA DISTRIBUTION
SATELLITE AND TIME PERIOD SEASAT-1 SEPT 78

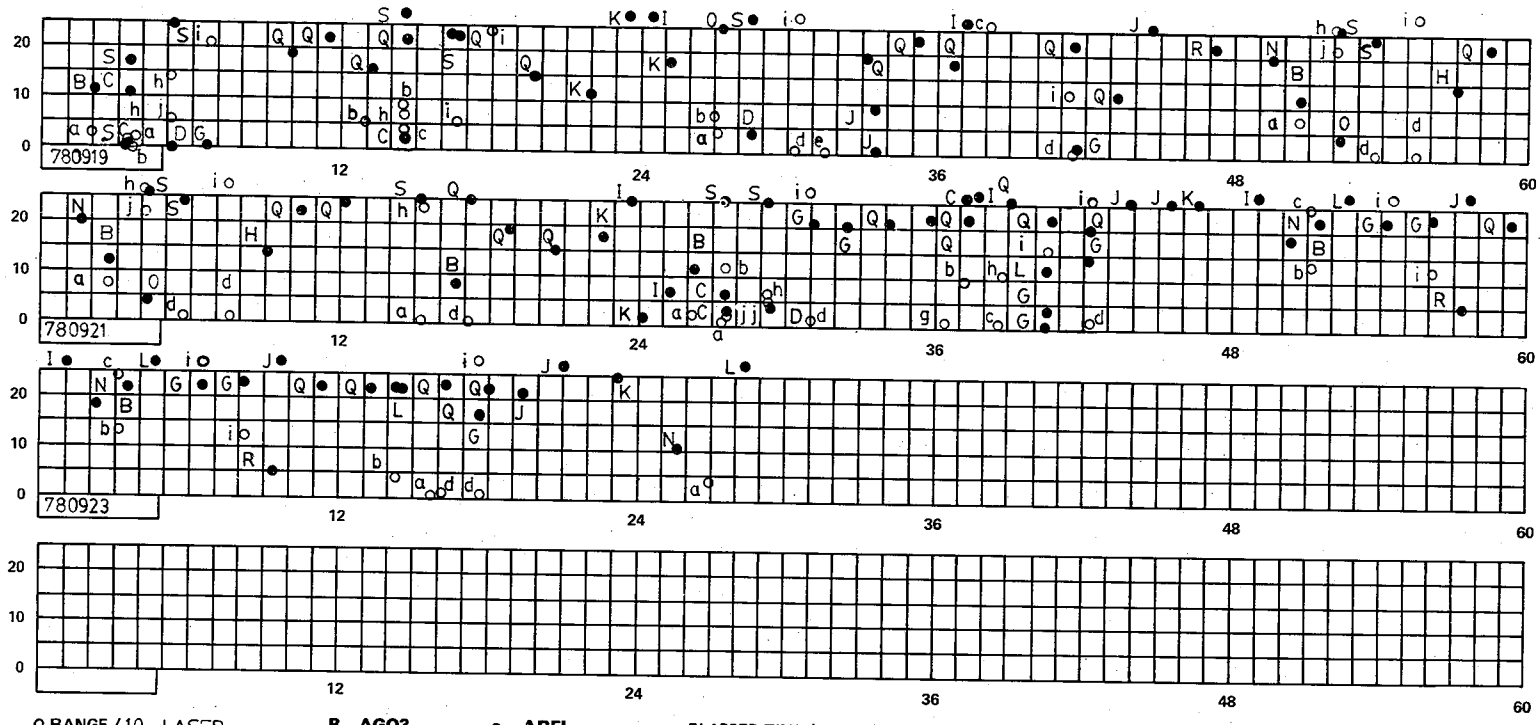

o RANGE / 10 - LASER
● DOPPLER - USB

B AGO3
C BDA3
D ETCA
G GDS3
H GDS8
I GWM3
J HAW3
K MAD8
L MIL3
N ORR3
Q ULA3
R MAD3
S MILA

a AREL
b BDAL
c GTKL
d HOPL
e KOOL
g ORRL
h RAML
i SNDL
j STAL

ELAPSED TIME (HOURS)

DATA RATE: 2 PER MINUTE
NOTES: LASER RATE VARIES

Figure 1

TRACKING DATA DISTRIBUTION
SATELLITE AND TIME PERIOD SEASAT-1 AUG 78

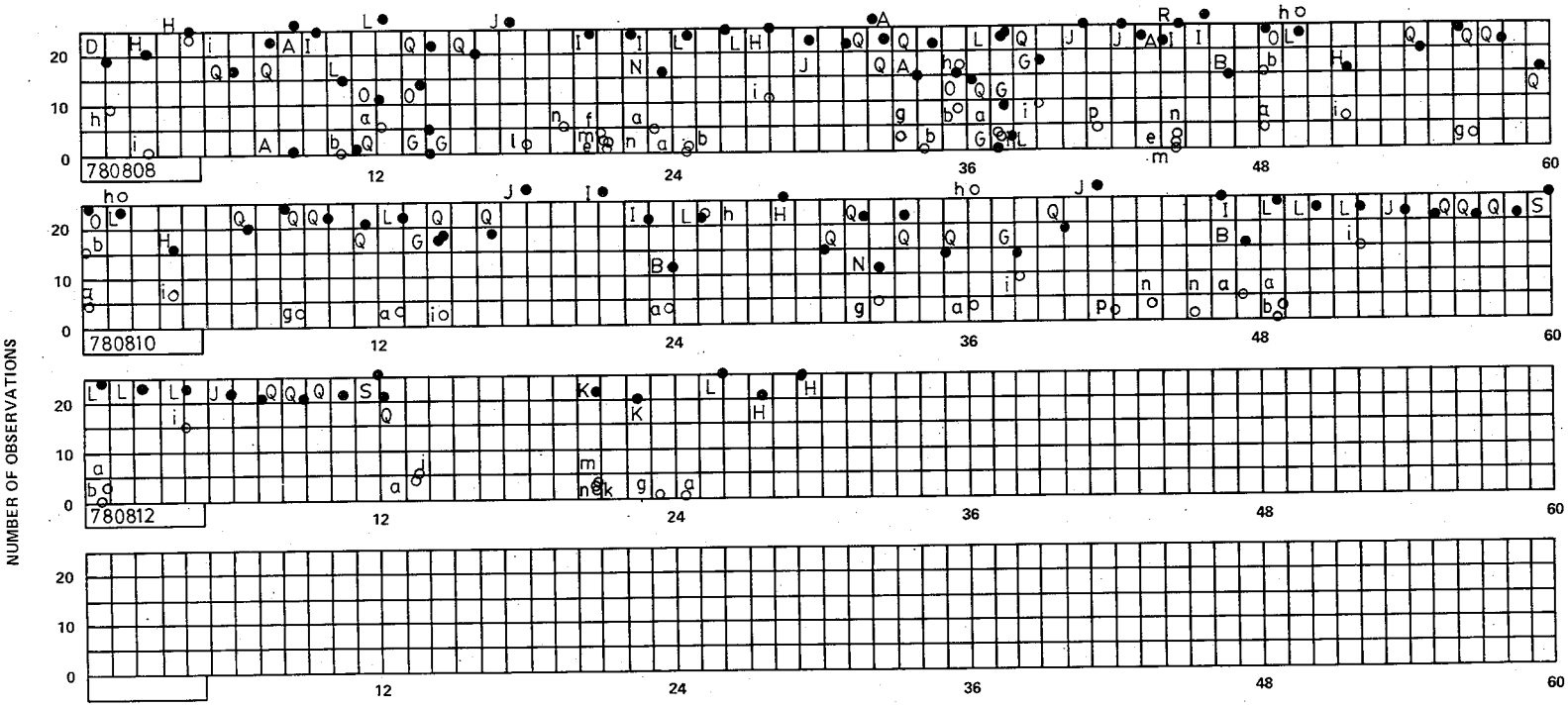

O RANGE/10 - LASER
● DOPPLER - USB

A	ACN3	a	AREL
B	AGO3	b	BDAL
G	GDS3	e	KOOL
H	GDS8	f	NATL
I	GWM3	g	ORRL
J	HAW3	h	RAML
K	MAD8	i	SNDL
L	MIL3	k	WE2L
N	ORR3	m	SAFL
O	QUIS	n	GRAL
Q	ULA3	p	HLWL
R	MAD3		
S	MILA		

ELAPSED TIME (HOURS)

DATA RATE: 2 PER MINUTE
NOTES: LASER RATE VARIES

Figure 2

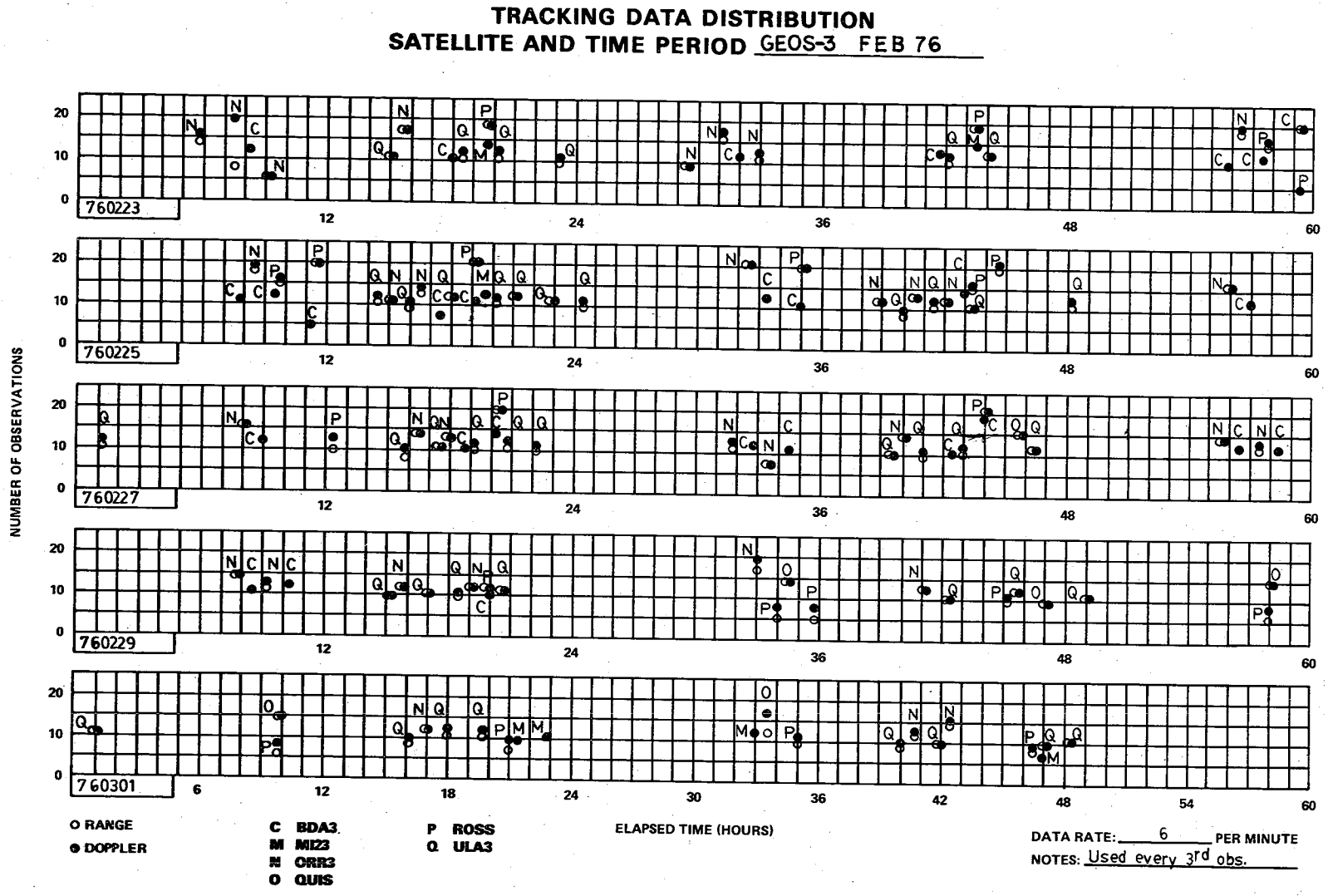
TRACKING DATA DISTRIBUTION
SATELLITE AND TIME PERIOD GEOS-3 FEB 76
NUMBER OF OBSERVATIONS
760223
760225
760227
760229
760301
ELAPSED TIME (HOURS)
O RANGE
DOPPLER
C BDA3
M MIZ3
N ORR3
O QUIS
P ROSS
Q ULA3
DATA RATE: 6 PER MINUTE
NOTES: Used every 3rd obs.

Figure 3

Observational Tracking Data for Seasat

The observational tracking data used for precision orbit computations for Seasat were a combination of USB/SRE range rate data from STDN and Laser data from STDN and SAO. The USB/SRE range rate data provided the strong global coverage both in terms of geographical distribution and in time. The Laser observational tracking data provided strength in terms of accuracy for the precision orbit computations.

An analyses of both the USB/SRE range rate data and the Laser data in terms of distribution and time provided two specific time intervals, September 19 through September 26, 1978 and August 8, 1978 through August 15, 1978 over which the precision orbit computations were performed. The amount of observational tracking data during these two particular time intervals contained approximately 20 passes of USB/SRE data and 12 passes of Laser data for each typical twenty-four hour interval. Figures 1 and 2 give the station and data distribution for the September 1978 period and the August 1978 period.

Orbital Analyses for Seasat

In determining the consistency between orbital solutions to the 1 to 5 meter level for the Seasat spacecraft, a number of gravitational field models, station geodetics and integration step size were evaluated. Through these evaluations with the use of GTDS, it has been established that the PGS-1040 gravitational field and the station geodetics, which have been designated Marsh II, have given the best results in terms of consistency between orbital solutions. The PGS-1040 gravitational field and the Marsh II station geodetics

have been determined at GSFC through the use of GEODYN. It should be pointed out that in the determination of the PGS-1040 gravity field that both Laser and USB/SRE observational tracking data from the Seasat spacecraft were used.

The length of the observational data arc was thirty hours for the orbital solutions which were determined for this investigation. In order to determine the consistency between successive orbital solutions for the Seasat spacecraft a six-hour interval was established as the time frame over which the consistency was to be determined. The maximum difference in a given six-hour overlap interval between two successive orbital solutions in terms of spacecraft position is the measure of consistency which has been determined by this process.

The orbital solutions for the Seasat spacecraft using only the USB Doppler tracking and the additional techniques for computations in the September and August 1978 time frames are given in Tables 4 and 8. Information pertaining to the individual solutions are given in these tables including the rho one solve-for parameter, which is equivalent to a density correction for each of the Seasat orbital solutions. In addition, the maximum discontinuties between successive solutions for each specific six-hour overlap interval are presented in terms of radial, cross track and along track differences. The results of this analysis indicate that using the Doppler only that an average 10-meter level of consistency for the September 1978 time frame can be obtained while for the August 1978 time frame only a 13-meter level of consistency was obtained. These results indicate that the 5-meter level of consistency between the orbital solutions is difficult to obtain using only USB Doppler data. An assessment of these results would indicate that there should be no problem with the number of tracking passes in the

individual solutions although the distribution of passes within the solutions could cause problems. It is felt that the mathematical modeling or the computational procedures should not cause problems in achieving the 5-meter level of consistency.

The next set of orbital solutions for Seasat were computed based on Laser tracking data only and the results of these computations are given in Tables 5 and 9. Information pertaining to these computations for the individual solutions are given in these tables including the rho one solve-for parameters. The maximum discontinuities between successive orbital solutions for each specific six-hour overlap interval are presented. The results of this analysis indicate that using the Laser tracking data by itself that an average 4.4 meter level of consistency can be obtained for the September 1978 time frame while for the August 1978 time frame only an 8.8-meter level of consistency was obtained. These results indicate the 5-meter level of consistency between individual solutions can be obtained when using only Laser tracking data for certain time frames during the Seasat satellite lifetime. Again, an assessment of these results would indicate that since the mathematical modeling and the computational procedures are the same then the differences in the August and September 1978 time frames has to be in another area. The only other area where differences can be attributed has to be in the Laser tracking data, in other words the distribution of the data or the quality of data.

Another set of orbital solutions for Seasat were determined based on Laser and USB Doppler tracking data and the results of these computations are given in Tables 6 and 10. The information pertaining to these computations are given in these tables, including the rho one solve-for parameters. The maximum discontinuities between successive orbital solutions for each specific six-hour overlap interval are also presented in these tables. The results of this analysis indicate that using both the Laser and USB Doppler tracking data that an average 3.6-meter level of consistency was obtained for the September 1978 time frame while for the August 1978 time frame only a 7.4-meter level of consistency was obtained. These results indicate that making use of the combination of Laser and USB Doppler tracking data gives a little better overall consistency between successive solutions than when using the Laser observations only. Since the mathematical modeling and the computational procedures were the same then the slight improvements comes from the strength of more comprehensive distribution of observational tracking data throughout the individual orbital solutions.

Further analysis was performed to determine the affect of having equal number of observations per pass for both the Laser and USB Doppler tracking data in determining each orbital solutions and the level of consistency for the September 1978 time frame. The results of these individual orbit computations are given in Tables 6 and 7 along with the rho one solve-for parameters. The maximum discontinuities between successive orbital solutions for each six-hour overlap interval are also presented in these tables. The results of this analysis indicate that making use of the observational tracking data in this manner and using the same mathematical modeling and computational procedures an average of 4.1 meter level of consistency was obtained. This result of 4.1-meter level of consistency obtained in this process and the other average

values of 3.7- and 4.4-meter levels of consistency obtained when using Laser and USB Doppler data in another process of observations selection and using Laser data by itself are basically the same. In other words, at this particular level of consistency it is difficult to indicate in terms of an average value, which are the better results.

GEOS-III PRECISION ORBIT COMPUTATIONS

Observational Tracking Data for GEOS-III

GEOS-III orbital solutions were calculated for a period extending from February 23, 1976, to March 2, 1976. The available unified S-band range and range-rate data is shown in Figure 3. Only the range-rate data were used for the solutions described here. Unlike the tracking data distribution for Seasat, the GEOS-III tracking data distribution is not uniform, having intense tracking about once a day, and very little tracking at other times. On the average, there is available slightly less than one pass of tracking per orbital revolution.

Orbital Analysis for GEOS-III

Orbital solutions for GEOS-III were calculated using GTDS and the Goddard Earth Model 10B (GEM10B) gravity model. This gravity model is based, in part, on GEOS-3 altimetry data. Since the altitude of GEOS-III is about 50 kilometers greater than that of Seasat, the orbital effects of atmosphere drag are significantly smaller. Unlike Seasat, estimation of the drag parameter does not sppear to affect the accuracy of differential correction solutions. The GEOS-III solutions were calculated by solving only for the spacecraft state vector at epoch.

The GEOS-III solutions were 30 hours in length, each solution overlapping neighboring solutions by six hours. Because ephemeris comparisons in the solution overlap intervals are used for orbital accuracy estimates and because

of the strongly periodic characteristic of the tracking schedule, it might be expected that the overlap comparisons could be affected by the placement of the overlap interval relative to the periods of intense tracking. If the overlap intervals coincided with the intense tracking periods it might be expected that the ephemeris differences would be lower than if the overlap intervals were located in periods of little tracking.

In order to examine this possible effect, the solution intervals were placed in time two different ways. In the first scheme, the epochs of each 30-hour solution were located at 15^h on successive days. This procedure puts the periods of intense tracking into the six-hour solution overlap intervals, and each soluton has strong tracking at its start and end, but little in between. The second scheme placed the epochs at 0^h on successive days. This placed the intense tracking in the middle of each solution, with very little in the overlap intervals.

GEOS-III orbital solutions, along with the ephemeris overlap comparisons that were calculated using these two approaches are summarized in Tables 11 and 12. In these tables, the tracking observations for each solution are separated into two categories (indicated by the diagonal line) because of slightly different tracker types; this is not relevant for this study. The orbital fits, as indicated by the weighted RMS, (the assigned range-rate standard deviation was 2.0 centimeters per second) were about the same, overall, for the 0^h and 15^h solutions. Similarly, the standard deviations of the solution residuals were about one centimeter per second for each set of solutions.

The ephemeris overlap differences for both sets of solutions are also quite similar. The maximum total differences average about 7 meters for both the 0^h and 15^h solutions. Also the maximum cross-track differences average about 6 meters for both sets of solutions. On the other hand, the radial and along-track differences for the two sets of solutions are distinct. For the 15^h solutions, the maximum radial differences and the maximum along-track differences average to 0.5 and 2.4 meters, respectively. For the 0^h solutions, the corresponding averages are 1.0 and 4.9 meters. Thus, the placement of the intense tracking at the end of the solution intervals, rather than the middles, reduced the along-track and radial differences by about a factor of two.

This reduction in along-track and radial differences, and presumably, a corresponding reduction in along-track and radial orbit error may be explained as follows. It is well known that radial and along-track orbit displacements are coupled together in the equations of motion; thus it is natural that changes in along-track and radial orbit error should be correlated. Placement of the intense tracking at the ends of a solution interval causes the orbit solution to better average out along-track and radial force modeling errors, leading to smaller peak radial and along-track orbit errors than if the tracking data was concentrated in the middle of each solution, leaving both ends of a solution "floating".

COMPARISONS OF VARIOUS SETS OF TRACKING STATION COORDINATES

The GEOS-III solutions described in the previous section were calculated using tracking station coordinates derived by J. Marsh of GSFC. Corresponding GEOS-III orbital solutions were calculated using three other sets of tracking station coordinates. These three sets are NASA Spacecraft Tracking and Data Network coordinates (STDN), GEM9 coordinates, and World Geodetic System (Geoceiver) WGS(G) coordinates.

The STDN coordinates are those used for GSFC operational orbit determination (Reference A). The GEM9 coordinates were derived as a part of the GEM9 and GEM10 gravity models (Reference B). The WGS(G) coordinates for the NASA S-band tracking stations were specially derived for this study. These station coordinates were based upon coordinates of nearby geoceivers.

GEOS-III orbital solutions using the STDN, GEM9, and WGS(G) station coordinates are summarized in Tables 13, 14, and 15 respectively. These solutions were calculated using the same GTDS input parameters, except for station coordinates as the solutions in Table B (15^h epochs). Thus, comparisons among the results in these four tables are a direct comparison of the effect of various sets of tracking station coordinates. (The value of the semi-major axis of the earth, used for evaluation of the gravity force was slightly different for the solutions calculated using Marsh coordinates. Subsequently, tests showed the effect of this change negligible for these comparisons.)

Comparisons of Various Sets of Tracking Station Coordinates (continued)

None of the three additional sets of station coordinates performed as well in these solutions as the Marsh coordinates. In the order of increasing weighted RMS residuals and increasing overlap differences, these three sets of coordinates are ordered as follows: WGS(G), GEM9, and STDN. In the case of the STDN coordinates, the maximum radial differences average to 4.2 meters, while the total differences average to 21 meters. These results are consistent with the position differences of the GEOS-III tracking stations in the Marsh and STDN coordinates, which are typically 15 to 25 meters.

CONCLUSIONS

The results of this study have shown that orbital consistency at the five-meter level can be obtained for Seasat and GEOS-III using the operational Goddard Trajectory Determination System. The attainment of this orbital consistency level requires the use of the most precise gravity models and tracking station coordinates that are currently available. For Seasat, the use of Laser range tracking data was found to increase the level of orbital consistency when used alone or in combination with the unified S-band range-rate tracking data. For GEOS-III, the use of the unified S-band tracking data alone produced orbital consistency of the order of five meters.

Table 1 Physical, Geophysical, and Astronomical Parameters Used

QUANTITY	VALUE
UNIVERSAL CONSTANT OF GRAVITATION (G)	6.673×10^{-23} KM^3 S^{-2}KG^{-1}
ASTRONOMICAL UNIT	$1.495978930 \times 10^{8}$ KM
SOLAR MOMENTUM FLUX DENSITY	4.5 N KM^{-2}
EARTH GRAVITATIONAL CONSTANT (GM)	3.9860064×10^{5} KM^3 S^{-2} (GEM 9) 3.9860064×10^{5} KM^3 S^{-2} (GEM10B) 3.9860062×10^{5} KM^3 S^{-2} (PGS 1040)
EARTH MEAN EQUATORIAL RADIUS (a_e)	6378.140 KM (GEM 9) 6378.139 KM (GEM10B) 6378.140 KM (PGS 1040)
EARTH INVERSE FLATTENING FACTOR (1/f)	298.250 (GEM 9) 298.257 (GEM10B) 298.257 (PGS 1040)
SPEED OF LIGHT (c)	2.997925×10^{5} KM S^{-1}

8223/81

TABLE 2. Orbital and Spacecraft Parameters for the Spacecraft Studied

SPACECRAFT	NOMINAL ORBIT CHARACTERISTICS		SPACECRAFT CHARACTERISTICS	
	ALTITUDE (km)	INCLINATION (deg)	MASS (kg)	CROSS-SECTIONAL AREA (m^2)
GEOS-3	825 to 855	115.0	345.909	1.4365
SEASAT-1	770 to 800	108.0	2220.8	25.31

Table 3. Marsh II Tracking Station Coordinates

STATION	GEODETIC LATITUDE	GEODETIC LONGITUDE	HEIGHT ABOVE SPHEROID (m)	CODE
ACN3	−7°57′17″.289	345°40′22″.186	534.33	A
AGO3	−33°09′03″.946	289°20′00″.558	717.59	B
BDA3	32°21′04″.533	295°20′31″.325	−30.10	C
ETCA	38°59′54″.171	283°09′28″.749	12.35	D
GDS3	35°20′31″.789	243°07′35″.311	919.69	G
GDS8	35°20′29″.495	243°07′34″.792	925.69	H
GWM3	13°18′38″.243	144°44′12″.465	133.05	I
HAW3	22°07′34″.681	200°20′05″.231	1148.56	J
MAD8	40°27′19″.553	355°49′53″.216	819.66	K
MIL3	28°30′29″.250	279°18′23″.625	−38.24	L
ORR3	−35°37′40″.410	148°57′25″.169	934.39	N
QUIS	−0°37′18″.967	281°25′10″.404	3578.86	O
ULA3	64°58′19″.233	212°29′13″.235	333.90	Q
MAD3	40°27′22″.248	355°49′49″.163	816.80	R
MILA	28°30′29″.318	279°18′25″.474	−42.40	S
AREL	−16°27′56″.708	288°30′24″.533	2475.99	a
BDAL	−32°21′13″.767	295°20′37″.890	−36.87	b
GTKL	21°27′37″.770	288°52′04″.972	−32.36	c
HOPL	31°41′03″.201	249°07′18″.798	2334.76	d
KOOL	52°10′42″.215	5° 48′35″.055	75.0	e
NATL	−5°55′40″.145	324°50′07″.165	22.70	f
ORRL	−35°37′29″.741	148°57′17″.133	932.45	g
RAML	28°13′40″.630	279°23′39″.244	−37.24	h
SNDL	32°36′02″.628	243°09′32″.737	975.00	i
STAL	39°01′13″.359	283°10′19″.751	47.00	j

8223/81

[a]REFERENCE SPHEROID: SEMIMAJOR AXIS, 6378.155 km. INVERSE FLATTENING FACTOR, 298.255.

TABLE 4

SATELLITE AND TIME PERIOD SEASAT - September 1978

MAJOR RUN CHARACTERISTICS Approximately 30 Second Data Rate for Both Laser and USB Doppler

Geopotential Model PGS-1040**

Lunar/Solar Gravitation YES

Solar Radiation Parameter C_R=1.5

Drag Parameters C_D=2.1

Atmospheric Density Model H.P., F#150

Solve-For Parameters State and Rho one

Editing Parameters 3 Sigma

Other USB-Doppler, Earth Tides Polar Motion, Marsh II Geodetics***

Arc Start Time	Arc Length (hrs)	No. of Stations	Observations: Range No. Available	Observations: Range No. Used	Observations: Range-Rate No. Available	Observations: Range-Rate No. Used	Residual Statistics: Wtd. RMS	Residual Statistics: Standard Deviations: Range (m)	Residual Statistics: Standard Deviations: Range-Rate (cm/sec)	Maximum COMPARE Position Differences (m): Radial	Cross-Track	Along-Track	Total	Solve-For Parameters and Other Information: RHO ONE	PASSES	Run ID
780919	30	7*			403	345	.83		1.68	0.94	11.76	4.66	12.28	-.65	20*	
780920	30	9			371	325	.99		1.98	1.01	11.59	2.15	11.67	-.67	17	
780921	30	9			366	310	.96		1.93	2.20	5.04	7.60	8.37	-.53	20	
780922	30	10			513	426	.82		1.64	1.54	3.21	7.62	7.70	-.22	25	
780923	30	9			444	392	.82		1.65			AVER	10.00	-.21	21	

*Number of Stations and Passes - Laser/USB Doppler

**Computation based on PGS-1040: Gravitational Constant GM = 398600.62 km^3/sec^2, Equatorial Radius R_e=6378.140 km and Inverse Flattening Coefficient = 298.257

***Ellipsoid Parameters for Marsh II Geodetics: Equatorial Radius R_e=6378.155 km and Inverse flattening coefficient=298.255

TABLE 5

SATELLITE AND TIME PERIOD SEASAT - September 1978

MAJOR RUN CHARACTERISTICS Approximately 30 Second Data Rate for Both Laser and USB Doppler

Geopotential Model PGS-1040**

Lunar/Solar Gravitation YES

Solar Radiation Parameter C_R=1.5

Drag Parameters C_D=2.1

Atmospheric Density Model H.P., F#150

Solve-For Parameters State and Rho one

Editing Parameters 3 Sigma

Other Laser Range, Earth Tides, Polar Motion, Marsh II Geodetics***

Arc Start Time	Arc Length (hrs)	No. of Stations	Observations				Residual Statistics			Maximum COMPARE Position Differences (m)				Solve-For Parameters and Other Information				Run ID
			Range		Range-Rate			Standard Deviations										
			No. Available	No. Used	No. Available	No. Used	Wtd. RMS	Range (m)	Range-Rate (cm/sec)	Radial	Cross-Track	Along-Track	Total	RHO ONE		PASSES		
780919	30	6*	69	66			0.16	1.48						-.56		15*		
780920	30	8	79	77			0.17	1.67		0.81	0.83	3.41	3.45	-.63		12		
780921	30	6	89	85			0.17	1.60		0.28	2.16	1.28	2.39	-.49		14		
780922	30	8	79	77			0.12	1.03		1.98	1.52	7.39	7.43	-.55		17		
780923	30	5	64	64			0.12	1.15		0.80	3.73	3.09	4.50	-.11		10		
												AVER	4.44					

*Number of Stations and Passes - Laser/USB Doppler

**Computation based on PGS-1040: Gravitational Constant GM = 398600.62 km^3/sec^2, Equatorial Radius R_e=6378.140 km and Inverse Flattening Coefficient = 298.257

***Ellipsoid Parameters for Marsh II Geodetics: Equatorial Radius R_e=6378.155 km and Inverse flattening coefficient=298.255

TABLE 6

SATELLITE AND TIME PERIOD SEASAT - September 1978

MAJOR RUN CHARACTERISTICS Approximately 30 Second Data Rate for Both Laser and USB Doppler

Geopotential Model PGS-1040**

Lunar/Solar Gravitation YES

Solar Radiation Parameter C_R=1.5

Drag Parameters C_D=2.1

Atmospheric Density Model H.P., F#150

Solve-For Parameters State and Rho one

Editing Parameters 3 Sigma

Other Laser Range and USB-Doppler, Earth Tides, Polar Motion, Marsh II Geodetics***

Arc Start Time	Arc Length (hrs)	No. of Stations	Observations				Residual Statistics			Maximum COMPARE Position Differences (m)				Solve-For Parameters and Other Information				Run ID
			Range		Range-Rate			Standard Deviations										
			No. Available	No. Used	No. Available	No. Used	Wtd. RMS	Range (m)	Range-Rate (cm/sec)	Radial	Cross-Track	Along-Track	Total	RHO ONE		PASSES		
780919	30	6/7*	69	66	403	345	1.10	1.52	1.92					-0.64		15/20*		
										0.67	0.40	2.22	2.25					
780920	30	8/9	79	75	371	325	1.15	1.50	2.06					-0.71		12/17		
										0.93	2.02	3.25	3.80					
780921	30	6/9	89	83	366	310	1.16	1.34	2.08					-0.49		14/20		
										1.69	0.91	3.95	4.00					
780922	30	8/10	79	77	513	427	0.99	1.10	1.84					-0.14		17/25		
										0.66	2.72	4.18	4.69					
780923	30	5/9	64	63	444	392	0.96	1.11	1.84					-0.20		10/21		
												AVER	3.68					

*Number of Stations and Passes - Laser/USB Doppler

**Computation based on PGS-1040: Gravitational Constant GM = 398600.62 km^3/sec^2, Equatorial Radius R_e=6378.140 km and Inverse Flattening Coefficient = 298.257

***Ellipsoid Parameters for Marsh II Geodetics Equatorial Radius R_e=6378.155 km and Inverse flattening coefficient=298.255

TABLE 7

SATELLITE AND TIME PERIOD SEASAT - September 1978

MAJOR RUN CHARACTERISTICS Approximately Equal Laser and USB Doppler Observations Per Pass

Geopotential Model PGS-1040**

Lunar/Solar Gravitation YES

Solar Radiation Parameter C_R=1.5

Drag Parameters C_D=2.1

Atmospheric Density Model H.P., F#150

Solve-For Parameters State and Rho one

Editing Parameters 3 Sigma

Other Laser Range and USB-Doppler, Earth Tides, Polar Motion, Marsh II Geodetics***

Arc Start Time	Arc Length (hrs)	No. of Stations	Observations: Range No. Available	Observations: Range No. Used	Observations: Range-Rate No. Available	Observations: Range-Rate No. Used	Residual Statistics: Wtd. RMS	Residual Statistics: Standard Deviations: Range (m)	Residual Statistics: Standard Deviations: Range-Rate (cm/sec)	Maximum COMPARE Position Differences (m): Radial	Cross-Track	Along-Track	Total	Solve-For Parameters and Other Information: RHO ONE	PASSES	Run ID
780919	30	6/7*	318	305	403	344	1.02	0.94	2.01	0.43	0.95	1.54	1.59	-.61	15/20*	
780920	30	8/9	230	224	371	324	1.15	1.26	2.05	0.64	2.59	2.57	3.15	-.71	12/17	
780921	30	6/9	305	280	366	310	1.19	1.25	2.10	1.70	0.93	7.10	7.11	-.54	14/20	
780922	30	8/10	360	338	513	427	1.01	0.90	1.90	0.55	3.11	2.70	3.87	-.12	17/25	
780923	30	5/9	200	198	444	392	1.00	1.02	1.91					-.17	10/21	
												AVER	4.05			

*Number of Stations and Passes - Laser/USB Doppler

**Computation based on PGS-1040: Gravitational Constant GM = 398600.62 km^3/sec^2, Equatorial Radius R_e=6378.140 km and Inverse Flattening Coefficient = 298.257

***Ellipsoid Parameters for Marsh II Geodetics: Equatorial Radius R_e=6378.155 km and Inverse flattening coefficient=298.255

TABLE 8

SATELLITE AND TIME PERIOD SEASAT - August 1978

MAJOR RUN CHARACTERISTICS Approximately 30 Second Data Rate for USB Doppler

Geopotential Model PGS-1040**

Lunar/Solar Gravitation YES

Solar Radiation Parameter C_R=1.5

Drag Parameters C_D=2.1

Atmospheric Density Model H.P., F#150

Solve-For Parameters State and Rho one

Editing Parameters 3 Sigma

Other USB-Doppler, Earth Tides Polar Motion, Marsh II Geodetics***

Arc Start Time	Arc Length (hrs)	No. of Stations	Observations: Range No. Available	Observations: Range No. Used	Observations: Range-Rate No. Available	Observations: Range-Rate No. Used	Residual Statistics: Wtd. RMS	Residual Statistics: Standard Deviations: Range (m)	Residual Statistics: Standard Deviations: Range-Rate (cm/sec)	Maximum COMPARE Position Differences (m): Radial	Cross-Track	Along-Track	Total	Solve-For Parameters and Other Information: RHO ONE	PASSES	Run ID
780808	30	10*			470	400	.88		1.76	0.93	4.89	9.78	10.90	-.89	22*	
780809	30	10			538	429	.82		1.65	2.88	3.16	9.92	10.20	-.90	26	
780810	30	8			366	317	.55		1.11	1.41	6.64	10.20	11.90	-.11	17	
780811	30	8			335	276	.80		1.61	4.13	14.20	20.20	21.40	-.10	16	
780812	30	7			317	269	.83		1.66			AVER	13.60	-.74	14	

*Number of Stations and Passes - Laser/USB Doppler

**Computation based on PGS-1040: Gravitational Constant GM = 398600.62 km^3/sec^2, Equatorial Radius R_e=6378.140 km and Inverse Flattening Coefficient = 298.257

***Ellipsoid Parameters for Marsh II Geodetics: Equatorial Radius R_e=6378.155 km and Inverse flattening coefficient=298.255

TABLE 9

SATELLITE AND TIME PERIOD SEASAT - August 1978

MAJOR RUN CHARACTERISTICS Approximately 30 Second Data Rate for Laser

Geopotential Model PGS-1040**

Lunar/Solar Gravitation YES

Solar Radiation Parameter C_R=1.5

Drag Parameters C_D=2.1

Atmospheric Density Model H.P., F#150

Solve-For Parameters State and Rho one

Editing Parameters 3 Sigma

Other Laser Range, Earth Tides, Polar Motion, Marsh II Geodetics***

Arc Start Time	Arc Length (hrs)	No. of Stations	Observations				Residual Statistics			Maximum COMPARE Position Differences (m)				Solve-For Parameters and Other Information				Run ID
			Range		Range-Rate			Standard Deviations										
			No. Available	No. Used	No. Available	No. Used	Wtd. RMS	Range (m)	Range-Rate (cm/sec)	Radial	Cross-Track	Along-Track	Total	RHO ONE		PASSES		
780808	30	6*	135	87			2.05	1.85						-.81		11*		
780809	30	6	152	130			2.03	2.03		1.33	2.92	6.78	7.19	-.64		15		
780810	30	5	108	105			1.56	1.56		0.57	3.34	6.58	7.13	-.77		9		
780811	30	5	142	105			2.42	2.40		1.43	3.74	10.20	10.80	-.75		9		
780812	30	4	105	61			1.99	1.95		2.13	3.82	10.30	10.30	-.72		7		
												AVER	8.85					

*Number of Stations and Passes - Laser/USB Doppler

**Computation based on PGS-1040: Gravitational Constant GM = 398600.62 km^3/sec^2, Equatorial Radius R_e=6378.140 km and Inverse Flattening Coefficient = 298.257

***Ellipsoid Parameters for Marsh II Geodetics: Equatorial Radius R_e=6378.155 km and Inverse flattening coefficient=298.255

TABLE 10

SATELLITE AND TIME PERIOD SEASAT - August 1978

MAJOR RUN CHARACTERISTICS Approximately 30 Second Data for Both Laser and USB Doppler

Geopotential Model PGS-1040**

Lunar/Solar Gravitation YES

Solar Radiation Parameter C_R=1.5

Drag Parameters C_D=2.1

Atmospheric Density Model H.P., F#150

Solve-For Parameters State and Rho one

Editing Parameters 3 Sigma

Other Laser Range and USB-Doppler, Earth Tides, Polar Motion, Marsh II Geodetics***

Arc Start Time	Arc Length (hrs)	No. of Stations	Observations				Residual Statistics			Maximum COMPARE Position Differences (m)				Solve-For Parameters and Other Information				Run ID
			Range		Range-Rate			Standard Deviations										
			No. Available	No. Used	No. Available	No. Used	Wtd. RMS	Range (m)	Range-Rate (cm/sec)	Radial	Cross-Track	Along-Track	Total	RHO ONE		PASSES		
780808	30	6/10*	135	83	470	400	1.07	1.40	1.87	1.53	0.91	8.78	8.85	-.82		11/22*		
780809	30	6/10	152	122	538	429	1.02	1.37	1.78	0.66	1.70	2.90	3.36	-.83		15/26		
780810	30	5/8	108	102	366	317	1.01	1.48	1.61	1.36	4.67	3.87	5.93	-.89		9/17		
780811	30	5/8	142	103	335	276	1.45	2.25	1.99	2.30	2.91	11.25	11.26	-.82		9/16		
780812	30	4/7	105	60	317	269	1.15	1.79	1.87					-.74		7/14		
												AVER	7.35					

*Number of Stations and Passes - Laser/USB Doppler

**Computation based on PGS-1040: Gravitational Constant GM = 398600.62 km^3/sec^2, Equatorial Radius R_e=6378.140 km and Inverse Flattening Coefficient = 298.257

***Ellipsoid Parameters for Marsh II Geodetics: Equatorial Radius R_e=6378.155 km and Inverse flattening coefficient=298.255

TABLE 11

SATELLITE AND TIME PERIOD GEOS-III February and March 1976

MAJOR RUN CHARACTERISTICS Approximately 30 Second Data Rate for USB Doppler

Geopotential Model GEM 10B **

Lunar/Solar Gravitation YES

Solar Radiation Parameter C_R=1.45

Drag Parameters C_D=3.09

Atmospheric Density Model H.P., F#75

Solve-For Parameters State Vector

Editing Parameters 3 Sigma

Other USB-Doppler, Earth Tides Polar Motion, Marsh II Geodetics***

Arc Start Time	Arc Length (hrs)	No. of Stations	Observations				Residual Statistics			Maximum COMPARE Position Differences (m)				Solve-For Parameters and Other Information				Run ID
			Range		Range-Rate			Standard Deviations								PASSES		
			No. Available	No. Used	No. Available	No. Used	Wtd. RMS	Range (m)	Range-Rate (cm/sec)	Radial	Cross-Track	Along-Track	Total					
760223	30	5*		53/147	40/95		.67	.9/1.5								15*		
760224	30	5		41/79	34/59		.47	.8/1.0		1.0	1.4	4.7	4.8			9		
760225	30	5		65/181	34/125		.50	1.0/1.0		1.0	8.0	4.5	4.1			19		
760226	30	4		34/172	28/123		.63	1.5/.2		0.7	2.4	2.2	2.8			15		
760227	30	4		51/167	44/132		.69	1.0/.5		0.6	1.9	2.9	3.2			16		
760228	30	5		53/115	44/92		.53	1.3/.9		0.5	8.5	3.7	8.9			13		
760229	30	5		39/109	30/81		.61	1.4/1.2		1.5	10.8	9.8	14.6			12		
760301	30	4		116	85		.45	.9		1.0	6.2	4.4	7.4			10		
760302	30	5		20/88	8/72		.52	.6/1.1		1.5	8.5	6.9	10.4			10		
												AVER	7.6					

*Number of Stations and Passes for USB Doppler

**Computation based on GEM 10B: GM = 398600.64 km^3/sec^2, R_e=6378.139 km and 1/f = 1/298.257

***Ellipsoid Parameters for Marsh II Geodetics: R_e=6378.155 km and 1/f = 1/298.255

TABLE 12

SATELLITE AND TIME PERIOD GEOS-III February and March 1976

MAJOR RUN CHARACTERISTICS Approximately 30 Second Data Rate for USB Doppler

Geopotential Model GEM 10B **

Lunar/Solar Gravitation YES

Solar Radiation Parameter C_R=1.45

Drag Parameters C_D=3.09

Atmospheric Density Model H.P., F#75

Solve-For Parameters State Vector

Editing Parameters 3 Sigma

Other USB-Doppler, Earth Tides, Polar Motion, Marsh II Geodetics***

Arc Start Time Epoch at 15 hrs.	Arc Length (hrs)	No. of Stations	Observations: Range No. Available	Observations: Range No. Used	Observations: Range-Rate No. Available	Observations: Range-Rate No. Used	Residual Statistics: Wtd. RMS	Residual Statistics: Standard Deviations Range (m)	Residual Statistics: Standard Deviations Range-Rate (cm/sec)	Maximum COMPARE Position Differences (m): Radial	Cross-Track	Along-Track	Total	Solve-For Parameters and Other Information: PASSES	Run ID
760223	30	5*		69/159	55/121		.55	0.	8/1.2	1.1	10.8	3.5	11.2	17*	
760224	30	5		94/187	58/138		.51	1.	0/1.0	0.4	5.2	1.2	5.4	21	
760225	30	5		67/263	46/193		.60	1.	2/1.2	0.3	2.3	1.2	2.5	25	
760226	30	4		65/251	51/200		.65	1.	1/1.4	0.1	6.0	1.1	6.0	23	
760227	30	4		79/193	67/163		.63	1.	1/1.3	0.3	7.7	3.1	8.2	21	
760228	30	5		69/203	50/158		.65	1.	7/1.2	1.5	9.9	6.1	11.4	21	
760229	30	5		13/154	11/110		.61	0.	9/1.2	0.3	2.9	2.2	3.5	14	
760301	30	4			134	114	.57		1.1	0.2	5.2	0.9	5.3	12	
760302	30	5		32/134		8/105	.72	0.	8/1.5					15	
												AVER	6.7		

*Number of Stations and Passes for USB Doppler

**Computation based on GEM 10B: GM = 398600.64 km^3/sec^2, R_e=6378.139 km and 1/f = 1/298.257

***Ellipsoid Parameters for Marsh II Geodetics: R_e=6378.155 km and 1/f = 1/298.255

TABLE 13

SATELLITE AND TIME PERIOD GEOS-III February and March 1976

MAJOR RUN CHARACTERISTICS Approximately 30 Second Data Rate for USB Doppler

Geopotential Model GEM 10B **

Lunar/Solar Gravitation YES

Solar Radiation Parameter C_R=1.45

Drag Parameters C_D=3.09

Atmospheric Density Model H.P., F#75

Solve-For Parameters State Vector

Editing Parameters 3 Sigma

Other USB-Doppler, Earth Tides Polar Motion, STDN Geodetics***

Arc Start Time Epoch at 15 hrs.	Arc Length (hrs)	No. of Stations	Observations				Residual Statistics			Maximum COMPARE Position Differences (m)				Solve-For Parameters and Other Information				Run ID
			Range		Range-Rate			Standard Deviations										
			No. Available	No. Used	No. Available	No. Used	Wtd. RMS	Range (m)	Range-Rate (cm/sec)	Radial	Cross-Track	Along-Track	Total			PASSES		
760223	30	5*		69	159	55/123	1.88	3.	1/4.0							17*		
760224	30	5		94	187	58/123	1.08	2.	0/2.2	5.3	31.9	11.4	33.4			21		
760225	30	5		67	263	46/186	1.64	3.	2/3.1	10.4	21.1	41.9	42.0			25		
760226	30	4		65	251	51/196	1.90	3.	4/3.5	1.6	15.0	3.7	15.3			23		
760227	30	4		79	193	62/157	1.48	3.	2/3.6	3.0	3.7	7.3	7.5			21		
760228	30	5		69	203	48/153	1.59	3.	7/2.9	3.2	3.6	10.9	11.2			21		
760229	30	5		13	154	11/108	1.50	0.	5/3.0	3.5	14.5	14.0	17.2			14		
760301	30	4			134	115	1.21		2.4	5.2	29.9	16.2	33.2			12		
760302	30	5		32	134	8/98	1.08	1.	8/2.1	1.5	9.2	3.2	9.5			15		
												AVER	21.2					

*Number of Stations and Passes for USB Doppler

**Computation based on GEM 10B: GM = 398600.64 km^3/sec^2, R_e=6378.139 km and 1/f = 1/298.257

***Ellipsoid Parameters for STDN Geodetics: R_e=6378.139 km and 1/f = 1/298.255

TABLE 14

SATELLITE AND TIME PERIOD GEOS-III February and March 1976

MAJOR RUN CHARACTERISTICS Approximately 30 Second Data Rate for USB Doppler

Geopotential Model GEM 10B **
Lunar/Solar Gravitation YES
Solar Radiation Parameter C_R=1.45
Drag Parameters C_D=3.09
Atmospheric Density Model H.P., F#75
Solve-For Parameters State Vector
Editing Parameters 3 Sigma
Other USB-Doppler, Earth Tides
Polar Motion, GEM 9 Geodetics***

Arc Start Time Epoch at 15 hrs.	Arc Length (hrs)	No. of Stations	Observations: Range No. Available	Observations: Range No. Used	Observations: Range-Rate No. Available	Observations: Range-Rate No. Used	Residual Statistics: Wtd. RMS	Residual Statistics: Standard Deviations Range (m)	Residual Statistics: Standard Deviations Range-Rate (cm/sec)	Maximum COMPARE Position Differences (m): Radial	Cross-Track	Along-Track	Total	Solve-For Parameters and Other Information: PASSES	Run ID
760223	30	5*		69	159	55/122	.75	1.2	1.4	2.4	17.0	9.4	19.0	17*	
760224	30	5		94	187	58/138	.71	1.5	1.4	0.6	7.3	2.3	7.6	21	
760225	30	5		67	263	42/194	.78	1.4	1.5	0.5	0.5	1.5	1.5	25	
760226	30	4		65	251	51/202	.94	2.2	1.7	0.9	3.4	2.8	4.4	23	
760227	30	4		79	193	63/163	.77	2.0	1.3	1.2	1.2	5.1	5.2	21	
760228	30	5		69	203	47/151	.94	2.6	1.6	2.7	18.8	10.5	21.0	21	
760229	30	5		13	154	11/103	.74	0.9	1.3	2.6	12.8	10.3	16.0	14	
760301	30	4			134	105	.84		1.7	1.1	5.2	4.5	6.4	12	
760302	30	5		32	134	8/104	.89	1.1	1.8			AVER	11.8	15	

*Number of Stations and Passes for USB Doppler

**Computation based on GEM 10B: GM = 398600.64 km^3/sec^2, R_e=6378.139 km and 1/f = 1/298.257

***Ellipsoid Parameters for GEM 9 Geodetics: R_e=6378.139 km and 1/f = 1/298.255

TABLE 15

SATELLITE AND TIME PERIOD GEOS-III February and March 1976

MAJOR RUN CHARACTERISTICS Approximately 30 Second Data Rate for USB Doppler

Geopotential Model GEM 10B **

Lunar/Solar Gravitation YES

Solar Radiation Parameter C_R=1.45

Drag Parameters C_D=3.09

Atmospheric Density Model H.P., F#75

Solve-For Parameters State Vector

Editing Parameters 3 Sigma

Other USB-Doppler, Earth Tides Polar Motion, WGS Geodetics***

Arc Start Time Epoch at 15 hrs.	Arc Length (hrs)	No. of Stations	Observations				Residual Statistics			Maximum COMPARE Position Differences (m)				Solve-For Parameters and Other Information	Run ID
			Range		Range-Rate			Standard Deviations							
			No. Available	No. Used	No. Available	No. Used	Wtd. RMS	Range (m)	Range-Rate (cm/sec)	Radial	Cross-Track	Along-Track	Total	PASSES	
760223	30	5*		69/159	55/117		.43	.8/0.9						17*	
760224	30	5		94/187	58/138		.75	1.2/1.5		1.2	20.8	6.5	21.4	21	
760225	30	5		67/263	46/194		.85	1.7/1.6		0.4	4.7	1.8	5.0	25	
760226	30	4		65/251	51/199		.77	1.5/1.5		1.2	8.0	3.6	8.2	23	
760227	30	4		79/193	67/163		.78	1.6/1.4		0.7	9.2	2.8	9.5	21	
760228	30	5		69/203	51/158		.76	1.9/1.2		0.5	6.0	3.3	6.7	21	
760229	30	5		13/154	11/110		.84	0.4/1.5		1.7	13.4	7.4	14.8	14	
760301	30	4			134	114	.55		1.1	1.7	6.1	5.6	7.7	12	
760302	30	5		32/134		8/105	.68	0.6/1.4		0.6	12.6	2.0	12.6	15	
												AVER	10.7		

*Number of Stations and Passes for USB Doppler

**Computation based on GEM 10B: GM = 398600.64 km^3/sec^2, R_e=6378.139 km and 1/f = 1/298.257

***Ellipsoid Parameters for WGS Geodetics: R_e=6378.139 km and 1/f = 1/298.255

References

A. Goddard Space Flight Center, "NASA Directory of Station Locations", February 1978

B. Lerch, F.J., Klosko, S.M., Laubsher, R.E., Wagner, C.A., "Gravity Model Improvement Using GEOS-3 (GEM9 and 10)", Goddard Space Flight Center X-921-77-246, September 1977

TECHNIQUES FOR INCREASING THE EFFICIENCY OF EARTH GRAVITY CALCULATIONS FOR PRECISION ORBIT DETERMINATION*

Richard L. Smith

Anatoly S. Lyubomirsky

Computer Sciences Corporation

ABSTRACT

Two techniques for increasing the efficiency of Earth gravity calculations are analyzed. The first is a representation using Chebyshev expansions in three-dimensional cells. Mathematical formulas are given for converting the standard spherical harmonic representation (e.g., GEM10B 36 x 36) to the Chebyshev representation. The error in the truncated Chebyshev representation was measured as a function of cell size and degree of truncation. For example, with a sixth degree Chebyshev expansion, the maximum gravity error is about 10^{-10}g for a 36 x 36 parent representation in a cell extending 5 degrees in both latitude and longitude and having a thickness of 600 kilometers. Computer storage requirements and relative CPU time requirements are presented. The Chebyshev gravity representation can provide a significant reduction in CPU time in precision orbit calculations, but at the cost of a large amount of direct-access storage space, which is required for a global model.

The second technique employs a temporary file for storing the components of the nonspherical gravity force. In

*This work was supported by the Operations Analysis Section, Operational Orbit Support Branch, Goddard Space Flight Center, National Aeronautics and Space Administration, under Contract NAS 5-24300.

differential correction orbit solutions it is often unnecessary to repeat computations for most of the gravity terms during subsequent iterations for which the satellite's position changes only slightly. By saving a direct-access file of gravitational forces and partial derivatives it is possible to reduce CPU time without significantly affecting orbit accuracy. The gravity file is updated whenever the position tolerance is exceeded. The Goddard Trajectory Determination System was temporarily modified to test this technique, and the results of the test are presented.

1. INTRODUCTION

As the orbit determination accuracy for Earth-orbiting spacecraft is improved through the use of increasingly more accurate Earth gravity models, the computer time requirements increase rapidly. Using the customary global spherical harmonic expansion, the amount of computation time increases approximately as the square of the maximum degree and order of the expansion. For currently available gravity models, for example, the Goddard Earth Model 10B (GEM10B), most of the computation for an orbit solution is devoted to evaluations of the gravity force. Clearly, less time-consuming methods of gravity evaluation are required, particularly if precise gravity models are needed for future operational orbit determination. The need for faster methods is enhanced by the fact that the utilization of more precise gravity models requires the use of correspondingly smaller step sizes for numerical integration of the spacecraft equations of motion.

Table 1 shows the amounts of computer time (GSFC IBM S-360/75) currently required for orbit solutions calculated using the Goddard Trajectory Determination System (GTDS). In order to isolate the dependence of the computer time on the specified value of the maximum degree and order in the

Table 1. GTDS Computer Time Usage for Various Sizes of the Spherical Harmonic Gravity Expansion

SPACECRAFT: SEASAT-1
NUMERICAL INTEGRATOR: COWELL FIXED STEP, 12TH ORDER
FORCE MODEL:

- GRAVITY: SOLAR, LUNAR, GEM9
- DRAG, WITH HARRIS-PRIESTER ATMOSPHERE
- SOLAR RADIATION FORCE
- MEAN OF 1950.0 SYSTEM FOR INTEGRATION

EPOCH: 18^h ON JULY 10, 1978 ARC LENGTH: 30 HOURS
EPOCH – ARC LENGTH: 18^h ON JULY 10, 1978 – 30 HOURS
OBSERVATIONS: 391 DOPPLER USB, 100 LASER RANGE

SIZE OF EARTH GRAVITY MODEL	IBM S-360/75 COMPUTER TIME USAGE (MIN)			
	90-SECOND STEP SIZE		45-SECOND STEP SIZE	
	CPU	I/O	CPU	I/O
		EPHEM PROGRAM		
4 x 4	0.888	0.241	1.544	0.239
8 x 8	1.007	0.241	1.613	0.239
21 x 21	1.280	0.252	2.306	0.249
36 x 36 (GEM10B)	3.210	0.329	5.058	0.330
		DC PROGRAM[1]		
4 x 4	7.448	1.804	11.015	1.725
8 x 8	8.322	1.805	12.051	1.727
21 x 21	10.419	1.817	15.482	1.739
36 x 36 (GEM10B)	20.577	1.938	35.952	1.855

8339/81

[1] SIX ITERATIONS AND CONVERGENCE

spherical harmonic expansion, all other input parameters for these solutions were identical. Computer times for both GTDS Ephemeris Generation (EPHEM) and GTDS Differential Correction (DC) Program runs are shown in this table.

Two methods for efficiency improvement are examined in this paper. Section 2 outlines a gravity representation using Chebyshev polynomials rather than spherical harmonics. Section 3 considers a procedure for making use of previously computed values of the gravity force during the later iterations of differential correction orbit solutions. This procedure, unlike the Chebyshev representation, is not generally applicable to orbit prediction. Section 4 assesses the merit of these two methods and indicates directions for future work.

2. REPRESENTATION OF THE EARTH'S GRAVITY FIELD USING CHEBYSHEV POLYNOMIALS

2.1 OUTLINE OF THE METHOD

In order to accurately represent the Earth's gravity using Chebyshev polynomials, the region of interest is partitioned into cells, and for each cell the gravity force components are expressed as a series of Chebyshev polynomials. The numerical values of the expansion coefficients for a given cell are, in general, different from those of any other cell. With a suitable selection of the cell dimensions, the convergence of the Chebyshev series is sufficiently fast that the computational effort for its evaluation is significantly less than the effort required to evaluate the standard spherical harmonic expansion. In exchange for the reduction in computational effort, however, the Chebyshev representation requires a large data set containing the expansion coefficients for all of the cells.

The evaluation of the gravity force in GTDS is accomplished with the following standard spherical harmonic expansion:

$$F_r = -g \sum_{n=0}^{n_{max}} (n+1) \left(\frac{1}{r}\right)^n \sum_{m=0}^{n} P_n^m (\sin \phi) \cdot \left(C_n^m \cos m\lambda + S_n^m \sin m\lambda\right) \quad (1)$$

$$F_\phi = g \sum_{n=0}^{n_{max}} \left(\frac{1}{r}\right)^n \sum_{m=0}^{n} \left[P_n^{m+1} (\sin \phi) - m \tan \phi \, P_n^m (\sin \phi)\right] \cdot \left(C_n^m \cos m\lambda + S_n^m \sin m\lambda\right) \quad (2)$$

$$F_\lambda = \frac{g}{\cos \phi} \sum_{n=0}^{n_{max}} \left(\frac{1}{r}\right)^n \sum_{m=0}^{n} m \, P_n^m (\sin \phi) \left(S_n^m \cos m\lambda - C_n^m \sin m\lambda\right) \quad (3)$$

where r = radial distance in Earth radii (a)

ϕ = geocentric latitude

λ = geocentric longitude

P_n^m = Legendre function of degree n and order m

n_{max} = maximum degree of the spherical harmonic expansion for the Earth's gravity field

g = $GM/(ar)^2$, where G is the universal constant of gravitation, M is the Earth's mass, a is the Earth's radius, and r is defined above

C_n^m S_n^m = nonnormalized spherical harmonic expansion coefficients for the geopotential field model considered

The Chebyshev expansions used in this paper also yield the radial, latitudinal, and longitudinal gravity components, F_r, F_ϕ, F_λ. The Chebyshev expansions are applied only to that part of the gravity force described by spherical harmonic terms of degree greater than 4. Terms of degree less than or equal to 4 are still evaluated using spherical harmonics.

In each cell, independent position variables, x, y, and z, are designated. These variables are related to r, ϕ, and λ by means of the following equations:

$$\frac{1}{r} = \frac{1}{r_o} + Ax \qquad (|x| \leq 1) \tag{4}$$

$$\sin \phi = \sin \phi_o + Cy \qquad (|\phi| \leq 45^\circ,\ |y| \leq 1) \tag{5}$$

$$\cos \phi = \cos \phi_o + Cy \qquad (|\phi| > 45^\circ,\ |y| \leq 1) \tag{6}$$

$$\cos \lambda = \cos \lambda_o + Dz \qquad (|\lambda - 90^\circ| \leq 45^\circ,\ |z| \leq 1) \tag{7}$$

The cell origin is (r_o, ϕ_o, λ_o) and the physical size of a cell is controlled by the three parameters A, C, and D. The position variables x, y, and z describe displacements, relative to the cell origin, in the radial, latitudinal, and longitudinal directions, respectively. The locus of points such that x = +1 or x = -1 describes spherical surfaces bounding the top and bottom of a cell. The locus of points such that y = $\pm$1 defines cones of constant latitude bounding the north and south sides, and the locus of points such that x = $\pm$1 describes longitudinal planes bounding the cell on the east and west sides. This choice of independent variables leads to cell crowding near the poles, but allows a

fast and efficient procedure for calculation of the Chebyshev expansion coefficients.

As indicated by Equations (5) and (6), the latitude-like variable, y, is defined differently for the polar and equatorial regions. This difference is necessary to avoid slow convergence of the Chebyshev expansions close to the poles and close to the equator. This slow convergence problem also exists for $\lambda = 0$ or $\lambda = \pi$ using the definition given for z by Equation (7). However, it is only necessary to apply a longitude shift when the problem occurs (by suitably adjusting the C_n^m's and S_n^m's) and thus avoid a double definition.

The expansion of each factor of a typical spherical harmonic

$$\frac{1}{r^{n+1}} P_n^m (\sin \phi) \begin{matrix} \cos \\ \sin \end{matrix} m\lambda$$

into a series of Chebyshev polynomials follows the equations (for each cell)

$$\frac{1}{r^n} = \sum_{i=0}^{\infty} \left[\frac{2 - \delta_{io}}{\pi} \right] X_{ni} \; T_i(x) \tag{8}$$

$$P_n^m (\sin \phi) = \sum_{j=0}^{\infty} \left[\frac{2 - \delta_{jo}}{\pi} \right] Y_{nj}^m \; T_j(y) \tag{9}$$

$$\cos m\lambda = \sum_{k=0}^{\infty} \left[\frac{2 - \delta_{ko}}{\pi} \right] Z_{mk}^{(1)} \; T_k(z) \tag{10}$$

$$\sin m\lambda = \sum_{k=0}^{\infty} \left[\frac{2 - \delta_{ko}}{\pi}\right] Z_{mk}^{(2)} \; T_k(z) \qquad (11)$$

The Chebyshev polynomials, T_i, are functions of x, y, or z and satisfy the recurrence relation

$$T_{i+1}(x) = 2x \; T_i(x) - T_{i-1}(x) \qquad (12)$$

where the subscript indicates the degree of the polynomial. In several cases, the Chebyshev expansions indicated by Equations (8) through (11) are finite, not infinite, as a result of the definitions of x, y, and z. The X's, Y's and Z's are the Chebyshev expansion coefficients and their values depend on the cell parameters r_o, ϕ_o, λ_o, A, C, and D, in addition to the order and degree of the spherical harmonic.

The X's, Y's, and Z's are combined in the following way, according to Equations (1) through (3), to form the three subscripted Chebyshev expansion coefficients, e.g., $C_{ijk}^{(1)}$, used for the calculation of the force components:

$$C_{ijk}^{(1)} = Q \sum_{n=4}^{n_{max}} (n + 1) \; X_{ni} \sum_{m=0}^{n} Y_{nj}^{m} \left(C_n^m Z_{mk}^{(1)} + S_n^m Z_{mk}^{(2)}\right) \qquad (13)$$

$$C_{ijk}^{(2)} = Q \sum_{n=4}^{n_{max}} X_{ni} \sum_{m=0}^{n} Y_{nj}^{m+1} \left(C_n^m Z_{mk}^{(1)} + S_n^m Z_{mk}^{(2)}\right) \qquad (14)$$

$$C_{ijk}^{(3)} = Q \sum_{n=4}^{n_{max}} X_{ni} \sum_{m=0}^{n} m Y_{nj}^{m} \left(C_n^m Z_{mk}^{(1)} + S_n^m Z_{mk}^{(2)}\right) \qquad (15)$$

$$C^{(4)}_{ijk} = Q \sum_{n=4}^{n_{max}} X_{ni} \sum_{m=0}^{n} {}^{m}Y^{m}_{nj} \left(S^{m}Z^{(1)}_{mk} - C^{m}Z^{(2)}_{mk} \right) \qquad (16)$$

$$Q \equiv \frac{(2 - \delta_{0i})\ (2 - \delta_{0j})\ (2 - \delta_{0k})}{\pi^3} \qquad (17)$$

The three gravity force components are then calculated in the following way:

$$F_r = -g \sum_{i=0}^{I} \sum_{j=0}^{J} \sum_{k=0}^{K} C^{(1)}_{ijk}\ T_i(x) T_j(y) T_k(z) \qquad (18)$$

$$F_\phi = g \sum_{i=0}^{I} \sum_{j=0}^{J} \sum_{k=0}^{K} \left(C^{(2)}_{ijk} - \tan\ \phi\ C^{(3)}_{ijk} \right) T_i(x) T_j(y) T_k(z) \qquad (19)$$

$$F_\lambda = \frac{g}{\cos\ \phi} \sum_{i=0}^{I} \sum_{j=0}^{J} \sum_{k=0}^{K} C^{(4)}_{ijk}\ T_i(x) T_j(y) T_k(z) \qquad (20)$$

These three equations represent the calculation of gravity as it might be performed in an orbit determination program, using precalculated coefficients.

The formulation used in this paper required four types of three-subscripted Chebyshev expansion coefficients. With additional work, it should be possible to also expand the function

$$\tan\ \phi\ P^{m}_{n}\ (\sin\ \phi)$$

in a Chebyshev series, leading to a formulation using only three types of coefficients. This additional complication was omitted for the present for simplicity.

As indicated by Equations (8) through (16) the three-subscripted coefficients depend on the gravity model coefficients, C_n^m and S_n^m, the cell location, and the cell dimensions. The combined set of three-subscripted coefficients for all cells constitutes a Chebyshev representation for the given gravity model.

The calculation of the Chebyshev coefficients for the spherical harmonic factors, that is, the calculation of the X's, Y's, and Z's, can be easily accomplished using recurrence relations. These recurrence relations are as follows:

Recurrence relations for the radial Chebyshev coefficients:

$$X_{n+1,i} = \frac{A}{2} \left(X_{n,i+1} + X_{n,i-1}\right) + \frac{1}{r_0} X_{n,i} \qquad (n \geq 0, \text{ all } i) \quad (21)$$

$$X_{n+1,0} = \frac{1}{n+1} \left[(2n+1) \frac{1}{r_0} X_{n,0} + n \left(A^2 - \frac{1}{r_0^2} \right) X_{n-1,0} \right] \qquad (n > 0) \quad (22)$$

Recurrence relations for the longitudinal Chebyshev coefficients:

$$Z^{(1)}_{m+1,k} = D \left(Z^{(1)}_{m,k-1} + Z^{(1)}_{m,k+1} \right) + 2 \cos \lambda_0 \, Z^{(1)}_{m,k} - Z^{(1)}_{m-1,k} \qquad (\text{all } m, \text{ all } k) \quad (23)$$

$$Z^{(2)}_{m+1,k} = D\left(Z^{(2)}_{m,k-1} + Z^{(2)}_{m,k+1}\right) + 2\cos\lambda_0\, Z^{(2)}_{m,k} - Z^{(2)}_{m-1,k} \qquad \text{(all } m\text{, all } k\text{)} \tag{24}$$

Recurrence relations for the latitudinal Chebyshev coefficients ($|\phi| \leq 45^{\circ}$):

$$Y^m_{n+1,j} = \frac{2n+1}{n-m+1}\frac{C}{2}\left(Y^m_{n,j-1} + Y^m_{n,j+1}\right) + \frac{2n+1}{n-m+1}\sin\phi_0\, Y^m_{n,j} - \frac{n+m}{n-m+1}\, Y^m_{n-1,j} \qquad \text{(all } j,\ n \geq m \geq 0\text{)} \tag{25}$$

$$Y^n_{n,j} = (2n-1)(2n-3)\left[-\frac{C^2}{4}\left(Y^{n-2}_{n-2,j-2} + Y^{n-2}_{n-2,j+2}\right) - C\sin\phi_0\left(Y^{n-2}_{n-2,j-1} + Y^{n-2}_{n-2,j+1}\right) + \left(1 - \sin^2\phi_0 - \frac{C^2}{2}\right) Y^{n-2}_{n-2,j}\right] \qquad \text{(all } j,\ n \geq 2\text{)} \tag{26}$$

Recurrence relations for the latitudinal Chebyshev coefficients ($|\phi| > 45^{\circ}$):

$$
\begin{aligned}
Y^{m}_{n+2,i} = \frac{(2n+3)}{(n+1-m)(n+2-m)} \Bigg\{ & \left[-\frac{(n+m)(n+m-1)}{(2n-1)} \right] Y^{m}_{n-2,i} \\
& + \left[-(2n+1)(C\cos\phi_0) \right] \left(Y^{m}_{n,i+1} + Y^{m}_{n,i-1} \right) \\
& + \left[-(2n+1)\frac{C^2}{4} \right] \left(Y^{m}_{n,i+2} + Y^{m}_{n,i-2} \right) \\
& + \Bigg[-\frac{(n+1-m)(n+1+m)}{(2n+3)} \\
& + (2n+1)\sin^2\phi_0 - (2n+1)\frac{C^2}{2} \\
& - \frac{(n+m)(n-m)}{(2n-1)} \Bigg] Y^{m}_{n,i} \Bigg\} \qquad (\text{all } i,\ n \geq m \geq 0)
\end{aligned}
\tag{27}
$$

$$
\begin{aligned}
Y^{n+1}_{n+1,i} = (2n+1) \Bigg[& \cos\phi_0\, Y^{n}_{n,i} + \frac{C}{2} \left(Y^{n}_{n,i+1} \right. \\
& \left. + Y^{n}_{n,i-1} \right) \Bigg] \qquad (\text{all } i,\ n \geq 0)
\end{aligned}
\tag{28}
$$

The derivation of these recurrence relations is omitted here; some detail is given in Reference 1. It should be noted that, although the same symbol is used in each case, the Y's of Equations (25) and (26) are defined differently than the Y's of Equations (27) and (28). There should be no confusion since Equations (25) and (26) are intended only for the equatorial region, while Equations (27) and (28) apply to the polar regions.

2.2 ERROR MEASUREMENTS FOR THE CHEBYSHEV REPRESENTATION

This section addresses the question of how closely a Chebyshev gravity representation matches the gravity field defined by the parent spherical harmonic representation. In order to study the Chebyshev expansion error, a computer

program was written to numerically evaluate the error for any selected cell. The program first constructs the Chebyshev expansion coefficients for the given spherical harmonic expansion, using the recurrence relations given in Section 2.1. These Chebyshev expansion coefficients are functions of the C_n^m's and S_n^m's; the cell parameters r_o, ϕ_o, and λ_o; and A, C, and D. Then, for a selected maximum degree, the three gravity force components, F_r, F_ϕ and F_λ generated by the Chebyshev expansions (Equations (18) through (20)) are numerically compared with the corresponding force components calculated from the spherical harmonic expansion (Equations (1) through (3)), using a minimum degree of 4. This comparison is made at many points uniformly distributed throughout the given cell, and the maximum difference between the two representations provides a measure of the Chebyshev expansion error. All of the error measurements in this paper apply to Chebyshev representations based upon the GEM10B 36 x 36 gravity model.

Figures 1 and 2 show the numerically computed error as a function of the cell size parameter A. For simplicity, the latitude size parameter C, and the longitude size parameter D, remained equal to A as A was varied. Figures 1 and 2 show the error for cells at reference heights of 967 kilometers and 255 kilometers, respectively. On each figure, a reference error level at 10^{-10}g is indicated. Order of magnitude estimates place the resultant orbit error at less than 0.1 meters for a 5-day orbit propogation subject to a high-frequency gravity error having this amplitude. The maximum degrees for each of the Chebyshev components were equal to one another and are indicated for each group of curves in the figure. For example, in Figure 1, the upper group of curves represents the error in the three-force components as a function of A for a 3 x 3 x 3 Chebyshev expansion.

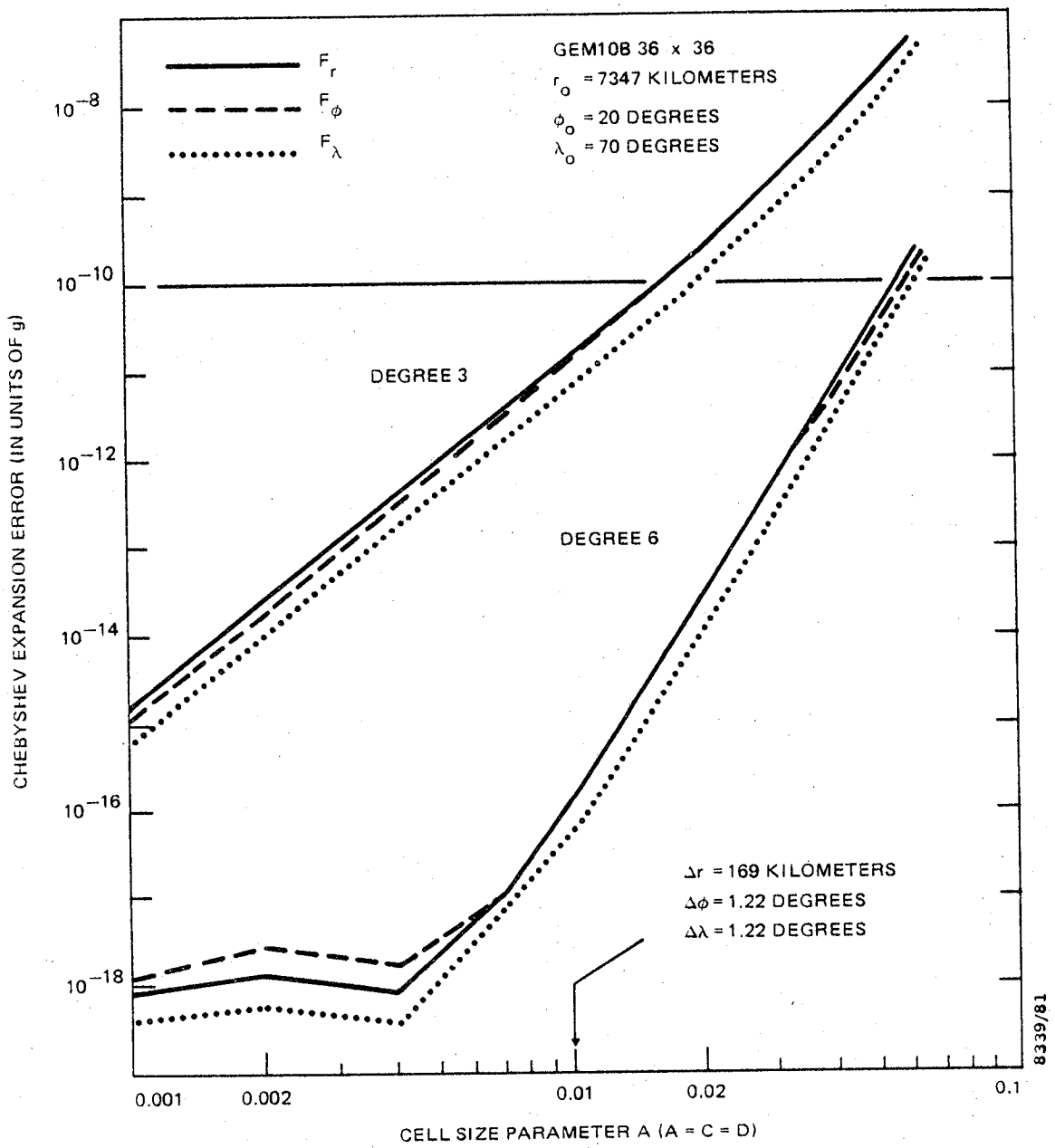

Figure 1. Numerical Measurement of Chebyshev Gravity Representation Error as a Function of Cell Size and Expansion Degrees (Height of Cell Center = 967 Kilometers)

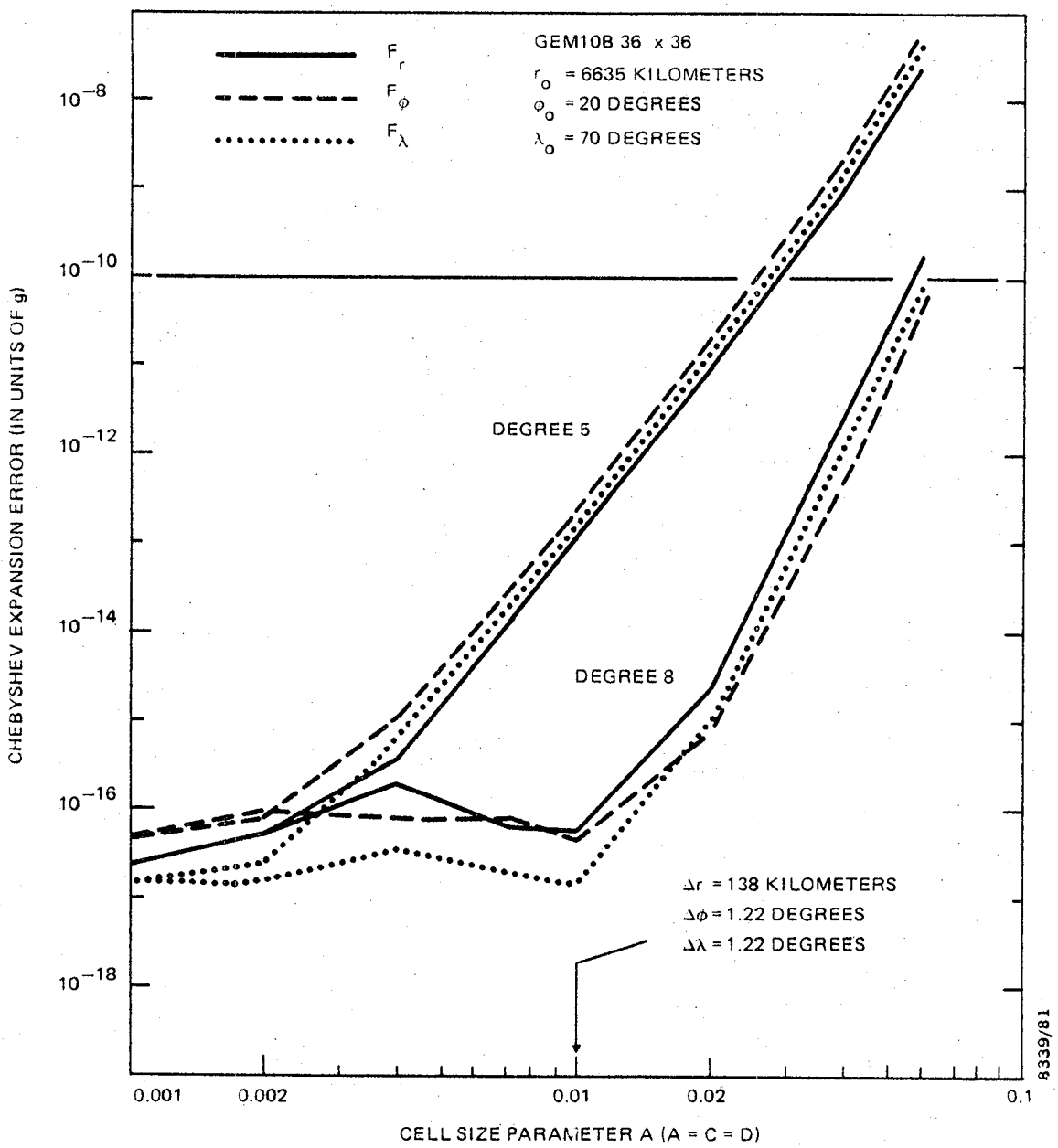

Figure 2. Numerical Measurement of Chebyshev Gravity Representation Error as a Function of Cell Size and Expansion Degrees (Height of Cell Center = 255 Kilometers)

Each of the error curves in Figures 1 and 2 has a range, for intermediate values of A, where the curve is nearly a straight line. In this range, the slope of this straight line, on a log-log scale, is one greater than the maximum degree of the Chebyshev expansion; i.e., the error varies as the cell size to the $K_{max}+1$ power, where K_{max} is the maximum Chebyshev degree. (This rule does not seem to be accurate for the larger values of K_{max}.) For larger values of A, the curves bend away from the straight line. For very small values of A, a numerical noise level is reached and the error reaches a lower limit--about 10^{-18}g for Figure 1 and 3×10^{17}g for Figure 2.

Figures 3 and 4 show the numerical error as a function of latitude for a $5^{\circ} \times 5^{\circ}$ cell, using a 6 x 6 x 6 polynomial degree expansion. The cell thickness was chosen to be small, at a value of 12.8 kilometers, to eliminate the effects of radial variation on the error. The results in Figure 3 were obtained using the equatorial zone formulation (Equations (5), (25), and (26)) and those in Figure 4 were obtained using the polar zone formulation (Equations (6), (27), and (28)). The former diverges near the poles and the latter diverges near the equator, so that a global Chebyshev gravity model must be based upon a combination of these two formulations. In Figures 3 and 4, the maximum error in each cell is plotted at the cell center, so that cells centered at 2.5 degrees latitude extend to the equator and cells centered at 87.5 degrees extend to within 0.001 degrees of the pole.

The slight rise in error near the pole in Figure 4 occurs at error sampling points that are 0.75 degrees from the pole. This slight rise is presumably due to factors of $\cos^{-1}\phi$ and an associated loss of precision in the calculation of F_{ϕ} and F_{λ} (Equations (2) and (3)).

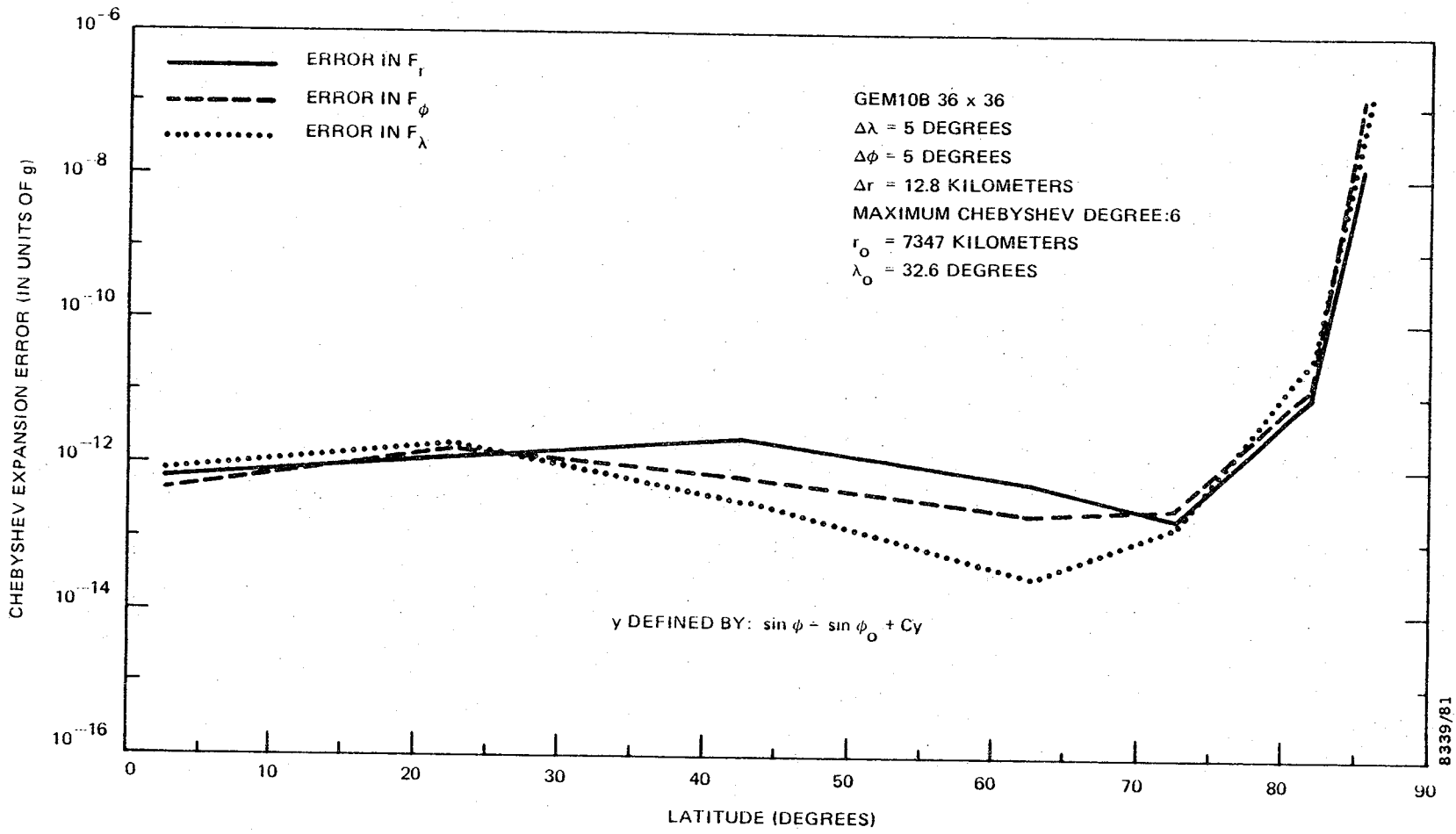

Figure 3. Numerical Measurement of Chebyshev Gravity Representation Error as a Function of Latitude (Equatorial Zone Expansion Used)

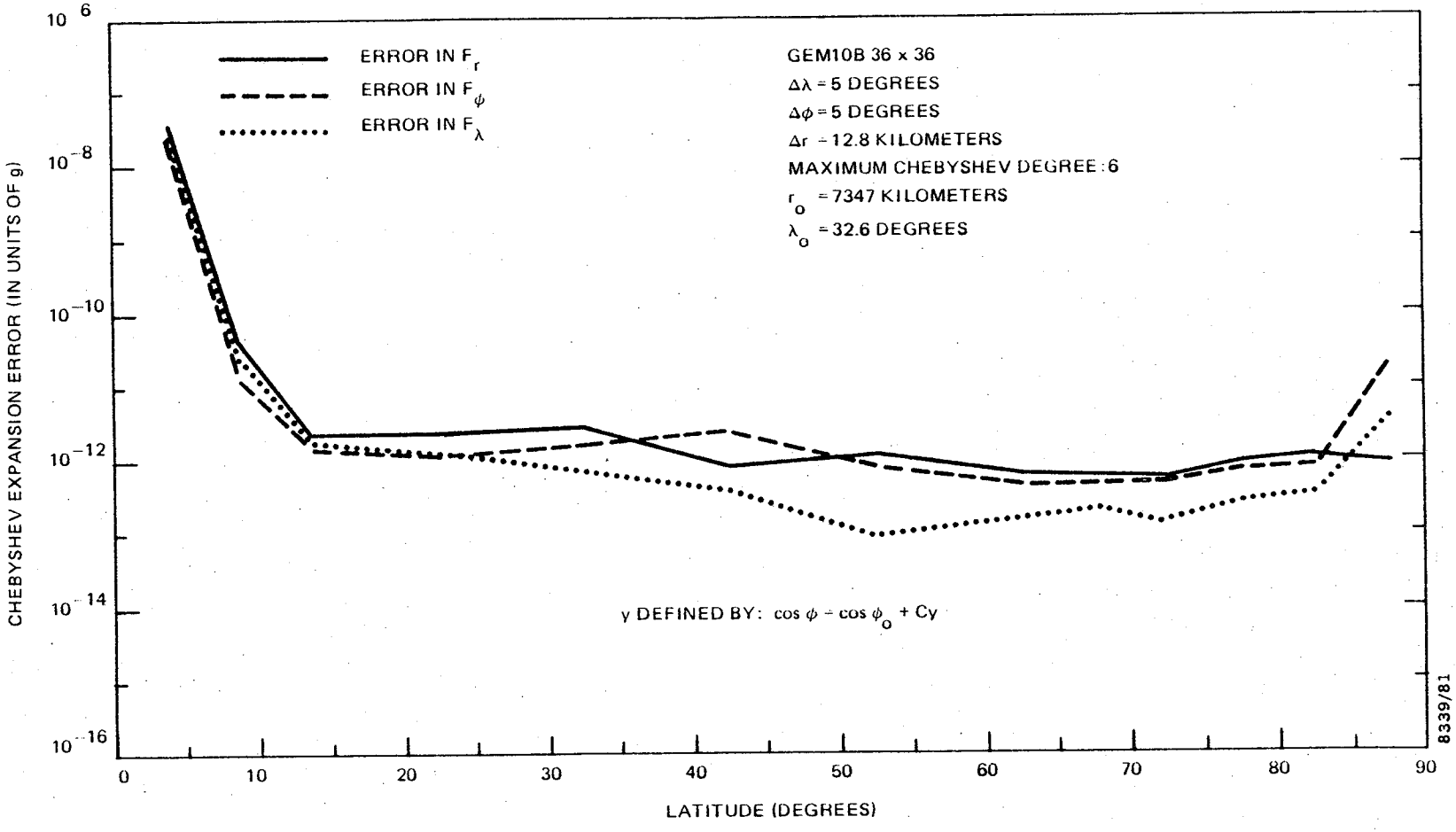

Figure 4. Numerical Measurement of Chebyshev Gravity Representation Error As A Function of Latitude (Polar Zone Expansion Used)

Outside of the latitude regions in which divergence of the Chebyshev expansions is approached, it is clear from Figures 3 and 4 that a uniform level of error is obtained using cells of constant latitudinal and longitudinal dimensions. The solid angle of these cells is much smaller near the poles than near the equator; leading to an unpleasant crowding of cells near the poles in a global Chebyshev model.

2.3 ESTIMATED CHARACTERISTICS OF A GLOBAL CHEBYSHEV GRAVITY REPRESENTATION

The use of the Chebyshev representation for precise satellite orbit determination requires a large, direct-access data set that contains the three-subscripted Chebyshev coefficients for a distribution of cells covering the entire spatial region of interest. The orbit determination program would retain in main memory the coefficients for a small number of cells and would update this working storage as necessary, drawing from the large, direct-access data set. In this section the general characteristics of a sample global Chebyshev representation are estimated.

Table 2 provides data for estimating the speed of the Chebyshev representation, relative to the spherical harmonic representation. For each representation, the table shows the number of machine multiplication or division operations required to evaluate the three force components at a single spatial point. The numbers given assume efficient coding. The maximum degree used in the Chebyshev representation, K_{max}, is assumed to be chosen to be the same for all three indices in the expansions. Comparing the 36 x 36 spherical harmonic representation with the 6 x 6 x 6 Chebyshev representation, the latter requires about 75 percent less time for force evaluation (1,736 operations versus 6,933 operations).

Table 2. Number of Computer Multiplication or Division Operations Needed for Gravity Force Evaluation in the Chebyshev and Spherical Harmonic Gravity Force Representations

CHEBYSHEV REPRESENTATION	
MAXIMUM DEGREE (K_{max})	NUMBER (N_1) OF MULTIPLICATIONS OR DIVISIONS*
3	332
4	640
5	1,098
6	1,736
8	3,669
10	6,685

*$N_1 = 5(K_{max} + 1)^3 + 3K_{max}$

SPHERICAL HARMONIC REPRESENTATION	
MAXIMUM DEGREE (n_{max})	NUMBER (N_2) OF MULTIPLICATIONS OR DIVISIONS**
4	116
8	409
16	1,473
21	2,463
30	4,875
36	6,933
48	12,129

8339/81

**$N_2 = 5n_{max}^2 + 13n_{max} - 15$

Since the number of operations in the Chebyshev representation increases as the third power of K_{max}, while the number of operations in the spherical harmonic representation increases as only the square of the maximum degree, it is desirable to choose as small a value as possible for K_{max} in order to achieve a computation time advantage. In order to simultaneously meet accuracy requirements, it is then necessary to properly adjust the cell dimensions.

The characteristics of the Chebyshev model presented in Figure 5 were based upon Table 2 and the results of Section 2.2. This sample model covers the range of many NASA low-altitude spacecraft; an additional layer could be added to extend the model to higher altitudes. The estimate of the total number of three-subscripted Chebyshev coefficients assumes that only three types were necessary. Although the formulation presented in Section 2.1 employed four types of these coefficients, it is expected that there would be no difficulty in modifying the formulation to require only three types.

From Figure 5, it is clear that the computation time advantage of the Chebyshev representation is accompanied by the need for a large, but not unreasonable, amount of direct-access storage.

3. FILE RETRIEVAL FOR GRAVITY FORCE EVALUATION

3.1 FILE RETRIEVAL METHOD

In standard GTDS Differential Correction orbit solutions, the full force model is reevaluated during every iteration. Except for the first and second iterations, corrections to the orbital position are generally so small that the change in position has a negligible effect on the numerical values of most of the spherical harmonic terms in the gravity model.

- ACCURACY: 10^{-10}g FOR GEM10B 36 x 36
- MAXIMUM DEGREE OF EXPANSION: 6 x 6 x 6
- NUMBER OF CHEBYSHEV COEFFICIENTS FOR EACH CELL: 3 x (7 x 7 x 7) = 1029
- CELL SIZE: Δh = 607 KILOMETERS (A = 0.04)
  $\Delta\phi$ = 5 DEGREES
  $\Delta\lambda$ = 5 DEGREES
- CELL DISTRIBUTION: SINGLE LAYER (r_o = 6954 KILOMETERS)
  h_{MIN} = 284 KILOMETERS
  h_{MAX} = 891 KILOMETERS
- NUMBER OF CELLS: 36 x 72 = 2592
- NUMBER OF CHEBYSHEV COEFFICIENTS IN STORAGE: 2592 x 1029 = 2.7 MILLION
- CPU TIME FOR GRAVITY EVALUATION (RELATIVE TO SPHERICAL HARMONICS): 0.25

8339/81

Figure 5. Characteristics of a Sample Chebyshev Gravity Model

Rough estimates have indicated that, for a 1-day orbit, a 10-meter error in the argument of the portion of the gravity force that does not include the monopole and quadrupole terms leads to orbital position errors that are well below 0.01 meter. These estimates suggest that considerable computation time could be saved, particularly for a 36 x 36 gravity model, if a file of gravity values was saved for use during the later iterations.

The method of gravity evaluation tested is shown in Figure 6. This figure is a flowchart representing the GTDS subroutine that evaluates the gravity force, F(N x N), for a given input position. A test is first made to determine whether a gravity file value exists for the given integration point. (This method is valid only for fixed-step numerical integration.) If the file value exists, then the position associated with the file is compared with the input position. If the difference is less than a prescribed tolerance, ε, then the file value is accepted. The file value describes that part of the gravity force represented by spherical harmonic terms of degree greater than four. This value is added to the 4 x 4 force calculated for the input position, F(4 x 4), to produce the total gravity force F(N x N).

If the file gravity value does not exist, or if the position deviation $|\vec{\Delta r}|$ is greater than the specified tolerance, ε, then the file is not used. Instead F(N x N), F(4 x 4), and F(FILE) are calculated, F(FILE) is stored for later use, and F(N x N) is returned by the subroutine. The resultant orbit precision of this method is controlled by the specified value of ε.

Not shown in Figure 6 is the treatment for partial derivatives of the gravity force with respect to position. These are stored, retrieved, and calculated in a manner parallel to that of the force components themselves.

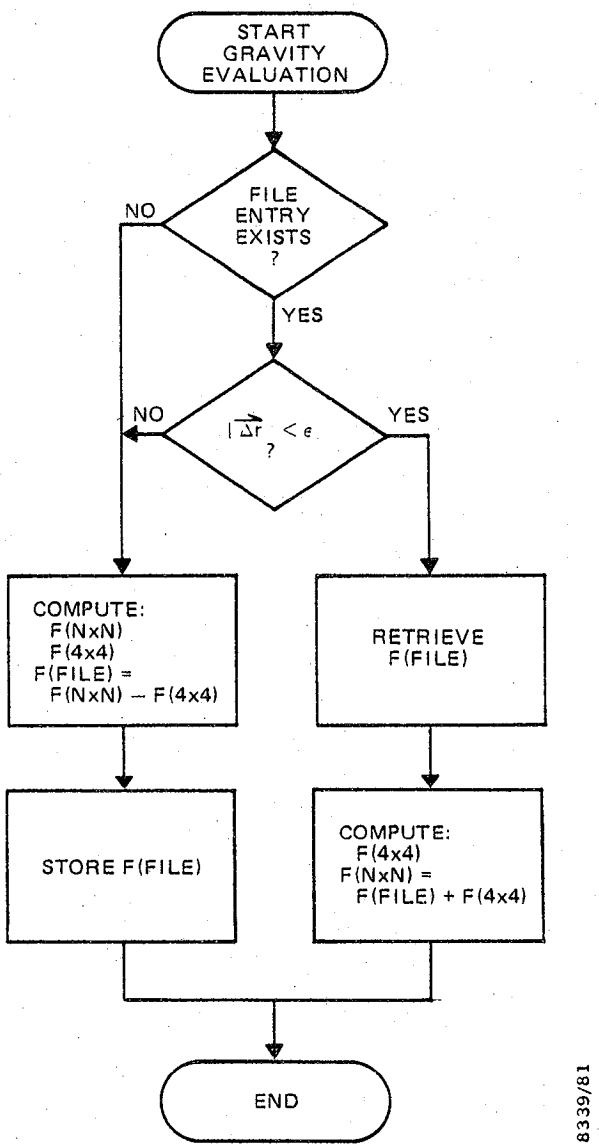

Figure 6. Method for Gravity Force Evaluation Using File Retrieval

3.2 FILE RETRIEVAL RESULTS

In order to test the file retrieval method, two GTDS differential correction orbit solutions, 12 hours in length, were calculated using a 36 x 36 Earth gravity model and using Unified S-Band and laser tracking data. One solution was calculated in the standard way, and the other used the file retrieval method. For the latter solution, the position tolerance, ε, was specified to be 500 meters. Each solution required four iterations to converge, and each differential correction solution was followed by 12-hour ephemeris generation, using the converged orbital elements. The a priori elements for the two solutions were identical, differing from the converged elements by about 80 meters.

A direct comparison between the ephemerides of the two solutions is shown in Figure 7. The position difference between the two solutions is plotted over the solution time interval. Examination of the intermediate results showed that for the first hour, the gravity file was built, but never subsequently updated since the 500-meter tolerance was never exceeded. On the other hand, for the following 11 hours, the gravity file was built during the first iteration, and since the 500-meter tolerance was exceeded during the second iteration (because the first-iteration orbit error progressively worsened with time, and this first-iteration orbit was the basis for the first-iteration file) the file was automatically updated, using positions generally accurate to 5 meters. The last two iterations were calculated with no further updates to the file. This file update history explains the sharp drop in orbit error over the first half hour in Figure 12--from 42 millimeters to the 5-millimeter level.

It is clear from this file update history that the file retrieval method reduces the number of standard gravity force

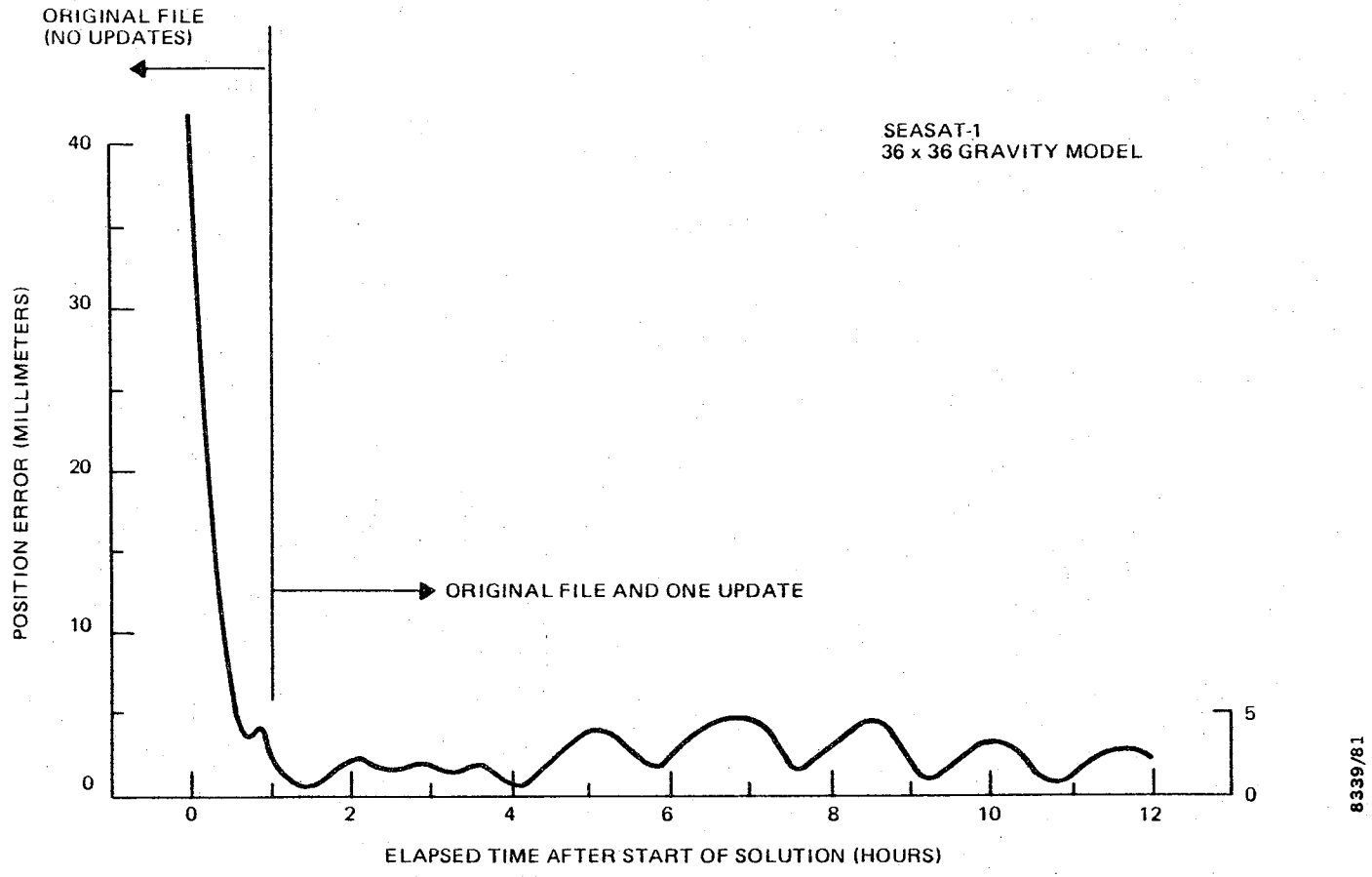

Figure 7. Orbit Error Resulting From Use of Gravity File With Position Tolerance Specified at 500 Meters

evaluations by more than a factor of two without substantial orbit precision loss. The CPU times for the two solutions were 1.23 minutes and 0.69 minutes (IBM S-360/95) for the standard and file retrieval solutions, respectively. These CPU times do not accurately show the full potential computation time reduction of the file retrieval method because, for simplicity, these test calculations did not incorporate file usage into the numerical integration starting algorithms.

4. CONCLUSIONS

The results presented in this paper show that the Chebyshev representation should provide substantial computation time savings for orbit determination using precise Earth gravity models, although its disadvantage is the requirement for a large file of pre-calculated Chebyshev coefficients. Tests of this representation in actual orbit calculations need yet to be performed.

Two areas for possible improvement for the Chebyshev representation are evident. First, truncation of terms in the three-dimensional expansion should be explored. Rather than summing over terms such that i, j, and k range from 0 to K_{max}, it may be possible to sum over terms such that $i + j + k$ ranges from 0 to K_{max}. This type of summation reduction could save a factor of approximately three in both execution time and in direct-access storage. The second improvement would be to extend the formulation so that Cartesian components of the gravity force are directly calculated, rather than spherical components. This would require the derivation of additional recurrence relations for evaluation of the Chebyshev coefficients.

The file retrieval method for gravity evaluation has been shown to be an effective method for reducing computation

time without sacrificing orbit accuracy. Combined with the Chebyshev representation, it could almost eliminate computation time problems in orbit determination using currently available, precise gravity models.

REFERENCES

1. Computer Sciences Corporation, CSC/TR-81/6008, A Chebyshev Representation of the Earth's Gravity Field for Precision Satellite Orbit Calculations, R. L. Smith, June 1981

AN ANALYSIS OF SIMULTANEOUS SATELLITE VISIBILITY TIME SPANS FOR TWO EARTH OBSERVATION STATIONS

F. K. Chan

Phoenix Corporation

1700 Old Meadow Road, McLean, Va. 22102

ABSTRACT

Analysis was performed to estimate the statistical visibility time spans of earth orbiting satellites as seen simultaneously by a ground station and a ship. The analysis covers topics such as time average population, average population times and also the percentage visibility times for a given number of satellites. These results are useful for specific communications satellite applications. Numerical results are obtained for various configurations of ground station and ship.

SECTION 1 - INTRODUCTION

This report is concerned with the analysis of the number and also the time of satellites mutually observed by both a ground station and a ship. Unlike the relatively simple case of a single observation station for which the region of observation is the volume bounded by a cone, the present more complicated case has a region of observation determined by the intersection of two cones. This region has a volume determined only by the separation distance between the ground station and the ship; but it also has a directional property determined by the relative position of the ship with respect to the ground station. Because the analysis becomes extremely complex, it is necessary to make certain simplifying assumptions.

The first assumption is that the satellites presently orbiting the earth may be broadly classified into a few categories. This simplification is supported by the fact that[1] since 1977 approximately 635 satellites have been launched and these may be characterized as in Table 1.1.

Table 1.1

Class	Average Period	Average Inclination	Average Altitude	Number
I	100 min.	80°	800 km	440
II	12 hr.	60°	20,000 km	106
III	24 hr.	0°	36,000 km	57
IV	Others			32

Thus, instead of having to deal with the volume of the region of observation, the analysis deals with the areas at the various altitudes. In this analysis, only Class I and II satellites are considered. Class III satellites are considered separately because they are geosynchronous. Class IV satellites are irregular and will not be considered at all.

(1) NASA, Satellite Situation Report, Volume 21, Number 1, February 28, 1981.

The second assumption is that within each of the two categories considered, the satellites have circular orbits which are uniformly distributed in terms of equatorial crossing and, moreover, the satellites are also uniformly distributed along the orbital arcs.

Section 2 deals with the derivation of the number density of satellites in this statistical distribution. Section 3 deals with the determination of the common region of observation of both the ground station and the ship. Section 4 is concerned with the computation of the time average population of satellites within the mutual region of observation. Section 5 briefly discusses the computation of the average population times of these satellites in the same region. Section 6 summarizes the results of this study for Class I and II satellites.

Readers who are strictly interested in the numerical results may go directly to Section 6 and omit the intervening sections which deal with the mathematical analysis.

SECTION 2 - STATISTICAL DESCRIPTION OF ORBITING SATELLITES

2.1 Distribution Function

Consider a statistical description of a system of N satellites as previously described in which the circular orbits are uniformly distributed in terms of equatorial crossing and the satellites are uniformly distributed along the orbital arc. Consider Figure 2.1 which illustrates a given orbit with inclination i. Let θ be the latitude, ϕ be the right ascension measured from the equatorial crossing, and σ be the orbital arc measured also from the equatorial crossing.

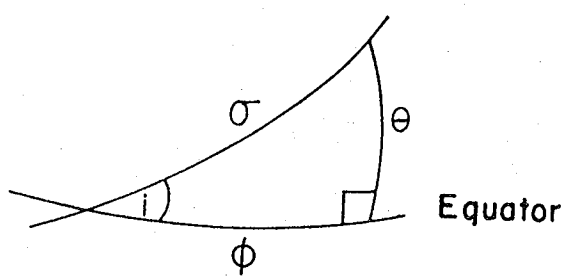

Figure 2.1

Consider Figure 2.2 which illustrates the area element dA_o at the equator

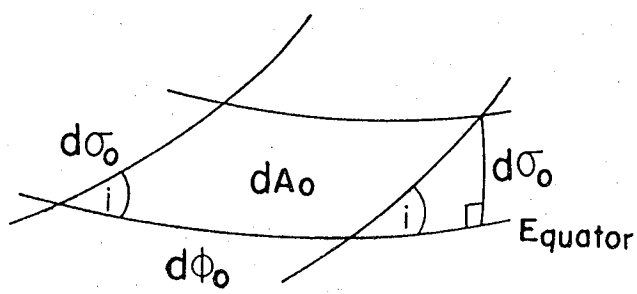

Figure 2.2

It is obvious that dA_o is given by

$$dA_o = r^2 \, d\phi_o \, d\theta_o \tag{2.1}$$

where r is the radius of the orbit. Let f_o denote the density of the satellites at the equator. Then, the number dN of satellites contained in dA_o is given by

$$dN = f_o \, dA_o \tag{2.2}$$

As these satellites move to latitude θ and right ascension ϕ, the corresponding area dA is then given by

$$dA = r^2 \cos\theta \, d\phi d\theta \tag{2.3}$$

and the density f is then obtained from

$$dN = f \, dA \tag{2.4}$$

Substitution of Equations (2.1) - (2.3) into (2.4) yields

$$f = \frac{f_o \, d\phi_o \, d\theta_o}{\cos\theta \, d\phi d\theta} \tag{2.5}$$

However, from Figure 2.1, we obtain the following spherical trigonometric formula

$$\sin\theta = \sin i \sin \sigma \tag{2.6}$$

so that at latitude θ we have

$$\cos\theta \, d\theta = \sin i \cos\sigma \, d\sigma \tag{2.7}$$

and at the equator we have

$$d\theta_o = \sin i \, d\sigma_o \tag{2.8}$$

Moreover, it is easily verified that we also have

$$d\phi = d\phi_o \tag{2.9}$$

$$d\sigma = d\sigma_o \tag{2.10}$$

Substitution of Equations (2.7) - (2.10) into (2.5) yields

$$f = \frac{f_o}{\cos\sigma} \tag{2.11}$$

which states that the density is inversely proportional to the cosine of the arc length.

Next, we obtain the equatorial density f_o as follows:

$$N = \int_{\theta\,min}^{\theta\,max} \int_{o}^{2\pi} f\, r^2 \cos\theta \, d\phi \, d\theta$$

$$= 2\pi r^2 \int_{\theta min}^{\theta max} f \cos\theta \, d\theta$$

$$= 2\pi r^2 \int_{-\pi/2}^{\pi/2} f \sin i \cos\sigma \, d\sigma$$

$$= 2\pi r^2 \int_{-\pi/2}^{\pi/2} f_o \sin i \, d\sigma$$

$$= 2\pi^2 r^2 f_o \sin i \tag{2.12}$$

in which Equations (2.7) and (2.11) have been used.

Substitution of Equation (2.12) into (2.11) yields

$$f = \frac{N}{2\pi^2 r^2 \sin i \cos \sigma} \tag{2.13}$$

which expresses the density in terms of the total number, the radius, the inclination and the orbital arc. However, it is more convenient to obtain an expression in terms of latitude than orbital arc. This is accomplished as follows: Using the identity

$$\cos^2 \sigma = 1 - \sin^2 \sigma \tag{2.14}$$

and also Equation (2.6), we obtain

$$\sin i \cos \sigma = \sqrt{(\sin^2 i - \sin^2 \theta)} \tag{2.15}$$

so that Equation (2.13) becomes

$$f = \frac{N}{2\pi^2 r^2 \sqrt{(\sin^2 i - \sin^2 \theta)}} \tag{2.16}$$

2.2 Angular Separation

The system of N satellites under discussion is considered to be uniformly distributed in terms of equatorial crossing and also along the orbital arc. It is easily verified that the angular separations between the satellites are given by

$$\Delta\phi = \frac{2\pi}{\sqrt{N}} \tag{2.17}$$

$$\Delta\sigma = \frac{2\pi}{\sqrt{N}} \tag{2.18}$$

SECTION 3 - REGION OF OBSERVATION

3.1 Geocentric Conical Angle

Consider a ground station G on the earth's surface. Let β denote the conical observation angle at the earth's surface, α the conical angle subtended at the earth's center, r_e the mean radius of the earth, h the satellite's altitude, and a the conical distance as illustrated in Figure 3.1.

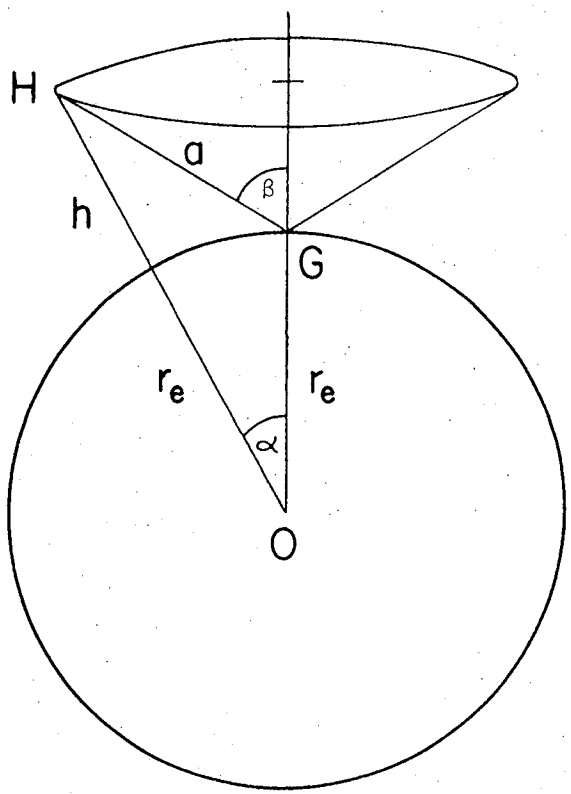

Figure 3.1

The geocentric conical angle α may be obtained as follows: For the triangle OGH, we have the sine formula

$$a = \frac{(r_e + h) \sin \alpha}{\sin (\pi - \beta)} \tag{3.1}$$

and the cosine formula

$$a^2 = r_e^2 + (r_e + h)^2 - 2r_e (r_e + h) \cos \alpha \tag{3.2}$$

Substitution of Equation (3.1) into (3.2) and use of the identity

$$\sin^2 \alpha = 1 - \cos^2 \alpha \tag{3.3}$$

yield the following quadratic equation for $\cos \alpha$

$$\cos^2\alpha - 2\left(\frac{r_e}{r_e + h}\right) \sin^2\beta \cos\alpha + \left[\left(\frac{r_e}{r_e + h}\right)^2 \sin^2\beta - \cos^2\beta\right] = 0 \tag{3.4}$$

whose solution is given by

$$\cos\alpha = \left(\frac{r_e}{r_e + h}\right) \sin^2\beta \pm \cos\beta \sqrt{\left[1 - \left(\frac{r_e}{r_e + h}\right)^2 \sin^2\beta\right]} \tag{3.5}$$

It may be verified that the physically acceptable solution is the one which yields the smaller angle α, i.e., the one with the positive sign in Equation (3.5). The other solution yields the larger angle α which results in a cone going into the earth, which is thus rejected.

3.2 Boundaries of Intersection Region

Consider Figure 3.2 which illustrates a ground station G and a ship S, and also the region of observation Ω common to both of them. Let C be the central point of the great circular arc GS, and γ the angle GOC.

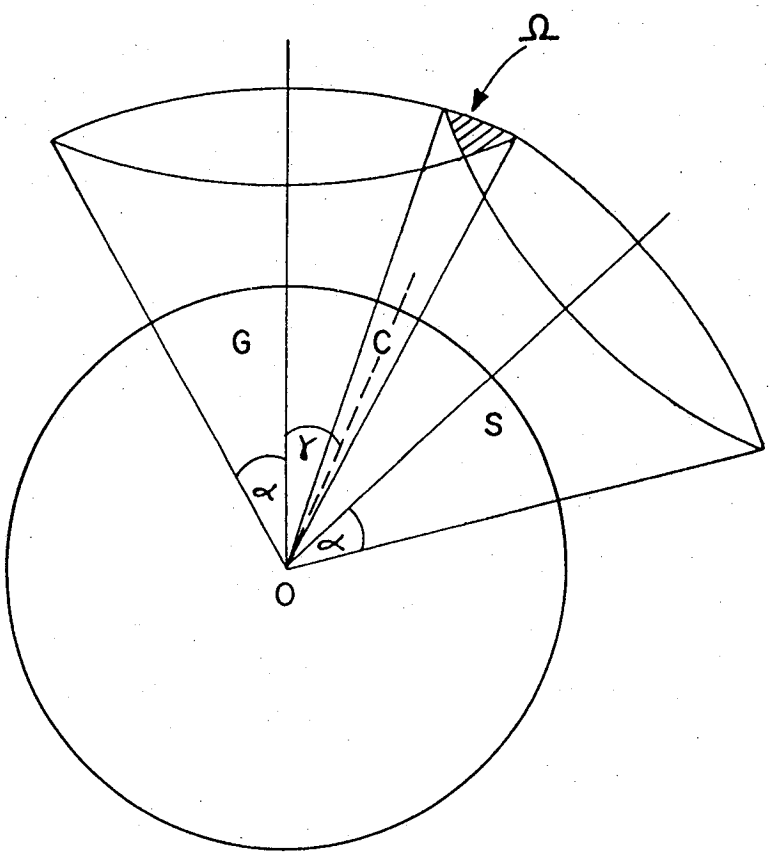

Figure 3.2

For simplicity, let G be on the equator and let S be at latitude θ_s and longitude ψ_s with respect to G, as illustrated in Figure 3.3.

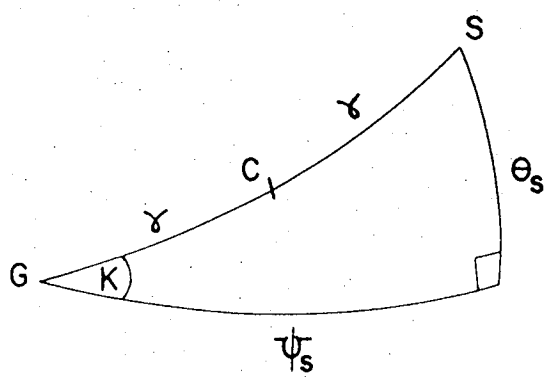

Figure 3.3

Then, from spherical trignometry, the arc length 2γ between G and S is given by

$$\cos 2\gamma = \cos \theta_s \cos \psi_s \tag{3.6}$$

and the inclination κ of S with respect to G is given by

$$\sin \theta_s = \sin \kappa \sin 2\gamma \tag{3.7}$$

Next, consider Figure 3.4 which illustrates the boundaries R and L of the intersection region Ω. It is to be noted that these boundaries are not arcs of great circles, but are arcs of small circles.

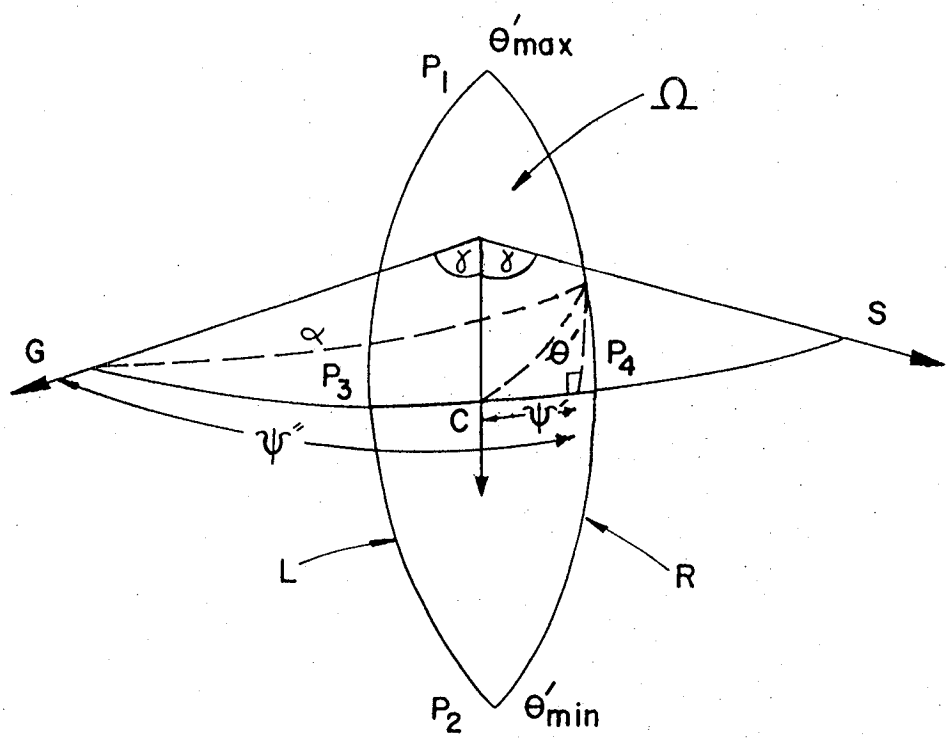

Figure 3.4

In order to obtain expressions for the boundaries R and L, it is convenient to consider the arc GS as the equator in an oblique coordinate system. First, consider the curve R.

Let θ' be the latitude and ψ'' be the longitude of a point with respect to G. Then, from spherical trigonometry, the equation of the curve R is given by

$$\cos\alpha = \cos\theta' \cos\psi'' \tag{3.8}$$

However, if ψ' denotes the longitude measured from C, then we have

$$\psi'' = \psi' + \gamma \tag{3.9}$$

and Equation (3.8) becomes

$$\cos\alpha = \cos\theta' \cos(\psi' + \gamma) \tag{3.10}$$

which is the equation for the boundary R in the oblique geographical system having C as the origin of latitude and longitude. Similarly, the equation for the boundary L is given by

$$\cos\alpha = \cos\theta' \cos(\psi' - \gamma) \tag{3.11}$$

The points of intersection of the curves R and L are given by P_1 ($\psi' = 0$, $\theta' = \theta'_{max}$) and P_2 ($\psi' = 0$, $\theta' = \theta'_{min}$) where

$$\theta'_{max} = \cos^{-1}\left(\frac{\cos\alpha}{\cos\gamma}\right) \tag{3.12}$$

$$\theta'_{min} = -\theta'_{max} \tag{3.13}$$

3.3 Regular to Oblique Geographic Transformation

Let $\vec{r} = (x,y,z)$ denote the coordinates of a point in the regular geographic system, and $\vec{r}' = (x', y', z')$ denote the corresponding coordinates of the same point in the oblique geographic system. Figure 3.5 illustrates the angular rotations to accomplish the necessary coordinate transformation.

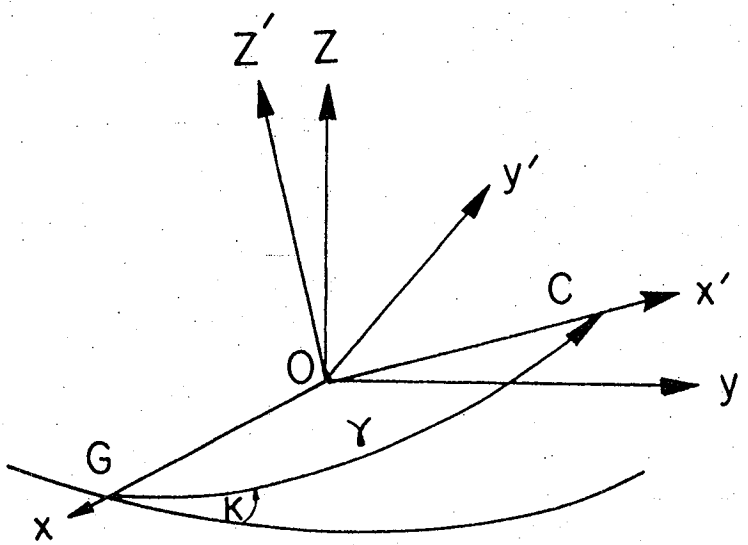

Figure 3.5

Let A denote the transformation matrix from $\vec{r}$ to $\vec{r}'$, i.e.,

$$\vec{r}' = A\vec{r} \tag{3.14}$$

Then, it is well-known that A is given by

$$A = \begin{bmatrix} c_\gamma & c_K s_\gamma & s_\gamma s_K \\ -s_\gamma & c_K c_\gamma & c_\gamma c_K \\ 0 & -s_K & c_K \end{bmatrix} \tag{3.15}$$

where the symbols s and c respectively denote the sine and cosine functions of the argument which appears as the subscript. Next, it is also noted that r and r' may be respectively expressed in terms of their latitude and longitude as follows:

$$\left.\begin{aligned} x &= r\, c_\theta c_\psi \\ y &= r\, c_\theta s_\psi \\ z &= r\, s_\theta \end{aligned}\right\} \tag{3.16}$$

$$\left.\begin{aligned} x' &= r c_{\theta'} c_{\psi'} \\ y' &= r c_{\theta'} s_{\psi'} \\ z' &= r s_{\theta'} \end{aligned}\right\} \tag{3.17}$$

Thus, Equations (3.14) - (3.17) may now be used to express the oblique latitude and longitude in terms of the regular ones. The final results are given by

$$s_{\theta'} = - s_\kappa c_\theta s_\psi + c_\kappa s_\theta \tag{3.18}$$

$$\tan\,(\psi' + \gamma) = \frac{c_\kappa c_\theta s_\psi + s_\kappa s_\theta}{c_\theta c_\psi} \tag{3.19}$$

3.4 Oblique to Regular Geographic Transformation

Next, to obtain the regular latitude and longitude in terms of the oblique ones, we proceed as follows: We note that

$$\vec{r} = A^T \vec{r}' \tag{3.20}$$

where A^T denotes the transpose matrix of A.

Then, proceeding as before but now using Equations (3.20) and (3.15) - (3.17), we obtain

$$s_\theta = s_\gamma\, s_\kappa\, c_{\theta'}\, c_{\psi'} + c_\gamma\, s_\kappa\, c_{\theta'}\, s_{\psi'} + c_\kappa\, s_{\theta'} \tag{3.21}$$

$$\tan\psi = \frac{c_\kappa\, c_{\theta'}\, s_{(\psi' + \gamma)} - s_\kappa\, s_{\theta'}}{c_{\theta'}\, c_{(\psi' + \gamma)}} \tag{3.22}$$

SECTION 4 - TIME AVERAGE POPULATION

4.1 Exact Folmulation

Let N_Ω denote the number of satellites (time average population) within the common domain of observation Ω. It is obviously given by

$$N_\Omega = \iint_\Omega f \, d\Omega \tag{4.1}$$

where the density f is given by Equation (2.16) and the element of area $d\Omega$ is given by

$$d\Omega = r^2 \cos\theta \, d\psi \, d\theta \tag{4.2}$$

It appears that the above integral may be trivially expressed in terms of the regular latitude θ and longitude ψ as follows:

$$N_\Omega = \int_{\theta \text{ min}}^{\theta \text{ max}} \int_{\psi_L(\theta)}^{\psi_R(\theta)} \frac{N \cos\theta \, d\psi \, d\theta}{2\pi^2 \sqrt{(\sin^2 i - \sin^2\theta)}} \tag{4.3}$$

where $\psi_R(\theta)$ denotes the expression obtained by solving for ψ in terms of θ using the equation for the R curve given by Equations (3.10), (3.18), and (3.19), and similarly for $\psi_L(\theta)$ in terms of the L curve. Not only is this process difficult, but it is noted that the integral on the RHS of Equation (4.3) may not even be valid or, worse yet, amenable to numerical evaluation even in principle. This point becomes evident by combining Figures 3.3 and 3.4. It is possible that the location of the ship S with respect to the ground station G can give rise to the case where, in performing the

integration with respect to ψ, the process does not take place from the L curve to the R curve and, furthermore, in performing the integration with respect to θ, the process also does not take place from θ min to θ max . This difficulty can be circumvented by writing the element of area $d\Omega$ as follows

$$d\Omega = r^2 \cos\theta' \, d\psi' \, d\theta' \tag{4.4}$$

so that the integral becomes

$$N_\Omega = \int_{\theta'min}^{\theta'max} \int_{\psi'_L(\theta')}^{\psi'_R(\theta')} \frac{N \cos\theta' \, d\psi' \, d\theta'}{2\pi^2 \sqrt{(\sin^2 i - \sin^2\theta)}}$$

$$= \frac{N}{2\pi^2} \int_{\theta'min}^{\theta'max} \int_{\psi'_L(\theta')}^{\psi'_R(\theta')} \frac{\cos\theta' \, d\psi' \, d\theta'}{\sqrt{\left[s_i^2 - (s_\gamma s_\kappa c_{\theta'} c_{\psi'} + c_\gamma s_\kappa c_{\theta'} \, s_{\psi'} + c_\kappa s_{\theta'})^2\right]}} \tag{4.5}$$

in which Equation (3.21) has been used. It is to be noted the ψ' integration will always proceed from the L curve to the R curve, and the θ' integration will always proceed from θ' min to θ' max.

4.2 Approximate Formulation

An approximate formulation may be obtained by going back to the original Equation (4.1) which may be used to yield the following

$$N_\Omega = f_{ave} \Omega \tag{4.6}$$

where

$$\Omega = \iint_{\Omega} r^2 \cos\theta' \, d\psi' \, d\theta'$$

$$= 4r^2 \int_0^{\theta'_{max}} \int_0^{\psi_R'(\theta')} \cos\theta' \, d\psi' \, d\theta'$$

$$= 4r^2 \int_0^{\theta'_{max}} \cos\theta' \left[\cos^{-1} \left(\frac{\cos\alpha}{\cos\theta'} \right) - \gamma \right] d\theta' \qquad (4.7)$$

in which Equations (3.10) and (3.12) have been used. This integral may be evaluated numerically once the relative position of the ship S is specified. The average value of f to be used may be obtained by averaging the 4 values at the mid-points on the axes of symmetry of Ω. These, in turn, may be obtained by averaging the values at the center C and those at the extremities P_i illustrated in Figure 3.4. Thus, we may write

$$f_{ave} = \frac{1}{8} \left[f(P_1) + f(P_2) + f(P_3) + f(P_4) + 4f(C) \right] \qquad (4.8)$$

SECTION 5 - AVERAGE POPULATION TIMES

5.1 Exact Formulation

First consider Figure 2.1, for which we may write the following spherical trigonometric formulas

$$\sin\theta = \sin i \sin\sigma \tag{5.1}$$

$$\cos\sigma = \cos\theta \cos\phi \tag{5.2}$$

where the relevant quantities have already been previously defined in Section 2. Next, consider Figure 5.1 which illustrates the ground station at G, when the satellite crosses the equator at N_1. Subsequently, when the satellite has moved to latitude θ, the rotation of the earth has taken the ground station to the point G.

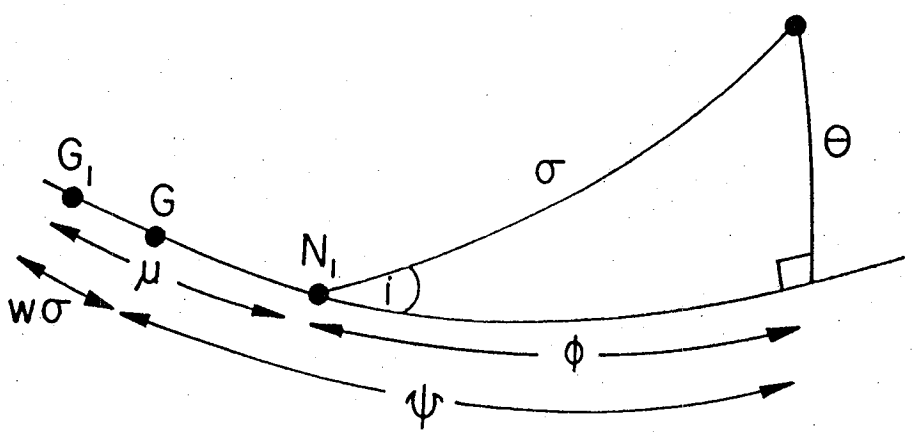

Figure 5.1

Then, it is obvious that the following relation holds for both direct ($i < \pi/2$) and retrogade ($i > \pi/2$) orbits

$$\mu + \phi = \psi + \omega\sigma \tag{5.3}$$

where

$$\omega \equiv \frac{P}{P_e} \tag{5.4}$$

μ = longitude of satellite crossing measured from ground station

ϕ = right ascension of satellite measured from equatorial crossing

ψ = longitude of satellite measured from ground station

σ = orbital arc of satellite measured from equatorial crossing

ω = ratio of satellite orbital period P to earth rotational period P_e

Substitution of Equation (5.3) into (5.2) yields

$$\cos\sigma = \cos\theta \cos(\psi + \omega\sigma - \mu) \tag{5.5}$$

Equations (5.1) and (5.5) express the latitude and longitude in terms of the orbital arc. Symbolically, we may write

$$\theta = \theta(\sigma; i) \tag{5.6}$$

$$\psi = \psi(\sigma; i, \mu) \tag{5.7}$$

In turn, these equations may be substituted into Equations (3.18) and (3.19) to yield expressions for the oblique latitude θ' and longitude ψ' in terms of orbital arc σ. Thus, we have

$$\theta' = \theta'(\theta, \psi; \kappa, \gamma) = \theta'(\sigma; i, \mu, \kappa, \gamma) \tag{5.8}$$

$$\psi' = \psi'(\theta, \psi; \kappa, \gamma) = \psi'(\sigma; i, \mu, \kappa, \gamma) \tag{5.9}$$

which constitute 2 equations in the 3 unknowns θ', ψ' and σ. If we wish to determine the point of intersection with the R curve bounding one side of the common region of observation Ω, we also have Equation (3.10) which is

$$\cos\alpha = \cos\theta' \cos(\psi' + \gamma) \tag{5.10}$$

Substitution of Equations (5.8) and (5.9) into (5.10) yields a complicated equation for σ which may then be solved numerically to obtain

the value $\sigma = \sigma_R$ corresponding to the intersection point. Next, to obtain the point of intersection with the L curve, we have Equation (3.11) which is really Equation (5.10) with γ replaced by $-\gamma$. Thus, the same process may be used to obtain the value $\sigma = \sigma_L$ corresponding to the intersection point. Thus, the population time τ of the satellite within the region Ω is <u>exactly</u> given by

$$\tau = \frac{P}{2\pi} (\sigma_R - \sigma_L) \tag{5.11}$$

Let μ_c denote the value of μ which corresponds to the orbit passing through the central point C. The above process is first performed with a value $\mu = \mu_c + \Delta\phi_o$ where $\Delta\phi_o$ is a random number in the range $0 \leq \Delta\phi_o < \Delta\phi$ where $\Delta\phi$ is given by Equation (2.17) which is

(5.12)

The process is then repeated with values $(\mu + n\Delta\phi)$ where $n = \pm 1, \pm 2, \ldots$ until no more orbits intersect the region Ω. After this, the entire above process is then repeated with other random values of $\Delta\phi_o$. The average population times are then obtained by averaging the results of all these processes.

5.2 Approximate Formulation

Consider Figure 5.2 which illustrates the spherical triangle formed by the equator, the meridian and the arc length of the central point C measured from the ground station G. This spherical triangle is fixed on the rotating earth.

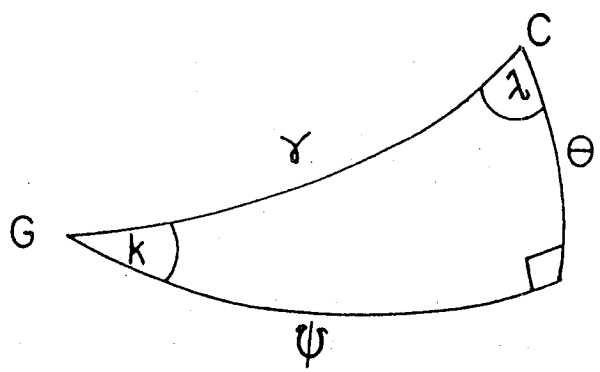

Figure 5.2

Then, we have the following spherical trigonometric formulas

$$\sin\theta = \sin\kappa \sin\gamma \tag{5.13}$$

$$\cos\gamma = \cos\theta \cos\psi \tag{5.14}$$

$$\sin\gamma \sin\lambda = \sin\psi \tag{5.15}$$

which may be used to compute the latitude and longitude of C and also the angle λ the arc GC makes with the meridian through C.

Next, consider Figure 5.3 which illustrates the spherical triangle formed by the equator, the meridian and the orbital arc of a satellite just passing through the point C. This spherical triangle is fixed on the celestial sphere, which is inertial.

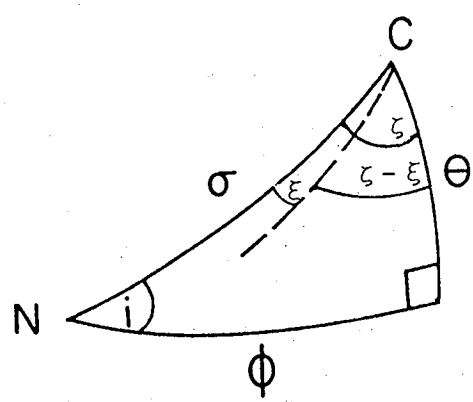

Figure 5.3

Then, we have the following spherical trigonometric formulas

$$\sin\theta = \sin i \sin\sigma \tag{5.16}$$

$$\cos\sigma = \cos\theta \cos\zeta \tag{5.17}$$

$$\sin c \sin\zeta = \sin\phi \tag{5.18}$$

which may be used to compute the orbital arc, the right ascension and also the angle ζ the arc NC makes with the meridian through C.

However, because of the earth's rotation, the satellite's ground track does not really make an angle ζ with the meridian through C. Rather, it is deflected through an angle ξ which is, in general, given by

$$\tan \xi = \frac{\omega \cos\theta \cos\zeta}{1 - \omega \cos i} \tag{5.19}$$

where ω is defined by Equation (5.4). (It may be verified that this deflection causes direct orbits to be more inclined and retrograde orbits to be less inclined as viewed by their ground tracks.) Thus, the angle between the satellite ground track and the meridian at point C is given by $(\zeta-\xi)$, as shown in Figure 5.3. Next, consider Figure 5.4 which illustrates the inclination η of the orbital arc with the oblique equator

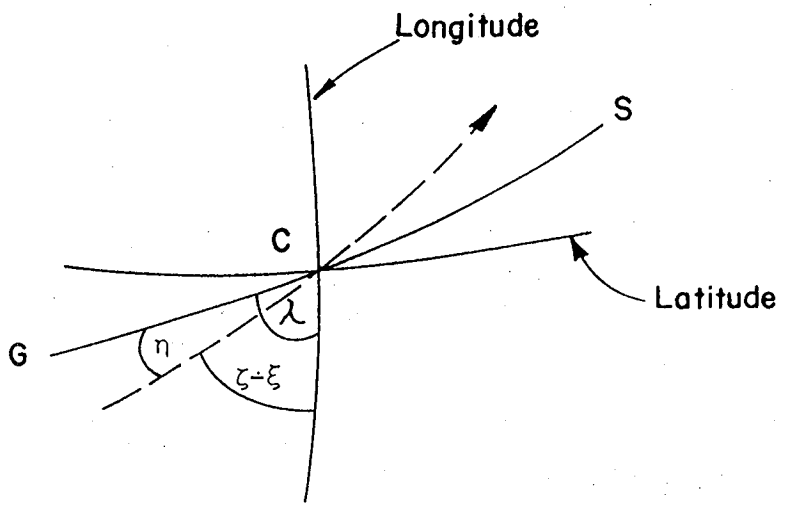

Figure 5.4

Hence, it is seen that we have

$$\left.\begin{aligned} \eta &= \lambda - \zeta + \xi \quad \text{for ascending orbits} \\ \eta &= \lambda + \zeta - \xi - \pi \quad \text{for descending orbits} \end{aligned}\right\} \tag{5.20}$$

It may also be verified that these equations are algebraically valid for both direct and retrograde orbits.

Next, consider Figure 5.5 which illustrates the case of a satellite just passing through the point D which is displaced by $\Delta\gamma$ from the central point C. This corresponds to an orbit whose equator crossing is displaced by $\Delta\phi$ from the point N.

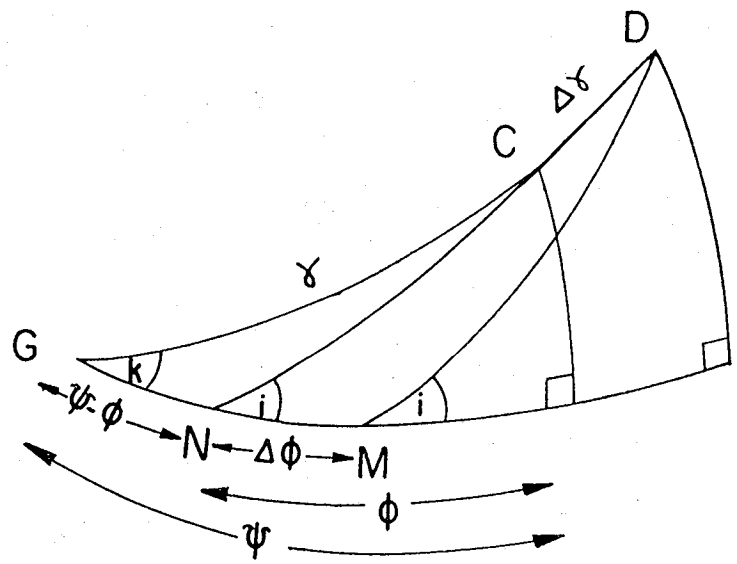

Figure 5.5

Then, using spherical trigonometric formulas, it may be shown that $\Delta\gamma$ is related to $\Delta\phi$ by the following equation

$$\tan(\gamma + \Delta\gamma) = \frac{\tan i \sin(\psi - \phi + \Delta\phi)}{\tan i \cos\kappa \cos(\psi - \phi + \Delta\phi) - \sin\kappa} \qquad (5.21)$$

Thus, by replacing γ with $(\gamma+\Delta\gamma)$, Equations (5.13) - (5.20) may be used to compute the inclination η of the new orbital arc with the oblique equator. It may be verified that Equation (5.21) is also algebraically valid for both the cases of $i > \kappa$ and $i < \kappa$. Moreover, it is also valid for both direct and retrograde orbits. Furthermore, it is valid for arbitrary finite differences $\Delta\phi$ and $\Delta\gamma$, but considerable care must be exercised when taking the inverse tangent to obtain $(\gamma + \Delta\gamma)$ in the correct quadrant corresponding to the increment $\Delta\phi$.

Up to this point, no approximations have been made. It is now assumed that the satellite's ground track is an arc of a great circle lying within the region Ω and making an angle η with the oblique equator GS. Figure 5.6 illustrates the cases of orbital arcs passing through the points C and D.

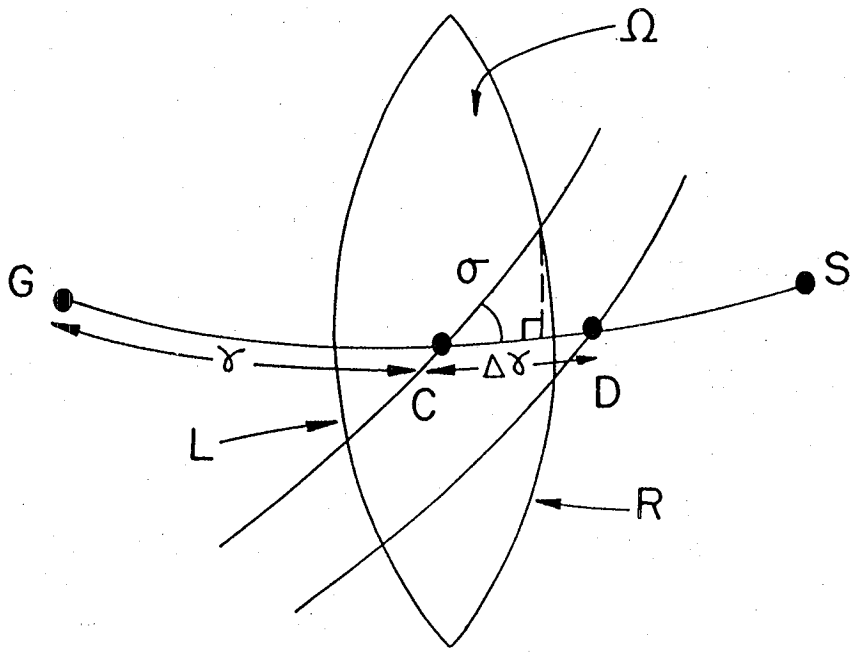

Figure 5.6

Now, it is possible to write the following two approximate relations for the orbit passing through the central point C

$$\sin \theta' = \sin\eta \sin \sigma' \qquad (5.22)$$

$$\cos \theta' = \cos \theta' \cos \psi' \qquad (5.23)$$

where σ' is the arc length measured from the oblique equatorial crossing. These two equations are the crude analogs of Equations (5.8) and (5.9) of the exact case. If we wish to determine the point of intersection with the R curve, we also have Equation (3.10) which is

$$\cos\alpha = \cos \theta' \cos (\psi' + \gamma). \qquad (5.24)$$

However, instead of substituting Equations (5.22) and (5.23) into (5.24) to yield a complicated equation for σ', it turns out to be the case that an algebraic equation can be obtained involving sin θ'. This is accomplished as follows: From Equations (5.22) and (5.23), the following auxiliary equation is obtained

$$\sin \psi' = \frac{\tan \theta'}{\tan \eta} \tag{5.25}$$

Equation (5.24) is then written as

$$\begin{aligned} \cos\alpha &= \cos \theta' (\cos \psi' \cos\gamma - \sin \psi' \sin \gamma) \\ &= \cos \sigma' \cos\gamma - \cos \theta' \frac{\tan \theta'}{\tan \eta} \sin\gamma \\ &= \cos\gamma \sqrt{\left(1 - \frac{\sin^2 \theta'}{\sin^2 \eta}\right)} - \frac{\sin \theta'}{\tan \eta} \sin\gamma \end{aligned}$$

or equivalently

$$\cos \gamma \sqrt{(\sin^2\eta - \sin^2 \theta')} = \sin\eta \cos\alpha + \cos\eta \sin\gamma \sin \theta'. \tag{5.26}$$

By squaring both sides of this equation, it is obvious that a quadratic equation is obtained involving sin θ'. After much simplification, it may be shown that we have

$$\frac{\sin \theta'}{\sin \eta} = \frac{- \cos\alpha \sin\gamma \cos\eta \pm \cos\gamma \sqrt{(\sin^2\alpha - \sin^2\gamma \sin^2\eta)}}{(1 - \sin^2\gamma \sin^2\eta)} \tag{5.27}$$

A little consideration will reveal that for the intersection point with the R curve, it is necessary to retain only the positive sign in the above equation. Thus, this expression corresponds to the value at $\theta' = \theta'_R$.

However, from Equation (5.22), it is seen that the value σ_R' is given by

$$\sin\theta_R' = \sin\eta \quad \sin\sigma'_R \tag{5.28}$$

Consequently, we have

$$\sin\sigma_R' = \frac{-\cos\alpha \sin\gamma \cos\eta + \cos\gamma \sqrt{(\sin^2\alpha - \sin^2\gamma \sin^2\eta)}}{(1 - \sin^2\gamma \sin^2\eta)} \tag{5.29}$$

Next, to obtain the intersection point with the L curve, we have Equation (3.11) which is really Equation (5.24) with γ replaced by $-\gamma$. Thus, the same process may be used to obtain σ_L' which can be shown to be given by retaining the negative sign in Equation (5.27). Consequently, we have the following result

$$\sin\sigma_L' = \frac{\cos\alpha \sin\gamma \cos\eta - \cos\gamma \sqrt{(\sin^2\alpha - \sin^2\gamma \sin^2\eta)}}{(1 - \sin^2\gamma \sin^2\eta)} \tag{5.30}$$

which states that $\sigma_L' = -\sigma_R'$ as expected (only for the case of the orbit passing through the central point C). Thus, the population time τ of the satellite within the region Ω is approximately given by

$$\tau = \frac{P}{2\pi} \quad (\sigma_R' - \sigma_L') \tag{5.31}$$

which is the crude analog of Equation (5.11).

Next, to obtain the intersection point between the R curve and the orbit passing through the point D, a little consideration will reveal that it suffices to replace γ by $(\gamma + \Delta\gamma)$ and also use the

corresponding value of η and then repeat the process above for computing σ_R' as given by Equation (5.29). However, to obtain the intersection point between the L curve and the orbit passing through D, a little more caution is now necessary. It now suffices to replace γ by $(-\gamma + \Delta\gamma)$ and also use the corresponding value of η and then repeat the process above for computing σ_R' but now retain the negative sign. This result yielding the value of σ_L' is no longer trivially the negative of σ_R' as for the special case of C.

The above process is first performed with a random value $\Delta\phi_o$ in the range $0 \leq \Delta\phi_o < \Delta\phi$ where $\Delta\phi$ is given by Equation (2.17) which is

$$\Delta\phi = \frac{2\pi}{\sqrt{N}} \tag{5.32}$$

The process is then repeated with values $(\Delta\phi_o + n\Delta\phi)$ where $n = \pm 1, \pm 2, \ldots$ until no more orbits intersect the region Ω. After this, the entire above process is then repeated with other random values of $\Delta\phi_o$. The average population times are then obtained by averaging the results of all these processes.

Finally, it must be mentioned that in order to insure that the correct segment of the R circle (see Figure 5.6) is identified to yield the desired intersection point as given by the general analog of Equation (5.29), a little consideration will reveal that we must have η in the range $-\pi/2 < \eta \leq \pi/2$. Thus, if η is outside this range, we must accordingly add to or subtract π from η. Similarly, the same procedure applies to insure the identification of the correct segment of the L circle to yield the desired intersection point as given by the general analog of Equation (5.30). Furthermore, considerable thought will reveal that this assignment of the η range not only correctly gives the desired intersection points for orbits crossing the oblique equator within the observation region Ω, but also for the case of equatorial crossings outside it for a range of $\Delta\gamma$ exceeding $\pi/2$ measured from the central point C. The reasons for this are not apparent and, at first sight, it would seem that this assignment of η values outside the region Ω leads to incorrect answers. But this is not so because of the manner in which the inverse

trigonometric functions are assigned their principal values. Thus, Equations (5.29) and (5.30) contain many subtle features in logic which automatically combine to yield, in mutual accord, the correct intersection points regardless of the equatorial crossing. In particular, additional consideration will reveal that it is only necessary to consider equatorial crossings such that the orbits intersect the oblique meridian through the central point C at an oblique latitude θ' not greater than θ^* given by

$$\theta^* = \min\left\{ \left|\eta\right| , \cos^{-1}\left(\frac{\cos\alpha}{\cos\gamma}\right)\right\} \tag{5.33}$$

This corresponds to a range $\Delta\gamma^*$ given by

$$\Delta\gamma^* = \sin^{-1}\left(\frac{\tan\theta^*}{\tan\left|\eta\right|}\right) \tag{5.34}$$

so that

$$\Delta\gamma^* = \min\left\{ \pi/2, \sin^{-1}\left(\frac{\tan\left[\cos^{-1}\left(\frac{\cos\alpha}{\cos\gamma}\right)\right]}{\tan\left|\eta\right|}\right)\right\} \tag{5.35}$$

or equivalently

$$\Delta\gamma^* = \min\left\{ \pi/2, \sin^{-1}\sqrt{\left(\frac{\cos^2\gamma - \cos^2\alpha}{\cos^2\gamma - \cos^2\alpha + \cos^2\alpha\,\tan^2\eta}\right)}\right\} \tag{5.36}$$

It is not difficult to see that if an orbit intersects the oblique equator outside the range $\Delta\gamma^*$ and also eventually intersects the observation region Ω, then this orbit would already have been counted as lying within the acceptable range on the other side of the central point.

SECTION 6 - RESULTS FOR ORBITING SATELLITES

6-1 Average Population Time Computations

Computations were performed, except for minor modifications, according to the method discussed in Section 5.2 to obtain the average population times for Class I and II satellites. The representative values of parameters used are shown in Table 6.1.

Table 6.1

Quantity	Class I	Class II
Period P (minutes)	100.9	717.9
Inclination i (degrees)	74.0	63.9
Altitude h (km)	800	20,178.5
Number N	400	100

The value of β, the conical observation angle at the earth's surface, is taken to be 80° for both the ground station and the ship. The ground station is taken to be at the origin of longitude and latitude while the ship is taken to be at various values of longitude ψ_s and latitude θ_s only in the first quadrant. It may be verified that for locations of the ship in the other quadrants, the corresponding results may be obtained by taking mirror reflections about the primary axes.

After the average population times τ have been obtained, the results were divided by the characteristic time T defined by

$$T = \frac{P}{\sqrt{N}} \tag{6.1}$$

to obtain the number of satellites visible to both the ground station and the ship. (T is the time for a satellite to travel the intra-satellite distance $\Delta\sigma$ where $\Delta\sigma$ is given by Equation (2.18).) The relevant results for Class I and II satellites are respectively summarized in Figures 6.1 and 6.2, each of which was obtained by averaging the results using ξ given by Equation (5.19) and those using $\xi = 0$.

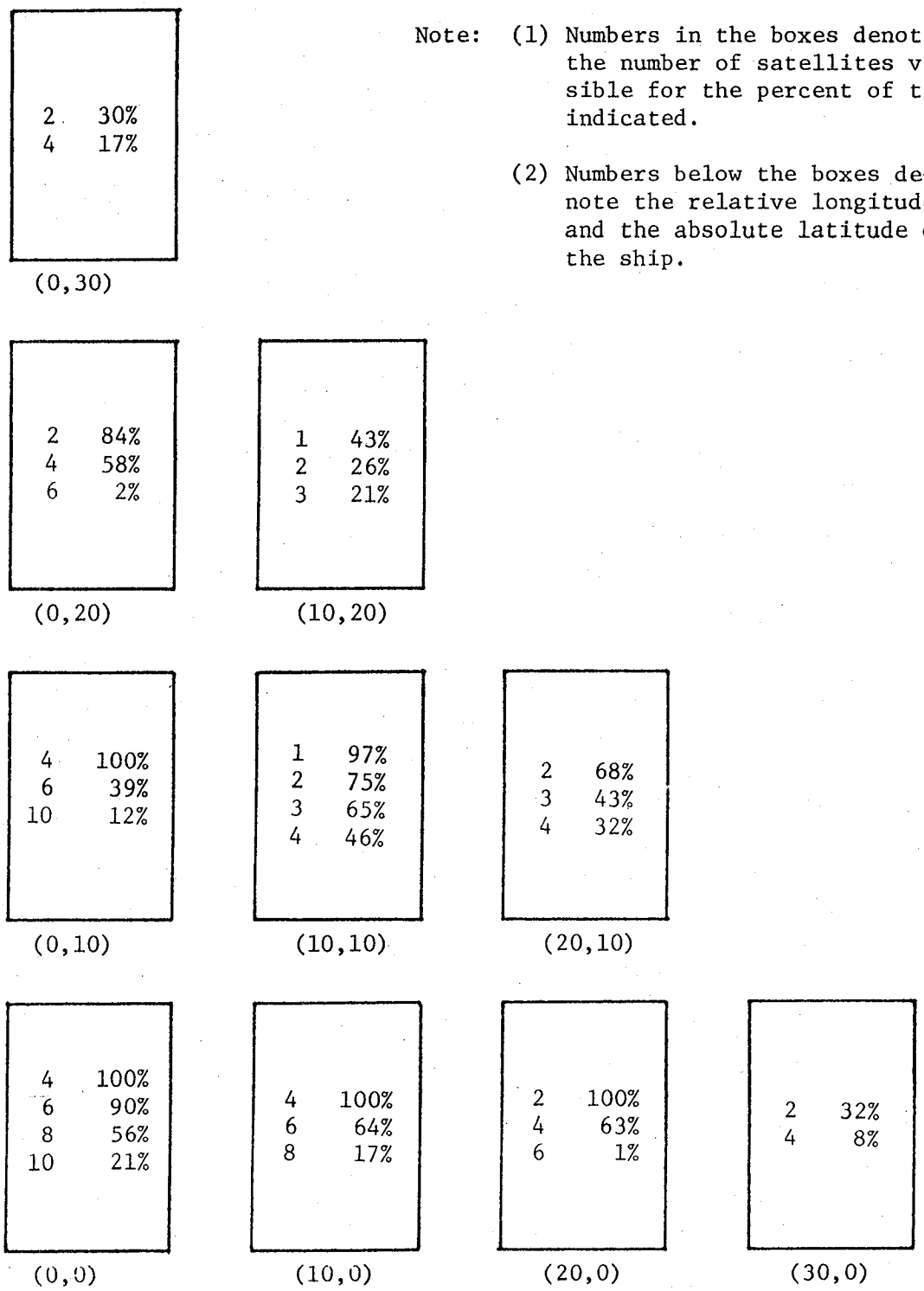

Note: (1) Numbers in the boxes denote the number of satellites visible for the percent of time indicated.

(2) Numbers below the boxes denote the relative longitude and the absolute latitude of the ship.

Figure 6.1 - Results for 100 Minute Orbiting Satellites

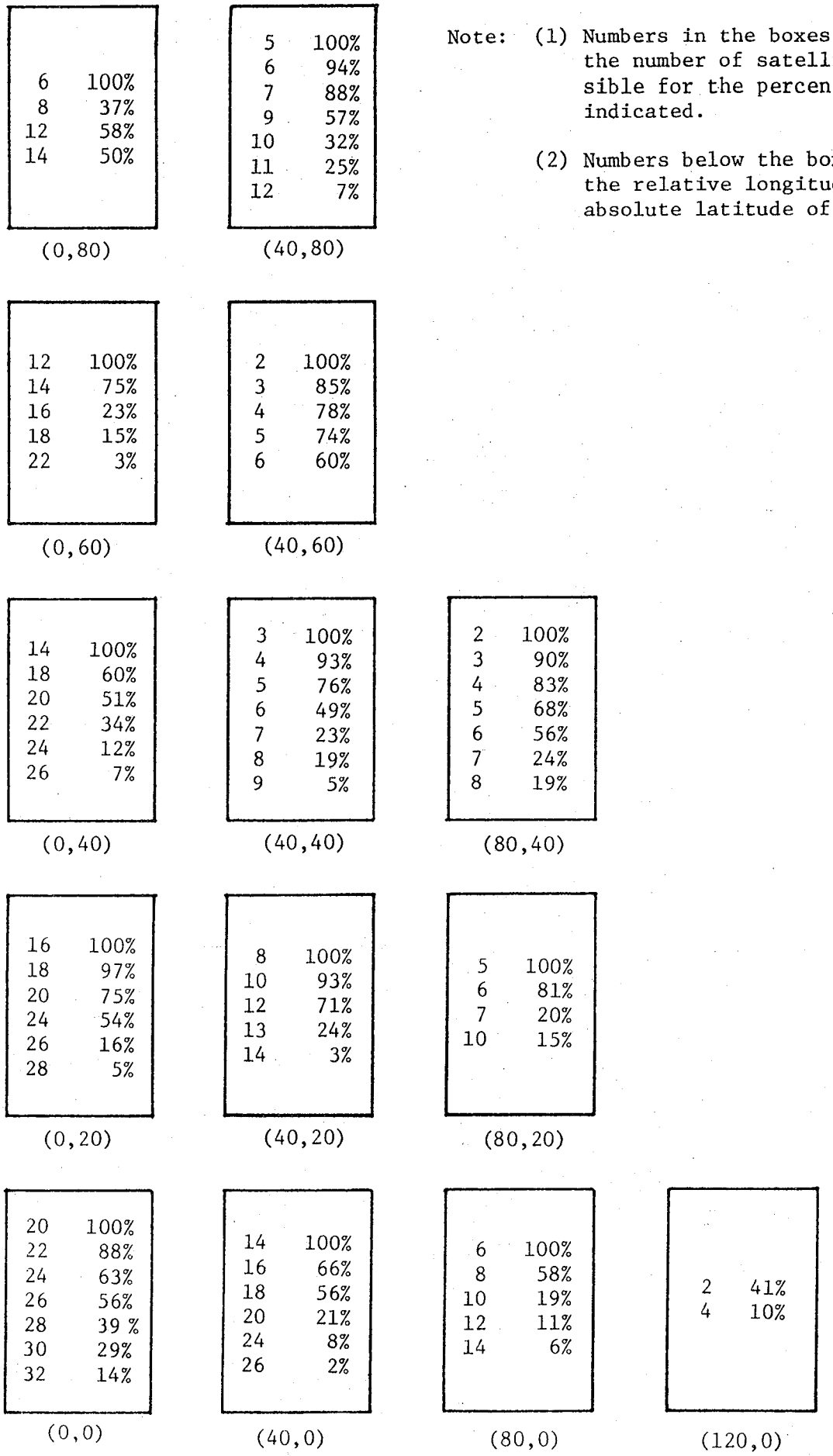

Note: (1) Numbers in the boxes denote the number of satellites visible for the percent of time indicated.

(2) Numbers below the boxes denote the relative longitude and the absolute latitude of the ship.

Figure 6.2 - Results for 12 Hour Orbiting Satellites

6.2 Time Average Population Computations

For the special case of the ship at the origin of longitude and latitude, the time average population N_Ω may be computed by Equation (4.3). Numerical integration yields a value of about 28.48% for N_Ω/N for Class II satellites. That is, on the average, 28.48 satellites are mutually visible to the ground station and the ship when they are together.

As a comparison, it may be shown that the ratio of the area of common visibility Ω to the area of the zonal belt A covered by the satellite orbits is given by

$$\frac{\Omega}{A} = \frac{[1 - \sin(\pi/2 - \alpha)]}{2 \sin i} \qquad (6.2)$$

when the ground station and ship are together. Hence, for Class II satellites, we obtain a value of about 22.4% for Ω/A. As expected, this value is smaller than that for N_Ω/N because the density f increases with latitude and hence contributes toward giving a higher value of N_Ω in the numerical integration.

The other comparison is made with the results displayed in the (0,0) box of Figure 6.2 which are seen to yield a smaller value than that for N_Ω/N. This is also to be expected because the approximation made in Section 5.2 assumed that the satellite orbits are arcs of great circles within the region Ω and hence yields a smaller value of the average population time τ than that obtained by considering the actual satellite ground track.

SESSION II

H. Heuberger, Chairman

DISTORTION-FREE MAPPING OF VISSR IMAGERY DATA FROM GEOSYNCHRONOUS SATELLITES

F. K. Chan

Scientific Analysts and Consultants, Inc.

4114 Heathfield Road, Rockville, Md. 20853

ABSTRACT

Analysis has been performed for mapping VISSR imagery data so as to eliminate all geometrical distortions. The formulation is rigorous and includes all misalignment angles of the VISSR, the sun sensor and the instantaneous spin axis with the satellite's body axis. It also includes the effects due to the motion of the satellite's suborbital point. All the mapping equations for distortion removal are reduced to simplest forms, and all the algorithms are optimized as much as possible.

An approach is then formulated for implementing these algorithms for in-line operational use. It covers the computations involved in determining benchmarks, the interpolation methodology for filling in the points interspaced between benchmarks, and the correction procedure for computing the radiometric values at the center of the pixel in the distortion-free image. It is also concerned with the time requirements, data storage, and output data accuracy. With the present microprocessor technology, it is concluded that this in-line distortion removal is possible in real-time processing of infra-red but not visible VISSR imagery data.

This work was supported by NOAA Contract Nos: 01-8-M01-1864 and NA-79KAC-00026

SECTION 1 - INTRODUCTION

In the Visible and Infra-red Spin Scan Radiometer (VISSR) data obtained from the present geosynchronous satellites, distortions are observed in the images of the earth. As illustrated in Figure 1.1 which is exaggerated for clarity, these image deformations appear as vertical compression and expansion of the image, non-vertical alignment of the North and South Poles, and multi-representation of some points or omission of other points.

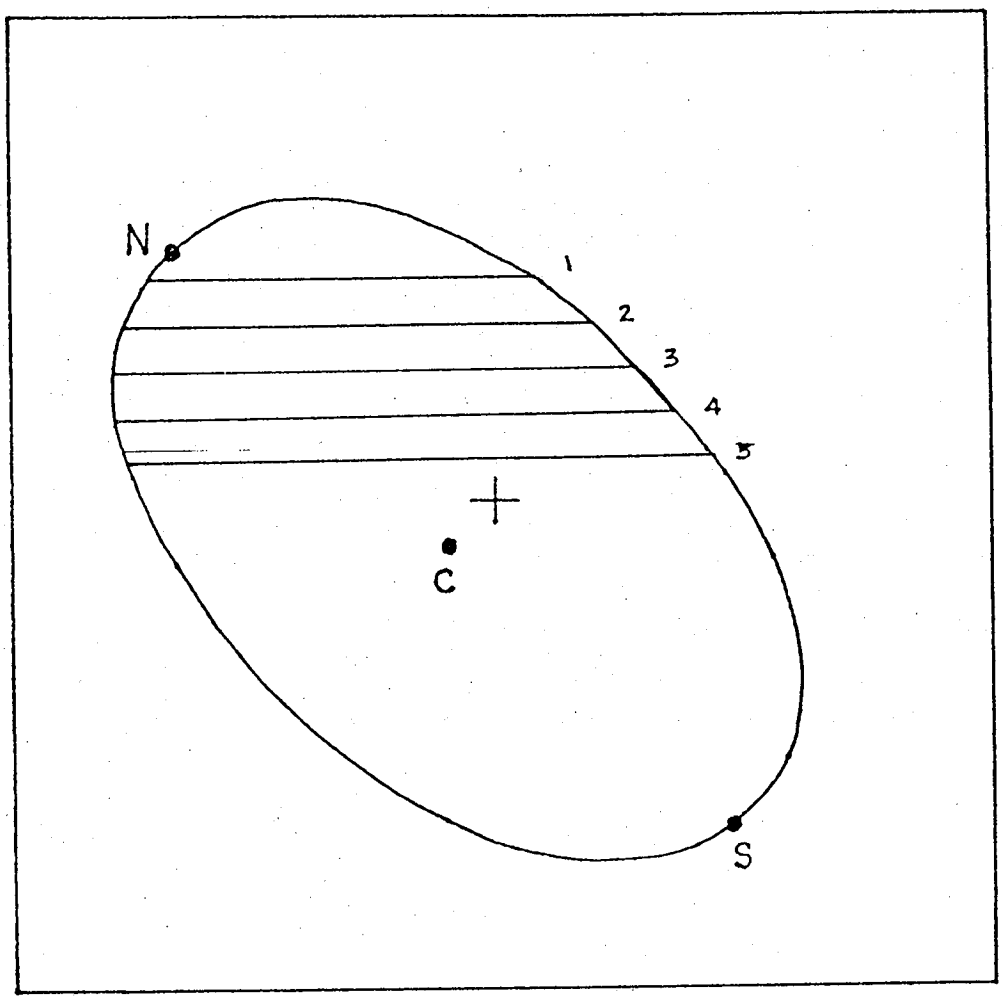

Figure 1.1 Exaggerated VISSR Image of Earth

These distortions may well be explained by considering Figure 1.2 which illustrates the same scan-lines on the projection plane of the earth. Again, for clarity, these scan-lines are depicted to be non-parallel and unevenly spaced to a degree more so than the realistic cases.

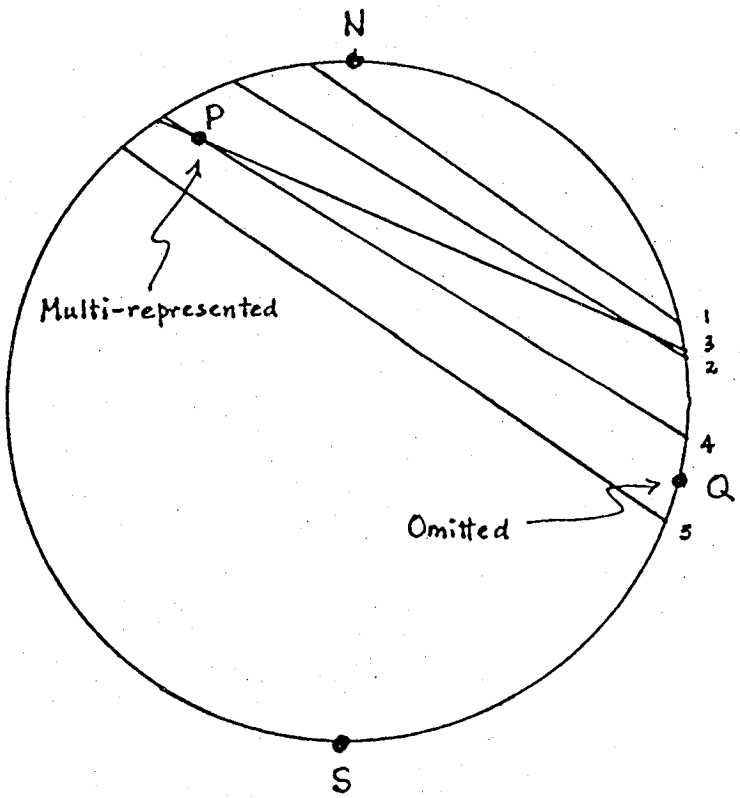

Figure 1.2 Projection Plane Image of Earth

If one were to relate these two images, one would find, for example, that a triangular figure in the projection plane image becomes distorted into a curved figure in the VISSR image. This is illustrated in Figure 1.3 which is obtained by superimposing a triangle on Figure 1.2 and then mapping it onto Figure 1.1.

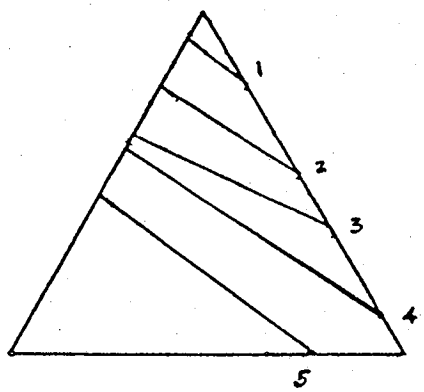

Projection Plane Image

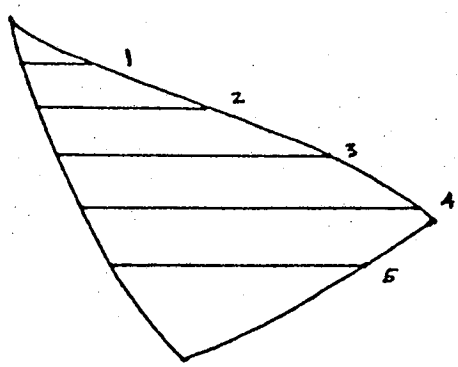

VISSR Image

Figure 1.3 Distortion of Image

The general causes for these image deformations may be broadly classified as follows:

1. Orbit not circular and equatorial
2. Spin axis not perpendicular to orbital plane
3. Misalignment of the VISSR, the sun sensor, and the instantaneous spin axis with the satellite's body axis
4. Biases due to varying sun size and varying sun elevation effect on threshold of the sun sensor triggering.

To remove these distortions, it is necessary to include all the above factors in the formulation of the mapping equations. However, it is feasible to consider only the first three. The corresponding equations have been derived in Reference 1 in which it was convenient to introduce the following coordinate systems:

The Inertial System: This is well-known and is defined such that the x_I-axis is in the direction of the vernal equinox, the z_I-axis is perpendicular to the equatorial plane (in the direction of the North Pole), and the y_I-axis is given by $\hat{y}_I = \hat{z}_I \times \hat{x}_I$.

The Body System: This system is defined such that the z_B-axis is along the longitudinal axis of the satellite, the x_B-axis is the intersection line between the VISSR stepping plane and the plane perpendicular to the z_B-axis, and the y_B-axis is given by $\hat{y}_B = \hat{z}_B \times \hat{x}_B$.

The VISSR System: This system is defined such that the x_V-axis is in the direction of the mid-scan, the z_V-axis is perpendicular to the x_V-axis and lies in the VISSR stepping plane, and the y_V-axis is given by $\hat{y}_V = \hat{z}_V \times \hat{x}_V$.

The Sun Sensor System: This system is defined such that the x_U-axis

is in the direction of the bisector of the angle fanned out by the sun sensor, the z_U-axis is perpendicular to the x_U-axis and lies in the sun sensor fan plane, and the y_U-axis is given by $\hat{y}_U = \hat{z}_U \times \hat{x}_U$.

The Spin System: Let $\hat{z}_S$ denote the unit spin axis vector around which the satellite is instantaneously rotating. Let $\vec{r}'$ denote the position vector of the satellite. Then, the y_S-axis and the x_S-axis are respectively defined by

$$\hat{y}_S = \overbrace{\vec{r}' \times \hat{z}_S} \tag{1.1}$$

$$\hat{x}_S = \hat{y}_S \times \hat{z}_S \tag{1.2}$$

The Auxiliary System: In this system, illustrated in Figure 1.4, the unit base vectors are defined by the following equations:

$$\hat{x}_A = -\hat{r}' \tag{1.3}$$

$$\hat{y}_A = \overbrace{\hat{z}_I \times \hat{x}_A} \tag{1.4}$$

$$\hat{z}_A = \hat{x}_A \times \hat{y}_A \tag{1.5}$$

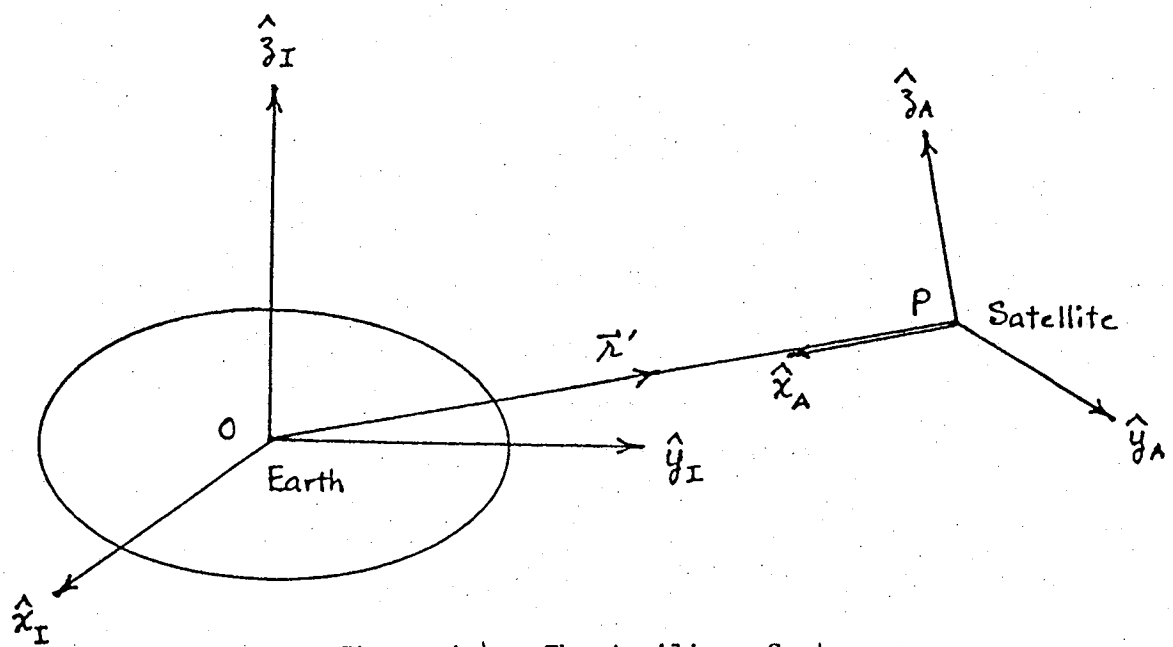

Figure 1.4 - The Auxiliary System

The Normalized System: Consider a system, referred to as the normalized system, as illustrated in Figure 1.5. The origin R of this system is defined at a point $\vec{r}$ on the earth's equatorial plane and fixed in the earth's rotating system. The satellite P at point $\vec{r}'$, however, is not necessarily on the earth's equatorial plane or fixed in the earth's rotating system. In this normalized system, the unit base vectors are defined by the following equations:

$$\hat{x}_N = -\hat{r} \tag{1.6}$$

$$\hat{z}_N = \hat{z}_I \tag{1.7}$$

$$\hat{y}_N = \hat{z}_N \times \hat{x}_N \tag{1.8}$$

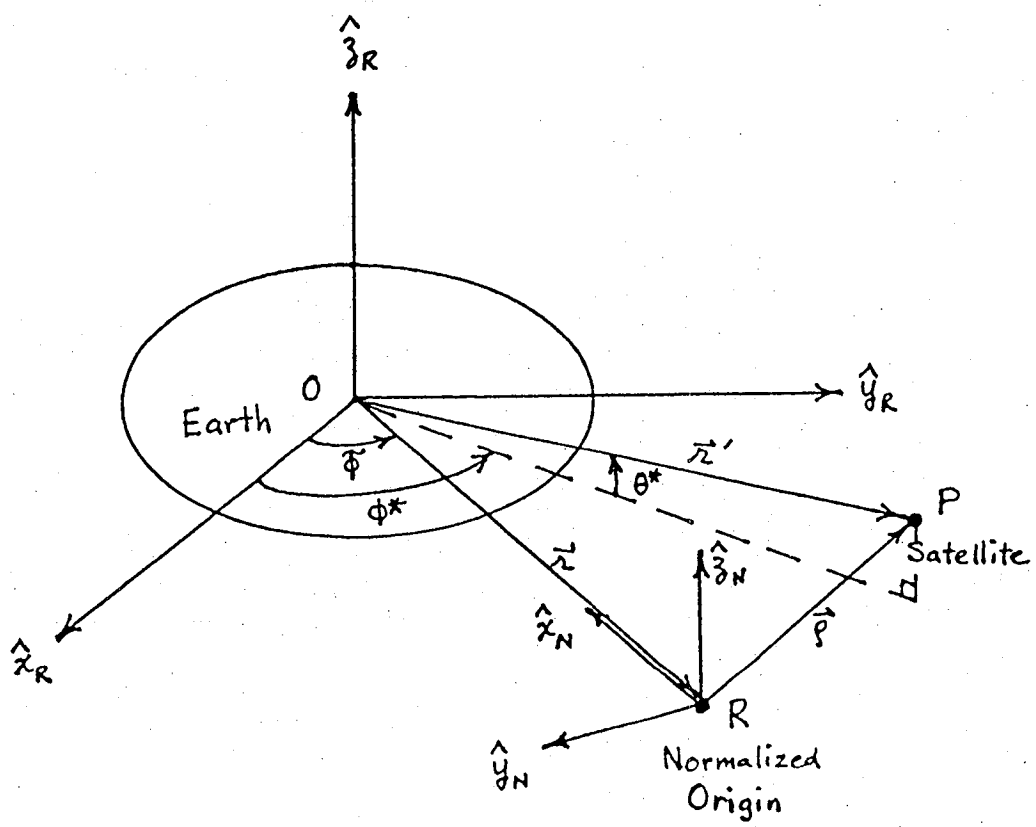

Figure 1.5 - The Normalized System

In the present study, the results obtained in Reference 1 are used to formulate algorithms for mapping the data coming out of the Synchronous Data Buffer (SDB) so as to obtain a distortion-free imagery. Moreover, this rectified imagery also has the desirable feature that it is referred to a normalized satellite position which is therefore the same for all imageries. Thus, if the distortion-free mapping is performed in-line during data processing, the transmitted VISSR data will provide a uniformly compatible data base for all users in their scientific work. Furthermore, it will also facilitate in the future development of a composite data base for different kinds of data obtained from various satellites.

Mapping of the data may be further optimized the use of interpolation with the aid of appropriately chosen benchmarks. Section 2 deals with the computation of these benchmarks, while Section 3 covers the interpolation methodology for filling in the points interspaced between benchmarks. Section 4 is concerned with the correction procedure for computing the radiometric values at the center of the pixel in the distortion-free image. Section 5 discusses the time requirements, data storage and output data accuracy. Section 6 summarizes the results of this study.

SECTION 2 - BENCHMARK COMPUTATIONS

This section deals with the computation of benchmark locations in the normalized distortion-free coordinate system. It discusses the relevant input parameters, computational equations, number of compuationál operations, and the requisite partial derivatives.

2.1 Input Parameters

The relevant input parameters are listed below:

N_η = scan number

N_{ξ_s} = sample number

M_η = mid-scan number

M_{ξ_s} = mid-sample number

$\Delta\eta$ = scan angular width

$\Delta\xi$ = sample angular width

ψ_s = scan angular bias (line bias)

$\vec{r}'$ = orbital position of satellite

α = right ascension of spin axis

δ = declination of spin axis

$\vec{r}$ = normalized position of satellite

a = earth's semi-major axis

c = earth's semi-minor axis

For convenience, two parameters dependent on the above are defined as follows:

$$\varepsilon \equiv \frac{a^2 - c^2}{c^2}$$

$$K^* \equiv \frac{r}{a} \frac{1}{\Delta\xi} \tan^{-1}\left(\frac{a}{r}\right)$$

2.2 Computational Equations

The following equations for computing benchmark coordinates have been extracted from Reference 1. They have been simplified and are listed below in the proper sequence for usage. The exact definitions of cursory intermediate variables may be obtained from the original report.

$$\eta = (M_\eta - N_\eta)\,\Delta\eta \tag{2.1}$$

$$\xi_s = (M_{\xi_s} - N_{\xi_s})\,\Delta\xi \tag{2.2}$$

$$\eta_s = \eta + \psi_s \tag{2.3}$$

$$\hat{u}_s = c_{\eta_s} c_{\xi_s} \hat{x}_s + c_{\eta_s} s_{\xi_s} \hat{y}_s + s_{\eta_s} \hat{z}_s \tag{2.4}$$

$$k = \frac{1}{\sqrt{[1 - (\hat{\lambda}' \cdot \hat{z}_s)^2]}} \tag{2.5}$$

$$k' = \frac{1}{\sqrt{[1 - (\hat{\lambda}' \cdot \hat{z}_I)^2]}} \tag{2.6}$$

$$(T_{13})_{SA} = -(\hat{\imath}' \cdot \hat{\jmath}_S) \tag{2.7}$$

$$(T_{23})_{SA} = k' \hat{\imath}' \cdot (\hat{\jmath}_I \times \hat{\jmath}_S) \tag{2.8}$$

$$(T_{33})_{SA} = k' \left[(\hat{\jmath}_S \cdot \hat{\jmath}_I) - (\hat{\imath}' \cdot \hat{\jmath}_S)(\hat{\imath}' \cdot \hat{\jmath}_I) \right] \tag{2.9}$$

$$T_{SA} = \begin{bmatrix} \frac{1}{k} & 0 & (T_{13})_{SA} \\ -k(T_{13})_{SA}(T_{23})_{SA} & k(T_{33})_{SA} & (T_{23})_{SA} \\ -k(T_{13})_{SA}(T_{33})_{SA} & -k(T_{23})_{SA} & (T_{33})_{SA} \end{bmatrix} \tag{2.10}$$

$$(T_{11})_{AN} = C_{\theta^*} C_{\phi^* - \tilde{\phi}} \tag{2.11}$$

$$(T_{21})_{AN} = C_{\theta^*} S_{\phi^* - \tilde{\phi}} \tag{2.12}$$

$$(T_{31})_{AN} = -S_{\theta^*} \tag{2.13}$$

$$T_{AN} = \begin{bmatrix} (T_{11})_{AN} & -k'(T_{21})_{AN} & -k'(T_{11})_{AN}(T_{31})_{AN} \\ (T_{21})_{AN} & k'(T_{11})_{AN} & -k'(T_{21})_{AN}(T_{31})_{AN} \\ (T_{31})_{AN} & 0 & \frac{1}{k'} \end{bmatrix} \tag{2.14}$$

$$\hat{z}_s = c_\alpha c_\delta \hat{x}_I + s_\alpha c_\delta \hat{y}_I + s_\delta \hat{z}_I \qquad (2.15)$$

$$\hat{x}_s = k\left[(\hat{r}' \cdot \hat{z}_s)\hat{z}_s - \hat{r}'\right] \qquad (2.16)$$

$$\hat{y}_s = \hat{z}_s \times \hat{x}_s \qquad (2.17)$$

$$T_{sI} = \begin{bmatrix} \hat{x}_s \cdot \hat{x}_I & \hat{y}_s \cdot \hat{x}_I & \hat{z}_s \cdot \hat{x}_I \\ \hat{x}_s \cdot \hat{y}_I & \hat{y}_s \cdot \hat{y}_I & \hat{z}_s \cdot \hat{y}_I \\ \hat{x}_s \cdot \hat{z}_I & \hat{y}_s \cdot \hat{z}_I & \hat{z}_s \cdot \hat{z}_I \end{bmatrix} \qquad (2.18)$$

$$\hat{u}_I = T_{sI}\, \hat{u}_s \qquad (2.19)$$

$$A = 1 + \varepsilon (u_z)_I^2 \qquad (2.20)$$

$$B = \vec{r}_I' \cdot \hat{u}_I + \varepsilon (r_z')_I (u_z)_I \qquad (2.21)$$

$$C = \vec{r}_I' \cdot \vec{r}_I' + \varepsilon (r_z')_I^2 - a^2 \qquad (2.22)$$

$$\lambda = \frac{-B - \sqrt{(B^2 - AC)}}{A} \qquad (2.23)$$

$$\hat{u}_N = T_{AN}\, T_{SA}\, \hat{u}_S \tag{2.24}$$

$$\vec{\rho}_N = (r - r' c_{\theta^*} c_{\phi^* - \phi})\hat{x}_N - r' c_{\theta^*} s_{\phi^* - \phi}\, \hat{y}_N + r' s_{\theta^*}\, \hat{z}_N \tag{2.25}$$

$$\vec{\rho}_N' = \vec{\rho}_N + \lambda \hat{u}_N \tag{2.26}$$

$$I^* = K^* \frac{(\rho_y')_N}{(\rho_x')_N} \tag{2.27}$$

$$J^* = K^* \frac{(\rho_z')_N}{(\rho_x')_N} \tag{2.28}$$

I^* and J^* are the coordinates in the normalized distortion-free system. At this stage, for the sake of greater accuracy in subsequent computations, it is preferable not to digitize them.

2.3 Computational Operations

For each benchmark, it may be verified that the computations in equations (2.1) - (2.28) may be achieved by performing:

51 additions

22 divisions

114 multiplications

4 divisions

11 trigonometric function evaluations

2 square root evaluations

Assuming that the following times are required:

Operation	Time (micro-seconds)
Addition	1.5
Subtraction	1.5
Multiplication	6
Division	11
Trigonometric function evaluation	50
Square root evaluation	50

it is seen that about 1487 microseconds are required for each benchmark computation.

2.4 Partial Derivatives

For convenience, it is desirable to choose the set of benchmarks so that they form a rectangular grid in the (N_{ξ_s}, N_η) -space as illustrated in Figure 2.1.

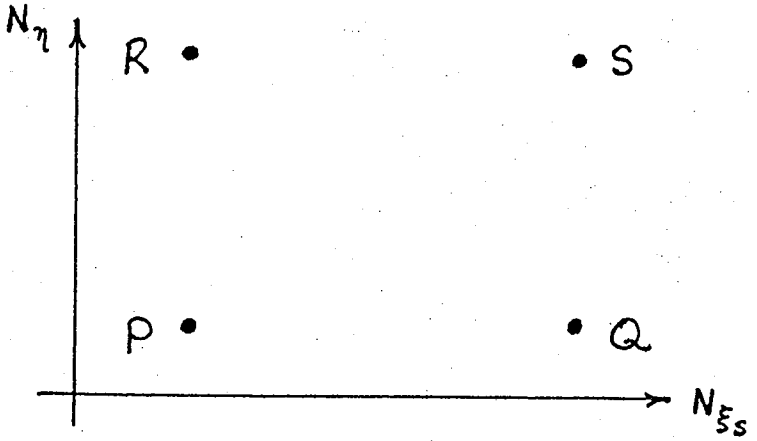

Figure 2.1 - Benchmarks in (N_{ξ_s}, N_η) - Space

Then, it is obvious that the partial derivatives of I^* and J^* with respect to N_{ξ_s} and N_η may be approximated by

$$\left[\left(\frac{\partial I^*}{\partial N_{\xi_s}}\right)_{N_\eta}\right]_P \simeq \frac{(I^*)_Q - (I^*)_P}{(N_{\xi_s})_Q - (N_{\xi_s})_P} \qquad (2.29)$$

$$\left[\left(\frac{\partial J^*}{\partial N_{\xi_s}}\right)_{N_\eta}\right]_P \simeq \frac{(J^*)_Q - (J^*)_P}{(N_{\xi_s})_Q - (N_{\xi_s})_P} \qquad (2.30)$$

$$\left[\left(\frac{\partial I^*}{\partial N_\eta}\right)_{N_{\xi s}}\right]_P \simeq \frac{(I^*)_R - (I^*)_P}{(N_\eta)_R - (N_\eta)_P} \qquad (2.31)$$

$$\left[\left(\frac{\partial J^*}{\partial N_\eta}\right)_{N_{\xi s}}\right]_P \simeq \frac{(J^*)_R - (J^*)_P}{(N_\eta)_R - (N_\eta)_P} \qquad (2.32)$$

For each benchmark, the four associated partial derivatives require 6 subtractions and 4 divisions. These operations consume about 53 microseconds.

These partial derivatives are used later in the method of interpolation for mapping points interspaced betweeen the benchmarks.

SECTION 3 - INTERPOLATION COMPUTATIONS

This section is concerned with the mapping of points which do not coincide with the chosen set of benchmarks. It discusses the input data, interpolation methodology, and number of computational operations.

3.1 Input Data

The input data consists of the coordinates (I^*, J^*) and their four associated partial derivatives for each benchmark. This information has already been obtained in Section 2.

3.2 Interpolation Methodology

Suppose there are m interspaced points between the horizontal benchmarks, and n interspaced points between the vertical benchmarks. Figure 3.1 illustrates a basic unit comprising benchmarks (denoted by solid circles) and interspaced points (denoted by open circles), Thus, there are $(m + 1)(n + 1)$ points altogether in a basic unit.

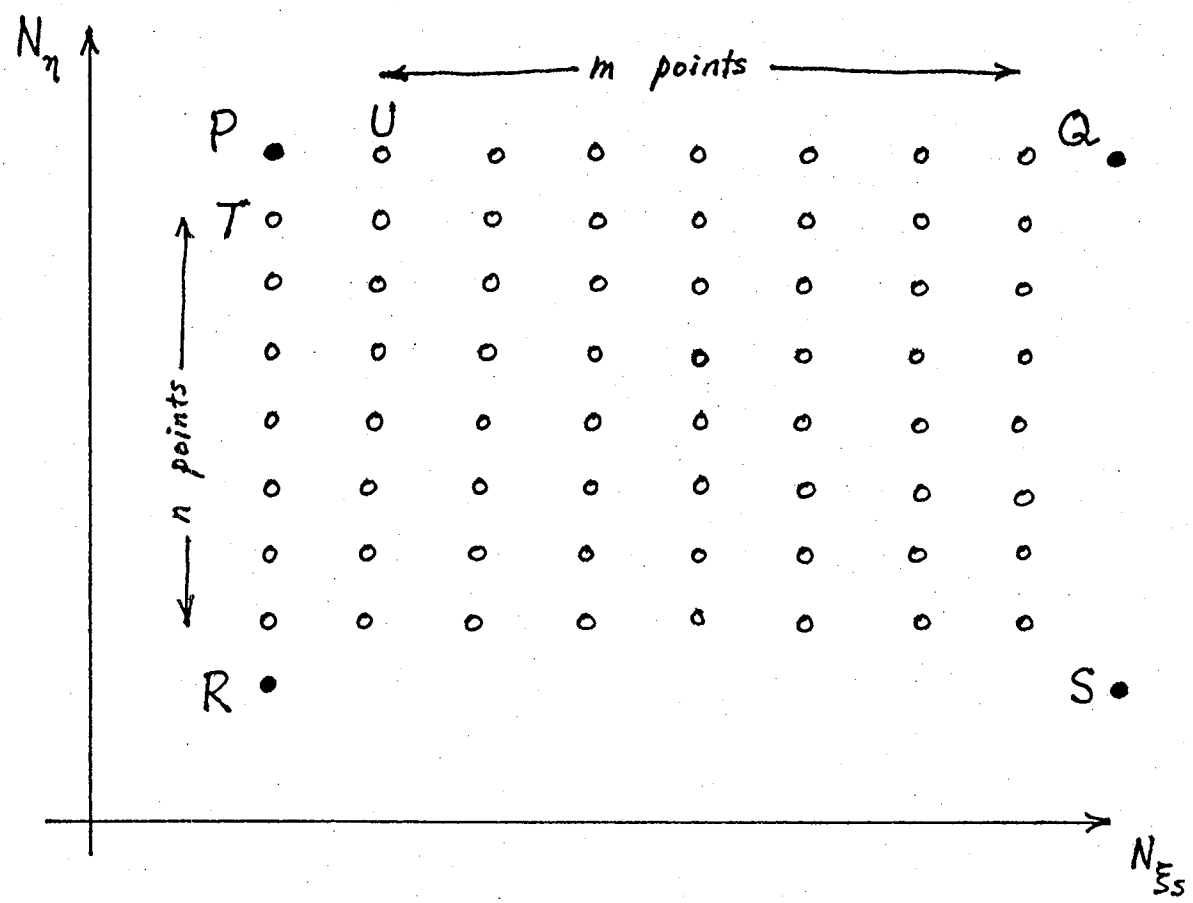

Figure 3.1 - Benchmarks for Interpolation

It is noted that the I^* coordinate of the point T directly below P is given by

$$(I^*)_T = (I^*)_P + \Delta I^* \tag{3.1}$$

But

$$\Delta I^* \simeq \left[\left(\frac{\partial I^*}{\partial N_\eta}\right)_{N_{\xi_s}}\right]_P \Delta N_\eta \tag{3.2}$$

and

$$\Delta N_\eta = +1 \,. \tag{3.3}$$

Therefore, it follows that

$$(I^*)_T = (I^*)_P + \left[\left(\frac{\partial I^*}{\partial N_\eta}\right)_{N_{\xi s}}\right]_P \tag{3.4}$$

A similar equation holds for any point and the point directly below it. Hence, the n interspaced points between P and R may be mapped by the following iterative algorithm:

Let

$$I_0^* = (I^*)_P \tag{3.5}$$

$$J_0^* = (J^*)_P \tag{3.6}$$

Then, perform the following computations

$$\left.\begin{aligned} I^*_{\ell+1} &= I^*_\ell + \left[\left(\frac{\partial I^*}{\partial N_\eta}\right)_{N_{\xi s}}\right]_P \qquad (3.7)\\ J^*_{\ell+1} &= J^*_\ell + \left[\left(\frac{\partial J^*}{\partial N_\eta}\right)_{N_{\xi s}}\right]_P \qquad (3.8) \end{aligned}\right\} \ell = 0, 1, 2, \ldots n$$

Similarly, it is noted that the I^* coordinate of the point U directly to the right of P is given by

$$(I^*)_U = (I^*)_P + \Delta I^* \tag{3.9}$$

But
$$\Delta I^* \simeq \left[\left(\frac{\partial I^*}{\partial N_{\xi s}}\right)_{N_\eta}\right]_P \Delta N_{\xi s} \tag{3.10}$$

and
$$\Delta N_{\xi s} = +1 \tag{3.11}$$

Therefore, it follows that
$$(I^*)_U = (I^*)_P + \left[\left(\frac{\partial I^*}{\partial N_{\xi s}}\right)_{N_\eta}\right]_P \tag{3.12}$$

Again, a similar equation holds for any point and the point directly to the right of it. Hence, the m(n + 1) interspaced points between the columns PR and QS may be mapped by the following iterative algorithm:

Let
$$\left.\begin{aligned} I^*_{0,\ell} &= I^*_\ell \\ J^*_{0,\ell} &= J^*_\ell \end{aligned}\right\} \ell = 0, 1, 2, \ldots n \tag{3.13, 3.14}$$

Then, perform the following computations
$$\left.\begin{aligned} I^*_{(k+1),\ell} &= I^*_{k,\ell} + \left[\left(\frac{\partial I^*}{\partial N_{\xi s}}\right)_{N_\eta}\right]_P \\ J^*_{(k+1),\ell} &= J^*_{k,\ell} + \left[\left(\frac{\partial J^*}{\partial N_{\xi s}}\right)_{N_\eta}\right]_P \end{aligned}\right\} k = 0, 1, 2, \ldots n \tag{3.15, 3.16}$$

After these computations, it is now permissible to digitize I^* and J^* to obtain the rounded integer values I and J.

3.3 Computation Operations

For each interspaced point, it is seen that the computations in equations (3.7) and (3.8) or those in equations (3.15) and (3.16) require 2 additions. Assuming a time of 1.5 microseconds for each operation, therefore about 3 microseconds are required to map each point by interpolation. Allowance is also to be make for converting two real numbers to integer values for each point. This will probably increase the time requirement by a factor of 2 so that about 6 microseconds are required for each point.

SECTION 4 - RADIOMETRIC COMPUTATIONS

This sections considers the methodology of correcting the radiometric values so as to reflect a more realistic value at the center of the pixel in the distortion-free image. It discusses the input data, correction methodology, and number of computational operations.

4.1 Input Data

For each point, the input data consists of the following and may be obtained either from the SDB output data stream or has already been obtained in Section 3:

N_η = scan number

N_{ξ_s} = sample number

$R(N_{\xi_s}, N_\eta)$ = radiometric value of N_η th scan and N_{ξ_s} th sample

$R(N_{\xi_s} - 1, N_\eta)$ = radiometric value of N_η th scan and $(N_{\xi_s} - 1)$th sample

$R(N_{\xi_s}, N_\eta - 1)$ = raidometric value of $(N_\eta - 1)$th scan and N_{ξ_s} th sample

I^* = interpolated horizontal coordinate of (N_{ξ_s}, N_η) in distortion-free system

J^* = interpolated vertical coordinate of (N_{ξ_s}, N_η) in distortion-free system

I = rounded integer value of I^*

J = rounded integer value of J^*

4.2 Correction Methodology

The radiometric value $R(I, J)$ may be obtained from the value $R(I^*, J^*)$ by using the Taylor's series expansion

$$R(I,J) = R(I^*, J^*) + \left(\frac{\partial R}{\partial I^*}\right)_{J^*} (I - I^*) + \left(\frac{\partial R}{\partial J^*}\right)_{I^*} (J - J^*). \quad (4.1)$$

The partial derivatives $\left(\frac{\partial R}{\partial I^*}\right)_{J^*}$ and $\left(\frac{\partial R}{\partial J^*}\right)_{I^*}$ may be written as

$$\left(\frac{\partial R}{\partial I^*}\right)_{J^*} = \left(\frac{\partial R}{\partial N_{\xi_s}}\right)_{N_\eta} \left(\frac{\partial N_{\xi_s}}{\partial I^*}\right)_{J^*} + \left(\frac{\partial R}{\partial N_\eta}\right)_{N_{\xi_s}} \left(\frac{\partial N_\eta}{\partial I^*}\right)_{J^*} \quad (4.2)$$

$$\left(\frac{\partial R}{\partial J^*}\right)_{I^*} = \left(\frac{\partial R}{\partial N_{\xi_s}}\right)_{N_\eta} \left(\frac{\partial N_{\xi_s}}{\partial J^*}\right)_{I^*} + \left(\frac{\partial R}{\partial N_\eta}\right)_{N_{\xi_s}} \left(\frac{\partial N_\eta}{\partial J^*}\right)_{I^*} \quad (4.3)$$

The partial derivatives $\left(\frac{\partial R}{\partial N_{\xi s}}\right)_{N_\eta}$ and $\left(\frac{\partial R}{\partial N_\eta}\right)_{N_{\xi s}}$ may be approximated by

$$\left(\frac{\partial R}{\partial N_{\xi s}}\right)_{N_\eta} \simeq \left(\frac{\Delta R}{\Delta N_{\xi s}}\right)_{N_\eta} = R(N_{\xi s}, N_\eta) - R(N_{\xi s}-1, N_\eta) \qquad (4.4)$$

$$\left(\frac{\partial R}{\partial N_\eta}\right)_{N_{\xi s}} \simeq \left(\frac{\Delta R}{\Delta N_\eta}\right)_{N_{\xi s}} = R(N_{\xi s}, N_\eta) - R(N_{\xi s}, N_\eta - 1). \qquad (4.5)$$

The four remaining partial derivatives on the RHS of equations (4.2) and (4.3) may be obtained as follows: Let A and B be matrices defined by

$$A = \begin{bmatrix} \left(\frac{\partial N_{\xi s}}{\partial I^*}\right)_{J^*} & \left(\frac{\partial N_{\xi s}}{\partial J^*}\right)_{I^*} \\ \left(\frac{\partial N_\eta}{\partial I^*}\right)_{J^*} & \left(\frac{\partial N_\eta}{\partial J^*}\right)_{I^*} \end{bmatrix} \qquad (4.6)$$

$$B = \begin{bmatrix} \left(\frac{\partial I^*}{\partial N_{\xi s}}\right)_{N_\eta} & \left(\frac{\partial I^*}{\partial N_\eta}\right)_{N_{\xi s}} \\ \left(\frac{\partial J^*}{\partial N_{\xi s}}\right)_{N_\eta} & \left(\frac{\partial J^*}{\partial N_\eta}\right)_{N_{\xi s}} \end{bmatrix} \qquad (4.7)$$

Then, from the theory of mathematical transformations, we have

$$A = B^{-1} \tag{4.8}$$

which explicitly yields

$$\left(\frac{\partial N_{\xi_s}}{\partial I^*}\right)_{J^*} = \frac{1}{C}\left(\frac{\partial J^*}{\partial N_\eta}\right)_{N_{\xi_s}} \tag{4.9}$$

$$\left(\frac{\partial N_{\xi_s}}{\partial J^*}\right)_{I^*} = -\frac{1}{C}\left(\frac{\partial I^*}{\partial N_\eta}\right)_{N_{\xi_s}} \tag{4.10}$$

$$\left(\frac{\partial N_\eta}{\partial I^*}\right)_{J^*} = -\frac{1}{C}\left(\frac{\partial J^*}{\partial N_{\xi_s}}\right)_{N_\eta} \tag{4.11}$$

$$\left(\frac{\partial N_\eta}{\partial J^*}\right)_{I^*} = \frac{1}{C}\left(\frac{\partial I^*}{\partial N_{\xi_s}}\right)_{N_\eta} \tag{4.12}$$

where

$$C = \left(\frac{\partial I^*}{\partial N_{\xi_s}}\right)_{N_\eta}\left(\frac{\partial J^*}{\partial N_\eta}\right)_{N_{\xi_s}} - \left(\frac{\partial J^*}{\partial N_{\xi_s}}\right)_{N_\eta}\left(\frac{\partial I^*}{\partial N_\eta}\right)_{N_{\xi_s}} \tag{4.13}$$

The partial derivatives appearing on the RHS of equations (4.9) - (4.13) may be obtained from equations (2.29) - (2.32), valid for a basic unit defined by benchmarks.

4.3 Computational Operations

For each point, it is seen that the computations in equations (4.1) - (4.5) require 4 additions, 6 subtractions and 6 multiplications. Assuming a time of 1.5 microseconds for each addition or subtraction , and 6 microseconds for each multiplication, therefore about 51 microseconds are required to correct the radiometric value for each point.

SECTION 5 - DISCUSSION

This section discusses relevant topics such as benchmark spacing, time requirements for mapping IR data, real and non-real time computations, data storage and buffering, input and output data accuracy, and computational accuracy requirements.

5.1 Benchmark Spacing

The IR samples have angular widths of about $0.01^{\circ} \times 0.005^{\circ}$ at the satellite position. This corresponds to a resolution of about 4 x 2 miles at the sub-satellite position on the earth's surface. In general, this resolution and the non-linearity of the mapping equations determine the requisite spacing of the benchmarks to be used for interpolation. The analytical approach to obtain this spacing involves comparatively complex mathematical analysis. Alternatively, it is also possible to obtain this value by actually performing the mapping munerically. At this stage, it is felt that the interpolation requirements can be met by choosing the IR benchmarks to be spaced 50 samples horizontally and 25 samples vertically. That is, it probably suffices to choose m = 50 and n = 25 in Section 3. In the full IR imagery, there are 1822 scans each containing 3822 samples. Consequently, about 5,600 benchmarks will be required.

5.2 Time Requirements

In Section 2, the computation of each benchmark and its associated partial derivatives requires about 1540 microseconds. Hence, a set of 5600 benchmarks requires about 8,624,000 microseconds $\simeq$ 8.6 seconds.

In Section 3, the mapping of each sample by interpolation requires about 6 microseconds. Therefore, an IR imagery of about 7×10^6 samples requires about 42 seconds. However, if the entire IR imagery is not to be mapped, then cropping out the edges will probably reduce time by a factor of 2/3 to yield a requirement of about 28 seconds.

In Section 4, the correction of radiometric value at the center of the pixel in the distortion-free image requires about 51 microseconds for each sample. Therefore, an IR imagery of about 7×10^6 samples requires about 357 seconds. Cropping will probably reduce this to about 238 seconds.

Consequently, about 399 seconds or 6.7 minutes will be needed to map the entire IR imagery comprising of coordinates and radiometric values of the samples. This time requirement drops to about 4.4 minutes if cropping is introduced.

If it is desired to map the visible imagery containing 1/2 x 1/2 mile samples, then the above times are increased by a factor of 32. Therefore, about 214 minutes will be required to map the entire imagery comprising of coordinates and radiometric values. If the edges are cropped out, then about 143 minutes will be needed.

5.3 Real and Non-Real Time Computations

From the discussion above, it is seen that it is possible to perform all the mapping computations in real-time in the case of IR imagery, and not possible in the case of visible imagery. However, in the latter case, the crucial point is whether the radiometric corrections are really necessary. If not, then the time requirements drops to 22.4 minutes for the entire imagery, and 14.9 minutes for the cropped imagery. Consequently, visible data-mapping becomes feasible in real-time.

Because the benchmark computation time is so small, it is desirable to perform the benchmark computations in real-time so that the relevant parameters may be easily extracted in-line from the data-stream coming out of the SDB.

5.4 Data Storage and Buffering

Because the imagery obtained from the SDB output data is distorted, it is necessary to store this data in a buffer before the distortion-free mapping can be performed. The buffer size may be estimated by allowing for a maximum 3° offset in the spin axis. Since the satellite is about 6.6 earth radii away, it may be verified that about 100 IR scan-lines (382,200 samples) to be buffered at a time. This will be sufficient to output a horizontal distortion-free line from end to end. In the case of visible data, the corresponding buffer will contain about 800 visible scan-lines (12,230,400 samples). If a realistic situation, the above numbers will probably be reduced by a factor of 3.

5.5 Input and Output Data Accuracy

The data coming out of the SDB will be used as input into the distortion-free mapping software system. The accuracy of this data may be roughly classified as perfect, normal or bad.

Perfect data corresponds to data having errors of less than one pixel (i. e. $\pm$ 2 km at the subsatellite point for IR data). The error in the output data from the distortion-free mapping is therefore determined by the pixel resolution of the benchmarks, the interpolation accuracy of interspaced points, and the correction accur-

acy of the radiometric values. Because the second and third factors depend on the benchmark-spacing, which in turn depends on the pixel resolution, therefore it is estimated that the error bound of the output data is about one pixel (i.e., $\pm$ 4 km for IR data).

Normal data corresponds to data having errors of about one or two pixels. The mapping error is determined by the benchmark accuracy corresponding to normal input error, the interpolation accuracy of interspaced points, and the correction accuracy of the radiometric values. In this case, the error bound of the output data is about two pixels.

Bad data corresponds to data having errors of about 4 or more pixels. The mapping error is determined mainly by the benchmark accuracy corresponding to these bad input errors. In this case, the error of the output data is probably about 5 or more pixels.

5.6 Computational Accuracy Requirements

It is desirable to investigate into the use of 16-bit words in the distortion-free computations.

Because of the complexity of the benchmark computations in equations (2.1) - (2.28), it is quite evident that sufficient accuracy will not be obtained by performing single-precision computations using 16-bit words.

However, for the partial derivatives computations in equations (2.29) - (2.32), the interpolation of interspaced points computaions in equations (3.7) - (3.8) and (3.15) - (3.16), and the radiometric correction computations in equations (4.1) - (4.5), it is possible to achieve the desired accuracy using single-precision computations involving 16-bit words. In this case, perhaps the best way to represent real numbers is as follows:

1 bit for sign of number
11 bits for range of number ($2^{11} - 1 = 2047$)
1 bit for sign of exponent
3 bits for range of exponent ($2^3 - 1 = 7$)

An alternative choice is as follows:

1 bit for sign of number
12 bits for range of number ($2^{12} - 1 = 4095$)
1 bit for sign of exponent
2 bits for range of exponent ($2^2 - 1 = 3$)

This second choice may not be as desirable because of the small range of the exponent.

SECTION 6 - CONCLUSION

From the preceding discussion, it is seen that it is possible to map in real-time the entire IR imagery comprising of coordinates and radiometric values of the samples. However, it is possible to map in real-time the entire visible imagery comprising of only the coordinates of the samples. This conclusion is based heavily on the assumption that it takes 1.5 microseconds for each addition or subtraction, and 6 microseconds for each multiplication.

The following table summarizes the time requirements for IR and visible imagery mapping:

	Entire IR	Cropped IR	Entire VIS	Cropped VIS
Benchmarks	8.6 sec.	5.7 sec.	4.6 min.	3.1 min.
Sample Coordinates	42 sec.	28 sec.	22.4 min.	14.9 min.
Radiometric Values	357 sec.	238 sec.	190.4 min.	126.9 min.
Total	6.8 min.	4.5 min.	217.4 min.	144.9 min.

The following table summarizes the expected accuracy of the distortion-free mapping (DFM) algorithms:

Input Data from SDB	Output Data from DFM
Perfect	1 pixel
Normal	2 pixels
Bad	5 or more pixels

REFERENCES

(1) Chan, F. K., "Distortion-Free Mapping of VISSR Imagery Data from Geosynchronous Satellites", Scientific Analysts and Consultants, Inc. Report. (1978).

Computational Aspects of Geometric Correction Data Generation in the Landsat-D Imagery Processing.*

I. Levine
General Electric, Space Division
4701 Forbes Blvd., Lanham, MD 20706

ABSTRACT

A method is presented for systematic and geodetic correction data calculation. It is based on presentation of image distortions as a sum of nominal distortions and linear effects caused by variation of the spacecraft position and attitude variables from their nominals. The method may be used for both MSS and TM image data and it is incorporated into the processing by means of mostly offline calculations. Modeling shows that the maximal errors of the method are of the order of 5m at the worst point in a frame; the standard deviations of the average errors less than .8m.

INTRODUCTION

The geometric correction of the Landsat-type imagery typically proceeds in two steps. The first, called the Systematic Correction, removes internal distortions imported in the raw image data by the sensor mechanism, spacecraft motion, inaccurate sensor pointing, earth's rotation, etc. These partly corrected images still contain distortions due to uncertainties in spacecraft position and orientation. The second step, Geodetic Correction, removes these residual distortions using refined values of the attitude and ephemeris estimates. The refined attitude and ephemeris are obtained by filtering of image dislocations at Control Points.

Application of the geometric correction requires the generation of the Correction Data - Systematic (SCD) or Geodetic (GCD), depending upon the processing step. This data is developed on a rectangular grid in input (pixel, scan line) coordinates and express the relationship between the input and output map coordinates, within a standard World Reference System (WRS) frame.

The central part of the SCD/GCD generation is the computation of the coordinates of the intersection of the sensor's line-of-sight vector, with the Earth's surface (lookpoint coordinates). The lookpoint coordinates must then be converted to geodetic coordinates followed by mapping into user's map projection. There are two user's map projections: Space Oblique Mercator (SOM) and either Universe Transverse Mercator (UTM) or Polar Stereographic (PS).

---

* Work performed under National Aeronautics and Space Administration Contract No. NAS 5-25300.

Finally, the data, computed for integer values of pixels and lines, is interpolated to integer values of output map coordinates. The grid spacing is chosen so that the data, together with properly defined interpolation techniques, represent the output coordinates to the desired precision everywhere in the frame.

It should be noted that all the calculations are performed twice at each grid point, once for each SCD and GCD. They consume a significant amount of the processing time, which needs to be minimized. At the same time, there are no essential differences between SCD and GCD. Both establish a pointwise transformation, which may be written generically as

$$\bar{X}_m = F(\text{pixel}, \text{line}, \bar{p}),$$

where $\bar{X}_m = (X_{m1}, X_{m2})$ are map coordinates of a grid point and $\bar{p}$ is a vector of variables characterizing the spacecraft motion, attitude pointing, sensor's mechanism, etc.

Letting $\bar{p} = \bar{p}^n + \bar{\delta}$, the sum of nominal values of the variables and the deviation from the nominals, in the first approximation

$$\bar{X}_m = \bar{X}_m^n + \mu\,\bar{\delta}, \qquad (1)$$

where $\bar{X}_m^n$ are the nominal map coordinates and μ is the matrix of the partial derivatives (PD)

$$\mu = \left[\frac{\partial \bar{X}_m}{\partial \bar{\delta}}\right]$$

Thus, SCD and GCD may be represented as a sum of the nominal correction data and pointwise adjustments.

This has significant advantages:

1) It provides a uniform approach to the SCD and GCD computations, considering each as one transformation, and

2) Because the nominal spacecraft motion is known for every WRS frame, the nominal coordinates and the partial derivatives may be computed and stored in a Data Base.

The implementation of such an approach depends a great deal on both the choice of an output map projection and $\bar{\delta}$. An analytic form of mapping not only has to allow derivation of the coefficients μ, but it should also afford rapid and precise online inversion to geodetic coordinates, from which the final map projection can be generated. In addition, it is desirable to have the nominal coordinates and the partial derivatives, as far as possible, insensitive to global position of the frame. Thus, although out technique may be applied to most standard map projections (such as UTM or PS), a special intermediate projection, Local Space Oblique Mercator (LSOM), has been employed. The LSOM is the Mercator projection for the sphere, with local 'equator' along the nominal spacecraft inertial velocity at the frame center. In that projection $\bar{X}_m^n$ and μ are longitude-undependent and thus, can be stored only for one path. A natural choice of variables $\bar{\delta}$ is the along-track, cross-track and radial deviations in spacecraft position, together with deviations in the attitude angles. The nominal spacecraft motion within a frame is assumed to be in a perfect circular orbit passing through the frame center.

NOTATIONS

$\bar{a}_p = (a_{p1}, a_{p2}, \ldots, a_{pK})$ - vector (Kx1 matrix)

$\|\bar{a}_p\|$ - the Euclidean norm of $\bar{a}_p$

A^T - transposed matrics A

$\bar{X}$ - spacecraft position vector in earth-centered earth-fixed coordinates

$\bar{X}_s$ - spacecraft position vector in nominal spacecraft coordinates

$\bar{X}_m = (X_{m1}, X_{m2})$ - output map coordinates

$\bar{g}^n$ - pointing vector in body coordinates

$\bar{g}$ - pointing vector in local vertical spacecraft coordinates

$\bar{f}$ - pointing vector in earth-centered fixed coordinates

$\bar{u}$ - coordinates of a lookpoint on the earth surface

h - distance from spacecraft to earth lookpoint

$\bar{v}$ - $\bar{u} \cdot \|\bar{u}\|^{-1}$ - normalized lookpoint vector.

R - local earth radius at WRS frame center

Ω - earth rotation rate

a_e, b_e - earth equatorial and polar radii

$e_1 = e_2 = 1$, $e_3 = a_e = a_e b_e^{-1}$

δ_1 - deviation in the pitch

δ_2 - deviation in the roll

δ_3 - deviation in the yaw

δ_4 - along track angular deviation

δ_5 - cross track angular deviation

δ_6 - relative departure in the radial direction

δ_7 - time deviation

μ_k - (2x1) matrix of the partial derivatives of $\bar{X}_m$ with respect to δ_k.

$\mu = (\mu_1, \mu_2, \ldots, \mu_7)$

$\hat{\theta}_p$, $\hat{\theta}_r$ - the 'equivalent' pitch and roll

Ω_s - spacecraft orbital rate

λ - geodetic longitude

ϕ - geocentric latitude

$\hat{\phi}$ - geodetic latitude

$$ROT_1(\Psi) = \begin{vmatrix} 1 & 0 & 0 \\ 0 & \cos\psi & -\sin\psi \\ 0 & \sin\psi & \cos\psi \end{vmatrix}$$

$$ROT_2(\psi) = \begin{vmatrix} \cos\psi & 0 & \sin\psi \\ 0 & 1 & 0 \\ -\sin\psi & 0 & \cos\psi \end{vmatrix}$$

$$ROT_3(\psi) = \begin{vmatrix} \cos\psi & -\sin\psi & 0 \\ \sin\psi & \cos\psi & 0 \\ 0 & 0 & 1 \end{vmatrix}$$

$$\frac{\partial}{\partial\psi}\ \mathrm{ROT}_i(\psi)_{\psi=0} = T_i$$

$$T_1 = \begin{vmatrix} 0 & 0 & 0 \\ 0 & 0 & -1 \\ 0 & 1 & 0 \end{vmatrix}$$

$$T_2 = \begin{vmatrix} 0 & 0 & 1 \\ 0 & 0 & 0 \\ -1 & 0 & 0 \end{vmatrix}$$

$$T_3 = \begin{vmatrix} 0 & -1 & 0 \\ 1 & 0 & 0 \\ 0 & 0 & 0 \end{vmatrix}$$

I - the three dimensional identity matrix

The upper index η indicates the nominal value of a vector.

T_{act} - active scan time

T_{round} - mirror turnaround time

THE NOMINAL SCD

Coordinate Transformations

The local (instantaneous) spacecraft coordinates are described in terms of the unit vectors $(\bar{\xi}_1,\bar{\xi}_2,\bar{\xi}_3)$, where $\bar{\xi}_3$ points towards the Earth center, the $\bar{\xi}_1$ vector is along the orbital angular momentum, and $\bar{\xi}_2 = \bar{\xi}_3 \times \bar{\xi}_1$ is roughly along the velocity direction. The local spacecraft coordinates at the WRS center is called the nominal spacecraft coordinates. The matrix A transforms a vector $\bar{X}_o$ in earth-centered inertial coordinates to the vector $\bar{X}_s$ in nominal spacecraft coordinates:

$$\bar{X}_s = A\bar{X}_o \qquad (2)$$

The inertial to earth-centered earth-fixed coordinate transformation is defined as

$$\bar{X} = E^T\bar{X}_o, \qquad (3)$$

where $E = E_o \cdot \mathrm{ROT}_3(\Omega t)$.

The matrix E_o gives the time-independent component of the transformation, $\mathrm{ROT}_3(\Omega t)$ describes the rotation about the earth axis at the rate Ω. We assume that $t = 0$ at the frame center. The corresponding nominal spacecraft to earth fixed coordinate transformation may be written as

$$\bar{X} = E^T A^T\bar{X}_s = P^T\bar{X}_s \qquad (4)$$

where $P = AE$.

The unit vector $\bar{g}^n$, given in body (sensor) coordinates, is transformed to local spacecraft coordinates as

$$g = ROT_3(-\theta_y) \cdot ROT_2(-\theta_r) \cdot ROT(-\theta_p)\ \bar{g}^n \tag{5}$$

where θ_y, θ_r, θ_p are the yaw, roll, and pitch.

In the nominal spacecraft coordinates, $\bar{g}_s$ may be expressed as

$$\bar{g}_s = ROT_1(\gamma)\bar{g}$$

where γ is the angle in the orbit plane between the spacecraft and the frame center. In the nominal spacecraft motion $\cos\gamma = -X_{s3}/\|\bar{X}_s\|$, $\sin\gamma = X_{s2}/\|\bar{X}_s\|$, and thus, the matrix $ROT_1(\gamma)$ is known completely.

A vector $\bar{X}_m = (X_{m1}, X_{m2})$ in LSOM coordinates is defined as

$$X_{m1} = \frac{R}{2} \ln \frac{1 + \sin\beta}{1 - \sin\beta} \tag{7}$$

$$X_{m2} = R\alpha$$

where R is the earth local radius at the frame center. The local polar angles, α and β, are given by

$$\begin{aligned} W_1 &= \sin\beta \\ W_2 &= \cos\beta \cdot \sin\alpha \\ W_3 &= -\cos\beta \cdot \cos\alpha \end{aligned} \tag{8}$$

where

$$\bar{W} = \|\bar{u}\|^{-1} A\bar{u} \tag{9}$$

and $\bar{u} = (u_1, u_2, u_3)$ are earth fixed coordinates of the corresponding point on the ground.

Generation of the nominal SCD

The nominal coordinates, $\bar{X}_m$, are computed on a grid, consisting of $2n_1+1$ fictitious scan lines, each line containing $2n_2+1$ points. Because the TM scans in two directions, it requires two sets of the nominal coordinates, for forward and backward scans. The computations may be fulfilled in the following order.

1. Generate the time of (i,j) point

$$t_{ij} = \frac{T_{scene}}{2\ n_1}\ (i-n_1-1) + \frac{T_{act}}{2n2}\ (j-n_2-1) + \Delta T$$

Here

$$T_{scene} = (T_{act} + T_{round}) \cdot (N_{scan} - K_1)$$

where T_{act} is the active scan time, T_{round} is the turnaround time, N_{scan} is the actual number of scans, and $K_1 = 1$ for MSS and 2 for TM.

The parameter $T = T_{scene}$ for backward scans of the TM and zero otherwise.

2. Generate $2n_2+1$ unit line-of-sight vectors $\bar{g}^n$ in body coordinates. An actual mirror velocity profile, together with constant sensor's misalignments may be employed.

3. Compute the spacecraft position vector $\bar{X}_s$ and the matrix P at t_{ij}.

4. Compute $\bar{g}_s$ according to (6).

5. Transform $\bar{X}_s$ and $\bar{g}_s$ in earth fixed coordinates, obtaining the vectors $\bar{X}$ and $\bar{f}$, respectively.

6. Determine the lookpoint coordinates, $\bar{u} = (u_1,u_2,u_3)$, and h from the equations

$$\bar{u} = \bar{x} + h\bar{f} \qquad (10)$$

$$(u_1^2 + u_2^2)\ a_e^{-2} + u_3^2\ b_e^{-2} = 1 \qquad (11)$$

7. Transform $\bar{u}$ into LSOM coordinates using (9), (8), and (7).

It is convenient to have all distances in units of the nominal orbit radius.

THE PARTIAL DERIVATIVES

Position and Pointing Vectors

Let $\bar{X}_s^n$ be a nominal spacecraft position vector at time t_o, δ_4 and δ_5 be the angular along-track and cross-track deviations in spacecraft position, and δ_6 be a relative deviation in the radial direction. Then the actual spacecraft position vector, $\bar{X}_s$, may be obtained by rotating $\bar{X}_s^n$ through δ_4 and δ_5. This is followed by stretching according to the ratio $1 - \delta_6$:

$$\bar{X}_s = ROT_2(\delta_5) \cdot ROT_1(\delta_4) \cdot \bar{X}_s^n(1-\delta_6)$$

Similarly, if δ_1, δ_2, and δ_3 are deviations in the pitch, roll, and yaw, the actual (unit) pointing vector $\bar{g}_s$ should be written as

$$\bar{g}_s = ROT_2(\delta_5) \cdot ROT_1(\delta_6)\bar{g}_s^n ,$$

where $\bar{g}_s^n$ is defined by (5) and (6) as

$$\bar{g}_s^n = ROT_1(\gamma)\ ROT_3(-\delta_3)ROT_2(-\delta_2) \cdot ROT_1(-\delta_1)\ \bar{g}^n$$

Let $t = t_o + \delta_7$. Remembering that $P = P(t_o) = AE_o \cdot ROT_3(\Omega t_o)$, we can write P^T at time t as

$$P^T(t) = ROT_3(-\Omega(t_o+\delta_7))E_o{}^T A^T = ROT_3(-\Omega\delta_7)\cdot$$

$$\cdot ROT_3(-\Omega t_o)E_o^T A^T = ROT_3(-\Omega\delta_7)P^T$$

and the actual position and pointing vectors in earth fixed coordinates as

$$\bar{X} = ROT_3(-\Omega\delta_7)P^T ROT_2(\delta_5)ROT_1(\delta_4)\bar{X}_s^n(1-\delta_6)$$

$$\bar{f} = ROT_3(-\Omega\delta_7)P^T ROT_2(\delta_5)ROT_1(\delta_4)ROT_1(\gamma)\cdot$$

$$ROT_3(-\delta_3) \cdot ROT_2(-\delta_2) \cdot ROT_1(-\delta_1)\bar{g}^n$$

The linear terms of the Taylor series expansions of $\bar{X}$ and $\bar{f}$ in the vicinity of $\delta_i = 0$ $(i = 1,2,\ldots,7)$ give

$$\bar{X} = P^T(I + T_1\delta_4 + T_2\delta_5 - \delta_6 - \Omega T_3\delta_7)\bar{X}_s^n$$

$$\bar{f} = P^T\left[I + T_1 ROT_1(\gamma)\delta_4 + T_2 ROT_1(\gamma)\delta_5 - ROT_1(\gamma)\cdot\sum_{i=1}^{3} T_i\delta_i - \right.$$

$$\left. - \Omega\cdot ROT_1(\gamma)\delta_7\right]\bar{g}^n$$

Here we used the fact that

$$\frac{\partial}{\partial\psi}\ ROT_i(\psi)_{\psi=0} = T_i$$

Introducing $\bar{f}^n = P^T ROT_1(\gamma)\bar{g}^n$ and

$\bar{X}^n = P^T \bar{X}_s^n$, we finally have

$$\bar{X} = \bar{X}^n + P^T(T_1\delta_4 + T_2\delta_5 - \Omega T_3\delta_7)P\bar{X}^n - \bar{X}^n\delta_6$$

$$\bar{f} = \bar{f}^n + P^T(T_1\delta_4 + T_2\delta_5 - \Omega T_3\delta_7)P\bar{f}^n - \tag{12}$$

$$- P^T ROT_1(\gamma)\left(\sum_{i=1}^{3} T_i\delta_i\right)\bar{g}^n$$

The Partial Derivatives of Lookpoint Coordinates

Henceforth, we will use a prime to denote the matrix of PD with respect to δ computed at the nominal point. From (10) it follows that

$$M \quad \frac{\partial \bar{u}}{\partial \delta} = \bar{u}^1 = \bar{X}^1 + h\bar{f}^1 + h^1\bar{f} \tag{13}$$

Introducing $e_1 = e_2 = 1$ and $e_3 = a_e b_e^{-1}$, Eq.(11) may be rewritten as

$$\sum_{i=1}^{3} e_i^2 (\bar{X}_i + h\bar{f}_i) = a_e^2$$

or,

$$h^2\left(\sum f_i e_i^2\right) + 2h\left(\sum f_i X_i e_i^2\right) + \sum X_i^2 e_i^2 = a_e^2$$

Differentiating the last expression as a inplicit function of h gives

$$h^1 = -\frac{\sum (X_i^1 + hf^1)(X_i + hf_i)e_i^2}{\sum f_i(X_i + hf_i)\, e_i^2} =$$

$$= -\frac{\sum u_i e_i^2 (X_i^1 + hf_i^1)}{\sum f_i u_i e_i^2}$$

and, after substitution h^1 in (13), we have

$$u_k^1 = C_o^{-1}\left[(X_i^1 + hf_k^1)\sum_{i\neq k} u_i f_i e_i^2 - f_k \sum_{i\neq k} (X_i^1 + hf_i^1)u_i e_i^2\right]$$

$$(i,k = 1,2,3)$$

where $C_o = -\sum f_i u_i e_i^2$

Using the matrix notations, $\bar{u}^1$ may be expressed as

$$u^1 = C(\bar{X}^1 + h\bar{f}^1), \tag{14}$$

where C is a 3x3 matrix with the elements

$$C_{kk} = 1 + U_k f_k e_k^2 C_o^{-1}$$

$$C_{kj} = u_j f_k e_j^2 C_o^{-1} \tag{15}$$

Transformation to LSOM Coordinates

To transform the lookpoint coordinates, u, to the LSOM coordinates, they must be represented in the normalized form $\bar{V} = \bar{u} \cdot \|\bar{u}\|^{-1}$.

Differentiation of $\bar{V}$ Yields

$V_k^1 = (U_k^1 - U_k \|\bar{U}\|^2 \sum U_i U_i^1) \|\bar{U}\|^{-1}$ and introducing the matrix B with the elements

$$B_{kk} = 1 - U_k^2 \|\bar{U}\|^2 \tag{16}$$

$$B_{kj} = - U_k U_j \|\bar{U}\|^{-2},$$

$\bar{V}^1$ may be written as

$$\bar{V}^1 = \|\bar{U}\|^{-1} B\bar{U}^1 = \|\bar{U}\|^{-1} BC(\bar{X}^1 + h\bar{f}^1) \tag{17}$$

The next step is transformation of $\bar{V}$ to $\bar{W}$ and then to $\bar{X}_m$. From (9) and (17) it follows that

$$\bar{W}^1 = \|\bar{U}\|^{-1} ABC(\bar{X}^1 + h\bar{f}^1). \tag{18}$$

From (7) and (8) it follows that

$$X_{m1} = \tfrac{1}{2} R \cdot \ln \frac{1 + W_1}{1 - W_1}$$

$$X_{m2} = R \cdot \arctan (-W_2/W_3) \tag{19}$$

and therefore,

$$X_{m1}^1 = R(1-W_1^2)^{-1} W_1^1$$

$$X_{m2}^1 = R(1-W_1^2)(W_2 W_3^1 - W_3 W_2^1).$$

Introducing the matrix

$$D = \begin{pmatrix} 1 & 0 & 0 \\ 0 & -W_3 & W_2 \end{pmatrix} \tag{20}$$

and using (18), we have

$$\bar{X}^1_m = R(1-W_1^2)^{-1}\bar{W}^1 =$$

$$R \left\|\bar{U}\right\|^{-1}(1-W_1^2)^{-1} \; DABC(\bar{X}^1 + h\bar{f}^1) \tag{21}$$

To obtain the final result, we must substitude an explicit expression for $\bar{X}^1 + h\bar{f}^1$, which follows immediately from (12):

$$X^1_k + hf^1_k = \begin{cases} -hP^T ROT_1(\gamma)\; T_k\; \bar{g}^n & k = 1,2,3 \\ P^T T_{k-3} P(\bar{X}^n + h\bar{f}^n) = P^T T_{k-3} P\bar{U}^n & k = 4,5 \\ -\bar{X}^n & k = 6 \\ -\Omega T_3 \bar{U}^n & k = 7 \end{cases}$$

Description of the Algorithm

Calculation of the partial derivatives is performed simultaneously with the LSOM coordinate generation in the following order.

1. Compute matrices C,B, and D, given by (15), (16), and (20).

2. Compute matrices

$$J = \frac{R}{\|u\|\ (1-W_1^2)}\ DABC$$

$$J_o = JP^T$$

3. Compute vector $\bar{Z} = P\bar{u}^n$

4. Form five vectors

$$J_1 = \frac{h}{r}\ (0,\ X_{s2}g_2^r - X_{s3}g_3^n,\ X_{s2}g_3^n + X_{s3}g_2^n)$$

$$J_2 = \frac{-h}{r}\ (g_3^n r, g_1^n X_{s2}, g_1^n X_{s3})$$

$$J_3 = \frac{h}{r}\ (g_2^n r, g_1^n X_{s3}, -g_1^n X_{s2})$$

$$J_4 = (0, -Z_3, Z_2)$$

$$J_5 = (Z_3, 0, -Z_1)$$

$$J_7 = (U_2, -U_1, 0)$$

Here $r = \| \bar{X}_s \|$.

5. Compute

$$\mu_k = J_o J_k \qquad (k = 1,2,\ldots,5)$$

$$\mu_6 = -J\bar{X}^n$$

$$\mu_7 = \Omega J J_7$$

Here μ_k is the 2x1 matrix of the partial derivatives with respect to δ_k and thus,

$$\mu = (\mu_1, \mu_2, \mu_3, \mu_4, \mu_5, \mu_6, \mu_7).$$

Note, that SCD/GCD calculations require only the first six pair of the PD. The partial derivatives with respect to time, μ_7, will be used only to generate the backward scan grid for Thematic Mapper.

The nominal SCD and PD are computed in double precision and stored in single precision. Because the PD are changing very slowly over a frame, they may be computed on a sparse grid followed by linear interpolation onto a finer grid. For instance, implementation of our technique for MSS requires calculation of PD on a 3x5 grid.

THE NOMINAL COORDINATES AND THE PARTIAL DERIVATIVES FOR BACKWARD SCANS OF TM

It should be remembered that application of the developed technique to Thematic Mapper data requires two sets of the nominal SCD and PD - for forward and backward scans. But actually only one set must be obtained by the direct lookpoint calculation: LSOM coordinates for, say, forward scans may be easily converted to LSOM coordinates for backward scans. Our calculations show also that, for sensor's misalignments less than $.1^o$, the derivatives are practically same for both grids; for bigger misalignment the second set of the derivatives can be obtained by the linear interpolation of the first one.

Let $\bar{X}_m(t_1)$ and $\bar{X}_m(t_2)$ be LSOM coordinates for adjacent forward and backward scans at time t_1 and t_2, respectively. Note, that for the TM

$$\delta t = t_2 - t_1 \leq 2\, T_{act} + T_{round} = .132205 \text{ sec}$$

So, we will neglect changes in the attitude angles during δt.

Considering $\Delta X_m = \bar{X}_m(t_2) - \bar{X}_m(t_1)$ as a function of changes in the spacecraft position, sensor pointing, and effects of the earth rotation, we may represent it as

$$\Delta \bar{X}_m = \left(\frac{\bar{X}_m}{\delta_4}\right)_{t_1} \Omega_s \delta t + \left(\frac{\bar{X}_m}{\delta_1}\right)_{t_1} \hat{\theta}_p + \left(\frac{\bar{X}_m}{\delta_2}\right)_{t_1} \bar{\theta}_r +$$

$$+ \left(\frac{\bar{X}_m}{\delta_1}\right)_{t_1} \delta t = (\mu_4 \Omega_s + \mu_7)\delta t + \mu_1 \hat{\theta}_p + \mu_2 \hat{\theta}_r$$

Here $\hat{\theta}_p$ and $\hat{\theta}_r$ are fictitious pitch and roll angles, reflecting a difference in sensor's pointing at t_1 and t_2, and Ω_s is the average orbital rate during δt.

Here we will denote the nominal pointing vector $\bar{g}^n$ at moments of time t_1 and t_2 as $\bar{P}$ and $\bar{q}$, respectively. The angle between their projections onto the $(\bar{\xi}_2, \bar{\xi}_3)$ plane, $(0, P_2, P_3)$ and $(0, q_2, q_3)$, can be written as

$$\cos \hat{\theta}_p = \frac{P_2 q_2 + P_3 q_3}{(P_2^2 + P_3^2)^{1/2}(q_2^2 + q_3^2)^{1/2}}$$

or, choosing the appropriate sign,

$$\hat{\theta}_p \simeq \sin \hat{\theta}_p = \frac{P_3 q_2 - P_2 q_3}{(1-P_1^2)^{1/2}(1-q_1^2)^{1/2}}$$

Analogously, $\hat{\theta}_r$ may be expressed as the angle between projections of $\bar{P}$ and $\bar{q}$ onto the $(\bar{\xi}_1, \bar{\xi}_3)$ plane:

$$\hat{\theta}_r \simeq \sin \hat{\theta}_r = \frac{P_1 q_3 - P_3 q_1}{(1-P_2^2)^{1/2}(1-q_2^2)^{1/2}}$$

For zero sensor's misalignments

$$\hat{\theta}_p \simeq - \frac{2 P_2 P_3}{(1-P_1^2)^{1/2}}$$

$$\hat{\theta}_r = 0$$

CONVERSION TO BASIC MAP PROJECTIONS

It should be remembered, that completely corrected imagery eventually must be presented in two basic map projections, SOM and either UTM or PS. To generate correction data in a basic map projection, it is required to invert LSOM coordinates to geodetic latitude and longitude and then perform the standard mapping into desirable projection.

Noting, that the normalized look point vector, $\overline{V}$, can be expressed through the geocentric latitude, ϕ, and the longitude, λ as

$$V_1 = \cos\lambda \cos\phi$$

$$V_2 = \sin\lambda \cos\phi$$

$$V_3 = \sin\phi \quad ,$$

and, employing well known formula for the geodetic latitude $\hat{\psi}$

$$\tan \hat{\phi} = a_e^2 b_e^{-2} \tan \phi ,$$

one can obtain

$$\lambda = \arctan (V_2 V_1^{-1})$$

$$\phi = \arctan \left[a_e^2 b_e^{-2} V_3 (1-V_3^2)^{-\frac{1}{2}} \right]$$

For a given $\overline{X}_m$, $\overline{V}$ is computed by the inverted formulae (10) and (9).

NUMERICAL RESULTS

The Accuracy of the Method

To evaluate the methods accuracy, differences between LSOM coordinates, computed directly on points of a grid, and those, corrected according to Eq.(1), were calculated for various spacecraft position and attitude deviations. It is convenient to characterize the upper level of errors by the maximal along-track (AT) and cross-track (CT) errors, which cooresponds to the errors at the worst points of a frame (possible different for AT and CT errors). It should be noticed, that the maximal errors always appear near the corner points and similar for TM and MSS. They are linearly dependent upon magnitude of deviations and practically independent upon WRS latitude.

The actual position and attitude departures for Landsat-D are expected to be $01^{o}(\sigma)$ for the pitch, roll, and yaw and less than 5km in the along and cross track directions. The radial departure is determined chiefly by the orbit fluctuations and it will not exceed 9.5km. Modeling shows, that for $\delta_1 = \delta_2 = \delta_3 = .03^{o}$, $\delta_4 = \delta_5 = 5$km, and $\delta_6 = 9.5$km, the corresponding maximal CT and AT errors have the order of 5m (CT = 4.87m, AT = 5.03m for MSS and CT = 4.97m, AT = 5.07m for TM). The inversion from LSOM to geodetic coordinates produces insignificant additional errors, therby preserving the same order of errors in UTM and PS projections.

For TM, the forward to backward scan conversion results in CT and AT errors less than .03m for zero sensor's misalignments; for extremely large misalignments of the order of $.5^{o}$, the maximal CT errors increase up to .5m.

Currently the SCD/GCD generation accuracy for Landsat-D are defined in terms of the average mean-squared errors (1m for TM and 1.5m for MSS). Table 1 represents the 90% maximal errors and the standard deviations of the average errors for Thematic Mapper, obtained by stochastic modeling. Here the attitude angles were normally distributed with zero means and $\sigma = .01^{o}$. Two cases of radial deviations were considered: a constant equal to 9.5 km, and a more plausible value from a uniform distribution (-9.5, 9.5) km. Because the errors do not depend significantly upon distribution of the cross and along track deviations, the latter were kept constant at 5 km.400 samples were used to establish results for each case. The table also represents a case when PD were computed on a 3x7 grid and then interpolated to a finer grid. The nominal SCD and PD for backward scans were recomputed from the data for forward scans. Note, that in all cases the standard deviations of the average errors are less 1 m and thus, the nominal SCD and PD, precomputed for mean orbit radius at the frame center, provide the geometric correction with the required accuracy.

Timing

On the VAX, the direct lookpoint calculations take about 11 msec per grid point, interpolation of PD - 1 msec, the nominal SCD to SCD/GCD correction- less than .5 msec, and inversion from LSOM to geodetic coordinates - 1.1 msec per point. Application of our technique for MSS requires interpolation PD to a finer grid, two corrections in LSOM coordinates, and inversion to geodetic coordinates; altogether it takes about 3.1 msec per point. The direct on-line SCD and GCD calculation takes about 22 msec per point.

It should be noted, that mapping to the SOM requires about 15 msec per point, which is considered excessive for on-line processing. This time may be significantly reduced if we take into consideration the fact that the LSOM closely approximates true SOM distances between points within each frame. The errors of the approximation are relatively small (less than 5m) and sufficiently regular to permit linear interpolation LSOM to SOM coordinates. It may be done by using a 9x9 grid of corrections, precomputed and stored in the Data Base (Ref. 1).

CONCLUSIONS

The SCD/GCD calculation technique is based on presentation of image distortions as a sum of nominal distortions and linear effects, caused by variation of the spacecraft position and attitude variables from their nominals. The implementation requires generation and storage of the nominal SCD and twelve (for MSS), or fourteen (for TM) matrices of PD for each distinct latitude of WRS, along one path. The maximal errors of the method do not exceed 5.1m at the worst point of a frame. The standard deviations of the average errors are less than 1m. The speed of the processing and the accuracy that is achieved by this technique makes it an elegant solution in the production environment.

Table 1.

The 90% maximal errors and the standard deviations of the average errors for constant and uniformally distributed radial deviations.

Distribution of the radial deviation	Interpolation of PD	Forward scans				Backward scans			
		90% max errors (m)		STD (m)		90% max errors (m)		STD (m)	
		CT	AT	CT	AT	CT	AT	CT	AT
constant	no	2.76	2.37	.61	.49	2.78	2.36	.61	.49
	yes	3.09	2.69	.63	.67	3.11	2.70	.70	.72
uniform	no	1.31	1.78	.29	.32	1.33	1.78	.58	.58
	yes	2.19	1.41	.42	.35	2.19	1.40	.53	.48

REFERENCES

1. J. Brooks, R. Kumar, I. Levine, "Implementation of the Space Oblique Mercator Projection in a Production Environment", Fifteenth Symposium on Remote Sensing of Environment, May 11-15, 1981, Ann Arbor, Michigan.

PAPER 9 DELETED

The MSS Control Point Location Error Filter for Landsat-D.*

I. Levine

General Electric Company Space Division

4701 Forbes Blvd., Lanham, MD 20801

ABSTRACT

The theory and results of modeling for the MSS Control Point Location Error Filter are presented. The filter produces the maximum-likelihood estimates for average values of the spacecraft position and attitude errors during a single scene. The quality of the filter performance is characterized by the maximal cross and along-track residual errors for which probability distributions can be calculated analytically for a given pattern of control points. The filter with an automatic selection of the best set of estimates provides geodetic correction at 90% of pixels with residual errors less than 40m for four or more control points and the mean-squared measurement errors of the order of 20-25m. The same accuracy can be preserved for eight or more control points and measurement errors of 30-35m.

INTRODUCTION

The ground control points (CP), whose locations are measured on systematically corrected imagery and whose true coordinates are known from maps, give highly precise information on image displacements at each of the CP's. The differences between true and measured locations provide the input to a filter, which produces refined estimates of the spacecraft ephemeris and attitude errors. Then these estimates are used for geodetic correction.

The MSS filter theory, represented in Section I, is based on

1) presentation of image distortions, expressed in Local Space Oblique Mercator coordinates, as a linear function of deviations in spacecraft attitudes and position (Ref.1), and

2) recognition of the fact, that MSS processing is limited to a single scene with no more than 20 CP's. It is unlikely that any filter can assess the true time dependence in the deviations during a single scene. But we still believe that in some cases the MSS filter will be able to produce an reliable estimate of average rates.

1.

* Work performed under National Aeronautics and Space Administration Contract No. NAS5-25300.

An accuracy of these estimates is discussed in Section 2. The covariance analysis of the estimate errors shows that image distortions caused by the roll and cross-track deviations are so similar that their origins can be determined only by near perfect measurements. Thus, the filter is unable to produce an reliable estimate of both deviations. At the same time, the filter can provide an equivalent estimate for either variable, say, roll, which compensates distortions due to both sources. Analogously, for the pitch and along-track deviations. The analysis of covariances shows also, that initial uncertainties in rates may be reduced only for the equivalent roll + cross-track and pitch + along-track rates if there are more than 15 CP's and the mean-squared measurement errors are of the order of 10-15m. So, in cases of few CP's, that is of interest to us, only four estimates should be taken into consideration: for the yaw, radial and equivalent pitch and roll deviations.

Section 3 introduces three global characteristics of filter performance: the maximal cross and along-track residual errors, together with combined error in distance. These characteristics can be obtained analytically and they establish upper levels of errors for any given configuration of CP's. The final formulae for probability distributions are presented; more details may be found in Ref.2. It is known that pattern, which CP's form on imagery, have a strong effect on filter performance. Examples, given in Section 4, show that one of the most important simple characteristics of CP's distribution is the maximal cross-track separation, which has been defined as the maximum of the cross-track distances between every pair of CP's.

The examples demonstrate also, that for every pattern of CP's, measurement errors, and initial uncertainties in deviations, there is an optimal set of estimates, minimizing the residual errors. An approximate algorithm, providing the automatic selection of such a set, is described in Section 5. Results of modeling indicate that the MSS filter with the automatic selection provides the 90% average errors less than .5 pixel (40m) for 4 or more CP's and the mean-squared measurement errors of the order of 20-25m, or for 8 or more CP's and measurement errors of 30-35m.

I. THE MSS FILTER EQUATIONS

Ref. [1] shows that the local SOM coordinates of a frame point, $\bar{X} = (X_1, X_2)$, may be represented as

$$\bar{X} = \bar{X}_o + \mu\bar{\delta}, \tag{1}$$

where $\bar{X}_o$ is true coordinates of the point, $\bar{\delta} = (\delta_1, \delta_2, \ldots, \delta_\ell)$ is a vector of the spacecraft position and attitude deviations, and μ is a $(2x\ell)$ matrix of the partial derivatives (PD), computed at the same point. Now let $\bar{Z} = (Z_1, Z_2)$ be the coordinates of a CP obtained from a map. We will assume that

$$\bar{Z} = \bar{X}_o + \bar{\xi}\ , \tag{2}$$

where $\bar{\xi} = (\xi_1, \xi_2)$ is a vector of Gaussian measurement errors with zero expectation values and the covariance matrix R.

From (1) and (2), it follows that the measured at a CP displacement,

$$\overline{\Delta X} = \overline{X} - \overline{Z} = \mu\overline{\delta} - \overline{\xi} \ , \tag{3}$$

is also normally distributed with

$$E(\overline{\Delta X}) = E(\mu\overline{\delta}) - E(\overline{\xi}) = \mu\overline{\delta}$$

$$\mathrm{cov}(\Delta\overline{X}) = E(\overline{\xi}\overline{\xi}^{T}) = R$$

Thus, the conditional probability density for $\overline{\Delta X}$ can be written as

$$P = (\overline{\Delta X}/\overline{\delta}) = \mathrm{const}\cdot\exp\left[-\tfrac{1}{2}(\overline{\Delta X} + \mu\overline{\delta})^{T} R^{-1}(\Delta\overline{X} + \mu\overline{\delta})\right]$$

Let us assume that $\overline{\delta}$ is constant during a scene. Then a joint density of displacements at N control point is

$$P(\overline{\Delta X}^{1},\overline{\Delta X}^{2},\ldots,\overline{\Delta X}^{N}/\overline{\delta}) = \mathrm{const}\cdot\prod_{k=1}^{N} \exp(-\tfrac{1}{2}\ (\overline{\Delta X}^{k} -$$

$$-\mu^{k}\overline{\delta})^{T}\ R^{-1}(\overline{\Delta X}^{k} - \mu^{k}\overline{\delta}))\ ,$$

where upper index k indicates $\overline{\Delta X}$ and μ associated with the k-th CP.

It is known, that the maximum likelihood estimate of $\overline{\delta}$ (we will denote it as $\hat{\delta}$) is a solution of equation

$$\nabla L\ (\overline{\delta}) = 0\ , \tag{4}$$

where

$$L(\overline{\delta}) = \ln P = -\tfrac{1}{2}\sum_{k=1}^{N} (\overline{\Delta X}^{k} - \mu^{k}\overline{\delta})^{T}\ R^{-1}(\overline{\Delta X}^{k} - \mu^{k}\overline{\delta}), \tag{5}$$

and differential operator ∇ is defined in Appendix.

It is known also that

$$E(\hat{\delta}) = \overline{\delta} \tag{6}$$

and in our case (Gaussian conditional density) the covariance matrix of $\hat{\delta}$ is

$$\mathrm{cov}(\delta) = E((\hat{\delta}-\overline{\delta})(\hat{\delta}-\overline{\delta})^{T}) = -\ (\nabla L(\overline{\delta})\nabla^{T})^{-1} \tag{7}$$

Note from here the summation index k will be omitted. Eq. (4) and (5) yield

$$\nabla L = -\tfrac{1}{2}\sum \nabla(\overline{\Delta X} - \mu\overline{\delta})^{T}\ R^{-1}\ (\overline{\Delta X} - \mu\overline{\delta}) =$$

$$= \tfrac{1}{2}\sum \mu^{T}\ R^{-1}(\overline{\Delta X} - \mu\overline{\delta}) = 0 \tag{8}$$

and thus, the solution $\hat{\delta}$ can be written as

$$\hat{\delta} = M_o^{-1} Y_o \ , \tag{9}$$

where

$$M_o = \sum \mu^T R^{-1} \mu$$
$$Y_o = \sum \mu^T R^{-1} \overline{\Delta X}$$

Noting that

$$\nabla L \nabla^T = - \sum \mu^T R^{-1} \mu = - M_o$$

we also have from (7) that

$$\mathrm{cov}(\delta) = M_o^{-1} \tag{10}$$

Now let ξ_1, ξ_2 be independent with the dispersions σ_1^2, σ_2^2. In that case

$$R = \begin{pmatrix} \sigma_1^2 & 0 \\ 0 & \sigma_2^2 \end{pmatrix}$$

and (9) and (10) yield

$$\hat{\delta} = M^{-1} Y \tag{11}$$

$$\mathrm{cov}(\hat{\delta}) = \sigma_1^2 M^{-1} \ , \tag{12}$$

where M, Y are matrices with elements

$$m_{ij} = \sum (\mu_{1i} \mu_{1j} + \frac{\sigma_1^2}{\sigma_2^2} \mu_{2i} \mu_{2j}) \tag{13}$$

$$y_i = \sum (\mu_{1i} \Delta X_1 + \frac{\sigma_1^2}{\sigma_2^2} \mu_{2i} \Delta X_2) \tag{14}$$

Elements of the matrix M^{-1} will be denoted as m_{ij}^{-1}, i.e. $M^{-1} = (m_{ij}^{-1})$.

Once $\hat{\delta}$ is determined, it can be used for geodetic correction. With geodetically corrected coordinates of a point being $\overline{X} + \mu\hat{\delta}$, the residual error at the point, $\overline{\varepsilon} = (\varepsilon_1, \varepsilon_2)$, can be written as

$$\overline{\varepsilon} = \overline{X} + \mu\hat{\delta} - \overline{X}_o = \overline{X} + \mu\hat{\delta} - (\overline{X} + \mu\overline{\delta}) =$$
$$= \mu(\hat{\delta} - \overline{\delta}) \tag{15}$$

Thus, $\bar{\varepsilon}$ is normally distributed with zero mean and the covariance matrix

$$\text{cov}(\bar{\varepsilon}) = E\left\{\mu(\hat{\bar{\delta}}-\bar{\delta})\left[\mu(\hat{\bar{\delta}}-\bar{\delta})\right]^T\right\} =$$
$$= \mu\, E\left\{(\delta-\bar{\delta})(\delta-\bar{\delta})^T\right\}\mu^T = \sigma_1^2\,\mu\, M^{-1}\mu^T \qquad (16)$$

Eq (16) defines local two-dimensional distribution of the residual errors at a given frame point. It can be used also for detection of 'outliers', i.e. bad measurements at CP's. From (3) it follows, that after geodetic correction, the measured displacement at the k-th CP's, $\bar{\varepsilon}_k$, can be expressed as

$$\bar{\varepsilon}_k = \overline{\Delta X} - \mu\hat{\bar{\delta}} = \mu(\bar{\delta}-\hat{\bar{\delta}}) + \bar{\xi}$$

As a sum of two independent Gaussian variables, $\bar{\varepsilon}_k$ also is Gaussian with zero mean and the covariance matrix.

$$\text{cov}(\bar{\varepsilon}_k) = \sigma_1^2\,\mu\, M^{-1}\,\mu^T + R = Q \qquad (17)$$

The two-dimensional probability density for $\bar{\varepsilon}_k$ is represented by the countour ellipses

$$\Phi(\bar{e}) = \bar{e}^T\, Q^{-1}\,\bar{e} = \text{const} = \lambda^2$$

It is well-known, that the probability that the 'point' $\bar{\varepsilon}_k$ is inside the countour ellipse is $\chi^2(\lambda^2)$, so the k-th CP should be treated as an outlier if

$$\Phi(\bar{\varepsilon}_k) > \lambda^2 ,$$

where λ^2 corresponds to a chosen confidence level. For instance, $\lambda^2 = 9.21$ for the 99% confidence level.

All derived above formulae can be easily generalized to include the case when $\bar{\delta}$ is a slow-changing function of time. Introducing the average deviations and rates during a scene,

$$\bar{\alpha} = (\alpha_1, \alpha_2, \ldots\ \alpha_\ell) \text{ and } \bar{\beta} = (\beta_1, \beta_2, \ldots\ \beta_\ell),$$

we can approximate the deviation at time t as

$$\bar{\delta} = \bar{\alpha} + \bar{\beta}t \qquad (18)$$

Now the displacement at the k-th CP at time t^k is

$$\overline{\Delta X}^k = \mu^k(\bar{\alpha} + \bar{\beta}t^k) + \bar{\xi}$$

and the maximum likelihood function of $\bar{\alpha}$, $\bar{\beta}$ can be written as

$$L(\bar{\alpha},\bar{\beta}) = -\tfrac{1}{2} \sum_{k=1}^{N} (\Delta\bar{X}^k - \mu^k(\bar{\alpha} + \bar{\beta}t^k))\ R^{-1}$$

$$(\Delta\bar{X}^k - \mu^k(\bar{\alpha} - \bar{\beta}t^k))^T.$$

From the above, one can obtain that the estimates of $\bar{\alpha}$ and $\bar{\beta}$ (denoted as $\hat{\alpha}$ and $\hat{\beta}$) are given by

$$\begin{vmatrix} \hat{\alpha} \\ \hat{\beta} \end{vmatrix} = M_1^{-1} \begin{vmatrix} Y \\ Y' \end{vmatrix} , \tag{19}$$

where Y is given by (14) and components of Y' are

$$y'_i = \sum (\mu_{1i}\ \Delta X_1 + \frac{\sigma_1^2}{\sigma_2^2}\ \mu_{2i}\ \Delta X_2)t \tag{20}$$

The matrix M_1 consists of four submatrices

$$M_1 = \begin{vmatrix} M & M' \\ M' & M'' \end{vmatrix} ,$$

where M is defined by (13) and elements of M' and M'', m'_{ij} and m''_{ij}, are

$$m'_{ij} = \sum (\mu_{1i}\mu_{1j} + \frac{\sigma_1^2}{\sigma_2^2}\ \mu_{2i}\ \mu_{2j})t \tag{21}$$

$$m''_{ij} = \sum (\mu_{1i}\mu_{1j} + \frac{\sigma_1^2}{\sigma_2^2}\ \mu_{2i}\ \mu_{2j})t^2 \tag{22}$$

We have also that $E(\hat{\alpha}) = \bar{\alpha}$, $R(\hat{\beta}) = \bar{\beta}$, and

$$\mathrm{cov}(\hat{\alpha},\hat{\beta}) = \sigma_1^2\ M_1^{-1} \tag{23}$$

Introducing the estimate of deviation at time t, $\hat{\delta} = \hat{\alpha} + \hat{\beta}t$, we have that

$$E(\hat{\delta}) = E(\hat{\alpha}) + t \cdot E(\hat{\beta}) = \bar{\alpha} + \bar{\beta}t = \bar{\delta}$$

and the covariance matrix of $\hat{\delta}$ is

$$\mathrm{cov}(\hat{\delta}) = E((\hat{\alpha}-\bar{\alpha})(\hat{\alpha}-\bar{\alpha})^T) + 2\,t\,E((\hat{\alpha}-\bar{\alpha})(\hat{\beta}-\bar{\beta})^T) +$$

$$+ t^2 E((\hat{\beta}-\bar{\beta})(\hat{\beta}-\bar{\beta})^T) =$$

$$= C + 2tC' + t^2C'', \qquad (24)$$

where C, C' and C'' are the $\ell x \ell$ submatrices of M_1^{-1}

$$M_1^{-1} = \begin{vmatrix} C & C' \\ C' & C'' \end{vmatrix} \qquad (25)$$

Further it will be considered that the filter can estimate, at the most, the along-track (AT), cross-track (CT), and radial (RAD) position deviations and rates, together with deviations and rates in the pitch (P), roll (R) and yaw (Y). σ_1 and σ_2 will correspond to the cross-track and along-track measurements.

II. COVARIANCE ANALYSIS

The covariance matrices, $\mathrm{cov}(\hat{\delta})$ and $\mathrm{cov}(\hat{\alpha},\hat{\beta})$, completely characterize an accuracy of estimates, which can be achieved by the filter for a given configuration of CP's and the mean-squared measurement errors σ_1 and σ_2. It is well-known, that a pattern, which CP's form on imagery, has a strong effect on filter performance, especially for a small number of CP's. At the same time, our calculations show that for $N \geq 10$ elements of the covariance matrices insignificantly depend upon a distribution of CP's. For $\sigma_1 \approx \sigma_2$ the standard deviation of the estimates are approximately proportional to $\sigma_1 N^{-\frac{1}{2}}$. At the present time, σ_1 and σ_2 are not expected to be less than 10 and 12m, respectively; the MSS filter will be processing up to 20 CP's per scene.

Table I shows the standard deviations of $\hat{\delta}$ computed for $\sigma_1 = 10$, $\sigma_2 = 12$m and 50 (randomly located in a frame) CP's. Comparison of the standard deviations with initial uncertainties in the spacecraft position and orientation, given in Table 2, demonstrates complete inefficiency of the filter in that case. The reason is simple: PD with respect to the R and CT deviations, as well as PD with respect to P and AT, are almost linearly dependent. As a result, the matrix M is nearly singular, and thus Eq.(9) can not give a reliable value of $\hat{\delta}$. In other words, distortions, caused by the R and CT (or P and AT) deviations, are so similar that the difference would be revealed only in near perfect imagery by near perfect measurements.

It prompts not to estimate CT and AP deviations at all, considering the corresponding image distoritons as a result of additional fictitious deviations in R and P, respectively. Thus, the filter should be treated as a source of appropriate geodetic corrections, rather than true estimates.

The covariance analysis for time-dependent deviations shows that the filter is unable to produce reliable estimates of the Y and RAD rates even for N = 50: the standard deviations of the estimates are 4-5 times as much as their initial uncertainties.

At the same time, the filter provides mediocre estimates for combined R + CT and P + AT rates when N = 15 - 20 and σ_1, σ_2 are of the order of 10-15m. Table 3 shows such an example for N = 20, σ_1 = 10, and σ_2 = 12m. Note, that initial uncertainties in the R + CT and P + AT rates are .83 and .82 μrad/sec (these values have been computed by data from Table 2).

Despite the fact, that in some favorable conditions the filter can cope with these rates, such a case will not be considered below. Being interested chiefly in the case of few CP's we will take into account only estimates of the P,R,Y and RAD deviations.

III. THE MAXIMAL RESIDUAL ERRORS

The current requirements to geometric correction accuracy are specified in terms of .5 pixel 90% of the time. Accordingly, we will evaluate the filter performance by the 90% guantile of probability distribution, computed for the residual errors which were observed at points of some, say 15x15, grid for randomly distributed deviations, measurement errors, and possibly, CP's locations. Three types of the 90% errors may be introduced on two-dimensional grids: for the CT and AT components of the residuals errors and for the total residual displacements $\bar{\varepsilon} = (\varepsilon_1^2 + \varepsilon_2^2)^{\frac{1}{2}}$. The last characteristic will be referred to as DIST.

It should be noted, that actually all these characteristics can be obtained only by stochastic modeling. At the same time there are two additional global characteristics, which can be computed relatively simply: probability distributions of the maximal CT and AT errors. These distributions describe errors at the worst frame points and thus establish the upper level of possible errors for given CP's.

Let us introduce the error in the j-th estimate, $\Delta_j = \delta_j - \hat{\delta}_j$. Now, Eq. (15) may be rewritten as

$$\varepsilon_1 = \sum \mu_{1j} \Delta_j$$

$$\varepsilon_2 = \sum \mu_{2j} \Delta_j \qquad (j = 1,2,3,4)$$

It is known that all PD increase towards the corner points of a frame. The CT and AT errors also reach maximal magnitudes at a corner point [1], although it is never known beforehand at what specific point. At the corner points only four PD, namely, μ_{21},μ_{12},μ_{23}, and μ_{14}, have significant values. Moreover, with an error less than .1%, they may be replaced with their maximum values, μ_{ij}^m (retaining, of course, correct sign). Thus, at the corner points

$$\varepsilon_1 \simeq \mu_{12}^m \Delta_2 + \mu_{14}^m \Delta_4$$

$$\varepsilon_2 \simeq \mu_{21}^m \Delta_1 + \mu_{23}^m \Delta_3$$

Noting that μ_{23} and μ_{14}, PD with respect to Y and RAD, have opposite signs at the ends of every scan line, we always can find a corner point, where $\mu_{12} \Delta_2$ and $\mu_{14} \Delta_4$ have the same sign (analogously, for $\mu_{21}\Delta_1$ and $\mu_{23} \Delta_3$). Being indifferent to signs of ε_1 and ε_2, we finally have that the maximal (absolute) CT and AT errors, γ_1 and γ_2, are

$$\gamma_1 = |\mu_{12}\,\Delta_2| + |\mu_{14}\,\Delta_4|$$
$$\gamma_2 = |\mu_{21}\,\Delta_1| + |\mu_{23}\,\Delta_3| \qquad (26)$$

Here we have omitted the superscript m.

Fortunately, Δ_2, Δ_4 and Δ_1, Δ_3 are practically independent and thus these expressions may be used separately to derive corresponding distribution and moments (Ref.2).

The following are the final formulae for mean value and variance of γ_i:

$$E(\gamma_i) = \sqrt{\frac{2}{\pi}}\ (S_1 + S_2) \qquad (27)$$

$$Var(\gamma_i) = (1 - \frac{2}{\pi})\ (S_1^2 + S_2^2) + \frac{4}{\pi}\ S_1\,S_2 \cdot (\rho \cdot \arccos(r) + r - 1)\ , \qquad (28)$$

where

$$\left.\begin{aligned} r &= (1 - \rho^2)^{\frac{1}{2}} \\ S_1^2 &= \sigma_1^2\,\mu_{12}\,m_{22}^{-1} \\ S_2^2 &= \sigma_2^2\,\mu_{14}\,m_{44}^{-1} \\ \rho &= \frac{|m_{24}^{-1}|}{\sqrt{m_{22}^{-1} \cdot m_{44}^{-1}}} \end{aligned}\right\} \text{ for } i = 1$$

$$\left.\begin{aligned} S_1^2 &= \sigma_1^2\,\mu_{21}^2\,m_{11}^{-1} \\ S_2^2 &= \sigma_2^2\,\mu_{23}^2\,m_{33}^{-1} \\ \rho &= \frac{|m_{13}^{-1}|}{\sqrt{m_{11}^{-1} \cdot m_{33}^{-1}}} \end{aligned}\right\} \text{ for } i = 2$$

The probability distribution of γ_i can be written as

$$Pr(\gamma_i < A) = \frac{A\ 2^{\frac{1}{2}}}{S_1\ \pi^{\frac{1}{2}}} \int_0^1 \exp(-\frac{A^2 t}{2S_1^2}) \times$$

$$\left[F(B(n + \rho \cdot t - n \cdot t) + F(B \cdot (n - \rho \cdot t - n \cdot t)) - 1 \right] dt,$$

where $n = \frac{S_1}{S_2}$, $B = \frac{A}{S_1 \cdot r}$,

$$F(u) = \frac{1}{\sqrt{2\pi}} \int_{-\infty}^{u} \exp(-t^2/2)\, dt,$$

and S_1, S_2, ρ are given by (29).

For a given value of error, A, the corresponding probability can be easily computed by means of standard subroutines. Modeling has shown an excellent coincidence of theoretical and empirical values of $E(\gamma_i)$ and $Var(\gamma_i)$. Smirnov's Test also demonstrates sufficient coincidence of theoretical and empirical distributions.

Eq. (26) may be used also for evaluation of the maximal residual error in distance, which we define as

$$d_m = (\gamma_1^2 + \gamma_2^2)^{\frac{1}{2}}$$

We could not derive an exact distribution for d_m. But we have noticed that empirical distribution of d_m^2 are similar to Gamma-distribution with the same means and variances. Because $E(d_m^2)$ and $Var(d_m^2)$ can be obtained analytically, we have decided to approximate distribution of d_m^2 by Gamma-distribution, which is written here as

$$Pr(A) = \frac{1}{b^a \Gamma(a)} \int_0^A u^{a-1} \exp(-\frac{u}{b}) \cdot du$$

where

$$a = \frac{E(d_m^2)^2}{Var(d_m^2)} \qquad (30)$$

$$b = \frac{Var(d_m^2)}{E(d_m^2)} \qquad (31)$$

Because, γ_1 and γ_2 are practically independent,

$$E(d_m^2) = E(\gamma_1^2) + E(\gamma_2^2) \qquad (32)$$

$$Var(d_m^2) = Var(\gamma_1^2) + Var(\gamma_2^2) \qquad (33)$$

In Ref.2 it is shown that

$$E(\gamma_i^2) = s_1^2 + s_2^2 + \frac{4 s_1 s_2}{\pi} (\rho \arccos(r) + r) \qquad (34)$$

and

$$\mathrm{Var}(\gamma_i^2) = 2(S_1^2 + S_2^2)^2 + 24S_1^2S_2^3\rho \quad +$$
$$+ \frac{32}{\pi}(S_1^2 + S_2^2)S_1S_2(r + \rho \arccos(r)) -$$
$$- \frac{32\, S_1^2\, S_2^2}{\pi 2}(r + \rho \arccos(r))^2 \qquad (35)$$

Here S_1^2, S_2^2 and ρ are given by (29). Eq. (30)-(35) yield a and b, which are used to compute a probability $Pr(A) = Pr(A^2)$ for any A by means of a standard subroutine for Gamma-distribution. Smirnov's Test shows sufficient coincidence of the approximations and empirical distributions for d_m; differences between values of errors for corresponding probabilities are less than 5-7%.

IV. EXAMPLES

Table 4 presents means, the standard deviations, and the 90% errors for the maximal CT and AT errors, together with the 90% errors in distance (DIST). These data have been obtained by modeling (M) and analytically (T) for $\sigma_1 = \sigma_2 = 10$m and initial uncertainties given in Table 2 (except example 9, where AT = 185m, CT = 35m, RAD = 65m, P = R = 120 μrad, and Y = 35 μrad).

From 300 to 600 samples have been used to establish results for each case. The examples correspond to five selected configurations of CP's, depicted in Fig.1. Table 5 describes the examples and shows the mean-squared errors of estimates. Examples 1-3 and 7-8 illustrate the fact that for given configuration of CP's, measurement errors, and initial uncertainties, there is an optimal set of estimates, which provides minimum errors. For distribution A, that set includes P and R for distribution C it includes P,R, and Y. Examples 8 and 9 demonstrate also that such a set depends upon initial errors in deviations.

As we already know, the partial derivatives μ_{12}, μ_{14}, μ_{21}, and μ_{23} represent the main effects of the position and attitude deviations on image distortions. At the same time, there is significant distinction between μ_{12}, μ_{21} and μ_{14}, μ_{23}: when the former are almost constant in a frame, the second increase their magnitudes along every scan line. Thus, up to the second order effects, P and R estimates do not depend upon position of CP's in a scene. Roughly speaking, they depend upon average CT and AT displacements at all CP's. On the contrary, to detect effects of the Y and RAD deviations, we should observe differences of these displacements, so the bigger the CT distances between CP's, the bigger differences in corresponding μ_{14} and μ_{23}, and the higher an accuracy of the Y and RAD estimates. Thus, a simple but important characteristic of CP's distribution is the maximal cross-track separation, H, which we define as the maximum of cross-track distances between every pair of CP's.

Example 1 shows that for small cross-track separations (H=29.7 km) the Y and RAD estimates are absolutely insufficient (457 μrad and 292 m) and, as a result, the residual errors are large even for very modest measurement errors. On the other hand, even smaller number of CP's may lead to better results if they are 'nicely' separated (example 4 for N = 2 and H = 169 km). Comparasion of examples 4 and 5 shows that an along-track shift of CP's does not affect significantly an accuracy of results if cros-track positions are preserved. In addition, example 6

suggests that a shift of CP's as a whole in the cross-track direction towards to the frame bounds increases errors. It implies that it is always desirable to have CP's placed symmetrically along the track.

Analyzing results of modeling, we have noted that the 90% CT and AT errors can be approximated as

$$\gamma_i = E(\gamma_i) + 1.5 \sqrt{Var(\gamma_i)} \qquad (36)$$

where $E(\gamma_i)$ and $Var(\gamma_i)$ are given by (27) and (28). We have no explanation of that fact, but it was verified on a large number of cases which have shown that an error of such an approximation usually does not exceed 5%.

V. AUTOMATIC SELECTION OF ESTIMATES

As it has been shown, for every pattern of CP's, measurement errors and initial uncertainties, there is an optimal set of estimates which reduces the residual errors. Consequently, the filter's performance can be improved if it will automatically select an appropriate set of estimates. Our approximate algorithm of selection is based on the fact that γ_1 and γ_2 are practically independent, and, bigger maximal errors almost always lead to bigger average errors. In our specific case, the a priori known uncertainties in P + AT and R + CT are always bigger than errors of corresponding estimates (at least, for mean-squared measurement errors less than 40m). Thus, these estimates always ought to be included in an optimal set. Now, all we need is to compute γ_1 twice, with and without the use of the RAD estimate. In the second case, the standard deviation of the RAD estimate must be replaced with the initial mean-squared error. Analogously γ_2 should be computed twice to determine when the Y estimates ought to be employed.

Table 6 presents the 90% CT, AT, and DIST errors, computed on a 15x15 grid as a function of σ_1 for various number of CP's.* Results for each case have been established by 300-500 randomly generated sets of CP, measurement errors and deviations. CP's were generated so that the distances between every pair of them were not less than 75 km for $N \leq 4$, 50 km for N = 5,6 and 25 km for $N \geq 7$. Additional restriction forbad generation of CP's on the frame borders. The 90% DIST errors also depicted in Fig.2.

As one can see, the filter provides geodetic correction with the 90% errors less than 40m if $\sigma_1 \leq 20$m and $N \geq 4$. For σ_1 = 30 m only 8 or more CP's can guarantee that accuracy. Note these results do not include errors due to neglected uncertainties in rates. These additional errors, accumulated during 15 sec (i.e. with respect to the frame center) can be evaluated as 8.6 m (σ) in either direction. Being relatively small, they do not affect significantly the total errors.

It should be pointed out, that the automatic selection only slightly reduces the average residual errors. At the same time, it essentially moderates errors in relatively rare cases of extremely bad distributions of CP's.

---

* Note, that the CT and AT errors are Gaussian and thus may be described also by the corresponding standard deviations.

REFERENCES

1. I. Levine, "Computational Aspects of Geometric Correction Data Generation in the Landsat-D Imagery Processing", The sixth annual Flight Mechanics/ Estimation Theory Symposium, NASA/Goddard Space Flight Center, October 27/28 1981.

2. I. Levine, "The MSS Control Point Location Error Filter: General Theory and Results of Modeling", GE 1T81-LSD-LAS-102, 3/6/81.

APPENDIX

$\bar{a}$ - ℓ x 1 matrix (vector)

$\bar{a}^T = (a_1, a_2, \ldots, a_\ell)$ - transposed vector $\bar{a}$

$E(\bar{a})$ - mathematical expectation of $\bar{a}$

$cov(\bar{a}) = E((\bar{a} - E(\bar{a}))(\bar{a} - E(\bar{a}))^T)$ - covariance matrix of $\bar{a}$

$Var(b)$ - variance of b.

$$\nabla = \left(\frac{\partial}{\partial \delta_1}, \frac{\partial}{\partial \delta_2}, \ldots \frac{\partial}{\partial \delta_\ell}\right)$$ symbolic differential

operator defined for $U = (u_1, u_2, \ldots, u_\ell)$ as

$$\nabla U^T = \begin{vmatrix} \frac{\partial u_1}{\partial \delta_1} & \cdots & \frac{\partial u_\ell}{\partial \delta_1} \\ \cdots\cdots\cdots\cdots & & \\ \cdots\cdots\cdots\cdots & & \\ \frac{\partial u_1}{\partial \delta_\ell} & \cdots & \frac{\partial u_\ell}{\partial \delta \ell} \end{vmatrix}$$

If A is a ℓ x ℓ matrix,

$$\nabla(\bar{\delta}^T A \bar{\delta}) \nabla^T = 2A$$

Table 1

Mean-squared errors in estimates

(N = 50, σ_1 = 10, σ_2 = 12)

P μrad	R μrad	Y μrad	AT m	CT m	RAD m
2591	34	375	2059	299	20

Table 2

Initial uncertainties in deviations and rates (1σ)

	P,R,Y	AT	CT	RAD
deviations	350 μrad	550m	110m	37m
rates	.81 μrad/sec	.16m/sec	.065m/sec	.65m/sec

Table 3

Mean-squared errors in estimates.

(N = 20, σ_1 = 10m, σ_2 = 12m)

deviations				rates	
R + CT μrad	P + AT μrad	Y μrad	RAD m	R + CT μrad/sec	P + AT μrad/sec
3.3	4.0	52.2	31.1	.5	.6

Table 4

The 90% maximal CT, AT, and DIST errors (in meters)

error			Example								
			1	2	3	4	5	6	7	8	9
γ_1 (CT)	mean	M	38.3	9.4	9.7	12.6	13.3	57.1	11.0	5.5	10.9
		T	38.1	8.6	8.6	12.2	12.2	55.6	11.0	5.3	11.0
	STD	M	26.0	4.6	4.8	6.6	6.7	40.3	6.1	3.2	5.7
		T	26.8	4.6	4.6	6.6	6.6	41.6	6.1	3.2	6.1
	90%	M	72.9	16.0	15.7	21.5	22.4	113.8	19.4	10.0	18.5
		T	75.9	14.8	14.8	21.2	21.2	115.0	19.3	9.6	19.3
γ_2 (AT)	mean	M	45.8	42.7	30.0	12.9	12.2	64.5	11.8	11.2	7.3
		T	42.1	42.0	30.7	12.3	12.2	61.0	10.9	10.9	6.5
	STD	M	30.3	30.7	20.4	6.7	6.5	44.4	6.0	6.2	3.5
		T	29.9	29.9	2.0	6.6	6.6	45.7	6.1	6.1	3.6
	90%	M	88.0	85.9	59.0	22.0	21.0	124.5	20.0	19.6	12.0
		T	84.3	84.2	57.9	21.2	21.1	126.7	19.3	18.9	11.3
d_m (DIST)	90%	M	110.0	86.4	60.2	27.3	27.8	154.8	24.6	20.6	20.3
		T	105.5	85.5	61.2	26.5	28.9	156.7	26.2	21.5	22.1

Table 5

Description of Examples in Table 4.

Example	N	distribution (See Fig1)	H (km)	mean-squared errors in estimates			
				P (μrad)	R (μrad)	Y (μrad)	RAD (m)
1	3	A	29.7	14	13	457	292
2	3	A	29.7	14	8	457	-
3	3	A	29.7	8	8	-	-
4	2	B	169.0	10	10	87	63
5	2	C	160.4	10	10	88	63
6	3	D	29.5	47	42	461	298
7	4	E	112.9	7	7	93	66
8	4	E	112.9	7	7	93	-
9	4	E	112.9	7	7	-	66

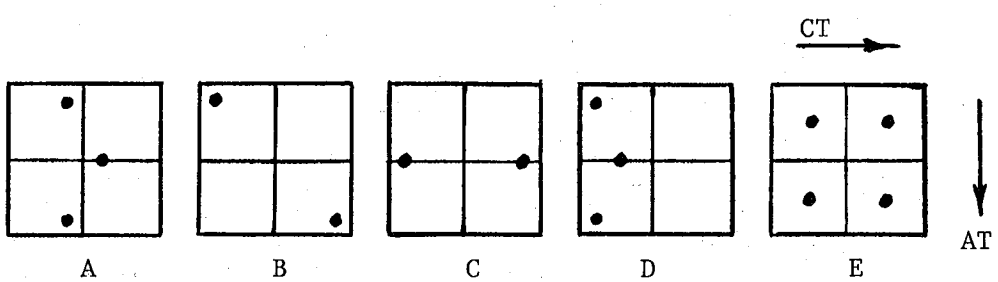

Figure 1. Control Point Distributions

Table 6

The 90% CT, AT, and DIST errors (in meters) as a function of N and σ_1 ($\sigma_2 = 1.2\ \sigma_1$).

N	σ_1 = 10m			σ_1 = 20m			σ_1 = 30m			σ_1 = 40m		
	CT	AT	DIST	CT	AT	DIST	CT	AT	DIST	CT	AT	DIST
1	19.0	51.5	53.1	33.4	59.9	65.7	49.5	73.3	81.6	68.1	87.4	104.
2	13.4	31.5	33.0	24.2	47.0	49.7	34.9	57.4	63.0	49.0	65.1	74.4
3	10.8	20.6	22.1	19.8	38.8	40.8	28.4	47.5	52.0	38.2	58.5	65.3
4	10.0	16.5	18.3	17.6	31.1	33.7	25.0	45.9	49.4	33.9	51.2	57.3
5	9.5	14.4	16.2	16.5	29.9	32.4	23.4	43.4	46.4	32.5	49.8	55.1
6	9.0	13.8	14.9	14.7	26.6	28.6	20.8	39.6	42.5	28.3	49.2	53.3
8	9.0	12.9	14.4	13.6	23.5	25.3	18.5	35.1	37.4	24.7	43.0	47.1
10	8.3	11.0	13.0	12.2	22.5	24.1	17.8	30.6	33.3	22.1	42.3	45.2
15	7.8	8.8	9.9	9.9	16.3	18.1	14.2	24.4	26.5	16.9	33.4	35.2

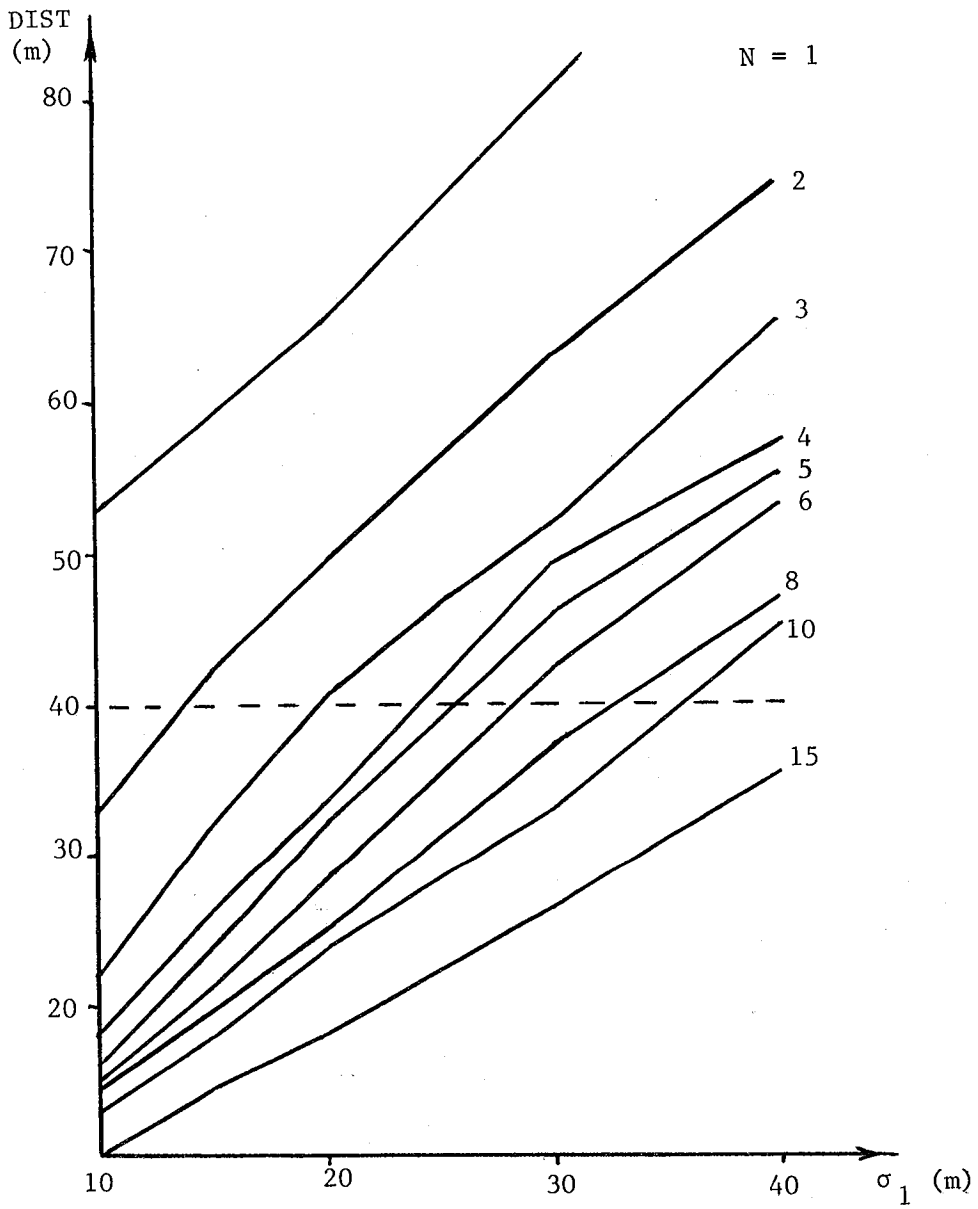

Figure 2.

90% errors in distance as a function of measurement errors ($\sigma_2 = 1.2\sigma_1$).

"ONBOARD UTILIZATION OF GROUND CONTROL POINTS FOR IMAGE CORRECTION"

J. Lowrie (Martin Marietta Corporation)

ABSTRACT

Future remote sensing missions require real-time knowledge of the sensor boresight in earth fixed coordinates for calculation of image distortion coefficients and control of a pointing mount for acquisition of off-nadir data. An analysis of inertial navigation systems reveals an inability of these systems to adequately solve for the sensor boresight position due to dynamic misalignments between the sensor coordinate frame and the gyro coordinate frame.

A conceptual navigation system consisting of a GPS receiver, two NASA standard star trackers, a NASA standard gyro package, and a landmark tracker is presented. The landmark tracking algorithms have been developed and analyzed, and results show that the position of the landmark can be determined to within two tenths of the sensor resolution. The navigation system has been simulated, and a thorough error analysis has been performed. Results indicate that this combination of sensors can continuously solve for sensor boresight position in earth fixed coordinates to within 15 meters.

SESSION III

E. Lefferts, Chairman

"Effective Covariance Deweighting for Precision Estimation"

by C. E. Velez, V. L. Tate,
Computer Technology Associates

Abstract

The Air Force's Sunnyvale Satellite Test Center has had a continuing need for near real-time high precision orbit estimates derived from S-Band tracking in the presence of severe atmospheric and geopotential modeling errors. Techniques based on sequential estimation using dynamically derived time-correlated process noise models have been developed and successfully shown to improve state and state covariance predictability for these cases. This paper will present the overall approach to sequential estimation currently planned for the upcoming data system upgrade to the current Sunnyvale system. In addition, test-bed results utilizing actual data taken for a medium altitude (e.g. 300 nmi) orbiter will be shown indicating the nature and magnitude of the improved performance resulting from the proposed estimator.

Spin-Axis Attitude Estimation and Magnetometer Bias Determination for the AMPTE Mission*

R.H. Thompson†

Naval Electronic Systems Command
Washington, D.C. 20360

G.F. Neal§

Computer Sciences Corporation
Silver Spring, Maryland 20910

M.D. Shuster**

Business and Technological Systems, Inc.
Seabrook, Maryland 20706

Abstract

Algorithms are developed for the determination of magnetometer biases and spin-axis attitude for the AMPTE mission. Numerical examples of the performance of the algorithm are given.

---

* Presented at the Flight Mechanics/Estimation Theory Symposium, NASA Goddard Space Flight Center, Greenbelt, Maryland, October 27-28, 1981.

† Physicist, Electronic Special Warfare and Space Division

§ Technical Staff, System Sciences Division

** Staff Scientist, Research and Development Division

I - Introduction

This paper describes methods for determining spin-axis attitude (i.e., the direction in space of the spacecraft spin axis) and magnetometer biases which are being investigated for ground support of the Active Magnetospheric Particle Tracer Explorer (AMPTE) mission.

The AMPTE mission will consist of two spacecraft.[1] The first is the Ion Release Module (IRM), provided by the Federal Republic of Germany, which will be placed in a highly elliptical orbit with apogee at approximately 19 Earth radii in order to release lithium tracer ions outside the magnetosphere. This spacecraft will be spin stabilized at a rate of 30 rpm. The second spacecraft is the Charge Composition Explorer (CCE), which will detect the tracer ions inside the magnetosphere at altitudes of from 300 km to 7.5 Earth radii. The CCE will be spin stabilized at 10 rpm.

Estimation of spin-axis attitude for both AMPTE spacecraft will be based on the measurements of the geomagnetic field and the projection of the Sun line on the spacecraft spin-axis, which we take nominally to be the symmetry axis $\hat{Y}_A$ of the spacecraft bus.

For the purpose of this study, the attitude sensors are assumed to consist of a three-axis magnetometer and a Sun sensor which measures the angle between the Sun line and $\hat{Y}_A$. For simplicity it is assumed likewise that one axis of the magnetometer is along $\hat{Y}_A$. The other two axes of the magnetometer define $\hat{X}_A$ and $\hat{Z}_A$.

The measured quantities are taken to be

$\underset{\sim}{M}$ = magnetic field vector in body coordinates

$\cos\beta = \hat{S}\cdot\hat{Y}_A$, where $\hat{S}$ is the unit vector directed from the spacecraft to the Sun (β is the "Sun angle").

Attitude determination activities fall into two areas:

- Determination of spin-axis attitude
- Determination of the magnetometer biases

Because the orbit-apogee distance for these two spacecraft is so great, accurate geomagnetic field data for attitude estimation is available only for the segment of the orbit near perigee. This is due to the poor accuracy of the magnetic-field model at such high altitudes resulting from both the small magnitude of the geomagnetic field as well as from fluctuations in the field caused by extraterrestrial phenomena. However, because of the large spacecraft angular momenta, it can be assumed for both spacecraft that the spin-axis attitude at apogee will not differ markedly from that at perigee of the same orbit.

Algorithms for spin-axis attitude and magnetometer bias determination are now being investigated. These are:

- attitude-independent estimation of three-axis magnetometer biases and

- estimation of spin-axis attitude from measurements of the Sun and geomagnetic field angle.

Each of these algorithms are batch estimators utilizing a long segment of magnetometer and Sun data. The algorithms are developed in succeeding sections and then tested using simulated AMPTE data.

II - Magnetometer Bias Determination

The attitude of the spacecraft is usually not known before the magnetometer biases must be determined. Here an algorithm is developed which determines the magnetometer bias vector by minimizing a loss function which is independent of the attitude.

The quantities used throughout this section are defined as follows:

$H_j(i)$ = jth component of the model magnetic field in the geocentric inertial (GCI) system at time i

$M_j(i)$ = jth magnetometer reading at time i

B_j = jth component of the magnetometer bias vector, which is taken to be independent of the spacecraft position

For the ith point, an error $\delta(i)$ is defined by the following equation:

$$\delta(i) = \left|\underset{\sim}{H}(i)\right|^2 - \left|\underset{\sim}{M}(i) - \underset{\sim}{B}\right|^2 \qquad (1)$$

The objective of this equation is to minimize the quantity $\delta(i)$ by adjusting the bias vector $\underset{\sim}{B}$ to its optimal value. Thus, the loss function to be minimized is given by

$$L(\underset{\sim}{B}) = \sum_{i=1}^{N} \omega(i)\left|\delta(i)\right|^2 \qquad (2)$$

where $\omega(i)$ is the weight associated with the ith data point. The weights are assumed to be normalized to unity, that is,

$$\sum_{i=1}^{N} \omega(i) = 1 \qquad (3)$$

Determining the minimum value of $L(\underset{\sim}{B})$ first requires that its derivatives with respect to the components of the bias vector be set equal to zero:

$$\frac{\partial L}{\partial B_m} = 0 \qquad m=1,2,3 \qquad (4)$$

where

$$\frac{\partial L}{\partial B_m} = -4 \sum_{i=1}^{N} \omega(i) \left[\left| \underset{\sim}{H}(i) \right|^2 - \left| \underset{\sim}{B} - \underset{\sim}{M}(i) \right|^2 \right] (B_m - M_m(i)) \qquad (5)$$

Combining Eqs. (3-5) leads to the following results:

$$\sum_{k=1}^{3} G_{mk} B_k = b_m + F_m(\underset{\sim}{B}) \qquad (6a)$$

or in matrix form,

$$G \underset{\sim}{B} = \underset{\sim}{b} + \underset{\sim}{F}(\underset{\sim}{B}) \qquad (6b)$$

where

$$G_{mk} = \delta_{mk}(\langle \left| \underset{\sim}{H} \right|^2 \rangle - \langle \left| \underset{\sim}{M}^2 \right| \rangle) - 2 \langle M_m M_k \rangle \qquad (7a)$$

$$b_m = \langle (\left| \underset{\sim}{H} \right|^2 - \left| \underset{\sim}{M} \right|^2) M_m \rangle \qquad (7b)$$

$$F_m(\underset{\sim}{B}) = \left| \underset{\sim}{B} \right|^2 \langle B_m - M_m \rangle - 2 \underset{\sim}{B} \cdot \langle \underset{\sim}{M} \rangle B_m \qquad (7c)$$

The bracket denotes the weighted average

$$\langle A \rangle = \sum_{i=1}^{N} \omega(i) A(i) \qquad (8)$$

δ_{mk} is the Kronecker delta defined as unity when m=k and zero otherwise.

Eq. (6) can be solved directly to obtain the best value for the bias vector $\underset{\sim}{B}$.

General Description of the Iterative Solution

Eq. (6) is nonlinear in $\underset{\sim}{B}$ and must be solved iteratively. The zero-th order (trial) solution to Eq. (6), is obtained by dropping the nonlinear terms in comparison to the linear terms. This approximation is valid only when the bias is small in comparison with the actual magnetic field. This point is not critical, as the iteration scheme constructs an accurate solution even when the trial solution is not close to the true solution. This will be discussed in more detail in the treatment of the numerical example.

The trial solution is given by

$$\underset{\sim}{B}^{(0)} = G^{-1}\underset{\sim}{b} \tag{9}$$

where G^{-1} = inverse of the matrix G

$\underset{\sim}{B}^{(0)}$ = trial solution

This solution may be iterated as

$$\underset{\sim}{B}^{(j)} = \underset{\sim}{B}^{(0)} + G^{-1}\underset{\sim}{F}(\underset{\sim}{B}^{(j-1)}) \qquad j \geq 1 \tag{10}$$

The iteration continues until

$$\left| \frac{B_k^{(j)} - B_k^{(j-1)}}{B_k^{(j)}} \right| < \varepsilon \tag{11}$$

where ε = some arbitrarily small value depending on the accuracy desired.

Numerical Examples

The AMPTE engineering data simulator[2] was used to generate biased magnetometer data for the purpose of investigating the convergence properties of the iterative solution. Two cases were considered:

$$B/H \ll 1$$

and

$$B/H \gg 1$$

The first case considered was $B/H \ll 1$; in this case, 200 data points were used in the calculation. Data at the perigee point, at which the magnetic field attains its maximum value, was included. The magnetic field can be resolved into a component along the AMPTE spin axis, $H_{\parallel}$, and a component perpendicular to the spin axis, $H_{\perp}$. The maximum or perigee values for these components are $H_{\perp}^{MAX}$ = 240 milligauss (mG) and $H_{\parallel}^{MAX}$ = 90 mG. The input biases were chosen to be 5 mG, 10 mG, and 15 mG along the x, y, and z axes, respectively. The results of the bias determination calculation are shown in Table 1 taken from Reference 3. Rapid convergence and very high accuracy is obtained. The trial solution $B^{(0)}$ (iteration 0) initially was not accurate in the y component and needed to be iterated to obtain satisfactory results. Investigation of the case in which $B \gg H$ used a subset of the data used in the first test. Here, 100 data points well outside the perigee region were used. For this test, $H_{\perp}^{MAX}$ = 5 mG and $H_{\parallel}^{MAX}$ = 2 mG. As before, the input biases are 5 mG, 10 mG, and 15 mG. These results[3] are presented in Table 2. In this case, convergence is very slow and incomplete. Improved convergence cannot necessarily be obtained by using standard Newton-Raphson techniques.

ITERATION NUMBER	LOSS FUNCTION	B_x (mG)	B_y (mG)	B_z (mG)
0	54621.0	5.00288	12.0278	15.0213
1	5153.0	4.98344	9.38109	14.9473
2	370.0	5.00481	10.1647	15.0152
3	29.0	4.99870	9.95352	14.9959
4	2.0	5.00037	10.0128	15.0012
5	0.2	4.99990	9.99635	14.9997
6	0.01	5.00003	10.0009	15.0001

Table 1

Bias Determination Calculation for $B/H \ll 1$

ITERATION NUMBER	LOSS FUNCTION	B_x (mG)	B_y (mG)	B_z (mG)
0	24100.0	1.8	2.8	5.3
10	1460.0	3.7	5.5	11.0
20	501.0	4.1	6.1	12.4
30	240.0	4.4	6.3	13.1
40	133.0	4.5	6.5	13.6
50	81.0	4.6	6.6	13.9

Table 2

Bias Determination Calculation for $B/H \gg 1$

III - Spin-Axis Attitude Determination

Once the magnetometer biases have been chosen properly, data from the Sun sensor and the magnetometers may be used to determine the spin-axis attitude. It is assumed that the spin axis is not varying over the data interval examined.

The spin axis is denoted by $\hat{\underset{\sim}{a}}$. The data are

$\beta(i)$ = measured Sun angle at time i, $i=1,\ldots,N_S$

$\underset{\sim}{M}(i)$ = measured magnetic field at time i, $i=1,\ldots,N_M$

$\hat{\underset{\sim}{S}}(i)$ = (true) Sun vector in GCI at time i, measured from the spacecraft to the sun, $i=1,\ldots,N_S$

$\underset{\sim}{H}(i)$ = (true) geomagnetic field at time i, $i=1,\ldots,N_M$

Note that there will be no requirement of simultaneous Sun-sensor and magnetometer data.

The spin-axis (attitude) vector, $\hat{\underset{\sim}{a}}$, is subject to the following constraint:

$$\hat{\underset{\sim}{a}}\cdot\hat{\underset{\sim}{a}} = 1 \tag{12}$$

The spin-axis vector is chosen to minimize the following loss function:

$$L(\hat{\underset{\sim}{a}}) = \frac{1}{2}\sum_{i=1}^{N_S} \omega_S(i)\left|\hat{\underset{\sim}{a}}\cdot\hat{\underset{\sim}{S}}(i) - \cos\beta(i)\right|^2 \tag{13}$$

$$+ \frac{1}{2}\sum_{i=1}^{N_M} \omega_M(i)\left|\hat{\underset{\sim}{a}}\cdot\hat{\underset{\sim}{M}}(i) - \cos\eta(i)\right|^2 - \frac{1}{2}\lambda\,\hat{\underset{\sim}{a}}\cdot\hat{\underset{\sim}{a}}$$

where

λ = Lagrange multiplier chosen to satisfy the constraint equation

$\omega_S(i)$ = weight assigned to the jth magnetic field measurement

$\omega_M(j)$ = weight assigned to the jth magnetic field measurement

The quantity η is the angle between the geomagnetic field and the spacecraft spin axis given by

$$\eta = \cos^{-1}(M_y/|\underset{\sim}{M}|) \tag{14}$$

The weights are normalized to unity

$$\sum_{i=1}^{N_S} \omega_S(i) + \sum_{i=1}^{N_M} \omega_M(i) = 1 \tag{15}$$

The spin-axis vector $\hat{\underset{\sim}{a}}$ is chosen to minimize the loss function

$$\frac{\partial L(\hat{\underset{\sim}{a}})}{\partial a_m} = 0 \tag{16}$$

The derivative of the loss function is given by

$$\frac{\partial L}{\partial a_m} = \sum_{i=1}^{N_S} \omega_S(i)\,(\hat{\underset{\sim}{a}}\cdot\hat{\underset{\sim}{S}}(i) - \cos\beta(i))\,S_m(i) \tag{17}$$

$$+ \sum_{i=1}^{N_M} \omega_M(i)\,(\hat{\underset{\sim}{a}}\cdot\hat{\underset{\sim}{M}}(i) - \cos\eta(i))\,M_m(i) - \lambda a_m .$$

The solution to Eq. (16) may now be written as:

$$\sum_{k=1}^{3} (A_{mk} - \lambda\delta_{mk})a_k = b_m \tag{18}$$

where

$$A_{mk} = \langle S_m S_k \rangle_S + \langle M_m M_k \rangle_M \tag{19a}$$

$$b_m = \langle \cos \beta \; S_m \rangle_S + \langle \cos \eta \; M_m \rangle_M \tag{19b}$$

and the brackets denote weighted averages over the magnetometer and Sun data. That is,

$$\langle C_j \rangle_S \equiv \sum_{i=1}^{N_S} \omega_S(i) \; C_j(i) \tag{20}$$

Eq. (18) may be written in matrix notation as

$$(A - \lambda I) \; \underset{\sim}{a} = \underset{\sim}{b} \tag{21}$$

where I is the unit matrix.

Attitude Solution

A general solution to Eqs. (18) and (19) is constructed in this section. The solution to these equations leads to the spin axis attitude in the Geocentric Inertial (GCI) coordinate system. Again an iterative procedure is developed to construct a numerical solution to the equations. An approximate solution to the problem is to take $\lambda = 0$, i.e., to relax the constraint that a be normalized to unity. Given this

approximation, Eq. (18) may be solved to obtain

$$\underset{\sim}{a}^{(0)} = A^{-1}\,\underset{\sim}{b} \tag{22}$$

Note that this vector is not normalized. In practice this solution will be very close to having unit norm since even with $\lambda = 0$, $\hat{\underset{\sim}{a}}$ is overdetermined in general by Eq. (18). Thus, normalizing $\underset{\sim}{a}^{(0)}$ will lead to a very good approximation for $\hat{\underset{\sim}{a}}$ (see Ref. 4). An exact numerical solution is generated by solving for λ iteratively starting with a trial solution $\lambda = 0$ and $\underset{\sim}{a}^{(0)}$ given by Eq. (22).

Define the function $f(\lambda)$ by

$$f(\lambda) = \underset{\sim}{a}(\lambda)\cdot\underset{\sim}{a}(\lambda) - 1 \tag{23}$$

Given the numerical value of $\underset{\sim}{a}(\lambda)$, the Newton-Raphson method is used to determine λ. Differentiating Eq. (23) gives

$$\frac{\partial f}{\partial \lambda} = 2\underset{\sim}{a} \cdot \frac{\partial \underset{\sim}{a}}{\partial \lambda} \tag{24a}$$

and

$$\frac{\partial \underset{\sim}{a}}{\partial \lambda} = (A - \lambda I)^{-1}\,\underset{\sim}{a} \tag{24b}$$

The Newton-Raphson scheme gives

$$\lambda^{(j)} = \lambda^{(j-1)} - \frac{f(\lambda^{(j-1)})}{\frac{\partial f}{\partial \lambda}(\lambda^{(j-1)})} \tag{25a}$$

$$\underset{\sim}{a}^{(j)} = (A - \lambda^{(j)} I)^{-1}\,\underset{\sim}{b} \tag{25b}$$

Numerical Example

The spacecraft orbit in this example is of the AMPTE type, and the Sun and magnetometer data used covered the perigee point. The data is perfect (uncorrupted by random error) as generated by the AMPTE simulator. The "true" value of the right ascension, α, and declination, δ, were chosen to be

$$\alpha = 159.67 \text{ deg} \tag{26a}$$

$$\delta = 0.0 \text{ deg} \tag{26b}$$

The zero-order result as given by Eq. (22) was

$$\alpha = 159.55 \text{ deg} \tag{27a}$$

$$\delta = 0.073 \text{ deg} \tag{27b}$$

in very good agreement. After ten iterations, the values changed only slightly, as expected, namely

$$\alpha = 159.76 \text{ deg} \tag{28a}$$

$$\delta = 0.062 \text{ deg} \tag{28b}$$

IV - Conclusions

Efficient and reliable algorithms have been developed for spin-axis attitude and magnetometer bias determination for the AMPTE spacecraft. Using simulated numerical data it was demonstrated that the methods work well for AMPTE mission parameters. The present work does not address problems associated with noise, data rate, sensor misalignments and etc. These problems were investigated in references (3) and (5).

Acknowledgement

This work was performed while the authors were employed by the Attitude Systems Operation of the Computer Sciences Corporation. They wish to thank their colleagues there for numerous interesting discussions over the years. The encouragement and support of Roger D. Werking of the Attitude Determination and Control Section of NASA Goddard Space Flight Center is gratefully acknowledged.

References

1. Ousley, G., "Execution Phase Project Plan for Active Magnetospheric Particle Tracer Explorer (AMPTE)," NASA, August 1980.

2. Thompson, R., and Neal G., "Active Magnetospheric Particle Tracer Explorer (AMPTE) Engineering Data Simulator Description and User's Guide," Computer Sciences Corporation, CSC/TM-81/6069, April 1981.

3. Neal, G., and Thompson, R., "Inflight Estimation of Magnetometer Biases for the AMPTE Mission," Computer Sciences Corporation, CSC/TM-81/6070, May, 1981.

4. Shuster, M.D., "Efficient Algorithms for Spin-Axis Attitude Estimation," Flight Mechanics/Estimation Theory Symposium, NASA Goddard Space Flight Center, Greenbelt, Md., October 1981.

5. Thompson, R., and Neal, G., "Spin-Axis Attitude Determination Under Conditions of the AMPTE Mission," Computer Sciences Corporation, CSC/TM-81/6093, June 1981.

A MATHEMATICAL MODEL OF LANDSAT-D ATTITUDE DYNAMICS WITH INTERNAL MOTION

S. D. Oh, G. W. Abshire, and J. M. Buckley

Computer Sciences Corporation, Silver Spring, MD

ABSTRACT

An algorithm to model the effects of internal motion by the solar array and the high-gain antenna on the attitude of the Landsat-D spacecraft is presented here. The relative torque and angular momenta arising from the internal motions are assumed to be attitude-independent but are considered to be a source of attitude perturbations. The equation of motion for the three-body problem is derived and then compared with the one-body case. The effect of the internal motion on the control of the spacecraft is shown in a computer study of the problem.

1. INTRODUCTION

The paper presents algorithms for modeling the effects of internally moving parts on the attitude of the Landsat-D (LSD) spacecraft. The internal motions considered here include the rotations of the solar array to follow the Sun and the gimballed high-gain antenna to communicate with the Tracking and Data Relay Satellite (TDRS) (Reference 1). The LSD system is treated as a rigid three-body system for describing the equation of motion. Modeling the disturbance torques produced by moving appendages is very important for missions such as Landsat-D, which require accurate knowledge of the attitude and precise control of the spacecraft.

The relative torques and angular momenta arising from the internal motions are considered as attitude-independent variables and as a source of attitude perturbations. The

external disturbance torques and the angular momenta caused by the internal motions are generated in a profile program (called PROFILE) on an IBM S/360-95 computer, where null attitudes are assumed and are transmitted to a truth model on a DEC PDP-11/70 computer that simulates the effects on the attitude.

In this discussion, nonstandard rotations such as a 45-degree slew of the solar array to avoid interference with the antenna and the switching motion of the antenna from one TDRS to another are neglected. In addition to the rotational motions of the solar array and the antenna, the LSD spacecraft contains moving parts such as the thematic mapper and multispectral scanner (Reference 2). However, these motions are disregarded here because the motions are oscillatory with a high frequency (≈7 Hertz) and because they generate zero average angular momenta.

Section 2 discusses the mathematical derivations of the equation of motion and pertinent terms such as the moment of inertia (MOI) tensor and the center of mass (CM). When possible, these terms are compared with the form for the one-body system used by the Multimission Modular Spacecraft (MMS)/Solar Maximum Mission (SMM) spacecraft. Section 3 provides simulation results to compare the three-body and one-body cases. Conclusions resulting from the study are presented in Section 4.

2. ANALYTICAL CONSIDERATIONS

This section presents the mathematical modeling to describe the dynamic effects of the moving parts on the motion of the spacecraft. The equation of motion for the LSD mission is referenced at the CM of the entire system but is represented in a coordinate system that is fixed in the main vehicle. The CM of the entire system is calculated as a function of time. The MOI tensors for the moving parts are reevaluated

with respect to a set of time-independent axes parallel to a set in the main vehicle. Also calculated are the angular velocity of the appendages and the perturbation in the external torques due to the changing positions of the appendages. A comparison with the one-body problem is made.

2.1 COORDINATE SYSTEMS AND TRANSFORMATIONS MATRICES

The system under consideration, shown in Figure 1, consists of the main carrier vehicle, designated as body B_o, and n(=2) moving bodies B_j (j=1, n). Several coordinate systems are convenient for discussing the relative motions. These are as follows:

- Geocentric Inertial Coordinate System (GCI) (Reference 3)
- Orbit-Defined Coordinate System (OCS) where X (roll) is nearly along the spacecraft velocity vector, Y (pitch) is along the orbit normal vector, and Z (yaw) is along the nadir vector
- Spacecraft-Fixed Coordinate System (BCS), which is fixed in the main vehicle B_o
- Coordinate systems fixed in moving parts such as in the solar array (SACS) or in the high-gain antenna (ANTCS)

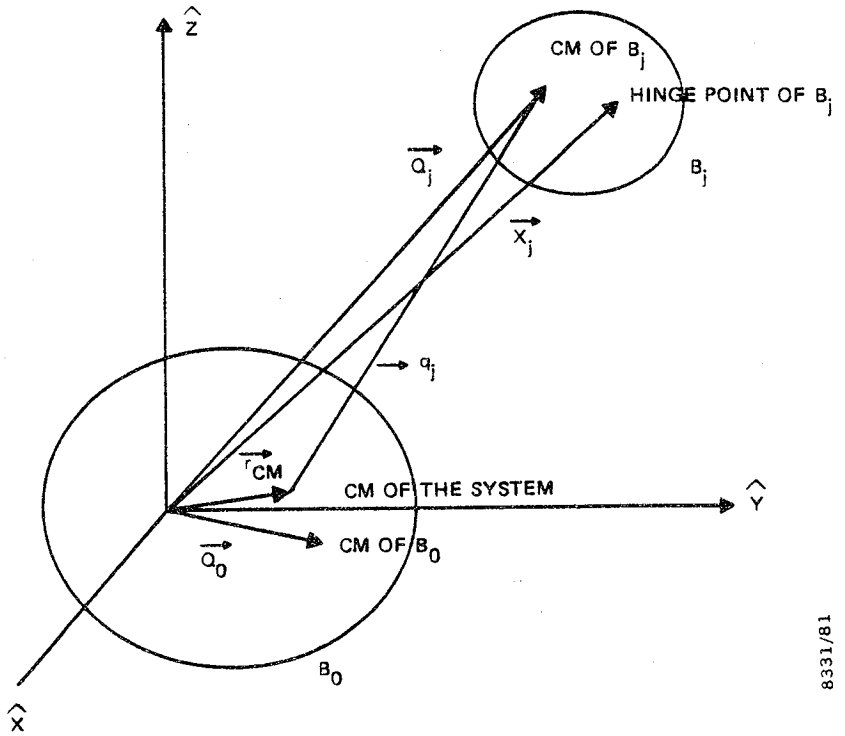

NOTE:
- $\vec{Q}_j$ = the CM of B_j
- $\vec{r}_{CM}$ = the CM of the entire system
- $\vec{q}_j$ = the CM of B_j from $\vec{r}_{CM}$
- $\vec{X}_j$ = the hinge point of B_j
- $\vec{\omega}_j$ = the angular velocity of B_j in inertial space
- $\vec{\omega}'_j$ = the angular velocity of B_j relative to the main body B_0 ($\vec{\omega}_j = \vec{\omega}_0 + \vec{\omega}'_j$)

Figure 1. Partitioning of the Satellite Into Main Body and Moving Parts

The transformation matrices (TRMA) to be used in this paper are defined as follows:

1. TRMA from GCI to OCS : [O]

$$[O] = \begin{bmatrix} \dfrac{(\hat{R}_I \times \hat{V}_I) \times \hat{R}_I}{\left|\hat{R}_I \times \hat{V}_I\right|} \\ \hline \dfrac{\hat{R}_I \times \hat{V}_I}{\left|\hat{R}_I \times \hat{V}_I\right|} \\ \hline \hat{R}_I \end{bmatrix} \tag{2-1}$$

where $\hat{R}_I$ and $\hat{V}_I$ denote the spacecraft position relative to the Earth and velocity unit vectors in the GCI frame, respectively.

2. Attitude direction cosine matrix from the OCS to the BCS : [A]. In the PROFILE Program [A] is given by the identity matrix because null attitudes are assumed. In the truth model, it is represented as

$$[A] = \begin{bmatrix} 1 & y & -p \\ -y & 1 & r \\ p & -r & 1 \end{bmatrix} \tag{2-2}$$

using the small angle approximation, which is sufficient and valid, since only small perturbations are assumed; r, p, and y denote roll, pitch, and yaw angles in radian units, respectively.

3. TRMA from BCS to SACS : $[C^{(SA)}]$. The solar array rotates around the $\hat{y}$-axis and is driven to follow the Sun. Thus, its orientation is determined from the Sunline angle α

$$[C^{(SA)}] = [\alpha]_y = \begin{bmatrix} \cos\alpha & 0 & -\sin\alpha \\ 0 & 1 & 0 \\ \sin\alpha & 0 & \cos\alpha \end{bmatrix} \tag{2-3}$$

Given the Sun unit vector, $\hat{S} = (S_x, S_y, S_z)^T$, in the BCS, the rotation angle α is given by

$$\alpha = \tan^{-1}\left(\frac{S_x}{S_z}\right) \tag{2-4}$$

because the Sun vector is perpendicular to the $\hat{x}$-axis of the SACS.

4. TRMA from BCS to ANTCS : $[C^{(ANT)}]$. The antenna has two gimbals with the inner gimbal angle, g_2, representing the elevation angle and the outer gimbal angle, g_1, representing the azimuth angle. The orientation of the antenna is determined from the gimbal angles

$$\begin{aligned}[C^{(ANT)}] &= [g_2]_y [g_1]_z \\ &= \begin{bmatrix} \cos g_1 \cos g_2 & \sin g_1 \cos g_2 & -\sin g_2 \\ -\sin g_1 & \cos g_1 & 0 \\ \cos g_1 \sin g_2 & \sin g_1 \sin g_2 & \cos g_2 \end{bmatrix}\end{aligned} \tag{2-5}$$

The unit vector pointing from the spacecraft to TDRS is represented by $\hat{P}$ where $\hat{P} = (P_x, P_y, P_z)^T$ in the BCS.

The gimbal angles are thus given by

$$g_1 = \tan^{-1} (P_y/P_x) \tag{2-6a}$$

and

$$g_2 = -\sin^{-1} P_z \tag{2-6b}$$

since g_1, g_2 should align the antenna boresight (the $\hat{x}$-axis in ANTCS) with the normalized pointing vector $\hat{P}$. ($\hat{P}$ can be obtained from the spacecraft and TDRS ephemerides.)

2.2 ANGULAR VELOCITY OF MOVING PARTS

The angular velocity of the moving parts is used to calculate the internal angular momentum of the spacecraft for use in the equation of motion. It is easily seen from Equation (2-3) that the angular velocity of the solar array is as follows:

$$\vec{\omega}'_{SA} = \frac{d\alpha}{dt} \hat{y} \tag{2-7a}$$

The time derivative of the rotation angle α can be computed numerically

$$\frac{d\alpha}{dt} = \frac{\alpha(t) - \alpha(t - \Delta t)}{\Delta t} \tag{2-7b}$$

Using Equation (2-5) the angular velocity of the high-gain antenna is

$$\vec{\omega}'_{ANT} = \frac{dg_1}{dt}\,\hat{z} + \frac{dg_2}{dt}\,\left[g_1\right]_z\,\hat{y} = \begin{pmatrix} \sin g_1 & \frac{dg_2}{dt} \\ \cos g_1 & \frac{dg_2}{dt} \\ & \frac{dg_1}{dt} \end{pmatrix} \qquad (2\text{-}8a)$$

where

$$\frac{dg_i}{dt} = \frac{g_i(t) - g_i(t - \Delta t)}{\Delta t} \qquad (2\text{-}8b)$$

For SMM, the angular velocity of the moving parts was not calculated.

2.3 CENTER OF MASS

For LSD, the CM of appendage B_j in the BCS is given by

$$\vec{Q}_j(t) = \left[C^{(j)}(t)\right]^T (\vec{Q}_{j0} - \vec{X}_j) + \vec{X}_j \qquad (2\text{-}9)$$

where $\vec{Q}_{j0}$ represents the CM of B_j at the initial time (see Figure 1). The rotation (or hinge) point is denoted by $\vec{X}_j$ and $\vec{Q}_{j0} - \vec{X}_j$ represents the CM of B_j from the hinge point at the initial time. Then, at any later time, the CM will be represented by the first term of the right-hand side of Equation (2-9). The CM of each appendage changes as a function of time because the high-gain antenna rotates to track the TDRS, and the solar array rotates to track the

Sun. Consequently, the CM of the system, $\vec{r}_{CM}$, changes in time and is represented by

$$\vec{r}_{CM}(t) = \sum_{r=0}^{n} M_r \vec{Q}_r(t) \Big/ \sum_{r=0}^{n} M_r \qquad (2\text{-}10a)$$

and the position of the CM of each appendage with respect to the CM of the system is

$$\vec{q}_j(t) = \vec{Q}_j(t) - \vec{r}_{CM}(t) \qquad (2\text{-}10b)$$

For SMM, the CM of the system was fixed in time in the BCS.

2.4 MOMENT OF INERTIA TENSOR OF THE SYSTEM

The MOI of the system, $[I_T]$, relative to axes parallel to the BCS axes passing through r_{CM} is expressed by

$$[I_T(t)]_{lm} = \sum_{r=0}^{n} \int dm_r \left\{ [\vec{q}_r(t) + \vec{\rho}_r]^2 \ \delta_{lm} - [\vec{q}_r(t) + \rho_r]_l \ [\vec{q}_r(t) + \rho_r]_m \right\} \qquad (2\text{-}11)$$

where $\vec{\rho}_r$ is the position vector of the mass dm_r of body B_r relative to the CM of B_r and the subscripts l and m represent the l and m components of the vector or tensor. Note that because $\vec{q}_r$ is time-dependent, $[I_T]_{lm}$ is also dependent on time; in the remainder of this paper, the explicit time-dependence will be dropped.

The above equation can be written as

$$[I_T]_{lm} = \sum_{r=0}^{n} \left\{ M_r \left[q_r^2 \delta_{lm} - (q_r)_l \, (q_r)_m \right] + \left[\tilde{I}^{(r)} \right]_{lm} \right\} \quad (2\text{-}12)$$

since

$$\int dm_r \, \vec{\rho}_r = 0$$

$[\tilde{I}^{(r)}]$ is the MOI tensor of B_r represented in the BCS frame but relative to the CM of B_r:

$$[\tilde{I}^{(r)}] = [C^{(r)}]^T \, [I^{(r)}] \, [C^{(r)}] \quad (2\text{-}13)$$

where $[I^{(r)}]$ is the MOI of B_r represented in the coordinate system fixed in B_r. Equation (2-12) can be simply reexpressed by

$$[I_T] = \sum_{r=0}^{n} [J^{(r)}] \quad (2\text{-}14)$$

with

$$\left[J^{(r)} \right]_{lm} = \left[\tilde{I}^{(r)} \right]_{lm} + M_r \left\{ q_r^2 \delta_{lm} - (q_r)_l \, (q_r)_m \right\} \quad (2\text{-}15)$$

For the one-body problem, as represented by SMM, I is defined to be a constant in time.

2.5 EXTERNAL TORQUES

Two external torques are discussed: the gravity gradient torque and the aerodynamic torque. The solar radiation

torque is similar to the aerodynamic torque, and the other external torques are not sensitive to the three-body problem.

The gravity gradient torque, N_{GG}, can be computed by

$$\vec{N}_{GG} = -\mu \sum_{r=0}^{n} \int (\vec{q}_r + \vec{\rho}_r) \times \frac{\vec{R} + \vec{\rho}_r + \vec{q}_r}{|\vec{R} + \vec{\rho}_r + \vec{q}_r|^3} \, dm_r \qquad (2\text{-}16)$$

where μ is the Earth gravitational constant ($\approx 3.986005 \times 10^{14}$ m^3/sec^2). $\vec{R}$ is the spacecraft position vector from the Earth. Considering that $|\vec{R}| >> |\vec{q}_r + \vec{\rho}_r|$, $\vec{N}_{GG}$ is simply,

$$\begin{aligned}
\vec{N}_{GG} &= \frac{3\mu}{R^3} \sum_{r=0}^{n} \int dm_r (\vec{q}_r + \vec{\rho}_r) \times \hat{R}\left[\hat{R} \cdot (\vec{q}_r + \vec{\rho}_r)\right] \\
&= \frac{3\mu}{R^3} \sum_{r=0}^{n} \left\{ M_r \, \hat{q}_r \times \hat{R}(\hat{q}_r \cdot \hat{R}) + \hat{R} \times [\tilde{I}^{(r)}] \, \hat{R} \right\} \qquad (2\text{-}17) \\
&= \frac{3\mu}{R^3} \sum_{r=0}^{n} \hat{R} \times [J^{(r)}] \, \hat{R} \\
&= \frac{3\mu}{R^3} \hat{R} \times [I_T] \, \hat{R}
\end{aligned}$$

The expression for the one-body system has the same form except for the replacement of $[I_T]$ by the constant $[I]$.

To simplify the calculation of the solar radiation and aerodynamic torques, the LSD spacecraft is modeled as an assembly of a cylinder for the main vehicle, flat plates for the solar array panels, and a sphere for the antenna. Only the aerodynamic torque is discussed here because the modifications to the center of pressure (CP) are common in solar radiation and aerodynamic torques.

The aerodynamic torque, $\vec{N}_{aero}$, is

$$\vec{N}_{aero} = -\frac{1}{2} C_D \rho v^2 \sum_{i=1}^{8} \int \hat{n}_i \cdot \hat{v}(\vec{q}_{cp,i} \times \hat{v}) \, dA_i \qquad (2\text{-}18)$$

Here, $\hat{v}$ denotes the spacecraft velocity unit vector, $\hat{n}_i$ denotes the normal unit vector for the ith surface, $\vec{q}_{cp,i}$ denotes the CP of the ith surface from $\vec{r}_{CM}$, ρ denotes the atmospheric density, and C_D denotes the drag coefficient. The normal vectors, $\hat{n}_i$, for the solar array and antenna surfaces are dependent on time by

$$\hat{n}_i = \left[C^{(i)}\right]^T \hat{n}_{io} \qquad (2\text{-}19)$$

where $\hat{n}_{io}$ represents the initial normal vector for the ith surface. $\vec{q}_{cp,i}$ for the solar array and antenna are computed by

$$\vec{q}_{cp,i} = \vec{Q}_{cp,i} - \vec{r}_{CM} \qquad (2\text{-}20)$$

with

$$\vec{Q}_{cp,i} = \left[C^{(i)}\right]^T (\vec{Q}_{cp,io} - \vec{X}_i) + \vec{X}_i \qquad (2\text{-}21)$$

More consideration is required to specify $[C^{(i)}]$ for the solar array surfaces that are canted. The transformation matrix from BCS to these surfaces, $[C^{(i)}]$, is given by

$$[C^{(i)}] = [C^{(SA)}] \, [\theta_c]_x \qquad (2\text{-}22)$$

with the canted angle θ_c.

For the one-body case of SMM, n_i and $\vec{q}_{cp,i}$ are constants.

2.6 EQUATION OF MOTION

The equation of motion for the LSD spacecraft is written in the form

$$\frac{d\vec{Y}}{dt} = \vec{f}(\vec{Y}(t),\ t) \tag{2-23}$$

where $\vec{Y} = (q_\mu,\ \vec{L}_T,\ \vec{L}_W)^T$; q_μ ($\mu = 1, 2, 3, 4$) denotes the Euler symmetric parameters representing a rotation from the GCI to the spacecraft-fixed coordinate frame, $\vec{L}_T$ is the total angular momentum of the spacecraft, and $\vec{L}_W$ is the wheel momentum.

The body angular momentum of the main vehicle, $\vec{L}_B$, is given by the total spacecraft angular momentum minus the sum of the wheel momentum, payload momentum, $\vec{L}_R$, and the angular momentum, $\vec{L}_{INT}$, caused by the internal motions

$$\vec{L}_B = \vec{L}_T - \vec{L}_{INT} - \vec{L}_W - \vec{L}_R \tag{2-24}$$

$\vec{L}_B$ depends on the angular velocity of the main vehicle, $\vec{\omega}_0$, and $\vec{L}_{INT}$ depends on the angular velocity of moving parts, $\vec{\omega}'_j$. To formulate these mathematically, the angular momentum of the total system, $\vec{L}_T$, ignoring wheel and payload momenta, is considered

$$\begin{aligned}
\vec{L}'_T &= \vec{L}_B + \vec{L}_{INT} \\
&= \sum_{r=0}^{n} \int (\vec{q}_r + \vec{\rho}_r) \times (\dot{\vec{q}}_r \times \dot{\vec{\rho}}_r)\, dm_r \\
&= \sum_{r=0}^{n} \left\{ M_r\, \vec{q}_r \times \dot{\vec{q}}_r + [\tilde{I}^{(r)}]\ (\vec{\omega}_o + \vec{\omega}'_r) \right\}
\end{aligned} \tag{2-25}$$

With some computation, L_T' can be shown as

$$\vec{L}_T' = [I_T]\ \vec{\omega}_o + \sum_{r=0}^{n} \left\{ [J^{(r)}] + [K^{(r)}]\ \vec{\omega}_r' \right\} \qquad (2\text{-}26)$$

where

$$[K^{(r)}]_{lm} = M_r \left\{ \vec{q}_r \cdot (\vec{r}_{CM} - \vec{X}_r)\ \delta_{lm} - (\vec{r}_{CM} - \vec{X}_r)_l\ q_m \right\}$$

Thus, the body rate of the main carrier is simply

$$\vec{\omega}_o = [I_T]^{-1}\ \vec{L}_B \qquad (2\text{-}27)$$

and $\vec{L}_{INT}$ caused by the internal motion, is

$$\vec{L}_{INT} = \sum_{r=1}^{n} \left\{ [J^{(r)}] + [K^{(r)}]\ \vec{\omega}_r' \right\} \qquad (2\text{-}28)$$

The time derivatives of the Euler symmetric parameter, q_μ, can be obtained as

$$\frac{dq_\mu}{dt} = \frac{1}{2}\ [\Omega(\vec{\omega}_o)]_{\mu\nu}\ q_\nu \qquad (2\text{-}29)$$

with

$$[\Omega(\vec{\omega})] = \begin{bmatrix} 0 & \omega_3 & -\omega_2 & \omega_1 \\ -\omega_3 & 0 & \omega_1 & \omega_2 \\ \omega_2 & -\omega_1 & 0 & \omega_3 \\ -\omega_1 & -\omega_2 & -\omega_3 & \omega_4 \end{bmatrix} \qquad (2\text{-}30)$$

The time derivative of the total angular momentum of the spacecraft is given by the Euler equation as

$$\frac{d\vec{L}_T}{dt} = \vec{N}_{ext} + \vec{L}_T \times \vec{\omega}_o \qquad (2\text{-}31)$$

For SMM, the body angular momenta, $\vec{L}_B$, is given by

$$\vec{L}_B = \vec{L}_T - \vec{L}_W - \vec{L}_R \qquad (2\text{-}32)$$

with the payload momentum $\vec{L}_R$. The spacecraft body rate, $\vec{\omega}$, is determined by

$$\vec{\omega} = \begin{pmatrix} \omega_1 \\ \omega_2 \\ \omega_3 \end{pmatrix} = [I]^{-1} \vec{L}_B \qquad (2\text{-}33)$$

where $[I]^{-1}$ is the inverse of the spacecraft MOI tensor. The time derivatives of the Euler symmetric parameters, q_μ, can be obtained as

$$\frac{dq_\mu}{dt} = \frac{1}{2} [\Omega(\vec{\omega})]_{\mu\nu} q_\nu \qquad (2\text{-}34)$$

The time derivatives of the total angular momentum of the spacecraft are given by the Euler equation as

$$\frac{d\vec{L}_T}{dt} = \vec{N}_{ext} + \vec{L}_T \times \vec{\omega} \qquad (2\text{-}35)$$

with the external torque, $\vec{N}_{ext}$.

3. SIMULATION RESULTS

A computer study of the effect of the three-body problem on the motion of the spacecraft has been made using the general equations derived here. Since the spacecraft is subject to noticeable external torques, a control law that provides compensatory torques was necessary to keep the spacecraft near null attitude. The one-body case, using the same control law, was also studied.

The roll, pitch, and yaw of the spacecraft main carrier for both cases is shown in Figures 2 through 4. The results of the three-body case are represented by the "X" points and the results of the one-body case are shown as open circles. Note that both cases are subject to the same control law. This control law attempts to make the pitch, roll, and yaw zero and to bring the spacecraft rate to null. This control law is the same one (Reference 4) that Landsat-D will use during its acquisition phases. The torque applied to each reaction wheel is as follows:

for the roll axis,

$$T_r = K_r(k_r \Delta r + \omega_r) \tag{3-1a}$$

for the pitch axis,

$$T_p = K_p\ [k_p(\Delta p + B) + \omega_p] \tag{3-1b}$$

and for the yaw axis,

$$T_y = K_y\ [\omega_y - k\ k_y\ \omega_r] \tag{3-1c}$$

where Δr and Δp are the roll and pitch attitude errors as determined by an Earth sensor; K_r, K_p, K_y, k_r, k_p, k_y, and k

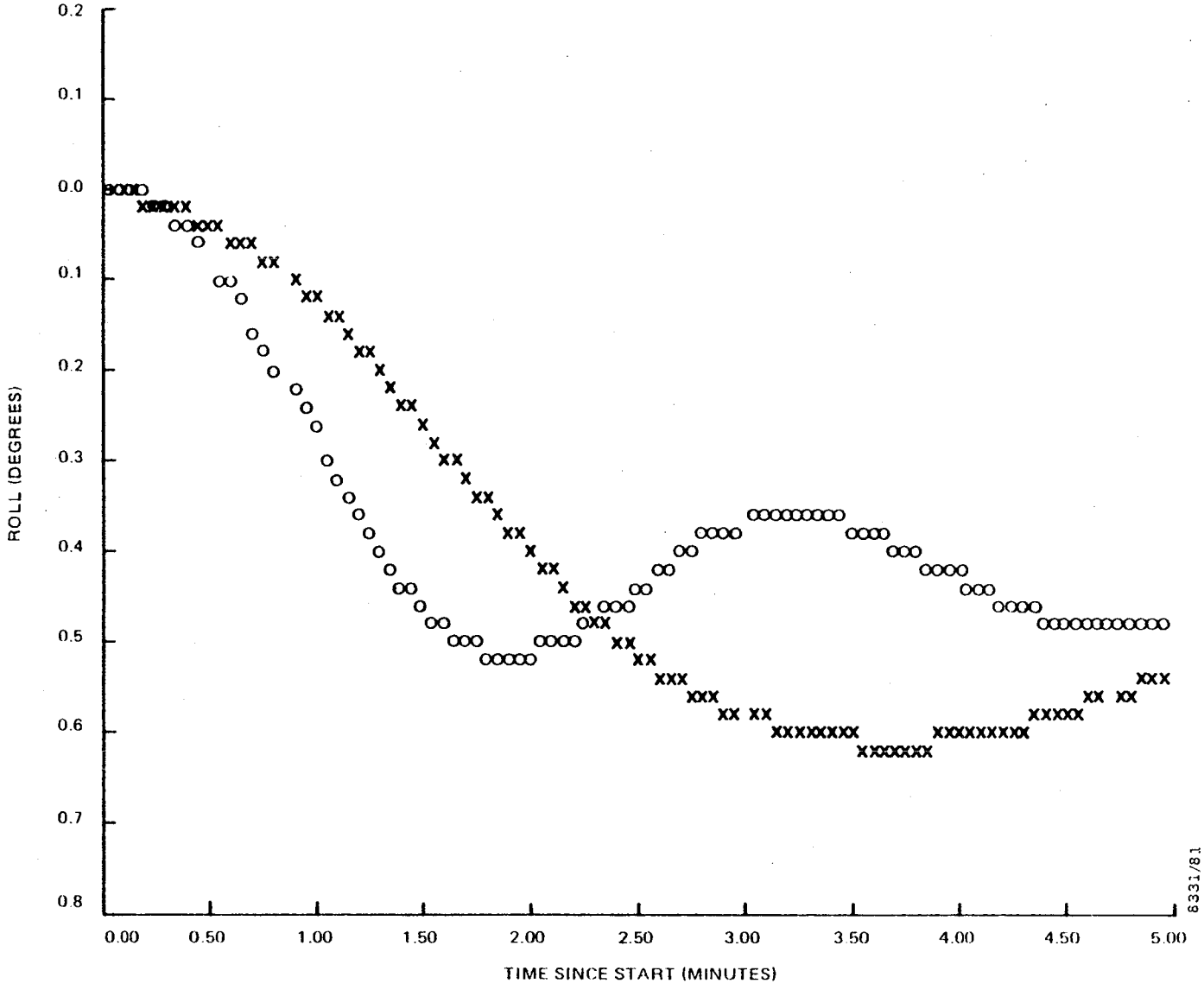

Figure 2. Spacecraft Roll Versus Time

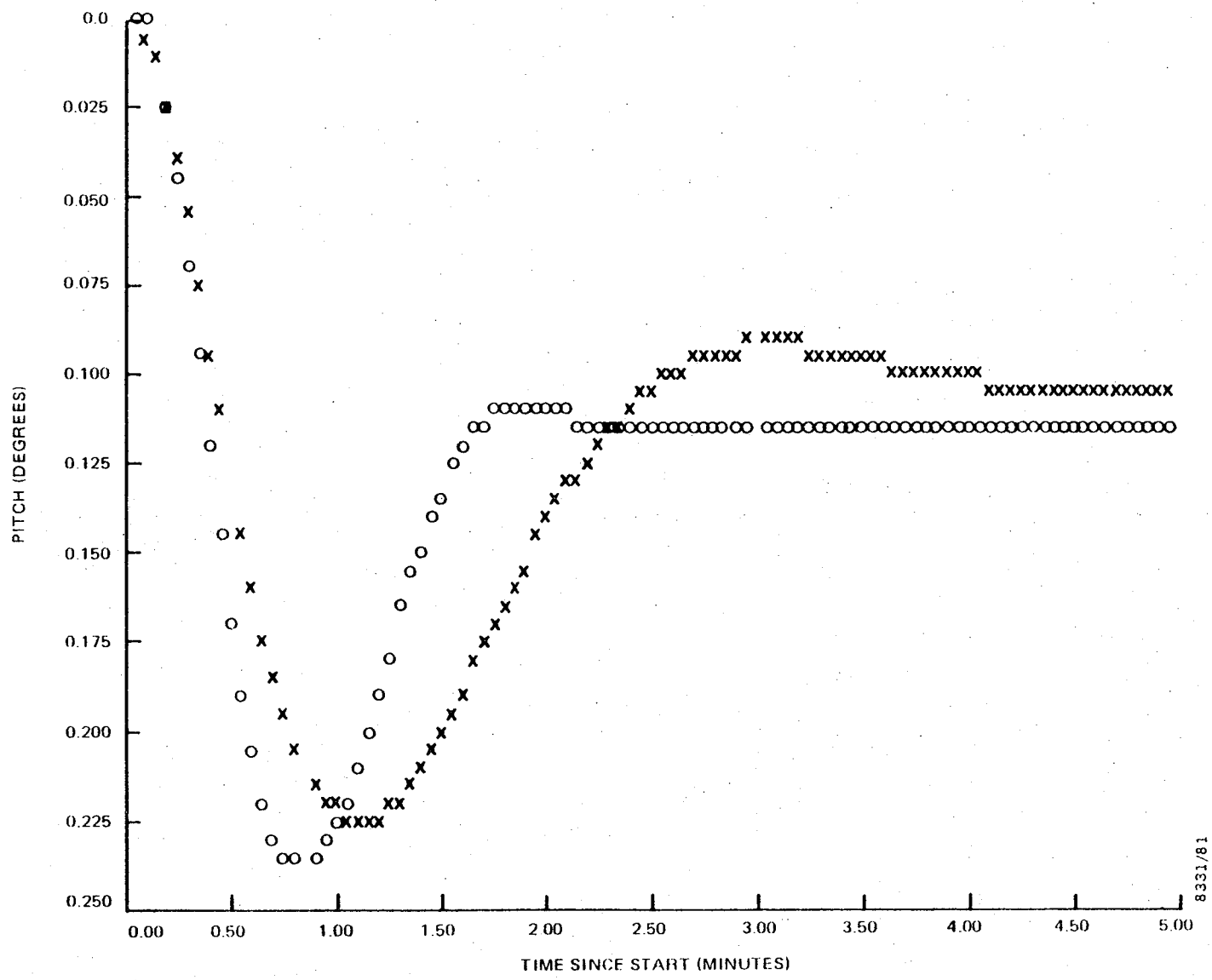

Figure 3. Spacecraft Pitch Versus Time

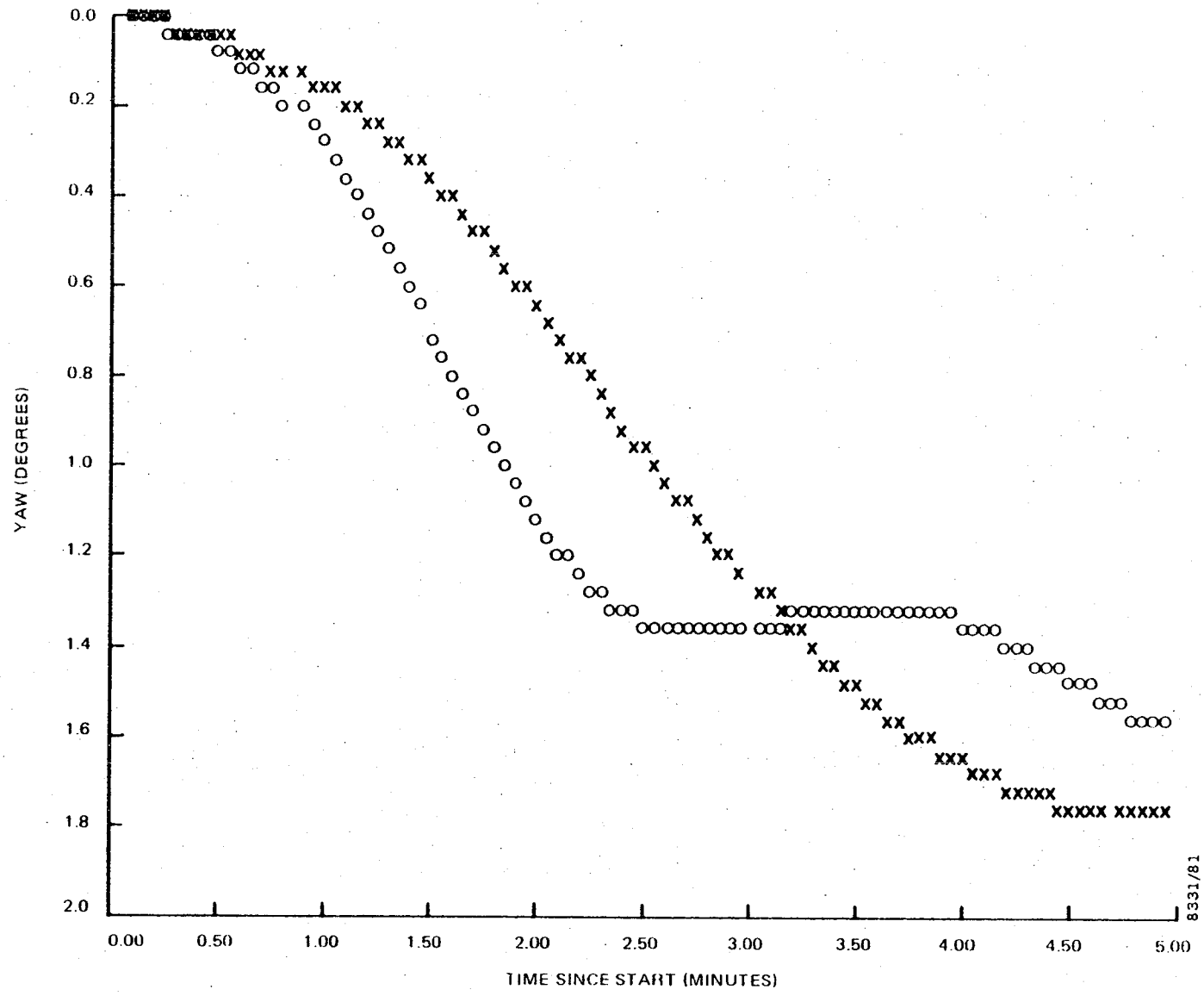

Figure 4. Spacecraft Yaw Versus Time

are constants; B is a bias to compensate for the orbital rotation; and ω_r, ω_p, and ω_y are the angular velocity along the roll, pitch, and yaw data. Because of the values used for k_r, k_p, and k_y, the control law is much more sensitive to the spacecraft rate than to the attitude error.

Most of the structure seen in the plots is a result of the control law. However, since the control law is the same, the differences in the plots are a result of the three-body problem. Note in Figure 2 that after 4.5 minutes the control law has the roll rate to zero for the one-body problem but not the three-body problem. Likewise, after 2.5 minutes, the pitch rate of the one-body problem is under control.

4. CONCLUSIONS

The conversion of the rigid one-body problem to the three-body problem has added another dimension to the study of dynamics. Although the exact perturbations in motion are obscured by the control law used, the effects are still important in control of the spacecraft.

The algorithms used in this paper can be applied to other spacecraft such as the Space Telescope to study important low-frequency effects, as in this paper, and also higher frequency effects that will cause jitter.

REFERENCES

1. General Electric, Landsat-D Flight Software Requirements Specification, December 1979

2. --, Landsat-D Jitter Review, May 1980

3. Computer Sciences Corporation, CSC/SD-79/6080, Solar Maximum Mission (SMM) Truth Model Attitude Simulator Algorithm Description and Operating Guide, F. E. Baginski and R. E. Galasso, June 1979

4. General Electric, PIR-1D50-LSD-714, Earth Acquisition and Pointing with the Earth Sensor Assembly, R. Wolfgang, October 1980

SPACECRAFT ATTITUDE POINTING PERFORMANCE DURING ORBIT ADJUST AS A FUNCTION OF COMPENSATOR ORDER

S. Basuthakur, R. Duelfer, A. Peckjian and T. Stick
General Electric Company
Space Systems Division
Control Systems Engineering Department
Building 100, Room U7025
P. O. Box - 8555
Philadelphia, PA 19101

SPACECRAFT ATTITUDE POINTING PERFORMANCE DURING ORBIT ADJUST AS A FUNCTION OF COMPENSATOR ORDER

For many communication satellite missions, it is required that the control system performance during velocity adjust mode does not degrade appreciably from the nominal pointing requirement. During velocity adjust, many factors contribute to the development of disturbance torques that exceed the capacity of the reaction wheels. This necessitates the use of thrusters to provide the control torques. The spacecraft weight constraints force the use of off-pulsing techniques. While off-pulsing the orbit adjust thrusters may eliminate propellant penalties, it also introduces additional disturbances. The thruster plume impingement torques increase dramatically when the balancing effect of both thrusters firing is lost.

In order to meet the attitude pointing error requirements under a set of constraints outlined above, a steady state compensator of specified order is proposed to estimate the required duty cycle needed to balance the disturbance torque. The compensator order has been increased gradually to demonstrate the improvement in pointing accuracy. The basic mathematical model of the flexible spacecraft and sensor used to characterize the performance of the compensator can be described as follows:

$$\dot{\theta}(t) = (\phi_1^2 + \phi_2^2)H - 2\xi\omega\phi_2\ \zeta(t) - \omega^2\phi_2\ \psi(t) \tag{1}$$

$$\dot{H}(t) = T_d - T_c \tag{2}$$

$$\dot{\theta}_1(t) = -\frac{1}{T_1}\theta_1(t) + \frac{1}{T_1}\theta(t) \tag{3}$$

$$\dot{\theta}_2(t) = -\frac{1}{T_2}\theta_2(t) + \frac{G}{T_2}\theta_1(t) \tag{4}$$

$$\dot{\psi}(t) = \zeta(t) \tag{5}$$

$$\dot{\zeta}(t) = -2\xi\omega\zeta(t) - \omega^2\psi(t) + \phi_2 H(t) \tag{6}$$

$$\dot{T}_d = 0 \tag{7}$$

$$y(t) = \theta_2(t) + \nu(t) \tag{8}$$

where,

T_1, T_2 = sensor time constant

T_d = disturbance torque

T_c = control torque

θ = spacecraft attitude

θ_1 = sensor output after first break

θ_2 = sensor output after second break

H = the spacecraft momentum

ϕ_1 = spacecraft rigid body admittance = $(\text{Inertia})^{-1/2}$

ϕ_2 = structural admittance at first symmetric (pitch) or asymmetric (roll/yaw) frequency

ξ = structural damping

ω = structural frequency

ζ = modal deflection

ψ = integral of modal deflection

y = noise corrupted sensor measurement

ν = measurement noise

G = sensor gain

The continuous model of the estimator has been represented as

$$\dot{\underline{z}} = F\underline{z} + \underline{h}\, y \tag{9}$$

$$u = -g^T\underline{z} \tag{10}$$

where matrices F, $\underline{h}$ define the compensator structure and g is the feedback gain. The vectors $\underline{z}$ and $\underline{u}$ define the compensator state and the control respectively.

The problem presented in this paper involves estimating the disturbance torque T_d using a compensator of specified order as represented in equations (9) - (10). As a baseline, the compensator is assumed to be a third order to estimate the rigid body position, the momentum and the disturbance torque. The compensator order is gradually increased to estimate the sensor states and the flexible modes. Having specified the dimension of the compensator, the matrices F, h and g have been chosen to minimize the performance criterion involving quadratic function

$$L = \frac{1}{2}\begin{bmatrix} x \\ z \end{bmatrix}^T \begin{bmatrix} Q_x & Q_{xz} \\ Q_{zx} & Q_z \end{bmatrix} \begin{bmatrix} \underline{x} \\ \underline{z} \end{bmatrix} + \frac{1}{2} \quad Ru^2 \qquad (11)$$

The performance criterion for this problem has been chosen as

$$J = \lim_{t \to \infty} E(L)$$

where E (•) denotes expection.

The attitude pointing performance has been documented as a function of the dimension of the compensator. The analysis thus provides a trade-off between increased pointing accuracy and increased complexity in on-board software.

Efficient Algorithms for Single-Axis Attitude Estimation[†]

M.D. Shuster[§]

Business and Technological Systems, Inc.
10210 Greenbelt Road
Seabrook, Maryland 20706

Abstract

Computationally efficient algorithms are presented for determining single-axis attitude from the measurement of arc lengths and dihedral angles. The dependence of these algorithms on the solution of trigonometric equations has been much reduced. Both single-time and batch estimators are presented along with the covariance analysis of each algorithm.

[†]Presented at the Flight Mechanics/Estimation Theory Symposium, NASA Goddard Space Flight Center, Greenbelt, Maryland, October 27-28, 1981.

[§]Staff Scientist, Research and Development Division

I. Introduction

Since nearly every spacecraft is spinning during part of its life--in particular, at the time of orbit injection--spin-axis attitude* estimation is an important segment of almost every mission support operation. Indeed, for spin-stabilized spacecraft there is often no need (or desire) to determine the complete three-axis attitude at every point and, in fact, when accuracy requirements for the spin-axis attitude dictate that many measurements taken at different times be processed simultaneously, the computation of a three-axis attitude may not even be possible.

Very often, three-axis attitude information is definitive data required chiefly by mission scientists and generally processed anytime from several days to several months after the receipt of telemetry. The need for efficient three-axis attitude estimation algorithms in those cases is determined by the definitive data rate. When three-axis attitude information is required in real-time for the purpose of attitude control, this is usually provided on-board by three-axis gyros (e.g. SMM) or on the ground by the spin axis and a third angle, which can be obtained by monitoring some other sensor reading such as IR scanner pitch (e.g. AEM, Magsat).

Spin-axis attitudes by contrast are usually required not only as definitive data but also by the ground support system in near real-time for the purpose of monitoring spacecraft performance and determining large scale attitude maneuvers. Thus, the efficiency of a spin-axis attitude estimation algorithm becomes a factor in the safety and daily operation of the spacecraft.

---

* Since the single-axis attitude of interest is invariably the spin-axis attitude these terms will be used almost interchangeably throughout this work.

While a number of highly-efficient algorithms exist for three-axis attitude estimation,[1] the computation of spin-axis attitude[2] is by comparison very clumsy. This is largely because the computation of three-axis attitude uses complete vector measurements in general and can take advantage of the linear properties of Euclidean three-space. The computation of spin-axis attitude, on the other hand, must rely on incomplete vector information (the measurement of arc lengths and dihedral angles) to determine a quantity (the spin-axis) which is restricted to the surface of a sphere. Thus, while three-axis attitude computations need only execute simple matrix operations, the computation of spin-axis attitude is beset with the burden of solving complex relations from spherical trigonometry.

Since spin-axis attitude is usually not computed frequently, the need for efficient algorithms is not immediate, at least not for ground support systems. The determination of the spin-axis attitude from batch measurements of arc lengths and dihedral angles has become highly standardized and reliable[3] and there is no obvious need to replace this software in normal ground support operations.

The need for more efficient algorithms lies in two areas: 1) the eventual implementation of spin-axis attitude computation in onboard microprocessor-based attitude determination systems; and 2) the computation of spin-axis attitude accuracies, which imposes a far greater computational burden than computing just the attitude due to the greater number of terms and because the computation of the attitude covariance involves implicitly the computation of derivatives of the attitude.

The large computational burden imposed by the need to solve spherical trigonometric equations in the computation of spin-axis attitude covariances is evident in the work of Wertz and Chen,[2,4-6] the most complete and careful work to date. The difficulties which are encountered in this approach are of two kinds: 1) the complexity of the trigonometric relations, themselves, and 2) the fact that for certain

cases the representation of the quantities being calculated becomes indeterminant while the quantities themselves are well defined. This last difficulty is simply a manifestation of the fact that the representation of rotations by Euler angles is sometimes ambiguous and is overcome in the same way, namely, by changing the representation.

The need for computing spin-axis attitude covariance matrices is two-fold. Firstly, it is necessary to be able to assess the accuracy of a spin-axis attitude computation during the spacecraft mission. Secondly, it is important to be able to predict spin-axis attitude accuracies for mission planning, particularly in the determination of launch windows. For an example of launch window computations using the geometrical approach see Chen.[7]

The purpose of the present work is to develop algorithms for computing spin-axis attitude and the associated covariance matrix without relying as heavily as do current methods on the solution of trigonometric equations. A completely vectorial approach is, of course, not possible owing to the nature of the measurements themselves. However, in large degree many of the trigonometric equations can be abandoned with the result that the spin-axis attitude and, particularly, the covariance matrix can be computed more efficiently.

The types of measurements studied here are of two kinds:

measurements of arc length, which will always be the angle between the observed direction and the spin axis.

measurements of dihedral angles, i.e., the angle between two planes, where the line of intersection is assumed to be the spin axis.[8]

Dihedral angles, in general, are measured by observing two crossing times in the spacecraft and multiplying by the angular velocity. Arc

lengths may be measured in a variety of ways, for example, by direct sighting (as of the Sun or a star) or by measuring the component of a vector along the spin axis (e.g., the magnetic field vector). The measurement of the nadir angle is hybrid in that an arc length (the nadir angle) is determined from the measurement of a dihedral angle (the Earth width). It is the measurement of the nadir angle which is the source of most of the computational complexity.

Estimation algorithms may be classified either as deterministic (usually single-frame, i.e., single-time) algorithms, in which a minimal subset of the available data is chosen to compute the spin-axis attitude, or as optimal (batch) algorithms, in which a larger quantity of data is used from which one computes a "best" result. Three cases are treated in this report

1) A deterministic estimator using two arc-length measurements,

2) A deterministic estimator using the measurements of two arc lengths and the included dihedral angle. (Since in this case the spin-axis attitude is over-determined the question of optimality is also discussed.)

3) An optimal batch estimator utilizing any number of measurements of dihedral angles and arc lengths.

In each case the covariance analysis is presented in detail.

In the appendix the measurement of the nadir angle is presented. It is at this point that trigonometric relations cannot be avoided, at least in so far as measuring instruments (horizon scanners) are presently constructed. The treatment is similar to that of Wertz and his collaborators (Ref. 2) but a method is given for avoiding sign ambiguities.

The treatment of single-axis attitude estimation presented here complements that of Wertz. The advantage of Wertz's treatment is that the variances along two great circles of the celestrial sphere intersecting at the direction of the spin axis and the dihedral angle between these two circles (the correlation angle) is given fairly directly. Much less direct is determining the covariance of the spin-axis vector in inertial space. This part of the calculation falls out simply in the present formalism.

The results presented here are quite simple although they do not seem to be generally known. An important result, which is demonstrated here, is that little accuracy is lost by relaxing the constraint in the optimization that the spin-axis vector be a unit vector and then unitizing post hoc. This is responsible for a great deal of simplification of the methods presented here, especially for batch estimation.

II. Single-Frame Spin-Axis Estimation from the Measurement of Two Arc Lengths

Consider the simplest case in which the measured quantities are β, the Sun angle (the angle between the spin axis and the Sun vector), and η, the nadir angle (the direction between the spin axis and the nadir vector). The case where one of these measurements is replaced by the magnetic field angle is analogous.

Let $\hat{\underset{\sim}{S}}$ denote the Sun unit vector, $\hat{\underset{\sim}{E}}$ the nadir vector, and $\hat{\underset{\sim}{n}}$ the spin axis. Then

$$\hat{\underset{\sim}{S}} \cdot \hat{\underset{\sim}{n}} = \cos \beta \equiv c_S \tag{1a}$$

$$\hat{\underset{\sim}{E}} \cdot \hat{\underset{\sim}{n}} = \cos \eta \equiv c_E \tag{1b}$$

The direction of the spin-axis can then be determined simply by using a method that has been published recently by Grubin,[9] though it has been in use since the beginning of the space program and probably has been known for several hundred years.

If $\hat{\underset{\sim}{S}}$ and $\hat{\underset{\sim}{E}}$ are not parallel, then it is always possible to write

$$\hat{\underset{\sim}{n}} = a_S\hat{\underset{\sim}{S}} + a_E\hat{\underset{\sim}{E}} + a_N\,\hat{\underset{\sim}{S}} \times \hat{\underset{\sim}{E}} \tag{2}$$

The problem is now to determine the coefficients a_S, a_E, a_N.

From Eqs. (1) and the normalization condition we have

$$c_S = \hat{\underset{\sim}{n}}\cdot\hat{\underset{\sim}{S}} = a_S + a_E(\hat{\underset{\sim}{S}}\cdot\hat{\underset{\sim}{E}}) \tag{3a}$$

$$c_E = \hat{\underset{\sim}{n}}\cdot\hat{\underset{\sim}{E}} = a_S(\hat{\underset{\sim}{S}}\cdot\hat{\underset{\sim}{E}}) + a_E \tag{3b}$$

$$1 = \hat{\underset{\sim}{n}}\cdot\hat{\underset{\sim}{n}} = a_S^2 + a_E^2 + 2a_Sa_E(\underset{\sim}{S}\cdot\underset{\sim}{E}) + a_N^2\left|\hat{\underset{\sim}{S}} \times \hat{\underset{\sim}{E}}\right|^2 \tag{3c}$$

which have the solution

$$a_S = \frac{1}{\left|\hat{\underset{\sim}{S}} \times \hat{\underset{\sim}{E}}\right|^2}\left[c_S - c_E(\hat{\underset{\sim}{S}}\cdot\hat{\underset{\sim}{E}})\right] \tag{4a}$$

$$a_E = \frac{1}{\left|\hat{\underset{\sim}{S}} \times \hat{\underset{\sim}{E}}\right|^2}\left[c_E - c_S(\hat{\underset{\sim}{S}}\cdot\hat{\underset{\sim}{E}})\right] \tag{4b}$$

$$a_N = \pm\frac{1}{\left|\hat{\underset{\sim}{S}} \times \hat{\underset{\sim}{E}}\right|^2}\left[\left|\hat{\underset{\sim}{S}} \times \hat{\underset{\sim}{E}}\right|^2 - (c_S^2 - 2c_Sc_E(\hat{\underset{\sim}{S}}\cdot\hat{\underset{\sim}{E}}) + c_E^2)\right]^{1/2} \tag{4c}$$

Note that there are two possible solutions for $\hat{n}$. These are shown geometrically in Figure 1.

It will be convenient to define the following quantities

$$\underset{\sim}{a} \equiv \begin{bmatrix} a_S \\ a_E \end{bmatrix} \qquad \underset{\sim}{c} \equiv \begin{bmatrix} c_S \\ c_E \end{bmatrix} \tag{5}$$

$$\underset{\sim}{U} \equiv \frac{1}{\left|\hat{\underset{\sim}{S}} \times \hat{\underset{\sim}{E}}\right|^2} \begin{bmatrix} 1 & -(\hat{\underset{\sim}{S}} \cdot \hat{\underset{\sim}{E}}) \\ -(\hat{\underset{\sim}{S}} \cdot \hat{\underset{\sim}{E}}) & 1 \end{bmatrix} \tag{6}$$

where the tilde below the letter denotes a two-dimensional vector or a 2×2 matrix.

Eqs. (4) can now be written

$$\underset{\sim}{a} = \underset{\sim}{U}\,\underset{\sim}{c} \tag{7a}$$

$$a_N = \pm \frac{1}{\left|\hat{\underset{\sim}{S}} \times \hat{\underset{\sim}{E}}\right|^2} \left[1 - \underset{\sim}{c}^T \underset{\sim}{U}\,\underset{\sim}{c}\right]^{1/2} \tag{7b}$$

The covariance analysis is now straightforward. Define the three-vector

$$\underset{\sim\sim}{a} \equiv \begin{bmatrix} a_S \\ a_E \\ a_N \end{bmatrix} \tag{8}$$

Then the covariance matrix of the measurements is given by

$$\underset{\sim}{P}_c \equiv \langle \delta\underset{\sim}{c}\ \delta\underset{\sim}{c}^T \rangle \tag{9}$$

where the bracket denotes the expectation value and $\delta\underset{\sim}{c}$ is the error in $\underset{\sim}{c}$. The covariance matrix of the spin-axis direction in the non-orthogonal coordinate system is

$$P_a \equiv \langle \delta\underset{\sim}{a}\ \delta\underset{\sim}{a}^T \rangle \tag{10}$$

and in an orthogonal coordinate system

$$P \equiv \langle \delta\hat{\underset{\sim}{n}}\ \delta\hat{\underset{\sim}{n}}^T \rangle \tag{11}$$

Substitution of Eqs. (7) in Eq. (10) gives readily

$$P_a = \left[\begin{array}{c|c} \underset{\sim}{M} & \underset{\sim}{V} \\ \hline \underset{\sim}{V}^T & S \end{array}\right] \tag{12}$$

with

$$\underset{\sim}{M} \equiv \langle \delta\underset{\sim}{a}\ \delta\underset{\sim}{a}^T \rangle = \underset{\sim}{U}\ \underset{\sim}{P}_c\ \underset{\sim}{U}^T \tag{13a}$$

$$\underset{\sim}{V} = \underset{\sim}{M}\ \underset{\sim}{b} \tag{13b}$$

$$S = \underset{\sim}{b}^T\ \underset{\sim}{M}\ \underset{\sim}{b} \tag{13c}$$

$$\underset{\sim}{b} = -\frac{1}{\left|\hat{\underset{\sim}{S}} \times \hat{\underset{\sim}{E}}\right|^2} \quad \frac{1}{a_N} \quad \underset{\sim}{c} \tag{13d}$$

The orthogonal representation of the covariance matrix is then obtained as

$$P = T\, P_a T^T \tag{14}$$

with

$$T = [\hat{\underset{\sim}{S}} \vdots \hat{\underset{\sim}{E}} \vdots \hat{\underset{\sim}{S}} \times \hat{\underset{\sim}{E}}] \tag{15}$$

where the right member of Eq. (13) denotes a matrix labeled by its column vectors.

It is easy to verify that

$$P\, \hat{\underset{\sim}{n}} = 0 \tag{16}$$

as required by the condition that $\hat{\underset{\sim}{n}}$ be a unit vector.

A further representation can be obtained by writing

$$P_a = B \left[\begin{array}{c|c} \underset{\sim}{M} & \underset{\sim}{0} \\ \hline \underset{\sim}{0}^T & 0 \end{array}\right] B^T = B\, M\, B^T \tag{17}$$

where

$$B = \left[\begin{array}{c|c} \underset{\sim}{I} & \underset{\sim}{b} \\ \hline \underset{\sim}{b}^T & 0 \end{array}\right] \tag{18}$$

Equations (17) and (14) may now be combined to give

$$P = \sum_{i=1}^{2} \sum_{j=1}^{2} M_{ij} \underset{\sim}{X}_i \underset{\sim}{X}_j^T \tag{19}$$

where

$$\underset{\sim}{X}_1 = \hat{\underset{\sim}{S}} + b_S(\hat{\underset{\sim}{S}} \times \hat{\underset{\sim}{E}}) \tag{20a}$$

$$\underset{\sim}{X}_2 = \hat{\underset{\sim}{E}} + b_E(\hat{\underset{\sim}{S}} \times \hat{\underset{\sim}{E}}) \tag{20b}$$

Eq. (16) is again satisfied since

$$\underset{\sim}{X}_i \cdot \hat{\underset{\sim}{n}} = 0 \qquad i=1,2 \tag{21}$$

III. Single-Frame Spin-Axis Estimation from the Measurement of Two Arc Lengths and the Included Dihedral Angle

The ambiguity in determining the spin-axis observed in the previous section is removed if the included dihedral angle is also measured. The dihedral angle ψ is defined as the angle between the $(\hat{\underset{\sim}{S}},\hat{\underset{\sim}{n}})$ and $(\hat{\underset{\sim}{E}},\hat{\underset{\sim}{n}})$ planes and is easily shown to be given by

$$\sin\psi = \frac{\hat{\underset{\sim}{n}} \cdot (\hat{\underset{\sim}{S}} \times \hat{\underset{\sim}{E}})}{\sqrt{(1-(\hat{\underset{\sim}{S}} \cdot \hat{\underset{\sim}{n}})^2)(1-(\hat{\underset{\sim}{E}} \cdot \hat{\underset{\sim}{n}})^2)}} \tag{22a}$$

$$\cos\psi = \frac{(\hat{S}\cdot\hat{E}) - (\hat{S}\cdot\hat{n})(\hat{E}\cdot\hat{n})}{\sqrt{(1-(\hat{S}\cdot\hat{n})^2)(1-(\hat{E}\cdot\hat{n})^2)}} \tag{22b}$$

$$\tan\psi = \frac{\hat{n}\cdot(\hat{S}\times\hat{E})}{(\hat{S}\cdot\hat{E}) - (\hat{S}\cdot\hat{n})(\hat{E}\cdot\hat{n})} \tag{22c}$$

The geometry is depicted in Figure 2.

To determine the spin axis attitude it will be convenient to define

$$c_N = \sqrt{(1-c_S^2)(1-c_E^2)}\,\sin\psi \tag{23}$$

and

$$\underset{\sim}{c} = \begin{bmatrix} c_S \\ c_E \\ c_N \end{bmatrix} \tag{24}$$

The vector $\underset{\sim}{a}$ is now determined by four equations

$$c_S = a_S + a_E(\hat{S}\cdot\hat{E}) \tag{25a}$$

$$c_E = a_S(\hat{S}\cdot\hat{E}) + a_E \tag{25b}$$

$$c_N = |\hat{S}\times\hat{E}|^2\, a_N \tag{25c}$$

$$1 = a_S^2 + a_E^2 + 2\,a_S a_E(\hat{S}\cdot\hat{E}) + a_N^2\,|\hat{S}\times\hat{E}|^2 \tag{25d}$$

The three components of $\underset{\sim}{a}$ are now overdetermined. The most convenient solution is obtained by solving the first three equations, which are linear, leading to

$$\underset{\sim}{a} = U \underset{\sim}{c} \tag{26}$$

where

$$U = \frac{1}{\left|\hat{\underset{\sim}{S}} \times \hat{\underset{\sim}{E}}\right|^2} \begin{bmatrix} 1 & -(\hat{\underset{\sim}{S}}\cdot\hat{\underset{\sim}{E}}) & 0 \\ -(\hat{\underset{\sim}{S}}\cdot\hat{\underset{\sim}{E}}) & 1 & 0 \\ 0 & 0 & 1 \end{bmatrix} \tag{27}$$

The spin-axis $\underset{\sim}{n}$ given by this $\underset{\sim}{a}$, however, is not properly normalized since the measurements are not exact. A properly normalized spin-axis vector is then obtained by simply normalizing the solution

$$\hat{n} = \underset{\sim}{n}/\left|\underset{\sim}{n}\right| \tag{28}$$

The covariance matrix of $\underset{\sim}{a}$ is given simply by

$$P_a = U P_c U^T \tag{29}$$

and the covariance matrix for the unnormalized spin-axis is given by

$$P_n = T P_a T^T \tag{30}$$

similarly to Eq. (14). The covariance matrix of the properly normalized spin-axis vector is recovered simply as

$$P = \frac{1}{\left|\underset{\sim}{n}\right|^2} Q P_n Q \tag{31}$$

where

$$Q = I - \hat{\underset{\sim}{n}}\,\hat{\underset{\sim}{n}}^T \tag{32}$$

It is well to ask how good is the approximation of ignoring the normalization condition and then normalizing the solution post hoc. Instead of this seemingly brutal approach one can find the best solution to Eqs. (25abc) subject to the constraint of Eq. (25d), i.e., one seeks to minimize the loss function

$$L(\underset{\sim}{a}) = (\underset{\sim}{c}-A\underset{\sim}{a})^T P_c^{-1} (\underset{\sim}{c}-A\underset{\sim}{a}) \tag{33}$$

subject to the constaint

$$\underset{\sim}{a}^T A \underset{\sim}{a} = 1 \tag{34}$$

where

$$A = U^{-1} = \begin{bmatrix} 1 & (\hat{\underset{\sim}{S}}\cdot\hat{\underset{\sim}{E}}) & 0 \\ (\hat{\underset{\sim}{S}}\cdot\hat{\underset{\sim}{E}}) & 1 & 0 \\ 0 & 0 & |\underset{\sim}{S}\times\underset{\sim}{E}|^2 \end{bmatrix} \tag{35}$$

The solution is straightforward and yields

$$\underset{\sim}{a}_{opt} = (A - \lambda P_c)^{-1} \underset{\sim}{c} \tag{36}$$

where λ is the Lagrange multiplier for the constraint and from Eq. (34) is the root of the equation

$$\underset{\sim}{c}^T \frac{1}{A-\lambda P_c} A \frac{1}{A-\lambda P_c} \underset{\sim}{c} = 1 \tag{37}$$

which yields the smallest value of the loss function.

Equation (36) may be rewritten

$$\underline{a}_{opt} = (I-\lambda P_c U)^{-1}\underline{a} \tag{38}$$

where $\underline{a}$ is given by Eq. (26). Since $\underline{a}_{opt}$ is expected to be close to $\underline{a}$, it follows that $\lambda P_c U$ must be small. An approximate solution for $\underline{a}_{opt}$ can be obtained by expanding Eqs. (37) and (38) in λP_{cc} and solving. This yields

$$\underline{a}_{opt} - \underline{a} \approx \frac{1}{2}\frac{(1-\underline{a}^T A\underline{a})}{a^T A P_c A^{-1} a} P_c U\, \underline{a} \tag{39}$$

Now

$$\langle 1-\underline{a}^T A\underline{a}\rangle = Tr(P_c U) \tag{40a}$$

$$\langle (1-\underline{a}^T A\underline{a})^2\rangle = 4\, \underline{a}^T P_c \underline{a} \tag{40b}$$

so that the additional root mean square (rms) error in $\underline{a}$ when optimality is not taken into account is of the same order of magnitude as the rms error in the cosine measurements. However, the source of this additional error, as shown by Eqs. (40) is the error in the normalization. Hence this error will be greatly reduced when the unit vector is normalized.

IV. Batch Estimation

The value of avoiding trigonometric expressions becomes more obvious in dealing with batch estimation. The computational advantage of the present approach over the geometrical approach[3] is substantial.

For batch estimation the non-orthogonal basis cannot be used since only the Sun vector is constant (and then only for relatively short data spans). The present treatment focuses on the case where the measurements consist of two arc lengths and the included dihedral angle. The extension to other cases is straightforward.

Let $c_S(i)$, $c_E(i)$, $c_N(i)$ be a series of measurements of the Sun projection, the nadir projection, and the Sun-nadir dihedral angle, respectively. Then the best solution for the spin-axis is obtained by minimizing

$$L(\hat{\underset{\sim}{n}}) = \sum_{i=1}^{N} \{ \frac{1}{\sigma_S^2} \left| c_S - \hat{\underset{\sim}{n}} \cdot \hat{\underset{\sim}{S}}_i \right|^2 + \frac{1}{\sigma_E^2} \left| c_E - \hat{\underset{\sim}{n}} \cdot \hat{\underset{\sim}{E}}_i \right|^2 + \frac{1}{\sigma_N^2} \left| c_N - \hat{\underset{\sim}{n}} \cdot (\hat{\underset{\sim}{S}} \times \underset{\sim}{E})_i \right|^2 \} \quad (41)$$

subject to the constraint

$$\hat{\underset{\sim}{n}} \cdot \hat{\underset{\sim}{n}} = 1 \quad (42)$$

In order to decrease the number of subscripts in the expressions it has been assumed that each data type is available at each time and that each measurement type has a single characteristic error. Except for a proliferation of subscripts the expressions which follow are not changed when this assumption is removed.

The minimization of Eq. (41) subject to the constraint is straightforward and leads to

$$\underset{\sim}{\hat{n}} = (M-\lambda I)^{-1} \underset{\sim}{V} \tag{43}$$

where

$$M = \sum_{i=1}^{N} \{\frac{1}{\sigma_S^2} \underset{\sim}{\hat{S}}_i \underset{\sim}{\hat{S}}_i^T + \frac{1}{\sigma_E^2} \underset{\sim}{\hat{E}}_i \underset{\sim}{\hat{E}}_i^T + \frac{1}{\sigma_N^2} (\underset{\sim}{\hat{S}} \times \underset{\sim}{\hat{E}})_i (\underset{\sim}{\hat{S}} \times \underset{\sim}{\hat{E}})_i^T\} \tag{44a}$$

$$\underset{\sim}{V} = \sum_{i=1}^{N} \{\frac{1}{\sigma_S^2} \hat{c}_S(i) \underset{\sim}{\hat{S}}_i + \frac{1}{\sigma_E^2} c_E(i) \underset{\sim}{\hat{E}}_i + \frac{1}{\sigma_N^2} c_N(i) (\underset{\sim}{\hat{S}} \times \underset{\sim}{\hat{E}})_i\} \tag{44b}$$

and λ is the root of

$$\underset{\sim}{V}^T \frac{1}{(M-\lambda I)^2} \underset{\sim}{V} = 1 \tag{45}$$

which leads to the smallest value of Eq. (41).

As in the previous section it can be expected that the constraint can be ignored ($\lambda \approx 0$) and the solution be approximated by

$$\underset{\sim}{\hat{n}} = \underset{\sim}{n} / |\underset{\sim}{n}| \tag{46}$$

where

$$\underset{\sim}{n} = M^{-1} \underset{\sim}{V} \tag{47}$$

This approximation has been tested for one spacecraft[10] and been observed to be quite good. The covariance of $\underset{\sim}{n}$ is given by

$$P_n = M^{-1} \tag{48}$$

and the covariance of the normalized solution is given again by

$$P = \frac{1}{|\underset{\sim}{n}|^2} \; Q \, P_n \, Q \tag{49}$$

V. Measurement Errors

The computation of the spin-axis covariance matrix requires as input a model for the covariance matrix of the cosine measurements. Expressions are derived here for computing these for the case of Sun and Nadir measurements. The treatment when one of these measured quantities is the magnetic field is treated in the same way.

Sun Measurements

The quantity measured is usually the Sun angle, β. Hence,

$$\delta c_S = -\sin\beta \, \delta\beta \tag{50}$$

Nadir Measurements

If the spacecraft has angular velocity ω, then the Earth width is given by

$$\Omega = \omega(t_0 - t_I) \tag{51}$$

where t_I and t_0 are the in- and out-triggering times, respectively, of the Earth scan (for a momentum-wheel mounted scanner, ω will be the

angular velocity of the momentum wheel).

Then, using the results from the appendix

$$\delta c_E = \delta \cos\eta$$

$$= \frac{\partial \cos\eta}{\partial \cos\frac{\Omega}{2}} \delta \cos\frac{\Omega}{2}$$

$$= -\frac{\sin\eta}{\cot\gamma - \cot\eta} \delta \cos\frac{\Omega}{2}$$

$$= \frac{\omega}{2} \frac{\sin\eta}{\cot\gamma - \cot\eta} \left(\sin\frac{\Omega}{2}\right) (\delta t_0 - \delta t_I) \qquad (52)$$

where γ is the scan-cone half angle.

Dihedral Angle Measurements

The dihedral angle ψ is determined from the time interval from the Sun crossing to the mid-point of the horizon scan

$$\psi = \omega\left[t_S - \frac{1}{2}(t_0 + t_I)\right] \qquad (53)$$

Thus, (β, Ω, ψ) or (β, η, ψ) is a set of statistically independent variables. The "dihedral cosine" c_N, however, is given by

$$c_N = \sin\beta \sin\eta \sin\psi \qquad (54)$$

hence

$$\delta c_N = c_N\left[\cot\beta \ \delta\beta + \cot\eta \ \delta\eta + \cot\psi \ \delta\psi\right] \qquad (55)$$

From Eqs. (50-55) the covariance matrix P_c can easily be calculated.

To a large degree, much of the trigonometric complexity which has been removed from the attitude solution has simply been shifted to the computation of a derived measurement covariance matrix. There is, however, a substantial gain because the covariance matrix need not be computed to the same degree of accuracy as the spin-axis attitude itself. Hence, a great deal of computational approximation is possible, such as approximation of the trigonometric functions by simple rational functions.

Appendix - Measurement of the Nadir Angle

Because the Earth is an extended body the nadir vector is not measured directly but determined from measurements of the Earth width. Earth widths are measured by a horizon scanner, which effectively is a sensor mounted on a rotating cone (of half-cone angle γ) about the spacecraft spin axis, which detects the crossings of the Earth horizon on the scan cone. The Earth has an effective angular radius of ρ, which is a function of altitude and (for a non-spherical Earth) latitude. The Earth width is the dihedral angle between the in- and out-crossings (H_I and H_O) the horizon by the scanner and is denoted by Ω. These quantities are related by the spherical law of cosines[2]

$$\cos\rho = \cos\gamma \cos\eta + \sin\gamma \sin\eta \cos(\Omega/2) \qquad \text{(A-1)}$$

The geometry is depicted in Figure 3.

Eq. (A-1) may be solved to give

$$\cos\eta = \frac{\cos\rho \cos\gamma \pm \sin\rho \cos(\Omega/2) \sqrt{A - \cos^2\rho}}{A} \qquad \text{(A-2)}$$

where

$$A = \cos^2\rho + \sin^2\gamma \cos^2(\Omega/2) \qquad \text{(A-3)}$$

The sign ambiguity may be eliminated if another measurement is present, say that of the Sun angle, β, and the Sun-Earth dihedral angle, γ. Let ξ be the arc length from the Sun direction to the mid scan point

$$\cos\xi = \cos\beta \cos\gamma + \sin\beta \sin\gamma \cos\psi \qquad \text{(A-4)}$$

Then it is possible to show that the underdetermined sign in Eq. (A-2) must be the same as that of

$$(\cos\beta - \cos\gamma)\ (\hat{E}\cdot\hat{S} - \cos\xi)$$

Alternatively, one may consider simultaneously Sun and horizon measurements. This leads to three simultaneous equations

$$\cos\beta \cos\eta + \sin\beta \sin\eta \cos\psi = \hat{E}\cdot\hat{S} \qquad \text{(A-5a)}$$

$$\cos\gamma \cos\eta + \sin\gamma \sin\eta \cos(\Omega/2) = \cos\rho \qquad \text{(A-5b)}$$

$$\cos^2\eta + \sin^2\eta = 1 \qquad \text{(A-5c)}$$

Equation (A-2) was obtained by solving Eqs. (A-5b) and (A-5c) simultaneously. One could just as easily solve Eqs. (A-5a) and (A-5b) for $\cos\eta$ and $\sin\eta$. The result will not necessarily satisfy Eq. (A-5c) but the two equations have the advantage of being linear. The solutions can then be renormalized to satisfy Eq. (A-5c).

This approach of ignoring the proper normalization for the trigonometric functions has another advantage in that a simultaneous solution to Eqs. (A-5b) and (A-5c) may not exist in certain extreme cases because the measurements are not exact. By solving Eqs. (A-5a) and (A-5b) a solution will always exist.

There is, however, one clear disadvantage. If Eq. (A-2) is used then β, η, and ψ will be statistically independent. If, however, the linear equations are solved, η will be correlated with β and ψ. Thus, the simplicity gained in computing cosη is counterbalanced by greater complexity in computing the measurement covariance matrix P_c.

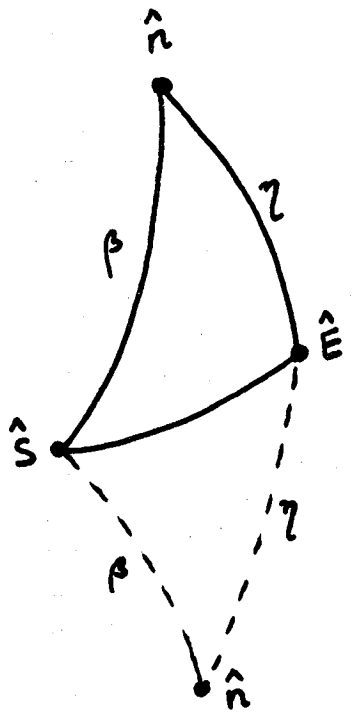

Figure 1
Single-Axis Attitude from Two
Arc-Length Measurements

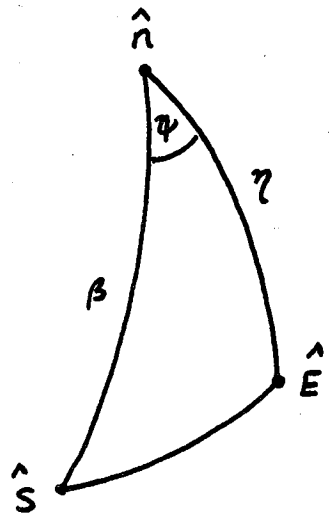

Figure 2

Single-Axis Attitude from Measurements of Two Arc Lengths and One Dihedral Angle

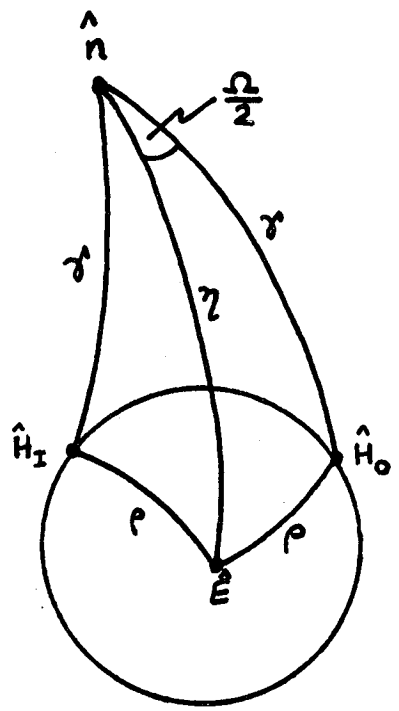

Figure 3

Geometry for Nadir-Angle Determination

References

1. Shuster, M.D., and Oh, S.D., "Three-Axis Attitude Determination from Vector Observations," Journal of Guidance and Control, vol. 4, no. 1, pp. 70-77, Jan.-Feb., 1981.

2. Wertz, J.R. (ed.), "Spacecraft Attitude Determination and Control" (Chapters 10 and 11), D. Reidel Publishing Co., Dordecht, the Netherlands 1981.

3. Werking, R.D., "A Generalized Technique for Using Cones and Dihedral Angles in Attitude Determination," NASA X-581-73-292, September 1973.

4. Wertz, J.R., and Chen, L.C., "Geometrical Procedures for the Analysis of Spacecraft Attitude and Bias Determinability," Paper No. AAS75-047, AAS/AIAA Astrodynamics Specialist Conference, Nassau, Bahamas, July 28-30, 1975.

5. ibid, "Geometrical Limitations on Attitude Determination for Spinning Spacecraft," J. Spacecraft, vol. 13, pp. 564-571, 1966.

6. Chen, L.C., and Wertz, J.R., "Single-Axis Attitude Determination Accuracy," AAS/AIAA Astrodynamics Conference, Grand Teton Nat. Park, Wyoming, Sept. 7-9, 1977.

7. Chen, L.C., Attitude Determination Accuracy Constraints on the SIRIO Launch Window, Computer Sciences Corporation, CSC/TM-76/6210, September 1976.

8. Wertz, J.R., "Spherical Geometry," in Wertz, J.R., (ed.) Spacecraft Attitude Determination and Control (Appendix A), D. Reidel Publishing Company, Dordecht, the Netherlands, 1978.

9. Grubin, C., "Simple Algorithm for Intersecting Two Conical Surfaces," J. Spacecraft, Vol 14, pp. 251-252, 1977.

10. Thompson, R.H., Neal, G.F., and Shuster, M.D., "Spin-Axis Attitude Estimation and Sensor Bias Determination for AMPTE," Flight Mechanics/Estimation Theory Symposium, NASA Goddard Space Flight Center, Greenbelt, Maryland, October 27-28, 1981.